Experimental study and numerical simulation of iron oxide scales mechanical behavior in hot rolling

Benjamin Picque

ECOLE DES MINES
DE PARIS

Ecole Doctorale 364 : Sciences Fondamentales et Appliquées

T H E S E

pour obtenir le grade de
Docteur de l'Ecole des Mines de Paris
Spécialité «Mécanique Numérique»

présentée et soutenue publiquement par

M. Benjamin Picqué

le 7 Septembre 2004

EXPERIMENTAL STUDY AND NUMERICAL SIMULATION OF IRON OXIDE SCALES MECHANICAL BEHAVIOR IN HOT ROLLING

(Etude expérimentale et simulation numérique
du comportement mécanique des calamines lors du laminage à chaud)

Directeurs de thèse :
Pierre MONTMITONNET, Pierre-Olivier BOUCHARD

Jury :

Pr. Gérard Moulin	Président
Pr. John H. Beynon	Rapporteur
Pr. Laurent Dubar	Rapporteur
M. Vincenzo Lanteri	Examinateur
M. Michel Picard	Examinateur

REMERCIEMENTS

Enfin, je voudrais remercier pour terminer les personnes les plus chères à mon cœur, ma famille et mes amis. Je pense que vous savez tous ce que vous représentez pour moi. Je ne m'étendrai donc pas, ce serait trop long et je préfère le faire de vive voix. En quelques mots :

Manue (la plus adorable, talentueuse et sexy des conseillères administratives), Jul (maille anglich titcheur, merci pour la relecture d'une partie de ce manuscrit : et dire que t'as raté la soutenance !), Tof (the best of crazy Fenwick drivers), Aurel (ma thésarde préférée du CEMEF). Merci pour votre amitié sans faille. Enfin, comme dirait le grand Djumbowitch « Si vous étiez vraiment des amis, vous viendriez habiter à Pamiers ! » :-(

Mes parents : Je ne vous remercierai jamais assez de m'avoir toujours poussé, soutenu et permis d'en arriver là. Merci aussi d'avoir organisé « champagnifiquement » ma soirée de thèse qui concluait en beauté une inoubliable journée.
Mam, ta cocotte restera comme pièce de musée !

Merci à ma grand-mère, Simonne, pour tout, pour son aide permanente, pour le fait d'accompagner ma vie tout simplement, sans jamais être trop loin de moi.

Merci à ma sœur d'avoir toujours été là quand j'en avais besoin. Qu'elle sache que notre complicité est extrêmement importante pour moi.

Merci à ma grand-mère Léonie, pour ses encouragements et pour être venue assister à ma soutenance.

Anne, merci d'avoir toujours su que ça se passerait bien, merci pour ta confiance et ton soutien.

Merci également à mon Beaup' Didier (même s'il ne connaît pas son do), ma marâtre préférée Nath, mon petit Xav, Aurélie Paulette, Guillaume alias Sir William (faudrait quand même qu'on commence à répéter notre prochain concert) et Manue pour votre soutien et vos encouragements.

Enfin, merci à mon p'tit bout, Salia. Merci de m'avoir supporté surtout lors des difficiles six derniers mois, de m'avoir toujours encouragé et motivé ; merci d'être toujours présente. Tu es mon petit soleil. Je t'aime.

A mon grand père …

A mon petit frère …

CONTENTS

INTRODUCTION

CHAPTER I. HOT ROLLING PROCESS

CHAPTER II. OXIDE SCALE PROPERTIES

CHAPTER III. NUMERICAL DEVELOPMENTS

CHAPTER IV. THE 4-POINT HOT BENDING TEST

CHAPTER V. EXTENSION TO OTHER STRAIN AND STRESS STATES: TENSION AND COMPRESSION

CHAPTER VI. HOT ROLLING SIMULATIONS

GENERAL CONCLUSION AND PERSPECTIVES

APPENDICES

TABLE DES MATIERES

INTRODUCTION

CHAPITRE I. LE LAMINAGE A CHAUD

CHAPITRE II. PROPRIETES DE LA CALAMINE

CHAPITRE III. DEVELOPPEMENTS NUMERIQUES

CHAPITRE IV. L'ESSAI DE FLEXION QUATRE POINTS

CHAPITRE V. EXTENSION AUX AUTRES ETATS DE CONTRAINTE ET DEFORMATION : TRACTION ET COMPRESSION

CHAPITRE VI. SIMULATIONS DU LAMINAGE A CHAUD

CONCLUSION GENERALE ET PERSPECTIVES

ANNEXES

Introduction

INTRODUCTION

Context and industrial stakes

Hot rolling of steels represents one of the **most critical** steps to achieve finished products having a **high surface quality**. The increasing productivity added to the rising customer requirements result in **more and more severe** scheduling rules for the HSM. Strip surface aspect is very important issue in terms of HSM **operation costs** and productivity limitation.

The present research was proposed by the **ARCELOR** group. ARCELOR is a merger of **Arbed, Aceralia**, and **Usinor**, and was created by the common will of these three European groups to mobilize their technical, industrial, and commercial skills to create a global leader aiming to be a major player in the steel industry. This group is developing its activities in four core businesses: it is the **world's biggest producer** of Flat Carbon Steel and Long Carbon Steel, among the **leaders** in Stainless Steel production, and among the largest firms in Europe for Distribution, Transformation and Trading.

In 2004, **non-quality** of coils represents 5.7% of the Dunkerque hot strip mill added costs. This cost is shared among the **end of line inspectors**, the maintenance of automatic **inspection system** and the cost due to **premature roll change.** Nevertheless, the direct costs of rolled-in scale defect are presently **much lower than a few years ago**. Indeed, apart from progress realized on new work-rolls grades, the rolling operators have established **tight programming rules**, which dramatically decrease **and nearly eliminate the rolled-in scale occurrence** (internal customer claim ratio is currently below 0.1 %).

Nevertheless, these rules are **important constraints** for ARCELOR Hot strip mills:
- use of lubricants;
- high work-rolls watering;
- limitation of schedule length;
- limitation of "hard" strips number per schedule;
- time increase between two bars.

These preventive measures **are costly,** especially because they **hamper the HSM productivity.** Actually, the indirect costs of rolled-in scale far exceed the direct costs. But they are difficult to estimate and may dramatically vary from one plant to another.

The first objective is to define enlarged "rolled-in scale safe" operating conditions. Today scheduling rules are very restrictive. The aim is to enlarge operating conditions so that the HSM would be more flexible and with a higher productivity.
The second objective is to establish an early and robust rolled-in scale warning indicator by linking data coming from the surface inspection system with process data.

So the main stake is the HSM productivity, and this is a major challenge. All ARCELOR plants aim to increase their production.

Scientific stake

Among all surface defects, the **most crippling** comes from the oxide scale formed at the surface of the steel during the hot rolling, at the entry of the **finishing mill** (last part of the hot strip mill): **the secondary scale**. Its mechanical behavior is still **poorly known**. This kind of defect involves, for hot strip mills, downgradings, customers litigations, but also many constraining manufacturing rules described previously.

The secondary scale can crack under the stresses imposed by the successive rolling passes, and can be embedded in its steel substrate: this defect is called **rolled-in scale defect**.
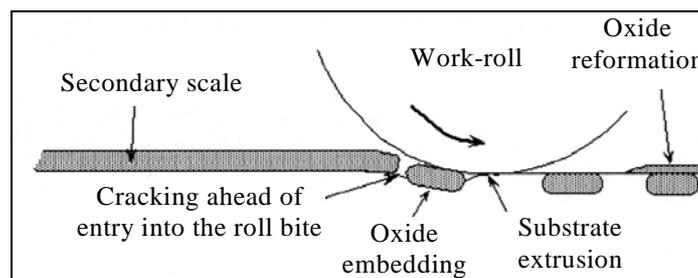
In addition, the **extrusion** of the subjacent metal inside the oxide cracks involves important local **modifications of friction** conditions and **heat transfer**. Consequently, a precise description of oxide scale deformation mechanisms is necessary to better define the boundary conditions in a roll bite and to better understand the initiation mechanisms of rolled-in scale defects. Previous industrial researches and observations have pinpointed different key parameters acting on rolled-in scale: secondary scale breaker, steel grade, strip temperature and work rolls degradation.

Currently, only one model of the oxide scale damage in a roll gap exists. It has been developed at the University of Sheffield by Professor Beynon and Doctor Krzyzanowski's research team, using the MARC finite element code.

Our scientific objective is then to provide a realistic physical and numerical model able to simulate the oxide scale flow in a roll bite and in particular, its damage.

Study development

This PHD study has implied a close collaboration between **ARCELOR RESEARCH S.A** (IRSID new name), the research centre of the ARCELOR group, and the **CEMEF**, the center of material forming processes of the **Ecole des Mines de Paris**. The first one allows having a direct contact with the **industrial process** and has different **experimental tests** able to characterize the oxide scales. On the other side, the CEMEF develops different **finite element codes** allowing simulating **materials forming**.

The study is then articulated around two extremely linked parts: numerics and experiments.

PHD manuscript outline

The objective of this PHD study is then to be able to **numerically reproduce the oxide scale behavior in a finishing mill stand**. The manuscript is divided in six chapters.

In the first chapter, **successive steps** of the extremely complex and precise **hot rolling process** are described, which progressively lead us to the stand of **finishing mill** we are interested in. A **thermo-mechanical description** of a finishing mill stand is realized, and several possible **origins of rolled-in scale defects** are presented. Several **rolling observations** (on industrial or pilot mills) are also given.

After the presentation of the industrial process and the context of the study, the second chapter highlights **the physical properties of the oxide scale in the finishing mill** (growth kinetics, morphology, temperature…) as well as its **mechanical properties**.

The third chapter introduces the **Forge2® finite element software** selected for this study to simulate the oxide scale behavior in a finishing mill stand. The **numerical developments** performed to simulate the different kinds of **oxide damage** (crack, decohesion, sliding, extrusion) are described.

The fourth chapter is devoted to **the mechanical test** selected at the origin of this study to reproduce the **solicitations undergone by the oxide scale at the entry of the roll gap** and suspected to be the critical stage for damage: **the 4-point bending test**. A **numerical study** is performed as well.

Due to important **limitations** of the previous test, a complementary experimental and numerical study using **tensile tests** and **plane strain compression tests** has been performed. With these three mechanical tests, **the mechanical description of a rolling stand is sufficiently complete to simulate the industrial process in good conditions**.

The sixth and last chapter then presents **several rolling simulations**.

INTRODUCTION

INTRODUCTION

Contexte et enjeux industriels

Le laminage à chaud des aciers représente une des étapes l**es plus critiques** dans l'obtention de produits finis ayant **une bonne qualité de surface.** L'augmentation de la productivité ajoutée à l'accroissement des besoins du client induit des règles de plus en plus sévères pour les trains à bandes. L'aspect de surface d'une bande est un enjeu très important en terme de coûts d'opérations du laminoir et de limitation de productivité.

Cette présente recherche a été proposée par le groupe **ARCELOR.** ARCELOR, issu de la fusion de **Arbed, Aceralia**, et **Usinor**, a été créé par un voeu commun de ces trois groupes européens pour conjuguer leurs techniques industrielles et leurs habiletés commerciales en vue de devenir un leader global et viser le leadership de l'industrie de l'acier. Ce groupe développe ses activités en quatre corps d'affaires : c'est le plus **grand producteur mondial** d'aciers plats au carbone et d'aciers longs au carbone, parmi les leaders dans la production de l'acier inoxydable, et parmi les plus grandes firmes en Europe pour la Distribution, la Transformation et le Commerce.

En 2004, la **non qualité** des bobines représente 5,7% des coûts ajoutés du laminoir à chaud de Dunkerque. Ce coût est partagé entre les **contrôleurs de ligne**, la maintenance du système d'**inspection automatique** et les coûts dus au **changement prématuré de cylindres**. Néanmoins, les coûts directs du défaut d'incrustation sont actuellement **bien moins élevés qu'il y a quelques années.** En effet, mis à part les progrès réalisés sur les nouvelles nuances de cylindres de travail, les opérateurs de laminage ont établi des **règles de programmation étroites,** qui diminuent significativement et éliminent presque l'apparition des défauts d'incrustations (pourcentage de réclamations clients fréquemment inférieures à 0.1 %).

Néanmoins, leurs rôles représentent d'importantes contraintes pour les trains à bandes d'ARCELOR :
- besoin de lubrifiants ;
- arrosage des cylindres ;
- limitation de la longueur ;
- limitation du nombre de bandes "dures" ;
- augmentation du temps entre deux brames.

Ces mesures préventives sont coûteuses, spécialement du fait qu'elles ralentissent la productivité des trains à bandes. Actuellement, les coûts indirects de calamine incrustée excèdent de loin les coûts directs. Ils sont cependant difficiles à estimer et peuvent varier dramatiquement d'une installation à l'autre.

L'objectif premier est de définir des plages de sécurité pour les conditions d'opération en terme de défaut d'incrustation. Aujourd'hui les règles de ligne sont très restrictives. Le but est d'élargir les conditions d'opération pour que les trains à bandes soient plus flexibles et aient une productivité accrue.
Le second objectif est d'établir un indicateur robuste d'avertissement de défauts d'incrustation, en reliant les données venant du système d'inspection de surface avec les données du process.

Le principal enjeu est donc la productivité des trains à bandes, et c'est un enjeu majeur. Toutes les usines ARCELOR visent à augmenter leur productivité.

Enjeu scientifique

Parmi tous les défauts de surface, **le plus défavorable** provient de la couche d'oxyde (calamine) formée à la surface de l'acier pendant le laminage à chaud, à l'entrée du finisseur (dernière partie du laminoir) : **la calamine secondaire**. Son comportement mécanique est toujours mal connu. Ce type de défaut engendre, pour les laminoirs à chaud, déclassements, litiges clients, mais aussi beaucoup de règles de fabrication contraignantes décrites précédemment.

La calamine secondaire peut être fissurée sous les contraintes imposées par les passes successives de laminage, et peut être incrustée dans son substrat en acier ; ce défaut est appelé « défaut de calamine incrustée ».
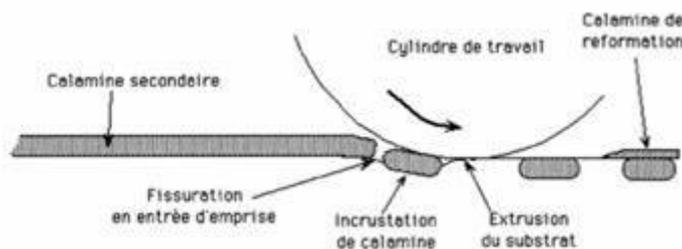
De plus, l'**extrusion** du métal sous-jacent dans les fissures de calamine engendre d'importantes **modifications** locales des **conditions de frottement** et de **transfert thermique**. En conséquence, une description précise des mécanismes de déformation de la calamine est nécessaire pour définir au mieux les conditions aux limites dans une emprise, et mieux comprendre les mécanismes de défauts d'incrustations. De précédentes études et observations industrielles ont mis en évidence différents paramètres clés agissant sur le défaut d'incrustation : fissuration de la couche d'oxyde, la nuance d'acier, la température de bande et l'usure des cylindres.

Actuellement, seul un modèle d'endommagement de calamine dans une emprise existe. Il a été développé à l'Université de Sheffield par l'équipe de recherche du Professeur Beynon et du Docteur Krzyzanowski, en utilisant le code éléments finis MARC.

Notre objectif scientifique est donc de réaliser un modèle physique et numérique réaliste, capable de simuler l'écoulement de la calamine dans une emprise de laminage, et en particulier son endommagement.

Déroulement de l'étude

Cette étude de thèse a impliqué une étroite collaboration entre le groupe **ARCELOR RESEARCH S.A** (nouveau nom de l'IRSID), centre de recherche du groupe ARCELOR, et le CEMEF, Centre de Mise en Forme des matériaux de l'**Ecole des Mines de Paris**. Le premier permet d'avoir un contact direct avec le **procédé industriel** et de réaliser différents **tests expérimentaux** capables de caractériser les calamines. D'un autre côté, le CEMEF développe différents **codes éléments finis** permettant de simuler la **mise en forme des matériaux**.

L'étude est donc articulée autour de deux parties extrêmement liées : une numérique et une expérimentale.

Plan du manuscrit de thèse

L'objectif de cette thèse est donc d'être capable de reproduire numériquement le comportement de la calamine dans une cage de finisseur. Le manuscrit est divisé en six chapitres.

Dans le premier chapitre, les étapes successives du procédé extrêmement complexe et précis de laminage à chaud sont décrites, ce qui nous mène progressivement à la cage du finisseur qui nous intéresse. Une description thermomécanique d'une cage de finisseur est réalisée, et plusieurs origines possibles du défaut de calamine incrustée sont présentées. Plusieurs observations (sur laminoirs industriels et pilotes) sont également données.

Après la présentation du procédé industriel et du contexte de l'étude, le second chapitre met en évidence les **propriétés physiques des calamines dans le finisseur** (cinétiques de croissance, morphologie, température…) ainsi que ses **propriétés mécaniques.**

Le troisième chapitre introduit le **logiciel éléments finis Forge2®** sélectionné pour cette étude pour simuler le comportement de la calamine dans une cage de finisseur. Les **développements numériques** réalisés pour simuler les différents types d'**endommagement de la calamine** (fissure, décohésion, glissement, extrusion) sont décrits.

Le quatrième chapitre est consacré au **test mécanique** sélectionné à l'origine de cette étude pour reproduire les **sollicitations subies par la couche d'oxyde en entrée d'emprise** et suspectées d'engendrer son endommagement critique : le **test de flexion 4 points**. Une **étude numérique** est réalisée en parallèle.

Du fait d'importantes **limitations** du test précédent, une étude complémentaire expérimentale et numérique utilisant des tests de traction et de bipoinçonnement a été réalisée.
Avec ces trois tests mécaniques, la description mécanique d'une cage de laminage est suffisamment complète pour simuler le procédé industriel dans de bonnes conditions.

Le sixième et dernier chapitre présente alors **plusieurs simulations de laminage**.

INTRODUCTION

The Hot Rolling Process

Résumé

Nous nous intéressons dans cette étude aux défauts de type "calamine incrustée". Pour comprendre ses mécanismes de formation, il est important de décrire dans un premier temps le contexte, le laminage à chaud, et de localiser son domaine d'existence.

Ce chapitre présente donc tout d'abord le procédé industriel de laminage pour arriver à la dernière partie du process, le finisseur, dans lequel les défauts d'incrustation s'initient.
La description thermomécanique du finisseur ainsi que celle d'une cage isolée montre la complexité du problème. En plus des déformations énormes engendrées par un tel procédé, les cycles thermiques s'avèrent également extrêmement critiques.

Les phénomènes thermiques sont observés macroscopiquement et microscopiquement. Le premier cas concerne principalement le cylindre froid. Son bref contact avec la bande chaude augmente sa température qui diminue dès que le contact se termine. Ces variations de température entraînent sa détérioration. Le deuxième cas concerne la couche de calamine qui joue le rôle de barrière thermique si elle n'est pas endommagée.
L'endommagement est très lié à la température. Les mécanismes de laminage doivent donc être étudiés avec beaucoup d'attention.

En terme de contraintes, deux contributions sont prises en compte dans le finisseur : les contraintes thermiques dans les intercages et les contraintes mécaniques à l'entrée et sous l'emprise des cages.
En terme d'incrustation de calamine, deux mécanismes sont à l'origine du défaut :
- *la fissuration de la calamine en entrée d'emprise, suivie de l'extrusion de l'acier dans les fissures sous les cylindres ;*
- *l'effet d'imprimerie sur la bande (lié à la rugosité des cylindres et à l'incrustation de résidus).*

Les contraintes de traction en entrée d'emprise restent la principale cause de l'endommagement de la calamine. Les contraintes compressives semblent intervenir majoritairement dans le défaut critique d'incrustation.

La grande difficulté de cette étude est que tous les paramètres sont étroitement liés (température, frottement, épaisseur de calamine, nuance d'acier, réduction ...).

I. INTRODUCTION

Our interest is in **the rolled-in scale defect**. To understand its initiation mechanisms, it is important to describe in a first stage the context, the hot rolling process, and to locate its domain of existence.

This first chapter is then divided in five parts:

First, the fabrication of steel sheets using the **hot rolling process** is presented.

In a second part, we see that rolled-in scale defects are initiated in the finishing mill, which represents the last part of the hot rolling process and consists in a succession of rolling stands.

Thus, a stand as well as complex thermo-mechanical mechanisms intervening in it are described in a third part.

In the fourth part, several possible origins of rolled-in scale defects are proposed.

Finally, the last part is devoted to industrial and pilot rolling mill observations.

II. HOT ROLLING PROCESS

The steel sheet fabrication consists of three stages:
- Ironmaking: to transform ore into desulfurized cast iron.
- The steel-works: to transform cast iron into steel and continuously cast it into a solid product (slab).
- Rolling: to transform slabs into finished products (coils). (Hot rolling and cold rolling).

Figure I-1: Schematic representation of Fos sur Mer HSM.
Représentation schématique du train à bande (TAB) de Fos sur Mer.
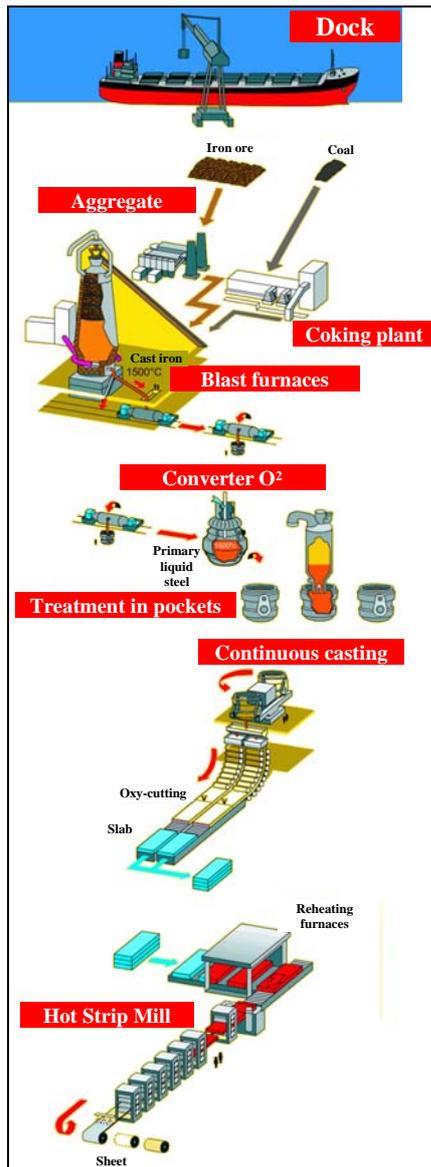
Let us take for example the **Fos sur Mer Hot Strip Mill (HSM)** (Figure I-1) [Fos]:

The steel elaboration **requires iron ore, coal, lime, ferro-alloys** (manganese, aluminium, silicon, chromium, vanadium, titanium, …) which bring it particular characteristics, according to its use. One also needs much water to cool the installations because steel is elaborated above 1500°C.

The raw materials (ore, coal) come from Brazil, Mauritania, Australia, Canada, USA and Colombia.

Coke is made with coal and is used as fuel for **blast furnaces** to reduce the ore. Coal cannot be used directly because it must be disencumbered of its impurities and its humidity. These operations are performed in a **coking plant**. The coal is distilled in furnaces during 17h to extract the volatile matters. **The cast iron** is also obtained in mixing ore and coke in the blast furnace. Iron liquid leaves for the **steel-works** in special coaches called "**barrel ladles**" enable to maintain the cast iron at high temperature (1500°C) during more than 48h; then it is transformed into steel. For this, the liquid cast iron is added to **scrap** in a converter (capacity: 350tons) and puffed up with oxygen during 15mn. It is poured in pockets in which ferro-alloys are added. The steel of precise composition is then cast in a **continuous caster** in order to solidify in the form of a long non-interrupted slab that will be cut out by blowtorches in order to give **slabs**. A slab thus produced is a steel parallelepiped approximately 10 m long, 1.5 m wide and 20 cm thick, weighing on average 25 tons.

It is finally rolled to become a coil.

Our interest is only in the **Hot Strip Mill** (HSM), from the furnaces to the coiling area through ca. 12 rolling stands. The importance of this process is reflected in the number of specialists devoting their time and care to its optimisation. Almost 1 kilometer in length, it is equipped with more computers than a space shuttle !

The HSM (Figure I-2) makes it possible to obtain, from a slab of 250mm, a sheet coil between 2 and 5mm thick. By successive passages between rolls (Figure I-3), the slab is progressively reduced to the finished product thickness. This operation is called **hot rolling**.
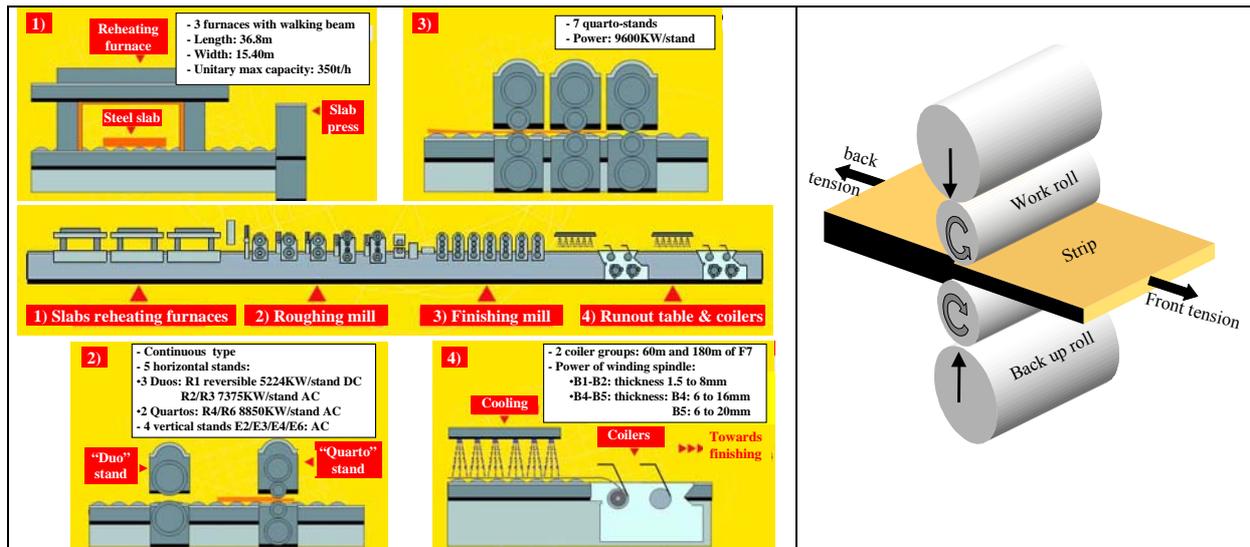
Figure I-2: General view of a HSM (Sollac – Fos sur mer) [Fos]

Vue générale du TAB (Sollac – Fos sur mer) [Fos]

Figure I-3: 4 high stand

Cage quarto

Principal steps of the hot factory:

Reheating furnace: the slab is a gross product of solidification. In order to give it a metallurgical structure and to put in solution additional elements, it undergoes a heat treatment during approximately 3 hours. The furnace temperature reaches 1200 to 1250°C. Burners are placed on the top and below the slab level to obtain an identical heating on both faces. During this stage an oxide scale, called primary scale approximately between 500 to 1000µm thick, grows on the steel slab. Then the slab is gently removed using an automatic lift and placed on a conveyor.

The slab is conveyed from the furnace to a series of automated roughing and finishing stands. This group of machines rolls it into sheet steel using a pressure above the yield stress (a few tens to a few hundred MPa).

RSB descaling (Roughing Scale Breaker): At the exit of the furnaces, the primary scale must be removed, not to be irreversibly embedded in the metal and form important defects. To avoid this, a descaling ramp is installed. Nozzles project water under-pressure (150 bars) on the product. A combination of thermal and mechanical effects removes the thick primary scale before the first roughing mill stand.

Roughing mill: One stand of width reduction is placed after the descaling. Indeed the continuous casting cannot change each time its mould to answer the schedule conditions. Slab width must be sometimes altered. This is performed by a stand with vertical rolls.

Slab thickness is reduced in the five roughing mill stands until being usable by the finishing mill (30-40mm). A descaling ramp is placed between each stand to obtain a better surface state.

At the exit, its temperature is ~1100°C and the oxide scale that covered it is between 60 and 100μm thick.
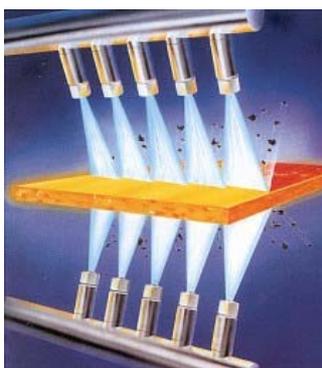
Shear and FSB descaling (Finishing Scale Breaker): Slab extremities are naturally deformed in the roughing mill. If they are rolled in the finishing mill, the deformations amplification can become dangerous in the last stands and during coiling. Thus they are cut to enter straight and perpendicular to the rolling direction in the first finishing stand. Just after the shear is the FSB. The scale previously formed is partially removed. It is very important to ensure the good surface state at the entry of the finishing mill. If it is not efficient, it will be a major source of **rolled-in-scale defects**.

Finishing mill: It is made (not in all rolling mill) of 7 identical quarto stands (two work-rolls and two support rolls to limit the deformation under loading) (Figure I-3). Strip thickness is reduced here from 30-40mm to 2-5mm and it leaves the last stand at around 60km/h.

In the finishing mill the product can be sprinkled between each stand, depending on the desired metallurgical treatment.
Finishing mill is precisely described in the next part.
After the last stand, the steel sheet is carried away on a table and cooled before being coiled.

Coiling: Finally steel sheets, 2 to 5mm thick and up to 700m long, are coiled for storage.

Cold factory: In the cold factory, coils are pickled in sulfuric or chlorhydric acid baths, then dried and cold rolled. This stage sometimes reveals defects initiated during hot rolling.

Between the moment when the slab leaves the furnaces at 1200°C and when it becomes a coil, 3mn have elapsed.
Automatic systems are used to make sure that the slab is handled delicately - the process is so precise that even the slightest scratch can ruin the product (tolerance levels are very small considering the precision required by the customer).

III. FINISHING MILL

Figure I-4 schematically represents a standard 7-stands finishing mill (FM).
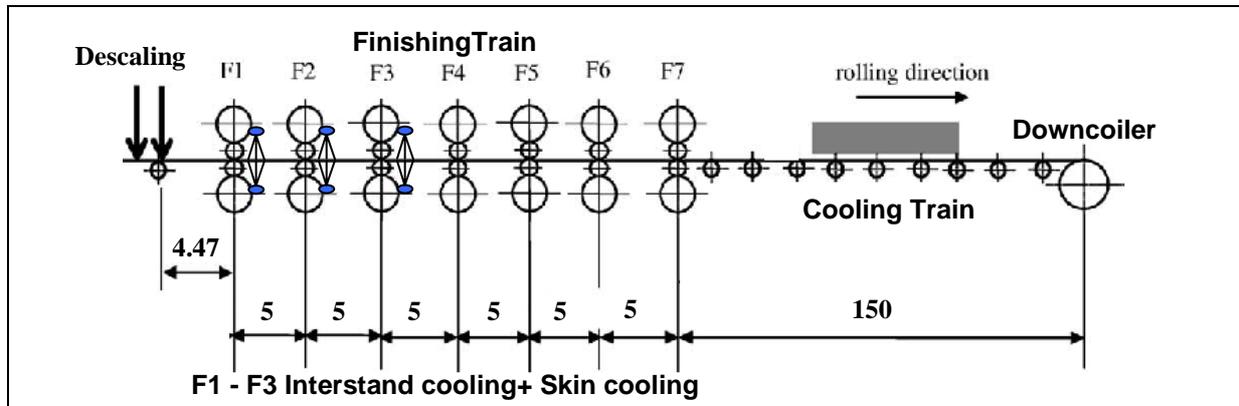
Figure I-4: Schematic view of a 7-stands finishing mill.

Vue schématique d'un finisseur 7 cages.

The FM is the most important part of the HSM, because at its exit is obtained the final product. In FM, the strip is engaged in all stands simultaneously. This allows imposing tensions to the strip in the interstands playing with the roll velocity (the strip velocity increases when it is reduced). Heat transfer is also complicated because it has to obey diverse conditions:
- temperature must be high enough not to necessitate too high rolling force;
- it must respect the structure to be given to the metal;
- it must not be too high not avoid too thick oxide scale…

Quantitative data are gathered in Table I-1.

	R5-FSB	FSB-F1	F1	interstand F1-F2	F2	interstand F2-F3	F3	interstand F3-F4	F4	interstand F4-F5	F5	interstand F5-F6	F6	interstand F6-F7	F7	interstand F7-coiler
Strip thickness (mm)	35.92	35.92	↘	18.91	↘	9.9	↘	7.76	↘	5.37	↘	3.84	↘	3.13	↘	2.82
Reduction (%)			47.355		47.647		21.616		30.799		28.492		18.49		9.9	
Strip temperature (entry) (°C)	1085	950	963		930.3		920.9		915.8		910.6		906.9		895.9	
Roll temperature (°C)			30		30		30		30		30		30		30	
Interstand distance (m)	139.74	4.47		5		5		5		5		5		5		150
Interstand velocity (m/mn)	120	45		67.0		118.1		156.7		227.6		320.4		402.4		500
Interstand time (s)	279	5.960		4.478		2.542		1.915		1.318		0.936		0.746		18
Roll diameter (mm)			676.2		722.4		748.5		760.3		703.3		746.4		771.5	
Roll Velocity (tr/mn)			26.38		44.38		66.62		95.3		145.03		171.6		184.27	
Neutral point velocity (m/mn)			56		118		156.7		227.6		320.4		402.4		446.6	
contact time (s)			0.086		0.031		0.016		0.009		0.005		0.003		0.002	
contact arc length (mm)			80.1		60.9		42.7		33.2		26.7		20.4		14	
Rolling load mesured (T)			2420.1		2281.2		2268.7		2076		1938.2		1659.7		928.2	
Strip width (mm)	953.9	953.9	953.9	953.9	953.9	953.9	953.9	953.9	953.9	953.9	953.9	953.9	953.9	953.9	953.9	953.9

Table I-1: Example of characteristics data in a finishing mill (assessment of Arcelor HSM data)

Exemple de données caractéristiques dans un finisseur (bilan de données des TAB d'Arcelor)

IV. A STAND

The deformation of the product needs an energetic contribution given by the roll drives. The metal deformation strength involves a force which separates, flattens and bends the rolls (Figure I-5). This loading is compensated by the elastic deformation of the stand: it is the machine yielding (Figure I-6) [Ber,Mon1].
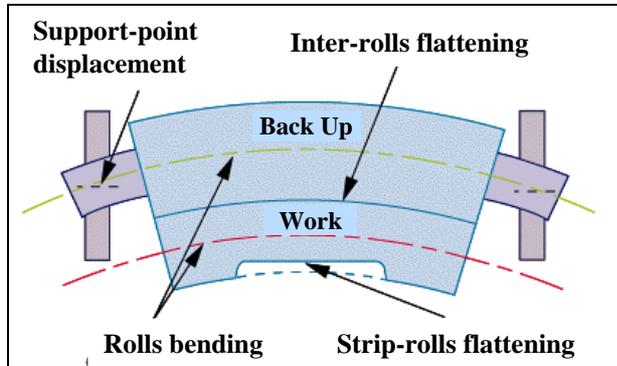
Figure I-5: Rolls bending and flatness [Ber].

Flexion et aplatissement des cylindres [Ber]
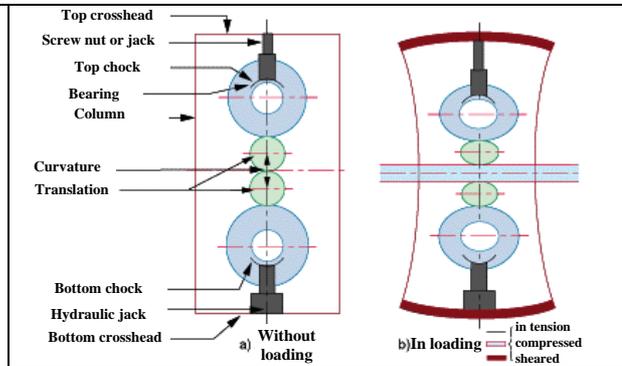
Figure I-6: 4 high stand elastic deformation [Ber].

Déformation élastique de cages quarto [Ber]
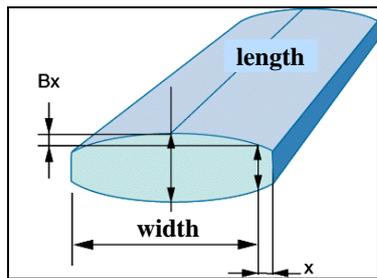
Figure I-7: Strip crown [Ber].

Bande bombée [Ber]

There are different kinds of stand. The simplest is the **2 high stand** made of two work-rolls (top and bottom). The roll bending can lead to strip crown (Figure I-7). The roll radius increase minimizes this phenomenon but increases in a same time the rolling load and torque. When necessary, **4 high stands** are used. Each work-roll is supported by a back-up roll. If it is not enough, it is possible to apply a load between the work-rolls extremities (WORB: work roll bending).

The strip control in a stand is difficult. A new or repaired mill is normally perfectly controlled. Rolls are horizontal and parallel, circumferential speeds are equal and the line of roll centers is vertical.

With time, under rolling loads, corrosion and tools wear, previous ideal conditions are not valid anymore and lead sometimes to incidents or accidents (Figure I-8).
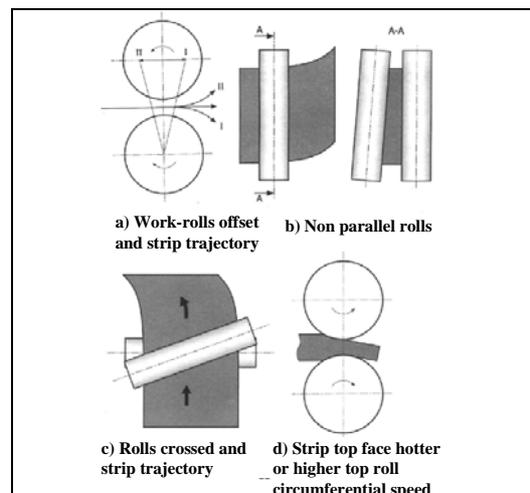
Figure I-8: Possible incidents [Mon1].

Incidents possibles [Mon1]

V. THERMO-MECHANICAL DESCRIPTION

V.1. Generalities

The reduction imposed in a stand "n" corresponds to an approximate deformation [Ber] :

$$\varepsilon = \ln\left(\frac{e_n}{e_{n-1}}\right)$$

eq. I-1

where e_n and e_{n-1} are respectively the strip thickness at the exit of the stand n and n-1.

Taking into account the volume conservation, the thickness decrease is compensated by the lengthening (ε_2) and the widening (ε_3). At high temperature and for flat products having a high width to thickness ratio, the latter is neglected. In reality, it only exists near the edges, where flow is free (tri-axial).

The main part of the product is therefore in **plane strain**:

$$\begin{cases} \varepsilon_1 + \varepsilon_2 + \varepsilon_3 = 0 \\ \varepsilon_3 = 0 \end{cases}$$

eq. I-2

The axis 1 represents the strip length direction, 2 the strip thickness direction and 3 the strip width direction.

As the thickness decreases in the roll bite, the average linear velocity of the product increases between entry (V_{entry}) and exit (V_{exit}).

$$V_{exit} = V_{entry}\,\frac{e_{n-1}}{e_n}$$

eq. I-3
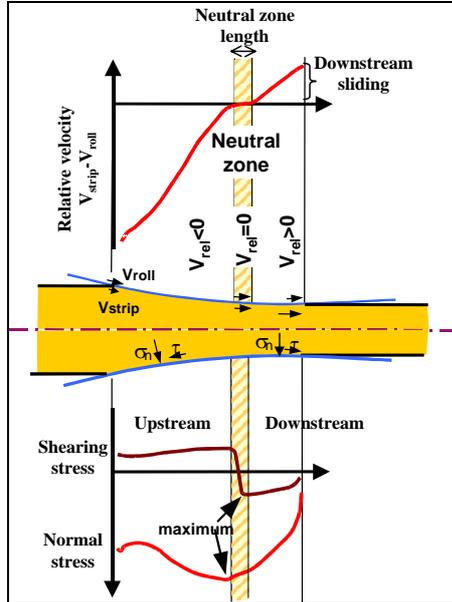
Figure I-9: Schematic representation of velocities and stresses in a stand.

Représentation schématique des vitesses et contraintes dans une cage

In a stand, the velocity at the entry of the roll gap is lower than the roll rotation velocity, whereas it is higher at the exit of the stand.

Let V_{rel} be the relative velocity between strip and roll:

$$V_{roll} = \omega R \; ; \; V_{rel} = V - \omega R$$

$$\begin{cases} V_{entry} < \omega R & \Leftrightarrow & V_{rel} < 0 \\ V_{exit} > \omega R & \Leftrightarrow & V_{rel} > 0 \end{cases}$$

R is the roll radius and ω its angular velocity.

This defines the forward slip: $G = \dfrac{V_{exit} - \omega R}{\omega R}$ **eq. I-4**

Thus, it exists under the roll a **"neutral point" or "sticking point"** where the velocity of the roll and the strip are identical (Figure I-9): $V_{rel} = 0$

This property may extend over a zone called "**neutral zone**".

Previous and next stands apply tensile horizontal forces respectively at the entry and at the exit**. They help rolling.**

Roll bite mechanism model [Mon2]

There exists different methods to solve plasticity problem. The main ones are [Che] :
• the **Slab method**: for simple geometry (flat products) in 2-D (plane strain approximation);
• the **Finite element method** (FEM): it is used in all cases where the slab method is insufficient because it has, compared to all the others, no restrictive hypothesis. For example, it is used for 3-D problems (strip widening; rolls deformation, flatness…) or when vertical or transverse gradients exist (temperature, deformation…).

Metallurgical structure
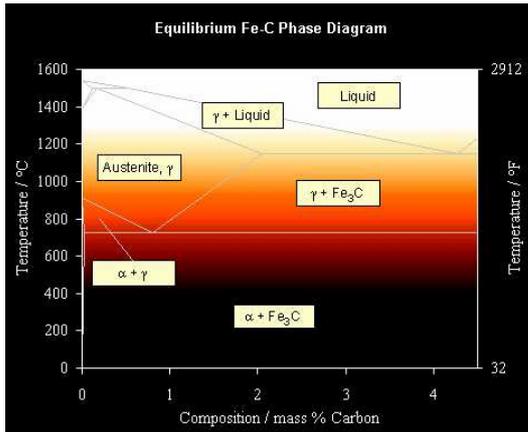
Figure I-10: Fe-C Phase diagram.

Diagramme de phase Fe-C.
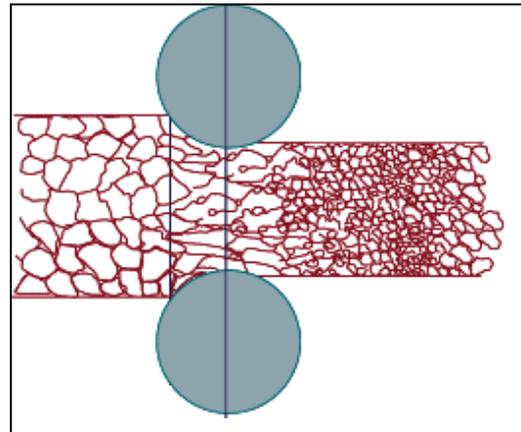
Figure I-11: Microscopic mechanisms of static recrystallization.

Mécanismes microscopiques de recristallisation statique.

In a stand [Ber, Zhou]:
Due to the temperature, steel is usually rolled in austenitic phase (Figure I-10).
Austenitic grains, polygonal at the equilibrium state, are deformed as the metal with a combination of flattening and lengthening (Figure I-11). Steel flow strength reflects its microstructure evolution. There is a quick consolidation at the beginning of the deformation through the initiation of defects. At rolling temperatures, the **recovery** mechanisms involving rearrangement and annihilation of dislocations, are very active. Grain boundary effects are important; they undergo the largest local deformation through a kind of "**viscous sliding**" [Ber].

Between two stands:

The stored energy of deformation promotes static recrystallization if it is high enough. It involves nucleation and growth of new grains preferentially in regions of high dislocation density (such as grain boundaries).

In hot rolling and moreover in the FM, static recrystallization has a dominant role in the softening process of carbon steel strips, compared to dynamic or meta-dynamic recrystallization, principally because of the high strain rates.
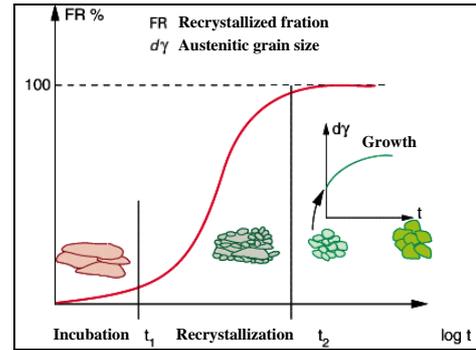
Figure I-12: Kinetics of static recrystallization.

Cinétique de recristallisation statique.

A complete recrystallisation is obtained when equiaxed grains integrally replace the hardened grains. The structure is then, in most cases, refined.

Due to short interstand times in the FM, the static recrystallization is sometimes partial at the entry of the next stand. There is also a mixture of recrystallized and hardened-recovered grains. Low recrystallization fraction can increase the deformation strength by 30%.

The kinetics is evaluated in terms of recrystallized fraction and average grain size. Static recrystallization is modeled by an Avrami type of law (Figure I-12):

$$FR(t) = 1 - \exp\left(-kt^n\right)$$
<div align="right">**eq. I-5**</div>

where *FR* is the fraction of static recrystallization and *t* the time; constants *k* and *n* characterize the kinetics.

On Figure I-12, a first phase of incubation corresponding to the germination phase can be distinguished, followed by the growth of recrystallized grains.

Sometimes, in the last stand of the FM, the temperature is lower than Ar_3 (transition temperature in austenite). In this case, ferritic and austenitic grains coexist (Figure I-10).

V.2. Friction

V.2.1. Friction and engagement conditions

In hot rolling, friction has a primordial role. Indeed, **without friction, it is impossible to roll**. There would be an engagement refusal or a slipping of the strip.

Friction laws depend on many parameters such as normal stress, relative velocity, interface temperature… Friction is usually modeled with two laws:

- Coulomb law (1781)

$\tau < \mu\sigma_n$: no slip (stick)
<div align="right">**eq. I-6**</div>

$\tau = \mu\sigma_n$: slip

where τ is the tangential stress, σ_n the normal stress and μ the Coulomb friction coefficient.

- Tresca law (1865)

$\tau = \overline{m}\tau_{max}$
<div align="right">**eq. I-7**</div>

where $\overline{m}$ is the Tresca friction factor ($0 < \overline{m} < 1$) and τ_{max} the shear stress of the deformed material. Very useful in hot rolling is Sims model which, in addition to the hypothesis of small angles, limits the friction stress by:

$$\tau_{max} = \frac{\sigma_0}{\sqrt{3}}$$

eq. I-8

Lagergren [Lagr] describes another law based on Kobayashi's friction model [Kob], in which the shear stress depends on the relative sliding and its direction:

$$\tau = -mk\left(\frac{2}{\pi}\arctan\left[\frac{u_s}{u_0}\right]\right).\hat{u}_s \qquad (\; k = \frac{\sigma_0}{\sqrt{3}})$$

eq. I-9

where u_s is the relative sliding velocity and u_0 is the die velocity. The expression eliminates the sudden change of the shear stress at the neutral point.

$\hat{u}_s$ represents the tangent unit vector: $\hat{u}_s = \dfrac{u_s}{\|u_s\|}$.

From Coulomb and Tresca laws, it is possible to estimate the minimal friction necessary to engage the product in a stand [Mon2].

From normal and tangential (driving) stresses assessment, respectively σ_n and τ, on a strip part in contact with the roll, the engagement is possible if the horizontal projection of both resultant loads is oriented toward the roll bite downstream part (Figure I-13).

$$-\sigma_n \sin\alpha + \tau\cos\alpha \geq 0$$

eq. I-10

where α is the **bite angle**.

Figure I-13: Slab method: Roll gap divided in verticals slabs of infinitesimal width dx.

Méthode des tranches : emprise divisée en tranches verticales de largeur infinitésimale dx.

- With the Coulomb law, we obtain for the **engagement condition**:

$$\mu \geq tg\alpha \qquad \text{and} \qquad tg\alpha = \sqrt{\frac{\Delta h}{R}} \cdot \frac{\sqrt{1 - \dfrac{\Delta h}{4R}}}{1 - \dfrac{\Delta h}{2R}} \approx \sqrt{\frac{\Delta h}{R}}$$

Then $\mu \geq \sqrt{\dfrac{\Delta h}{R}}$ **eq. I-11**

(in the Table I-1 HSM configuration, stand 2: $\mu \geq 0.16$).

For the **no-slipping condition**, when the strip is already engaged, it is admitted that:

$\mu \geq \dfrac{1}{2}tg\alpha$ **eq. I-12**

(in the Table I-1 HSM configuration, stand 2: $\mu \geq 0.08$).

- With the Tresca law, the **engagement condition** can be estimated too:

$\tau = \overline{m}\,\dfrac{\sigma_0}{\sqrt{3}}$

If $\sigma_n \approx \dfrac{2\sigma_0}{\sqrt{3}}$ then $\overline{m} \geq 2tg\alpha$ **eq. I-13**

V.2.2. Friction coefficient

J.G. Lenard gives in [Len] a good review on friction coefficient μ during hot flat rolling of steel. Different formulas have been proposed using different parameters and giving discordant results:

Roberts, in 1983, gives an increasing relation between friction and temperature:
$\mu = 2.7 \times 10^{-4}T - 0.08$ **eq. I-14a**
with T in °F. With T in °C, we obtain:
$\mu = 4.86 \times 10^{-4}T - 0.07136$ **eq. I-14b**
This result has been obtained combining experimental 2-high mill data, an 84 inch hot strip mill and a 132 inch hot strip mill, **all rolling descaled strips,** and using a simple mathematical model to calculate the friction coefficient.

Geleji, in 1969, explains an opposite influence of temperature on friction coefficient:
$\mu = 1.05 - 0.0005T - 0.056v$ **eq. I-15**
where T is in °C and the rolling velocity v in m/s. The first term depends on the roll grades, it is equal to 1.05 for steel rolls (as we can see above), 0.94 for double poured and cast rolls and 0.82 for ground steel rolls.

In a same way, **Underwood** in 1950 and **Rowe** in 1977 give **Ekelund**'s formulas for temperatures higher than 700°C, respectively noted:
$\mu = 1.05 - 0.0005T$ and $\mu = 0.84 - 0.0004T$ **eq. I-16a,b**

Nevertheless, all these old results that give often **significantly different results**, are insufficient and **will not be referred to here**. Munther and al. obtain more interesting results, closer to our subject. They put in evidence the scale thickness effect on friction in [Munt,Yu]:

$\mu = 0.369 - 0.0006h_{exit}$ **eq. I-17**
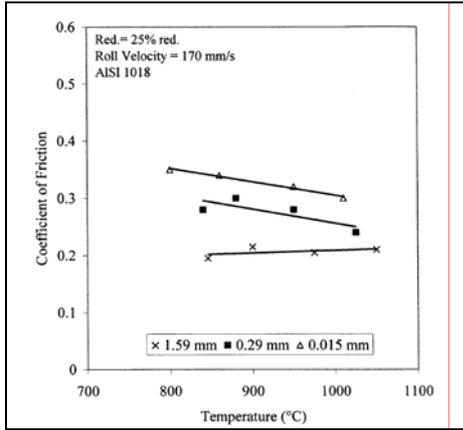
Figure I-14: Influence of scale thickness on friction coefficient [Munt].

Influence de l'épaisseur de calamine sur le coefficient de frottement [Munt].

They had previously rolled samples with different scale thickness at various temperatures in a laboratory rolling mill. Experimentally measured data (roll separating forces, torques and forward slip) lead to the determination of friction coefficient from a finite-element code. The most important observations on friction coefficient are:

- It increases with increasing reduction;
- It increases with decreasing temperature (Figure I-14);
- It increases with decreasing velocity;
- It increases with decreasing scale thickness (Figure I-14).

In 1984, Felder characterized the oxide scale behavior in hot rolling considering that it was highly influenced by the thermal regime [Fel]. He defined the ratio H between the scale thickness h and the scale thickness thermally affected by the contact with the tool h_t:

$$H = {h}/{h_t} = h.(6a_c \Delta t)^{-0.5} \qquad \text{eq. I-18}$$

where a_c is the oxide scale thermal diffusivity and Δt the contact duration. He distinguishes three regimes:

<u>$H>2$</u>: The oxide scale is slightly cooled by the contact with the roll. It gives a low, Tresca-type friction (insensitive to the pressure and the contact time). The scale is softer than the metal. In this domain, the oxide scale is ductile, strongly adherent and not very abrasive.

<u>$H<0.05$</u>: The oxide scale, strongly cooled by the contact with the cold work-roll, ensures a Coulomb-type friction (proportional to the shearing and not very sensitive to the contact time). It is harder than the metal and quasi-rigid. In this domain, the oxide scale has a low adherence, is brittle and abrasive.

<u>$0.05<H<2$</u>: Friction and wear increase and become complex functions of time and contact pressure.

<u>Numerical application for a F2 stand:</u>

$$a_c = {k}/{\rho c} = {3}/{5500 \times 780} = 9.4.10^{-7} m^2.s^{-1} \ ; \ \Delta t = 0.03s \ ; \ h \approx 20\mu m$$

k is the conductivity (W.m^{-1}.K^{-1}), ρ the density (Kg.m^{-3}) and c the specific heat capacity (J.Kg^{-1}.K^{-1}).

The scale thickness cooled by the contact is: $h_t = (6a_c\Delta t)^{0.5} \approx 411\mu m$

Then $H = {h}/{h_t} = h.(6a_c.\Delta t)^{-0.5} \approx {20}/{411} \approx 0.05$.

This numerical application highlights the **non-lubricant** and even **abrasive** character of the oxide scale in the FM.

V.3. **Thermal cycle in rolling**

Figure I-15 gives an example of thermal evolution in an industrial FM. Examples of scale thickness evolutions depending on the initial scale thickness at the entry of the F1 stand (thus to the descaling efficiency) are also calculated from oxide growth laws. In the case of perfect descaling before the FM entry, the oxide scale is thinner than 10µm. This result is in good agreement with [Col]. For an imperfect one, the initial thickness is not zero: the thicker scale thickness can then lead to defects initiation.
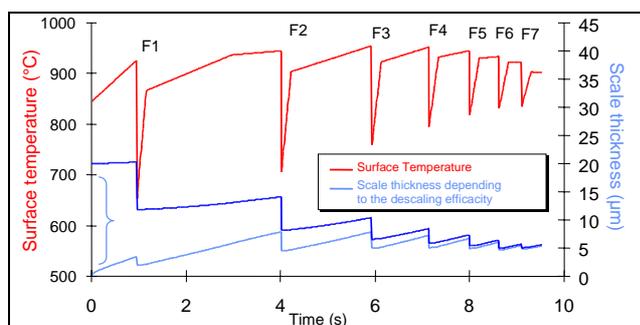
Figure I-15: example of thermal calculation and the corresponding thickness evolutions of a scale in an industrial FM (IRSID).

Exemple de calcul thermique (IRSID) et évolution d'épaisseur de calamine correspondante dans un finisseur industriel.

The knowledge of the **initial thickness** is then very important in terms of strip damage. This data is impossible to obtain in the case of an industrial FM, and is available only at the exit of FM. Moreover it is shown in [Cast] that final oxide scale thickness is the same whatever its value at the FM entry.

Another example (Figure I-16) of thermal and strip thickness evolution is given by Li and Sellars in [Li1]. The authors show that scale deformation patterns have considerable effects on the scale growth. When scale cracking takes place, the average scale thickness is higher than for the plastic deformation mode, because of the major contribution of the rapid oxide growth in the fresh steel zone (Figure I-16b).
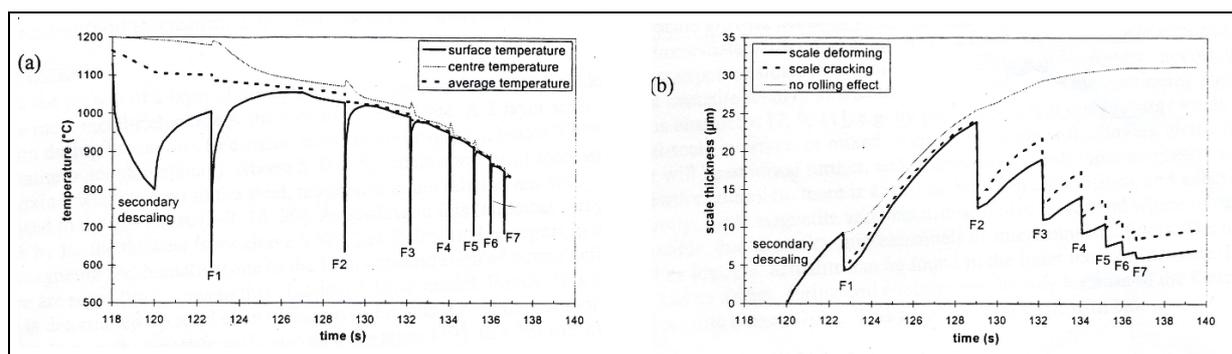
Figure I-16: a) Results of model calculations on the evolution of surface, center and average temperatures of a strip in a 7-stand finishing hot strip mill at the Corus Port Talbot works b) Calculated resulting scale growth on the same strip. [Li1]

a) Résultats du modèle de calcul sur l'évolution des températures en surface, au centre et moyenne de la bande d'un finisseur 7 cages à l'usine Corus Port Talbot b) Résultats calculés de la croissance de calamine sur la même bande. [Li1]

The oxide scale behavior in the FM is complex and remains nowadays quite mysterious. K.Schwerdtfeger et al. give in [Schw] a schematic representation (Figure I-17).
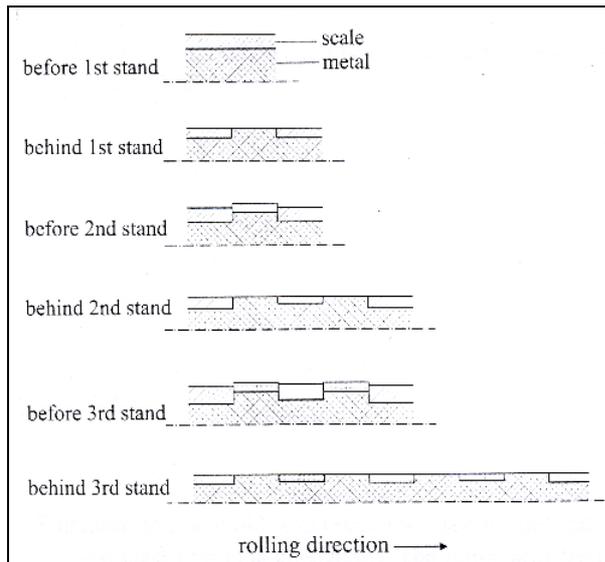
Figure I-17: Schematic representation of the oxide scale behavior in HSM.

Représentation schématique du comportement de la calamine dans un TAB.

At the entry of the 1st stand, the oxide scale is represented as a homogeneous, adhering and uniformly thick layer. At the roll bite entry, through-thickness cracks initiate at regular spacing due to a limited plasticity of the oxide. The substrate elongation opens cracks and compression under the rolls extrudes the soft steel inside them. After the 1st stand, this mechanism forms new metallic regions. After the oxidation in the interstand, there exists two classes of scale thickness at the entry of the 2nd stand, then three before the 3rd … It is assumed in their description that failures are always initiated at the boundary between zones of different scale thickness.

V.4. Heat transfer in a FM stand and their consequences

V.4.1. Heat exchanges assessment

The thermal behavior of a FM stand is particularly complex due to high-pressure contacts where very high heat fluxes are exchanged. The surface of the product undergoes high-amplitude thermal cycles, which have many consequences on its microstructure and on the oxide scale behavior. The roll skin endures cycles of thermo-elastic stresses that contribute to the inititation of "**firecracking**" and to its oxidation, which damage the product surface.

Thus, thermal behavior is a **product - tool coupled problem.**

In a stand, two distinct parts can be considered (Figure I-18):
- before and after the roll bite;
- under the work-rolls.
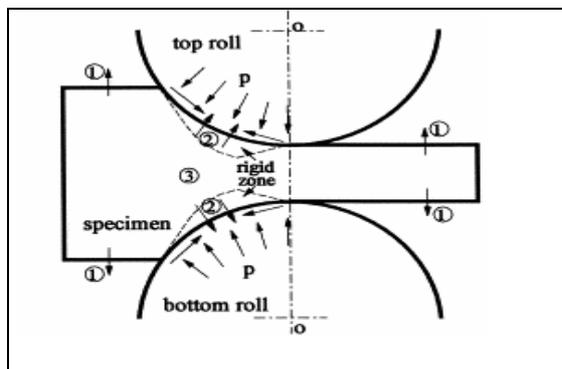
Figure I-18: Thermal exchanges [Li2]:
 (1) **Heat lost by heat radiation and convection**
 (2) **Heat lost during interfacial contact and heating by friction**
 (3) **Heating by plastic deformation.**

Echanges thermiques [Li2]:
   (1) Perte de chaleur par rayonnement et convection
   (2) Perte de chaleur pendant un contact interfacial et échauffement par frottement
   (3) Echauffement par déformation plastique.

Before the contact zone

The Finite Element technique is most often used to take into account gradients in two or three directions. Otherwise, if only an average temperature in the section is sought, the slab method is available. In this case, the **heat transfer equation** has the form:

$$\rho c v_x h \frac{dT}{dx} = \dot{W}_{int} - \phi_{rad} - \phi_c - \phi_{strip-table}$$ **eq. I-19**

where ϕ_{rad} represents the heat lost by radiation, ϕ_c the heat lost by convection and $\phi_{strip-table}$ the heat lost by the contact with the conveying table.

The convection can be decomposed into $\phi_c = \phi_{nc} + \phi_{fc}$, where ϕ_{nc} is the natural convection and ϕ_{fc} the forced convection (caused by the strip displacement).

The first term $\dot{W}_{int}$ reflects the possible internal heat sources due to, for example, phase transformations.

The strip loses heat from its surface towards the air by radiation and by convection (Figure I-18 (1)).

$$\phi_{rad} + \phi_c = \varepsilon\sigma(T^4 - T_\infty^4) + h_c(T - T_\infty)$$ **eq. I-20**

where the first term represents the **heat radiation** and the second one the **convection**. T is the temperature of the strip and T_∞ that of the air (in K), ε is the thermal emissivity, σ Stefan's constant (in $W.m^{-2}.K^{-4}$) and h_c the thermal convection coefficient (in $W.m^{-2}.K^{-1}$).

$$\phi_{strip-table} = h_{strip-table}(T - T_{table})$$ **eq. I-21**

$h_{strip-table}$ is the Interfacial Heat Transfer Coefficient (**IHTC**) between the strip and the table.

Thus, the surface temperature is cooled and a thermal gradient appears within the strip. A **conduction** phenomenon (heat transport by diffusion: Fourier law) is initiated from the hot heart of the metal toward the colder surface.

In the roll gap

The expression of the **heat transfer equation** is here:

$$\rho c v_x h \frac{dT}{dx} = \dot{W}_{int} + \dot{W}_{surf} - \phi_c$$ **eq. I-22**

There is a high temperature difference between the work-rolls (around 50°C) and the metal strip (around 950°C). Thus, the product heats the rolls by conduction.

One of major problems is the extremely short time of contact in a FM stand (around 0.03s for a F2 stand). Two possibilities are also envisaged:

- In a case of perfect contact, which is an often-made assumption, the surface temperature of the two bodies is the same during the contact.
- If the contact is imperfect, as in our case with the presence of an oxide scale and a rough surface for example, a complicated IHTC $h_{strip-roll}$ has to be calculated, as we will see in the next part.

$$\phi_c = \phi_{strip-roll} = h_{strip-roll}(T - T_{roll})$$ **eq. I-23**

In an opposite way, heat is generated by friction $\dot{W}_f$ and plastic deformation $\dot{W}_p$.

$\dot{W}_{surf} = \dot{W}_f$ (Figure I-18(2))

$\dot{W}_{int} = \dot{W}_p$ (Figure I-18(3))

The friction contribution at the strip-roll interface is expressed by:

$$\dot{W}_f = \tau.\Delta V \hspace{8cm} \textbf{eq. I-24}$$

where ΔV represents the velocity difference at the interface between the strip and the roll. This value is null at the neutral point.

Plastic deformation involves a heating of the concerned zone. This heat source is equal to:

$$\dot{W}_p = r\sigma_0\dot{\bar{\varepsilon}} \hspace{4cm} \text{(Von Mises)} \hspace{3cm} \textbf{eq. I-25a}$$

$$\text{or} \hspace{1cm} \dot{W}_p = rK(\sqrt{3}\dot{\bar{\varepsilon}})^{m+1} \hspace{2cm} \text{(Norton-Hoff)} \hspace{2cm} \textbf{eq. I-25b}$$

The constant r ($\approx 0.9\text{-}0.95$) is traditionally introduced to take into account the part of the mechanical power not dissipated into heat but stored for example as elastic energy of dislocation. This heat source locations map exactly as the strain rate.

After the contact zone

Just after the contact zone, metal as well as rolls quickly reach their steady temperature by conduction. Indeed, contact times are so short that only a small thickness is concerned.

V.4.2. The interfacial heat transfer coefficient (IHTC)

The IHTC between a strip and a work-roll traduces the contact resistance between them. In a FM stand, four phenomena influence heat transfer:

- surfaces roughness, which gives only punctual contact ("constriction effect", linked to the notion of real area of contact);
- surfaces are oxidized and the iron oxides are much less conducting than the metal (oxide: 3W/mK; steel: 30W/mK);
- residues, water, lubricants, i.e. more or less conducting third bodies between rolls and strips;
- in a stand, cracking of the oxide scale due to thermo-mechanical solicitations promotes direct contact between rolls and the fresh metal extruded inside cracks; contrary to the other three, this phenomenon enhances heat transfer.

Therefore, the heat transfer between the strip and the roll occurs along two paths (Figure I-19) [Fel,Li3,Li4] :
- through the extruded fresh steel and the free space due to a partial contact between roll and strip (boundary gap: roll roughness):
$$\text{Steel} \Rightarrow \text{boundary gap} \Rightarrow \text{roll} \hspace{0.5cm} \textbf{(path 1)}$$
- through the oxide scale and the boundary gap:
$$\text{Scale} \Rightarrow \text{boundary gap} \Rightarrow \text{roll} \hspace{0.3cm} \textbf{(path 2)}$$

To simplify the analysis, some assumptions are made on the surface geometry, the roll properties, the oxide scale and the substrate. The scale is supposed homogeneous, compact, adherent to the steel, and thicker than the roll surface roughness. The latter is simulated by a sinusoid. The roll surface is supposed to be clean, without any oxidation. The extrusion is supposed to be complete (steel in contact with roll).

Theoretically, during hot rolling, the strip surface temperature T_s and the roll surface temperature T_r are related to the effective heat flow through the interface q_e and to the effective IHTC C_e by the equation:

$$q_e = C_e(T_s - T_r)$$ **eq. I-26**

Thermal exchanges between the roll and the steel strip (Figure I-19) can also be modelled through an electric analogue with resistances placed in parallel (Figure I-20).
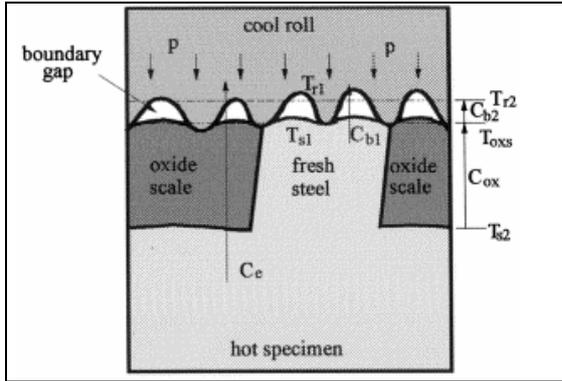
Figure I-19: Consequences of the oxide layer damage on the IHTC [Li3].

Conséquences de l'endommagement de la calamine sur le IHTC (coefficient de transfert thermique interfacial).
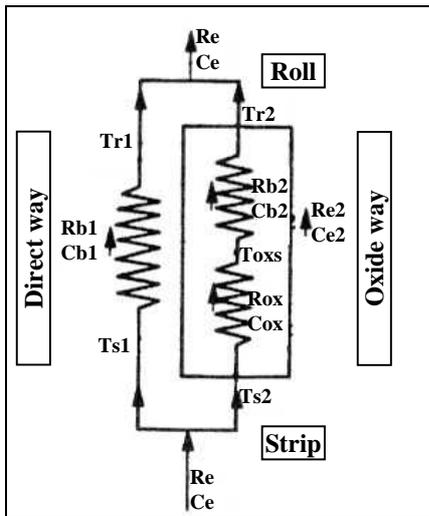
Figure I-20: Thermal circuit [Li3].

Circuit thermique [Li3].

The Ohm law gives the total thermal resistance R_e:

$$\frac{A_a}{R_e} = \frac{A_s}{R_{b1}} + \frac{A_{ox}}{R_{e2}} = \frac{A_s}{R_{b1}} + \frac{A_a - A_s}{R_{ox} + R_{b2}}$$ **eq. I-27**

A represents the apparent contact area. In term of IHTC:

$$C_e = \frac{1}{R_e} = C_{e1}\alpha_s + C_{e2}(1 - \alpha_s)$$

$$= C_{b1}\alpha_s + \frac{C_{ox}C_{b2}}{C_{ox} + C_{b2}}(1 - \alpha_s)$$ **eq. I-28**

with α_s the surface cracks fraction where the steel is in a direct contact with the roll, defined by $\alpha_s = A_s/A_a$

$$\alpha_s = \Delta h\left(\frac{2}{3h_0} + \frac{1}{8R}\right)$$ **eq. I-29**

where R is the work roll radius, h_o the steel initial thickness and Δh the absolute reduction.

This relatively simple method to calculate the IHTC seems to be ingenious, even in considering the complexity of the process. The approximations done are not too strong excepted, perhaps, not to take into account the oxide scale which always covers rolls during hot rolling, and assume a total extrusion between oxide rafts (steel extrusion is progressive and depends on many parameters such as crack width, scale thickness, roll reduction, position in the roll gap…). The first hypothesis decreases the IHTC value and the second one increases it… but to which degree?

Nevertheless, this model remains qualitative because parameters concerning structure and thermal properties of microscopic layers are known with too much imprecision.

To have a quantitative value of the IHTC, the only solution is the measurement with thermocouples in the extreme surface of the materials. From the $T(t)$ curve, $h_{strip-roll}$ (also called C_e depending on the author) is obtained.

Several authors have obtained relationships to describe this resistance between strip and rolls during rolling. Zhou summarizes the different forms of equations describing the IHTC C_e [Zhou] and gives values obtained by numerical modelling (Figure I-21). Chen et al. and Jin et al. illustrate the influence of roll pressure p_m (in MPa) on the IHTC C_e (in W/m^{2}K) [Chen, Jin, Sam] :

$$C_e = 696.5 p_m - 34396$$
<div align="right">**eq. I-30**</div>

A similar equation is obtained by Devadas and al. [Dev1].

It is very interesting to link the IHTC with the roll pressure p_m, but it should be perhaps more pertinent to take the ratio with the strip plastic strength p_m/σ_0.

In [Dev2], it has been shown from strips instrumented by thermocouples on pilot rolling mill, that IHTC increases with rolling reduction but decreases strongly with lubrication; finally it shows no important variation with the roll rotation velocity.

For Pawelski [Paw], more than the roll pressure, the main factor is the oxide scale on the strip:

$$C_e = \frac{\lambda_s}{h_s}$$
<div align="right">**eq. I-31**</div>

where λ_s is the scale conductivity and h_s its thickness. Wang and Tseng [Wang] try to mix both influences in a semi-theoretical equation:

$$\frac{1}{C_e} = \frac{h_s}{\lambda_s} + \frac{1}{C_{csm}}$$
<div align="right">**eq. I-32**</div>

where C_{csm} is an effective IHTC related to the microscopic gap formed at the interface between the roll and the strip.
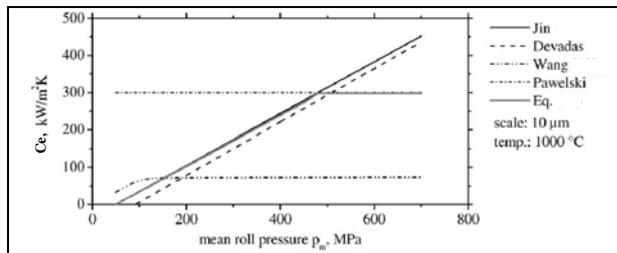
Figure I-21: Relationship between IHTC and mean roll pressure. [Zhou]

Relation entre IHTC et pression du cylindre. [Zhou]

A simple expression is finally (Figure I-21):

$$C_e = \min\left(\frac{\lambda_s}{h_s}, 696.5 p_m - 34396\right)$$
<div align="right">**eq. I-33**</div>

IHTC here depends on the scale thickness and the roll pressure. When the pressure is small the relation depends on it [Li2,Li3,Li6] and when it is high, IHTC depends on the scale thickness.

V.4.3. Work-rolls degradation

The metal-tool interfaces generally give rise to **two types of thermal problem** [Fel]:

- **initial thermal imbalance**: two bodies with different temperatures at the time of contact induce a heat transfer from the cold to the hot. This phenomenon is prevalent in hot rolling.
- **energy dissipated by friction**: it is distributed by conduction between the two bodies and heats a given depth.

During hot rolling of steel, an oxide layer covers its surface. This layer tries to extend in the same way and with the same ratio as the substrate, under shearing loads generated by the latter. Scale is cooled by the rolls. Its temperature is considerably lower than steel (Figure I-22).
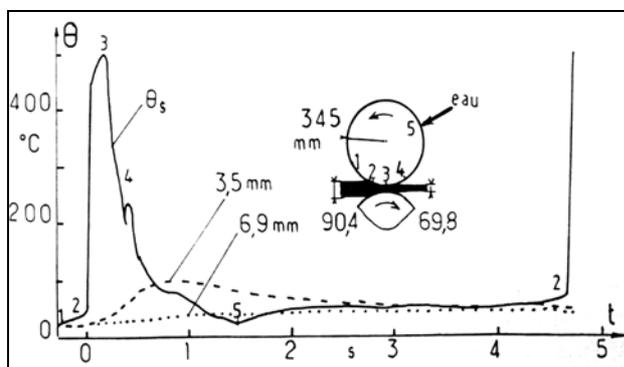
	F1	F2	F3	F4	F5	F6	F7
h_d (kW/m K)	54	66	69	71	65	60	56
$\vartheta_{roll,max}$ (°C)	466	458	405	354	272	202	147

Figure I-22: Superficial temperature field of a roughing mill top roll (second stand) measured from thermocouples [Ste].

Température de surface d'un cylindre de dégrossisseur (deuxième cage) mesurée par thermocouples [Ste].

Table I-2: IHTCs and maximum roll temperature in finishing mill [Zhou]

valeurs de IHTC et températures maximales des cylindres dans un finisseur[Zhou].

Stevens et al. [Ste] showed in 1971 that the surface temperature of the rolls in the roughing mill varies between 80 to 500°C. They noticed that roll heating by conduction and friction is very high when it comes into contact with the 1000°C-strip surface (from 30°C at (5) under water jets to 500°C at (3) in the roll bite). Only the surface is affected (3mm), which explains the quick cooling (1s), as soon as the contact is stopped, by thermal conduction between the surface and the bulk of the roll, and by water sprays on the roll surface. One understands here the oxide scale paramount role of protective thermal barrier between steel and roll.

Our interest is particularly in the FM rolls. The problem is their much higher velocities than in the roughing mill. The contact duration with the flat-rolled product is very short (around 0.03s in stand 2). Measurements thus become very difficult because they require thermocouples with very short response time. Zhou in 2002 [Zhou] simulated the thermal exchanges in the finishing mill and obtained data for the maximum roll surface temperature (Table I-2).

Consequences on the rolls

In hot rolling, interactions are particularly complex. Indeed, the high metal temperature has two main consequences:

- The high oxidation kinetics forms thick oxide layers with generally poorly known thermo-mechanical behavior (in particular a reduction in friction, all the more significant as the rolling temperature is higher and the duration of rolling shorter).
- The roll material undergoes high surface temperature fluctuations that induce, amongst other phenomena, a damage by thermal fatigue and a surface oxidation.
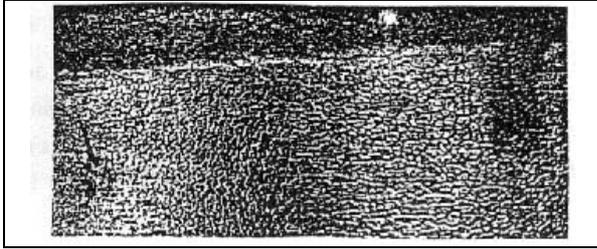
Figure I-23 represents a typical pattern of **"fire-cracking"**. It is a fine lattice of cracks induced by thermal fatigue that develops in rolling conditions without sliding.

Figure I-23: fire-cracking

Faïençage.

The abrasive wear can be calculated by Archard's law:

$$\dot{m} = k.\Delta V.F_n \qquad \text{or in integral for} \qquad \Delta m = k.L_g.F_n \qquad \qquad \textbf{eq. I-34}$$

where $\dot{m}$ represents the loss of mass by wear (Δm), ΔV the sliding velocity, L_g the sliding length and F_n the normal load (constant). The coefficient of proportionality k depends on material, temperature, and lubrication [Fel].

Roll degradation: CCD images

The roll surface is however very important for the surface quality of the rolled product. There are three prevalent factors of roll wear:
- the abrasion of the roll surface due to the contact with the strip;
- surface layer fatigue due to the mechanical loading applied by the strip;
- roll thermal fatigue due to its thermal cycle. The roll cooling is its principal factor of degradation.

It is thus important to distinguish the **normal abrasive wear** and the mechanism of **banding**. The first one induces progressive changes in the surface by repeated rolling / sliding friction (under compressive stress in the roll gap) and oxidation. The second, called banding, is due to the thermo-mechanical fatigue involved by the successive cycles of stresses and cooling-reheating (Figure I-22).

CCD Camera allowing to follow the evolution of rolls deterioration have been installed on three Hot Strip Mill (HSM) to observe the degradation of the bottom Hi-Cr work-roll surface in stand F2 and F3 of the FM [Uijt1,Uijt2]. On pictures obtained (Figure I-24), bright zones represent smooth oxide layer (without defect), and dark ones (that do not reflect the light) the rough surfaces (with defects).

8 mm			Wear
a) Ground phase	b) Oxidation phase	c) Wear phase	
d) Pitting	e) Comet tails	f) Banding	Banding
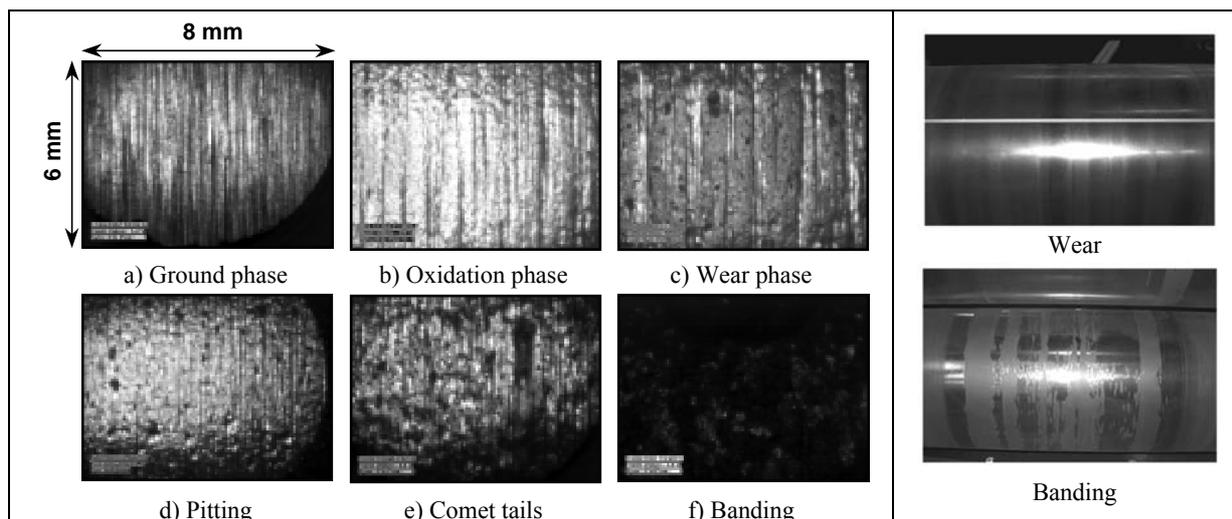
Figure I-24: Roll surface evolution during its lifetime.

Evolution de la surface d'un cylindre pendant sa durée de vie.

Figure I-25: Roll damage.

Endommagement de cylindre.

Authors give then an evolution of the roll surface during a production campaign: after the **oxidation** of the roll surface (Figure I-24b), the oxide layer thickness decreases due to **wear** (Figure I-24c). In the course of the rolling campaign, **small pits** are observed on the roll surface (breaking down of small surface particles) (Figure I-24d). The pit number increase, combined with **peeling** around them (breakdown of strip of roll surface, 10-30μm thick), leads to **comet tails** (Figure I-24e). Finally comes **banding** (Figure I-24f), i.e. the removal of a complete oxide layer (100-300μm thick) and some material from the roll (Figure I-25).

Pitting as well as thermal cracks and peeling also appear during wear phase. But they do not cause many problems in terms of strip surface quality or friction, compared to the initiation of comet tails and banding.

Influence of roll surface defects on friction coefficient
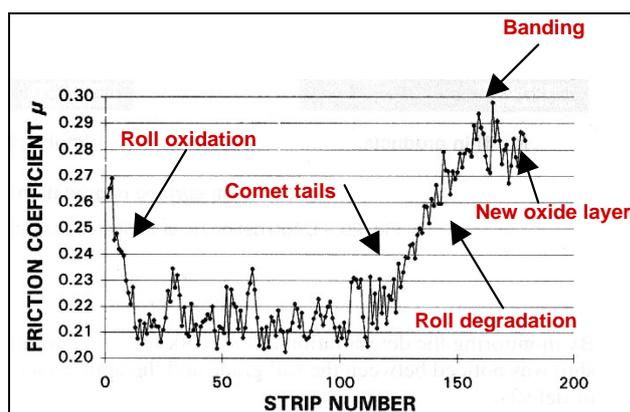
Figure I-26: Friction coefficient evolution in function of strip number and roll evolution. Stand F2. [Uijt2]

Evolution du coefficient de frottement en fonction du nombre de bandes et de l'évolution de la surface du cylindre. Cage F2. [Uijt2]

In [Keu], same authors use a rolling force model to study the relation between the roll surface degradation and the friction in the roll bite. Indeed, the roll deterioration influences the strip-roll friction coefficient and thus, the secondary scale damage. Using their CCD camera, they followed the surface aspect evolution of several rolls of stands F2, coil after coil, while noting the friction coefficient values (Figure I-26).

At the beginning of roll life, the friction coefficient decreases. This is due to the formation of an oxide layer on rolls. The occurrence of thermal cells, pits and peeling on the roll surface does not influence considerably the friction coefficient evolution which stays approximately constant. With the apparition of the comet tail, the coefficient increases. In all cases, the maximum is reached for a different coil number, but always coinciding with incipient banding. At the end, a slight reduction is visible, due to the formation of a new oxide layer.

They show in [Mor] that it is also possible to evaluate the rolls surface roughness using the same system of observation (between 1 and 4μm in their short feasibility study).

Influence of roll surface defects on strip surface quality

A majority of strip surface defects appears when comet tails and banding are initiated on work-rolls. It can be then deduced that strip defects increase when friction or roll surface roughness increase.

VI. ORIGIN OF SECONDARY SCALE DEFECTS

VI.1. Defects

Oxide scale is mainly useful in the FM as a **thermal barrier** between hot strips (~900°C) and cold work-rolls (~50°C) during a rolling pass.

During the process, thermal stresses imposed on this scale, joined to the degradation of the rolls, may cause delamination, cracks perpendicular to the direction of rolling (Figure I-27) and embedding in the strip metal.
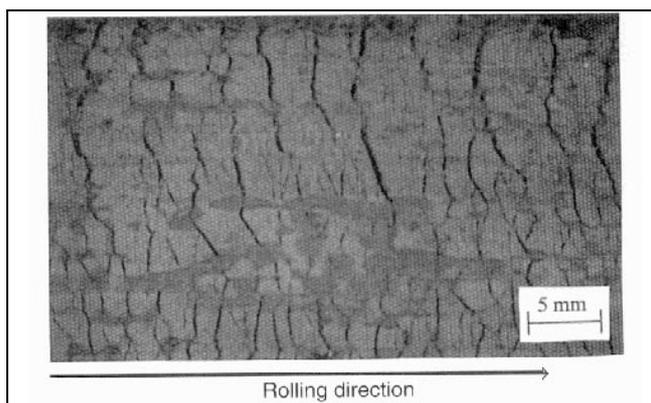
Figure I-27: Transversal cracks after hot rolling [Li5]

Fissures transverses après laminage [Li5].
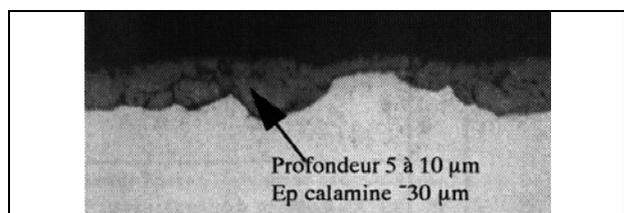
Figure I-28: Rolled-in scale defect: industrial strip; scale thickness=30μm; defect depth=5-10μm.

Défaut de calamine incrustée : bande industrielle ; épaisseur de calamine = 30μm ; profondeur du défaut = 5-10μm.

These defects are called "**rolled-in-scale**" defects (Figure I-28).

The embedding depth observed on an industrial strip [Garc] can reach 20μm and can affect all the surface of the strip.

After pickling, there are two possibilities:

- thin oxide particles embedded in the metal disappear and leave a rough surface (peeled aspect). Sometimes, if it is not too deep, cold rolling can erase it. Otherwise, sheet surface presents cavities;
- particles are not totally removed during the pickling stage. Some scale residues then remain on the sheet. They are particularly harmful for future use (Figure I-29).

| a | b | c |
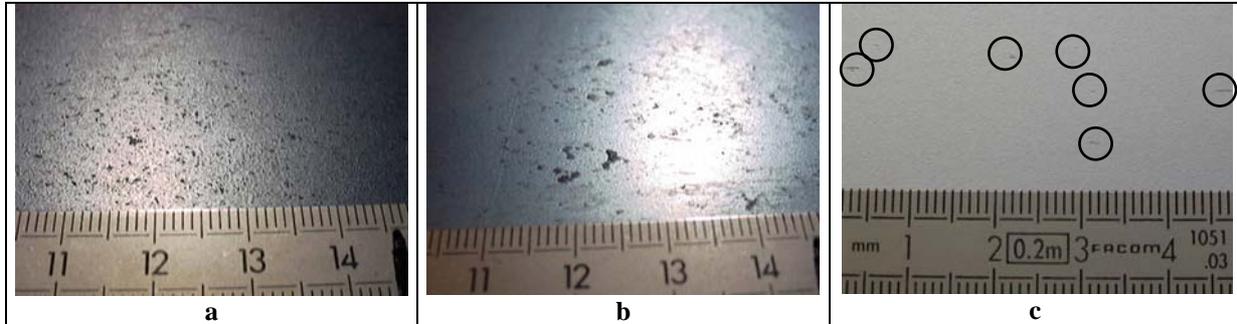
Figure I-29: Arcelor HSM observations: Consequences of rolled-in scale defects initiated in the FM (a), still present on the hot rolled coils (b) and on the cold rolled sheet (c).

Observations sur TAB Arcelor : Conséquences des défauts de calamine incrustée initiés dans le finisseur (a), toujours présents sur les bobines laminées à chaud (b) et sur les tôles laminées à froid (c).

The typology of defects on the strip surface is varied; one can distinguish:

- the rolled-in scale (Figure I-30)
- the peeled-rolls (Figure I-31)
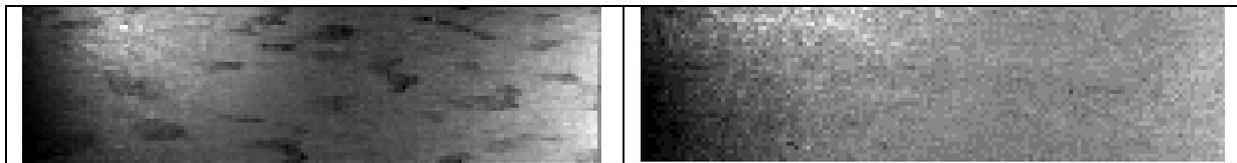
Figure I-30: a) Embedded scale waves, perpendicular to the rolling direction.

a) vagues de calamine incrustée, perpendiculaires à la direction de laminage.

b) Indents (or mouse-hair) in rolling direction.

b) Poils de souris, parallèle à la direction de laminage.
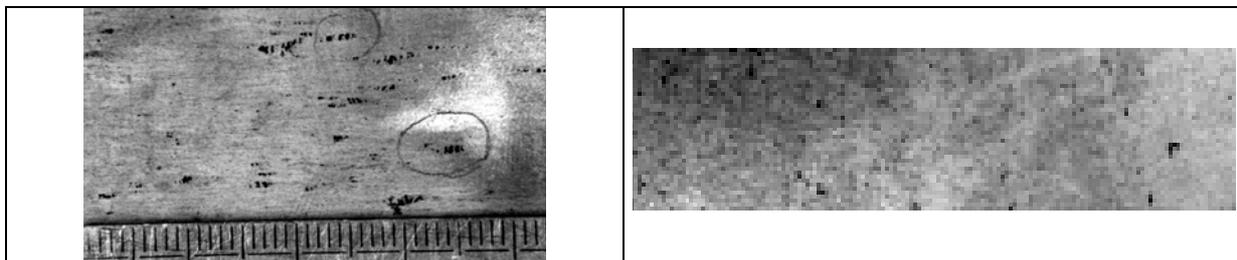
c) Beans, in rolling direction.

c) Haricots (direction du laminage)

d) Isolated punctiform rolled-in-scale, generalized or in lines.

d) Calamine incrustée en forme de points isolés, généralisés ou en bande.

In the most critical cases, the typology reflects the roll degradation:
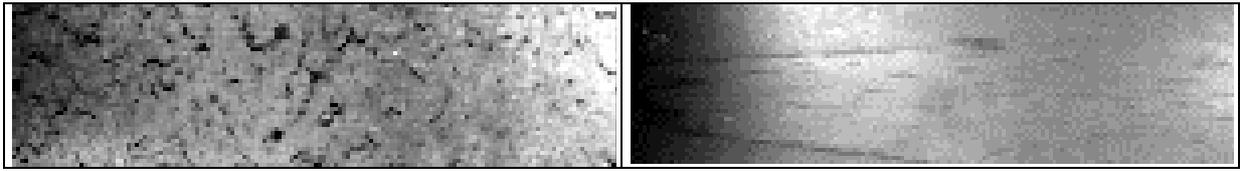
Figure I-31: a) Peeled roll scale or unpolished roll   b) Chevrons.

a) Cylindre pelé ou dépoli   *b) Chevrons.*

Most damaged mountings are those which generate the largest thermo-mechanical stresses within the scale and at the rolls surface. This corresponds to high temperatures at FM entry (low carbon grades), high reduction rates (low thickness) and hard grades.

Defects occurrence criterion is based on stresses imposed to the scale during hot rolling. Three kinds of stresses are present (Figure I-32):
- growth stresses within the oxide scale (negligible);
- thermal stresses, compressive during strip surface cooling, tensile during heating;
- mechanical stresses imposed by the rolling pass.
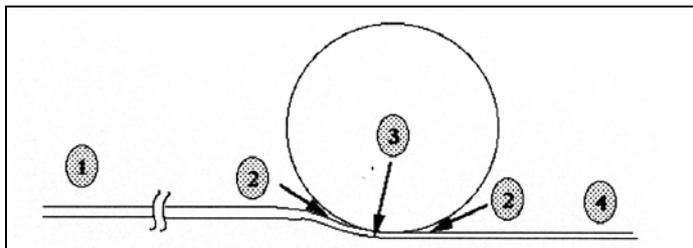
(1) and (4): thermal stresses;
(2): thermo-mechanical stresses before and after the rolling bite;
(3): thermo-mechanical stresses under rolls.

Figure I-32: Stresses developed in the secondary scale during hot rolling.

Contraintes dans la calamine secondaire pendant le laminage à chaud.

Stresses bring about the scale damage but the initiation of detrimental defects is function of scale/strip relative mechanical properties, scale thickness under rolls and stresses imposed by the rolling pass.

There exists two scale embedding mechanisms (Figure I-33a,b):
- the cracking of the oxide layer followed by the metal extrusion,
- the printing in the strip of work roll roughness.
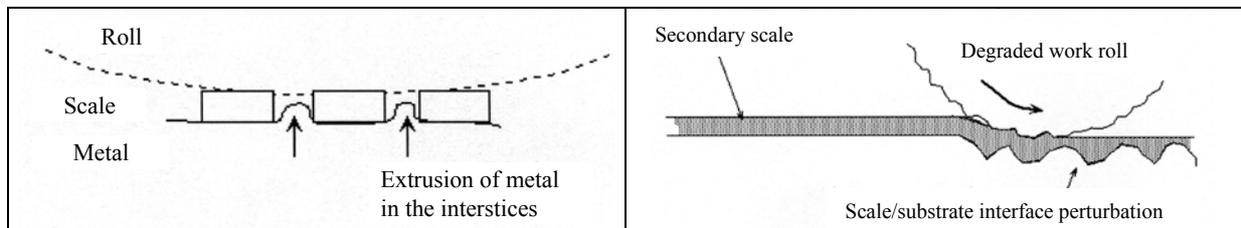
Figure I-33: a) Cracking and extrusion of metal because of its lower hardness compare to these of oxide scale.

b) Printing effect due to degraded rolls.

b) Effet d'imprimerie dû aux cylindres dégradés.

a) Fissuration et extrusion de metal due à sa plus faible dureté comparée à celle de la calamine.

The embedding will be all the stronger as the metal is softer (grade effect or temperature effect), the reduction rate higher and the scale thickness larger.

VI.2. <u>Initiation mechanisms of the rolled-in scale defect</u>

Many observations realized by the Arcelor production sites on the different defects have led IRSID to propose different defect formation mechanisms, which depend on the kind of stresses applied to it (Figure I-34).
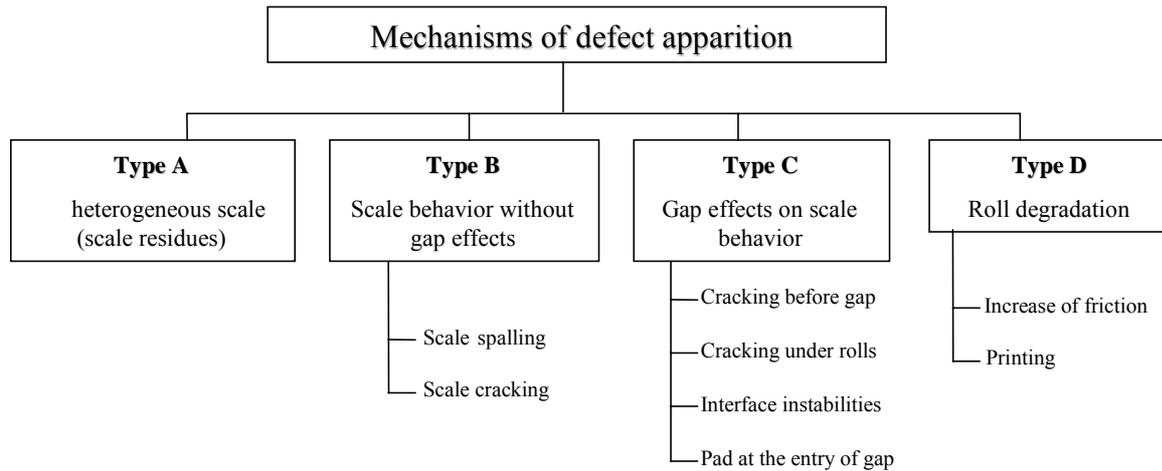
Figure I-34: Decomposition of defect formation related to secondary scale.

Décomposition de la formation de defauts liés à la calamine secondaire.

VI.2.1. Scale residues on exit of FSB descaling (Type A)

Scale residues subsist after descaling and are embedded in steel during their passage under rolls (Figure I-35).
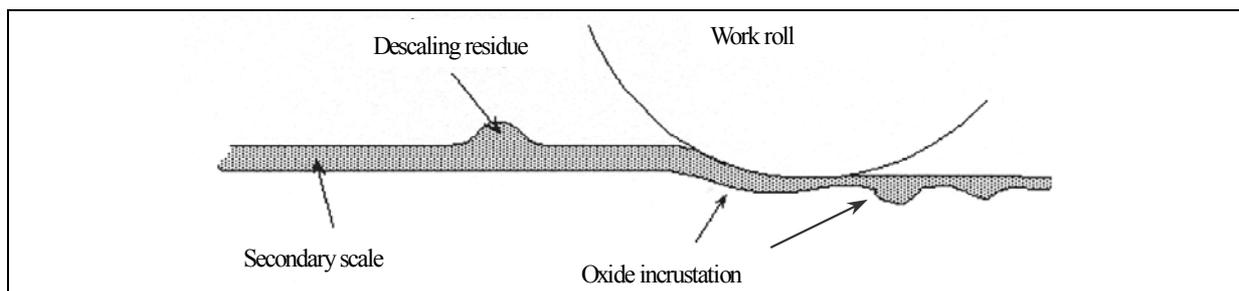
Figure I-35: Embedding of descaling residues in a FM stand.

Incrustation de résidus de décalaminage dans une cage finisseur.

VI.2.2. Stresses in scale without gap effects (type B)

Apart from bite effects, two kinds of stresses can modify the oxide scale:

- Thermal stresses due to the difference of dilatation coefficient between steel and oxide film (oxide coefficient lower than the steel one in the FM stand temperature range), and induced by thermal cycle undergone by the surface product.
- Compressive growth oxide film stresses on its substrate. Indeed, the scale is endogenous (formed from its metal substrate) and occupies a larger volume than the metal which gives rise to it. Growth stresses are of second order compared to thermal stresses.

Concerning thermal stresses:

If the oxide scale is cooled before the entry in the bite, the metal contracts more than the oxide scale. This latter is then compressed and able to initiate rolled-in scale defects through two mechanisms depending on the scale adherence on its substrate (Figure I-36):
- if the interface is strong: the oxide scale cracks, followed by chipping of oxide parts;
- if the interface is weak: the oxide scale buckles.
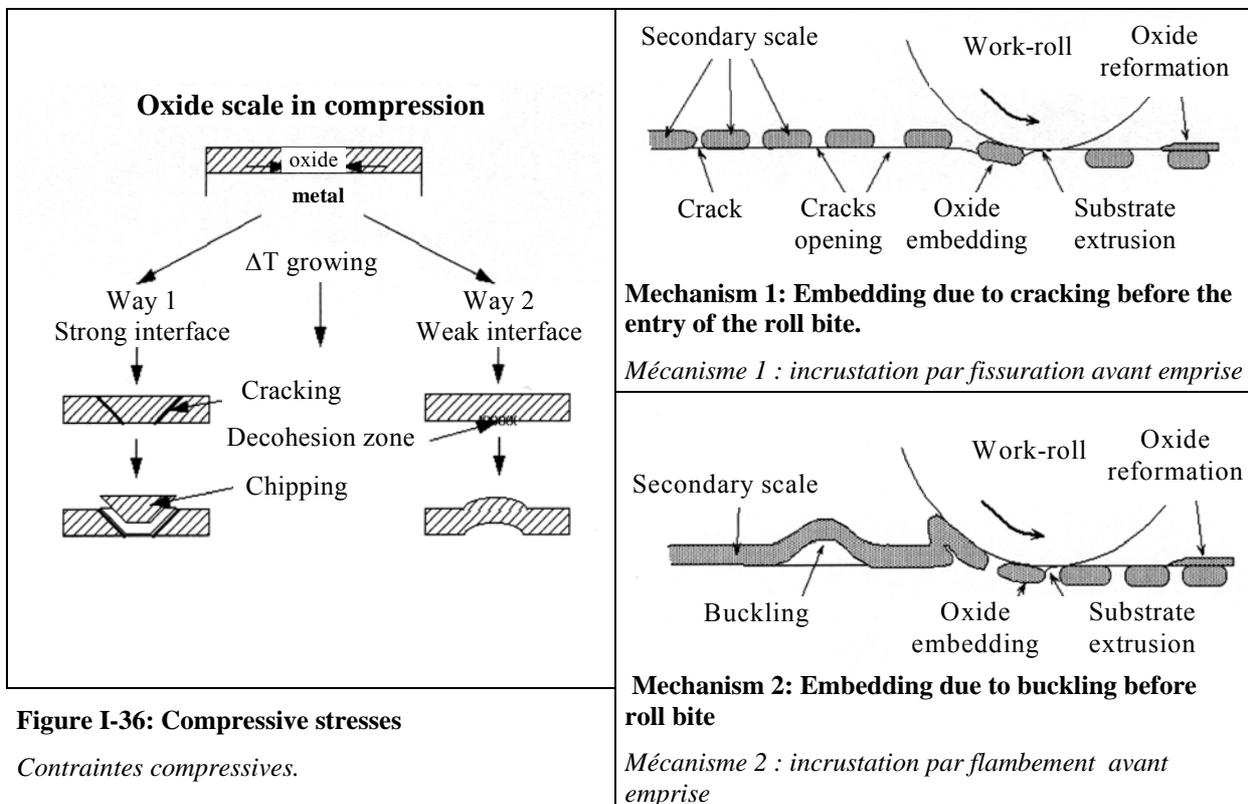
Figure I-36: Compressive stresses

Contraintes compressives.

Mechanism 1: Embedding due to cracking before the entry of the roll bite.

Mécanisme 1 : incrustation par fissuration avant emprise

Mechanism 2: Embedding due to buckling before roll bite

Mécanisme 2 : incrustation par flambement avant emprise

During reheating, tensile stresses are developed in oxide scale. Consequences are then identical to those obtained in compression with a strong interface (Figure I-36 way 1). Indeed the dilatation of the metal is higher than that of the scale. Tensile cracks initiate, open   and finally form a free space as in the chipping case. The space opens due to high tensile stress at the entry of the roll gap. Cracks appear only if $\sigma_{therm} > \sigma_{crit}$.

Concerning growth stresses:

[Tom] proposes a mechanism of rolled-in scale defect by growth stresses assuming that they would not be negligible (Figure I-37). As has been specified previously, we do not believe this is the case in the FM. Nevertheless, they describe a mechanism extremely close to those obtained in cooling a slightly adherent scale (Figure I-36 way 2).
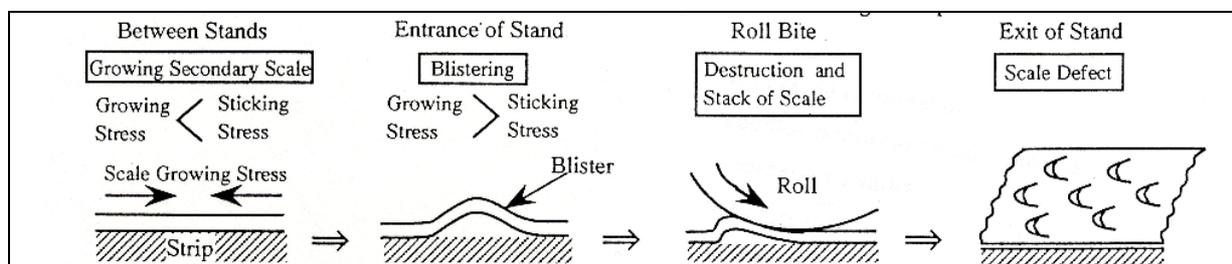
Figure I-37: Formation of secondary scale defect by oxide growth [Tom]

Formation de défauts de calamine secondaire par croissance d'oxyde [Tom].

VI.2.3. Defects related to rolling stresses (Type C)

Under the assumption that the scale is intact at the entry of the FM:

At the entry and exit of roll gap

Before the gap, the scale undergoes tensile stresses and fails if $\sigma_{tens} > \sigma_{crit}$. This step is followed during the same pass by the extrusion of the steel inside the scale cracks (Figure I-38). Tensile stresses are also high at the exit of the roll bite (the strip is faster than the rolls at the exit). If cracks are created at the exit of a stand n, the extrusion will be initiated in stand n+1 (if re-oxidation has not healed the cracks).
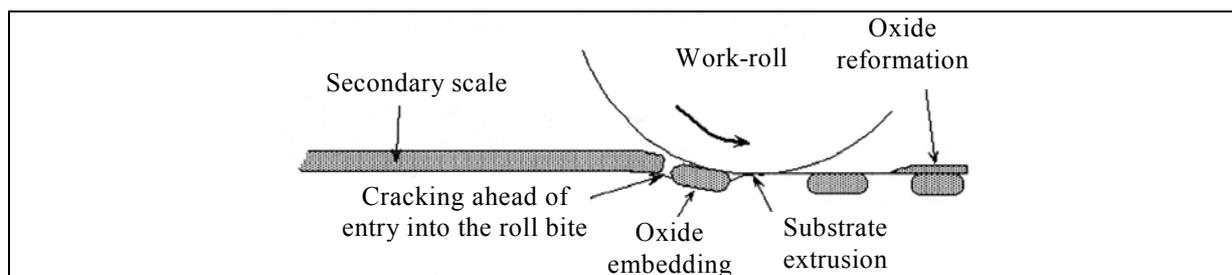
Figure I-38: Cracking at entry of roll gap followed by extrusion of steel. Tensile stresses at entry and exit. Compressive stresses under the rolls.

Fissuration en entrée d'emprise suivie d'extrusion de l'acier. Comtraintes de traction à l'entrée et la sortie. Contraintes compressives sous les cylindres.

Under work-rolls

Compression and shearing stresses under the rolls cause the scale failure and the embedding of oxide parts (Figure I-38).

Metal / oxide interface instabilities

Figure I-39: Metal/scale interface instabilities

Instabilités de l'interface métal / calamine.
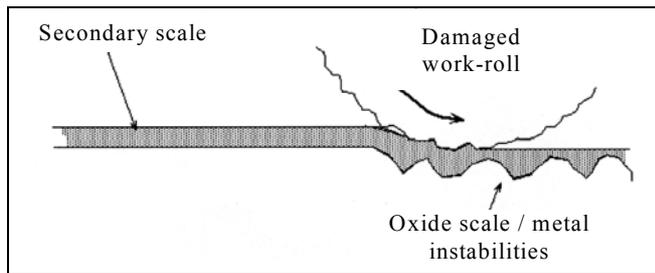
Stresses imposed by a rolling pass induce instabilities at the metal/oxide interface when no crack initiates. This phenomenon is often met in the co-rolling of materials having a different hardness at high temperature. It is very difficult to have a criterion for this kind of defect (Figure I-39).

Pad formation at the entry of the roll gap

Figure I-40: « Pad » formation at the roll gap entry

Formation de bourrelet en entrée d'emprise.
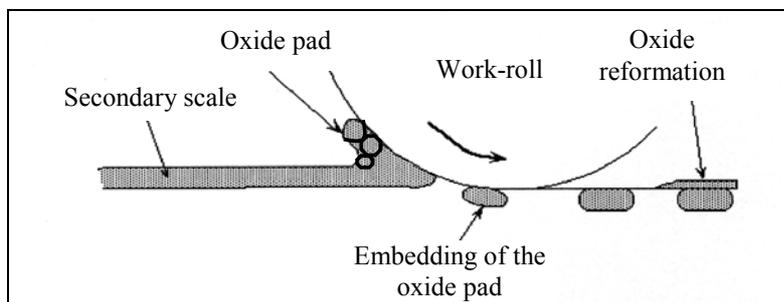
An accumulation of scale is possible at the roll gap entry (Figure I-40).
From a critical size, a « pad » thus formed can be embedded in the underlying metal. As in the previous case, this kind of defect cannot be predicted.

VI.2.4. Defects generated by roll degradation (Type D)

As seen previously, printing defects can be observed when work-rolls are degraded (the degradation of the roll increases its roughness). This degradation, which is one of the major concerns of the mill engineer, appears primarily at the end of the rolling campaign, contrary to the other mechanisms, which generate defects randomly during a mounting. From a mechanical point of view, this roll degradation increases friction and thus leads to higher stresses in the oxide scale, initiating cracks at the entry of the roll gap.

VI.2.5. Finally

```
┌─────────────────────┐              ┌──────────────────────────────┐
│   FSB DESCALING     │              │  THERMAL EVOLUTION OF STRIP  │
└─────────────────────┘              └──────────────────────────────┘
```

Scale thickness entry finishing mill

Scale thickness entry finishing mill
Thermal stresses
Scale / metal rheology

```
┌───────────────────────────────────────────────────────┐
│       EMBEDDED SECONDARY SCALE DEFECTS                 │
└───────────────────────────────────────────────────────┘
```

Thermomechanical stresses   Friction coefficient

```
┌─────────────────────────┐          ┌─────────────────────────┐
│   ROLLING PARAMETER     │          │   ROLLS DEGRADATION     │
└─────────────────────────┘          └─────────────────────────┘
```
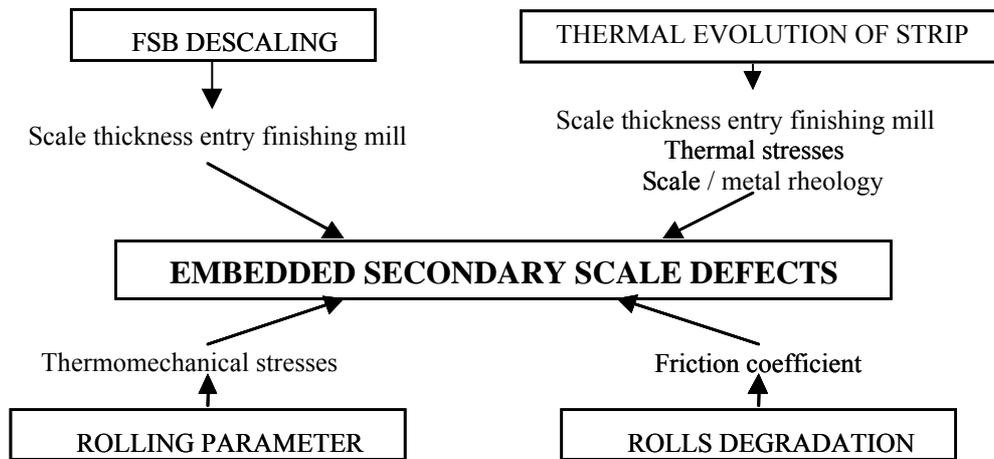
Figure I-41: Factors intervening in the rolled-in scale defect initiation.

Facteurs intervenant dans l'initiation de défauts de type calamine incrustée.

To avoid cracking, two criteria must be met :

- For temperature: $\sigma_{scale} < \mathrm{Min}\left[\sigma_{th.(crack)} , \sigma_{th.(decohesion)}\right]$ **eq. I-35**

- For mechanics: $\sigma_{scale} < \mathrm{Min}\left[\sigma_{crit\ (entry)}, \sigma_{crit\ (roll\ bite)} , \sigma_{crit\ (interface\ instabilities)}, \sigma_{crit\ (exit)}\right]$ **eq. I-36**

It is also necessary to take into account the scale thickness at the entry of the roll bite. Indeed, for each steel grade, each reduction, each temperature… there exists a critical scale thickness below which cracks can be initiated, but **without d**etrimental embedding to be generated. At the beginning of the mounting, the critical thickness is lower due to a higher roll / strip friction (the oxide layer that covers rolls is not formed yet). It is thus important to control the work-rolls degradation as well as the scale thickness at the entry of each FM stand (by the control of oxide growth kinetics).

Thermal and tensile stresses at the entry of the roll bites remain the main cause of oxide scale damage. The compressive stresses seem to mainly intervene in the detrimental embedding defect.

VII. EXAMPLES OF ROLLING

VII.1. Industrial rolling mill

Figure I-42 represents a steel strip rolled in good conditions in the Seremange roughing mill. The strip cross-section is observed at different locations in a roughing mill stand. It highlights the co-rolling of the oxide scale : the steel and the scale are deformed in the same way.
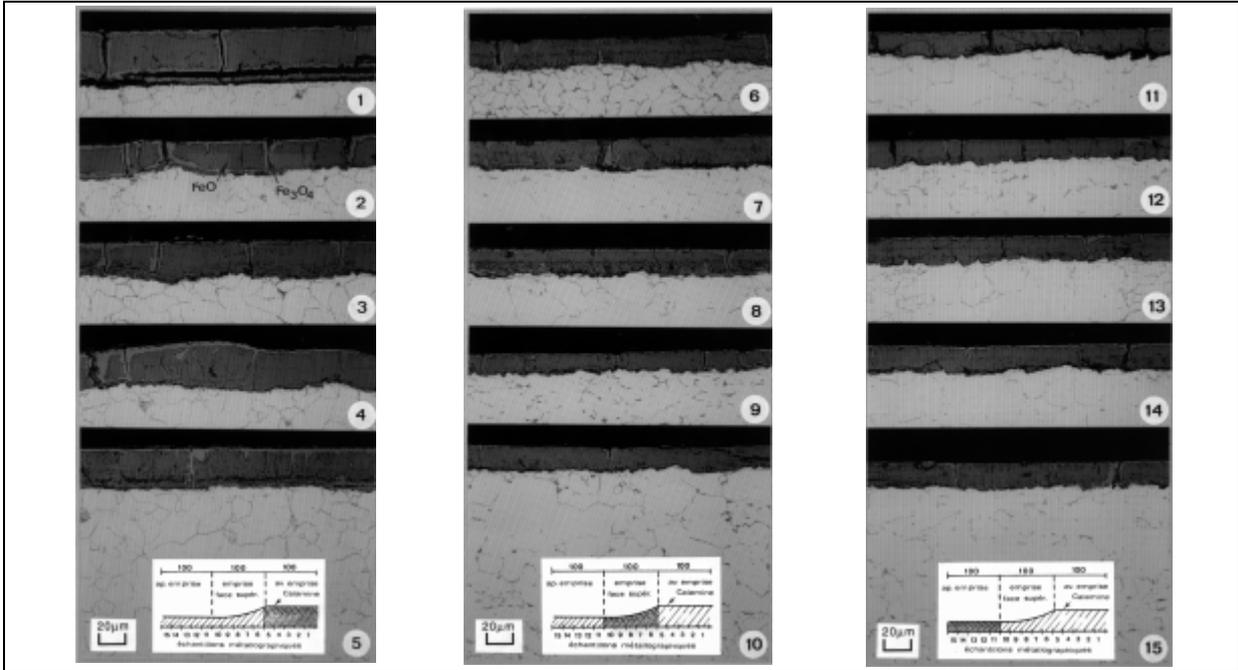
Figure I-42: Strip rolled in the Seremange roughing mill.

Bande laminée dans le dégrossisseur de Seremange.

After a problem on a stand F7 of the Dunkerque FM, a piece of strip (10 mm wide) has been taken at the F1 stand to be observed before, during and after the roll bite [Betr].
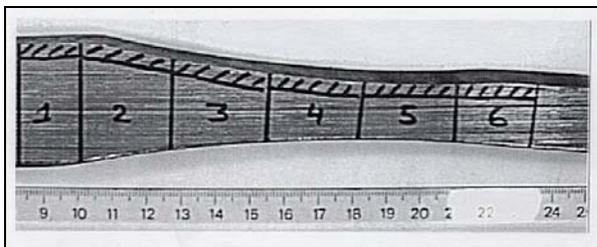
Figure I-43: Cutting of strip under F1 stand.

Découpe d'une bande dans une cage F1.

The piece of strip is cut in 6 parts and prepared to be observed on its cross-section, using an optical microscope (Figure I-43). Figure I-44 represents the film of the scale evolution per portion of strip. Each picture is taken at the same scale placed in the top left of them.

1-2   3

4   5

6   6'
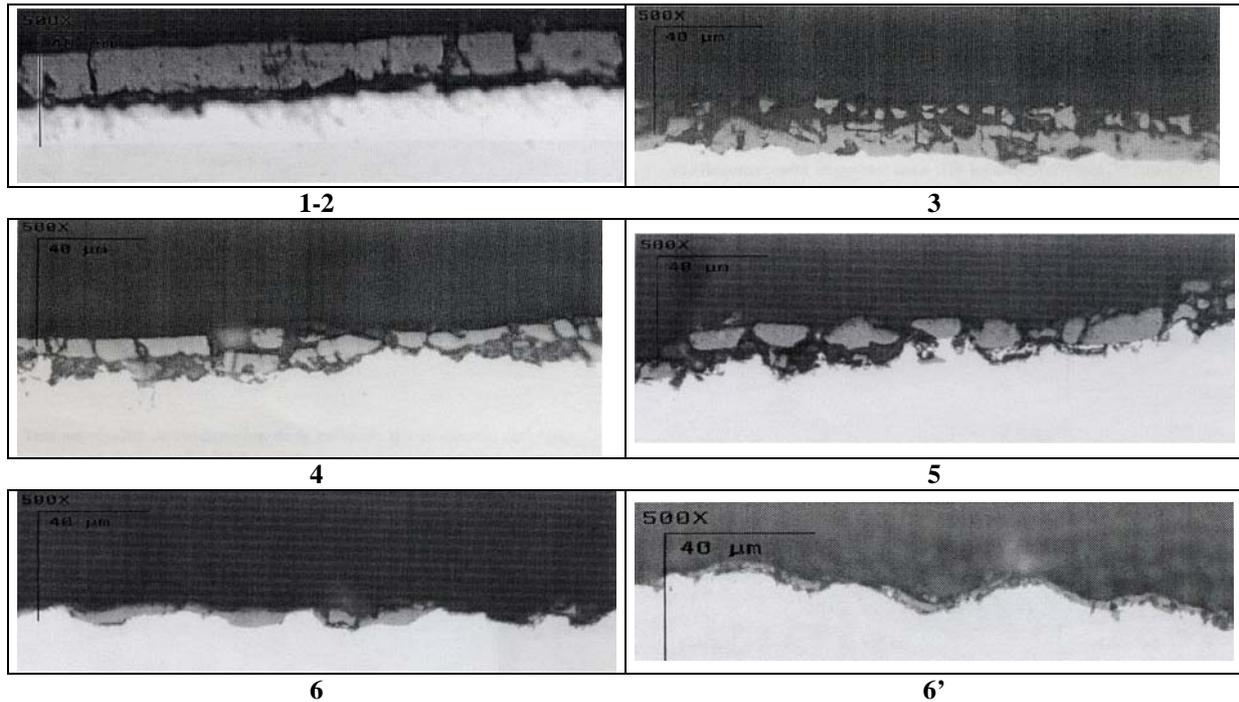
Figure I-44: Secondary scale evolution in stand F1 of the Dunkerque FM.

Evolution de la calamine secondaire dans une cage F1 du finisseur du laminoir de Dunkerque.

Before and at the entry of the roll bite (Figure I-44, 1-2) the oxide layer is uniformly thick and compact. In part 3, it is divided in two layers ; the most superficial one starts breaking (Figure I-44, 3). In part 4, the surface layer disappears (Figure I-44, 4). The remaining layer then begins to be broken. It is embedded in the soft steel under high compressive stresses in part 5 (Figure I-44, 5). At the exit of the roll bite, only an extremely thin scale remains on the rough steel surface, more adherent probably because of additional elements present at the steel-metal interface.
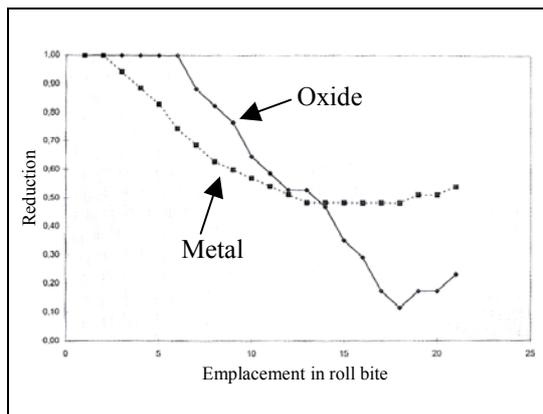
Figure I-45: Reduction in F1 stand

Réduction dans la cage F1.

Regarding the thickness evolution as a function of the position in the roll bite (Figure I-45), some remarks can be made. In the first part of the curve (until 6 on the x-coordinate), only the metal is deformed. There is high tensile stresses and low compression stresses. The scale is less ductile than the steel, which undergoes all the deformation. Between positions 6 and 9, the scale is co-rolled with the metal. After this point, the scale is highly cooled by the cold rolls and becomes brittle. It is divided in two layers, broken under high tensile and compressive stresses and embedded in the substrate.

The extremely low scale thickness after this point is probably due to the spallation of the scale during emergency stop. After this moment, the strip has been cooled in the air, undergoing thermal stresses and structure modifications, which have weakened it. The specimen preparation has probably been fatal to it. Without this stop, at the exit of the roll bite, cracks could have been repaired by reoxidation as on Figure I-42.

Feasibility tests performed by IRSID on the pilot rolling mill have shown that the reduction of the scale was approximately 2/3 of the steel one. Imagining that the reduction of the scale is smaller in the second part of the roll bite (cold scale around 600-700°C; steel around 900°C), results could be in good agreement with those from Dunkerque.

VII.2. Pilot rolling mill

Different authors have performed very interesting work to study the oxide scale damage in a roll bite. The University of Sheffield has made great advances in the domain thanks to Li and Sellars experimental tests, and Beynon and Krzyzanowski numerical simulations. The numerical modeling part will be described later.

In [Li7], it is explained that the oxide scale damage in the roll gap depends on its ductility, the latter varying with the scale thickness, the rolling temperature, the strain and the strain rate. All parameters can be determined except the surface temperature.

Authors then developed the hot sandwich rolling test that welds two C-Mn steel slabs together at the front end. Slabs are separately oxidized and closed together with the two scale layers trapped between the slabs. Thermocouples are inserted between them. With this technique, scale temperature remains the same during the test, without any gradient. The ductility of the material can thus be directly linked to the temperature. Figure I-46 presents the results of the test. Authors point out that there exist many differences between the test and the industrial hot rolling process (speed rolling for example), so that it is difficult to transfer results directly from one to the other.
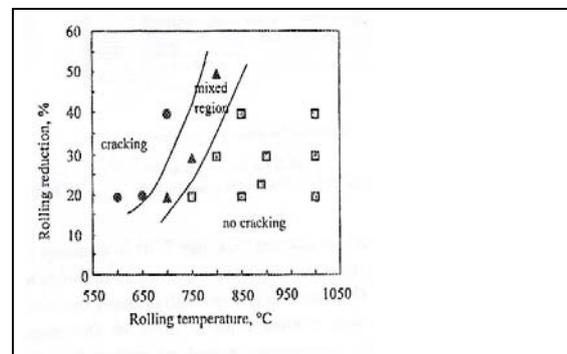
Figure I-46: Hot sandwich rolling results; Scale thickness: 100µm, Speed: 0.14m/s.

Résultats de laminage sandwich à chaud. Epaisseur de calamine : 100µm ; vitesse : 0,14m/s.

In [Krzy,Li6,Li8], the Sheffield university researchers present results obtained using interrupted hot rolling tests.
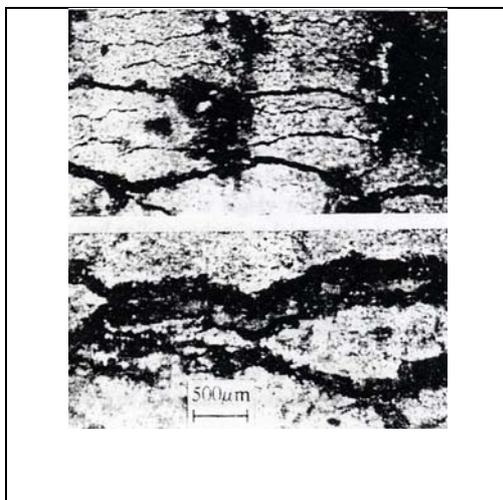
In [Li6], authors show the scale breaking during a rolling pass. Crack dimensions depend on the slab reduction. They highlight the crack widening with the reduction increase (18.9%-38.7%) as well as the increase of the extruded steel surface area (Figure I-47).

Figure I-47: Surface of steel slab after hot rolling. Photo above: scale thickness 210µm, reduction 18.9%. Below: scale thickness 240µm, reduction 38.7%.

Surface d'une brame d'acier après laminage à chaud. Photo du dessus : épaisseur de calamine 210µm, réduction 18,9%. Dessous : épaisseur de calamine 240µm, réduction 38,7%.
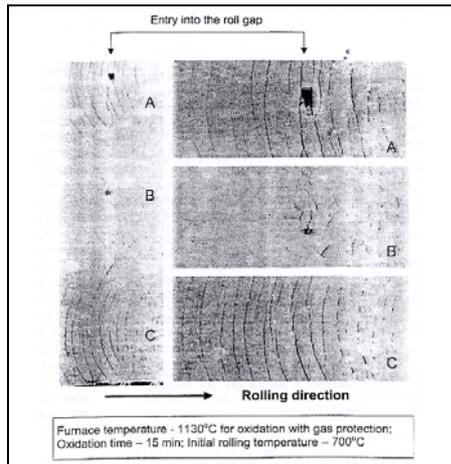
Figure I-48: Oxide scale on strip after testing. Reduction 30%.

Calamine sur la bande après test. Réduction 30%.

Another interrupted rolling test is presented in [Len, Krzy] (Figure I-48). These authors observe three zones in the slab width direction. The symmetrical border zones A and C, which are cracked before the entry in the roll gap under tensile stresses (on the sides, 3D-deformation), and the central zone C in which cracks only appear at the moment of the contact with the roll. These cracks are smaller and the inter-crack spacing is shorter.

Li and Sellars conclude their interrupted tests in [Li8] with a consequent study on mild steel slab behavior in a roll bite. More particularly, they observe the behavior of two kinds of layers on the steel substrate: lacquer layers in cold rolling and oxide scales layers in hot rolling.

Their conclusions show the very complex phenomena involved in the scale damage during rolling. It follows that oxide scales can have significantly different behaviors in and before the roll bite. They can be plastically deformed or cracked and delaminated, depending on the **scale thickness** (Figure I-49**,** Figure I-50**) and structure, the air cooling time before rolling, the rolling temperature, the reduction and the speed.** They conclude that the crack pattern after rolling is a combination of cracks formed **before** and **inside the bite**.
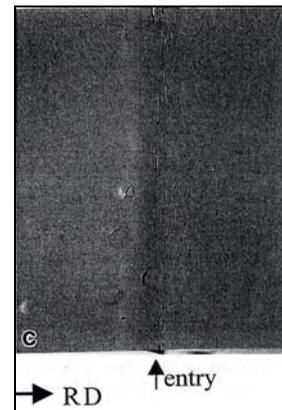
Figure I-49: Scale behavior before the roll gap of a hot rolling test with oxide scale. Temperature: 900°C, scale thickness: 20μm, reduction: 40%.

Comportement de la calamine avant l'emprise d'un test de laminage à chaud. T :900°C, épaisseur :20μm, réduction :40%.
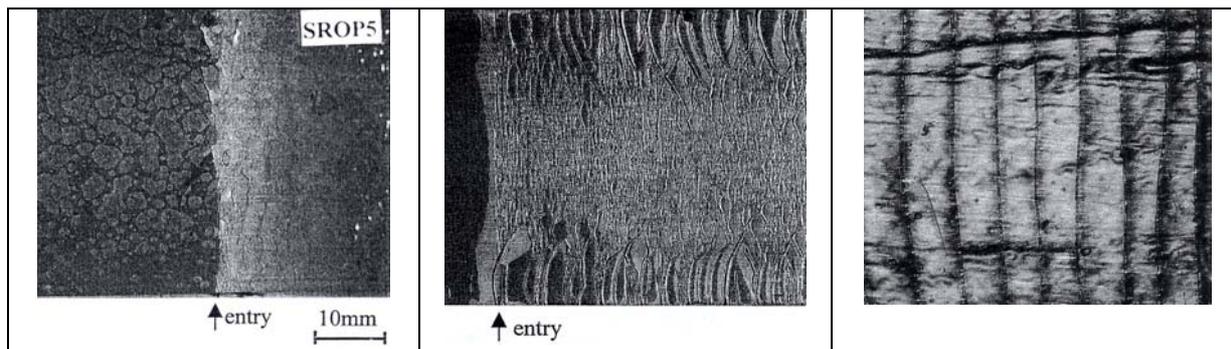
Figure I-50: Oxide scale. Temperature: 890°C, scale thickness: 40μm, reduction: 40%.

Calamine. T:890°C, épaisseur:40μm, réduction:40%.

Figure I-51: Lacquer behavior before the roll gap of a cold rolling. Thickness: 91μm, reduction: 29.7%.

Comportement d'une laque avant l'emprise d'un laminage à froid. Epaisseur :91μm, réduction :29,7%

Figure I-52: Lacquer. Temperature: 900°C, scale thickness: 20μm, reduction: 50%.

Laque. T:900°C, épaisseur:20μm, réduction:50%.

Principal results:

- Thin and soft scales at high temperature are deformed with the parent substrate at low reductions ; delamination wave bands at the entry occur at higher reductions.

- At low temperature, for thin and hard scales, cracking and delamination can occur. The same phenomena occur for thick and porous scales at high reductions. In the same case, authors remark that cracking and delamination start earlier before rolling for higher than for lower reduction.

- Higher reductions make cracks start earlier before rolling than for the lower reductions. More cracks are also observed in the roll bite due to a larger elongation of the metal (Figure I-51, Figure I-52). In this case, the extrusion inside cracks is more intense.

Okada [Oka] mentions the instabilities at the scale/metal interface as a source of embedding defects. Their experiments on a pilot rolling mill consisted in varying the scale thickness at the entry of the stand (between 4 and 15μm thick) as well as the reduction (between 1.5 and 35%). Results are presented Figure I-53 and Figure I-54. For a reduction of 1.5%, the metal/scale interface is smooth whatever the scale thickness, whereas the interface roughness increases with the entry scale thickness for a reduction of 35%.
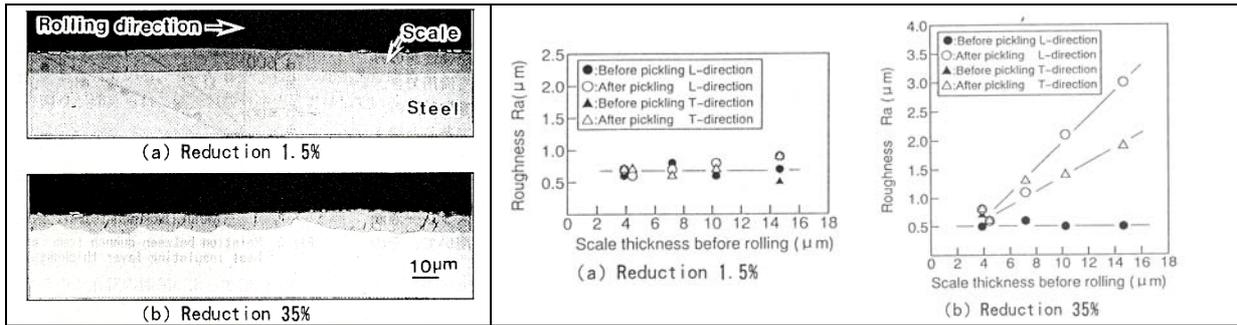
Figure I-53: Cross sectional images of scale/metal interface roughness depending on reduction [Oka].

Image de coupe de la rugosité d'interface calamine/metal en fonction de la réduction [Oka].

Figure I-54: Influence of scale thickness before rolling on the surface roughness [Oka].

Influence de l'épaisseur de calamine avant laminage sur la rugosité de surface [Oka].

The use of a descaling pilot coupled with a hot rolling pilot is more and more frequent to obtain quantitative information on the oxide scale flow. Thus, in [Lant], the main results of R. Boelen and al. [Boe] are presented. They have quantified the secondary scale critical thickness at the entry of a stand in terms of detrimental defect initiation.

They put in evidence the major influence of the scale thickness. The maximum thickness at the entry of a FM roll bite to obtain a **perfect** surface quality is **8µm,** which corresponds (from results on Figure I-15 and in [Col]) to a perfect descaling at the entry of the FM. Nevertheless, they remark that an entry **thickness of 20µm** gives **acceptable** results. For higher thickness, such as 28 and 45µm, the embeddings constitute extremely thick waves perpendicular to the rolling direction (equal or thicker than the initial scale thickness at the entry of the roll bite). Authors conclude that when there is embedding, the scale does not undergo reduction. This phenomenon implies the formation of scale-free surfaces at the exit of the roll bite.

In [Til], a two-high laboratory hot rolling mill and heating furnace is used, with a set of parameters as close as possible to those of FM. Tests are performed for a low and an ultra-low carbon steel. They obtain the same type of rolled-in scale defect than on an industrial mill (Figure I-55). For a scale of 100µm thick around 1100°C, we observe on Figure I-56 that the oxide is highly thinned (ductile behavior at high temperature), without cracks. Table I-3 and Figure I-57 present results of rolling tests in terms of crack initiation.
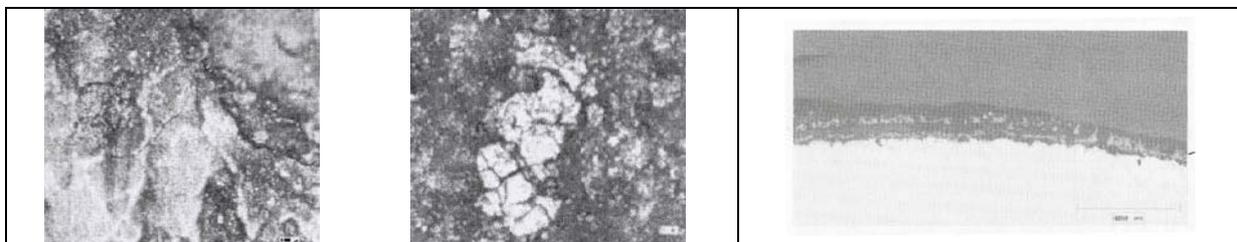
Figure I-55: Rolled-in scale defect. Left picture: commercial hot band. Right picture: Experimental hot band (same picture enlargement) [Til].

Défaut de calamine incrustée. Image de gauche : bande à chaud commerciale. A droite : bande à chaud expérimentale (même agrandissement d'image) [Ti1].

Figure I-56: Entry of the roll gap: scale thickness 100µm [Til].

Entrée d'emprise : épaisseur de calamine 100µm [Ti1].

43

Sample No.	Temperature (°C)		Rolling speed	Reduction	Scale Thickness
	Furnace	Rolling	(mm/s)	(%)	(µm)
yu4* [c]	976	842	728.4	10.3	63.89
yu14 [s]	978	848	160.6	39.6	17.39
yu25 [s]	1019	868	73.4	31.0	8.04
yu26** [s]	1019	874	169.8	31.6	9.23
yu28*** [c]	1019	910	612.5	31.6	52.08
yu29****[s]	1019	877	70.0	38.7	10.75
yu31 [s]	1019	852	294.9	36.6	13.75
yu38 [c]	1080	930	182.8	20.8	18.59

Table I-3: Results of low carbon tests. [c]racked; [s]mooth [Ti1].

Résultats pour aciers doux. [c] fissuré [s] lisse [Ti1].
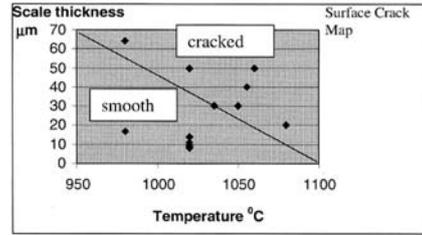
Figure I-57: Surface crack map for low and ultra low carbon steel [Ti1].

Carte de fissures de surface pour les aciers doux et extra doux [Ti1].

In [Yu], different steel strips are rolled at various temperatures, speeds and reductions. Scale thickness is carefully controlled before and after the rolling pass. The strip cooling is done in an inert atmosphere.
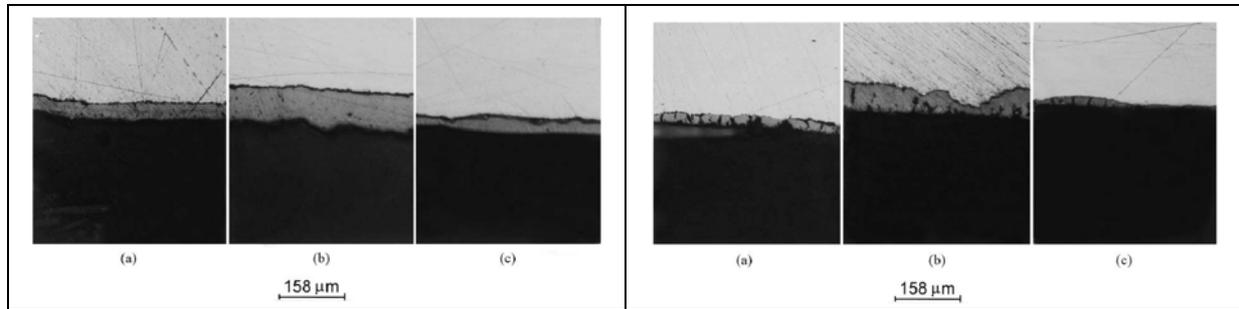
Figure I-58: 1) Thickness of the scale before the entry of the roll gap. Oxidation around 1100°C.

2) Scale thickness at the exit of the roll gap [Yu]

1) Epaisseur de calamine avant l'entrée d'emprise. Oxydation autour de 1100°C.

2) Epaisseur de calamine en sortie d'emprise [Yu]

	Strip temperature (°C)	Strip reduction (%)	Initial scale thickness (µm)	Final scale thickness (µm)	Scale reduction (%)
a	964	**31.48**	17.8	11.7	**34.3**
b	961	**31.2**	58	41.9	**27.8**
c	935	**20.56**	15.5	12.9	**16.8**

Table I-4: Scale thickness before and after rolling.

Epaisseur de calamine avant et après laminage.

Several ideas can be formulated from Figure I-58 and Table I-4:

- for a thin scale (a and c), the steel / scale interface is smooth. There are transverse cracks but without any extrusion;
- for a thicker scale (b), there are much less cracks. This observation will be confirmed in chapter II by a formula suggesting proportionality between the inter-crack distance and the scale thickness. The interface roughness is very large.
- as for scale reduction (Table I-4), the ratio between scale and steel reduction is for 108.9% for a), 74.5% for b) and 81.6% for c). It is difficult to conclude from this. A possible explanation of the behavior difference between a) and b) could be that when the scale is thin, it is more adherent and therefore deformed in the same way as its substrate (co-rolling: case (a)). For thicker scales (b) scale is more brittle and less adherent : cracks initiate as well as extrusion ; the oxide scale is then less reduced than its substrate. For b) and c) the reduction is in good agreement with previous observations (scale reduction lower than the steel one: 3/4 and 4/5 of the metal reduction).

In [Le] the surface oxide fracture is studied using aluminium cold rolling. Their results concerning the inter-crack distance and the extrusion conditions (for thicker scale) are in perfect agreement with previous observations (Figure I-59).
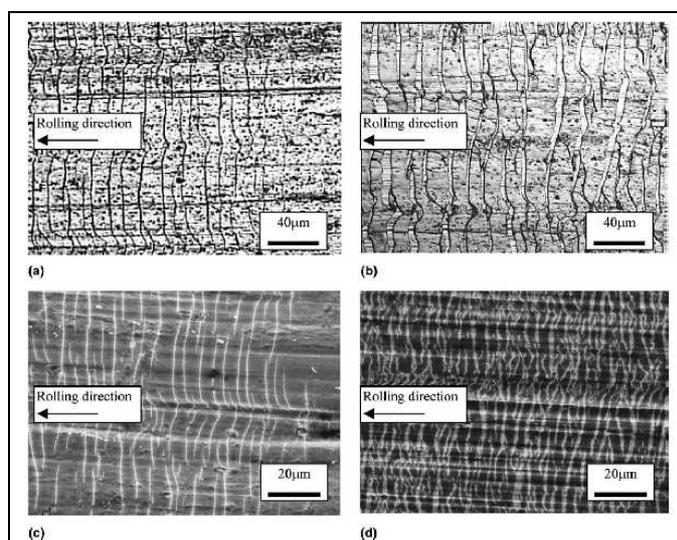
Figure I-59: Micrographs showing cracks on the strip surface. Reduction=30%: a,c) entry of roll bite; b,d) exit; a,b) h=1.8μm; c,d) h=0.22μm.

Micrographies montrant les fissures à la surface de la bande. Réduction=30% : a,c) entrée d'emprise ; b,d) sortie ; a,b) h=1.8μm; c,d) h=0.22μm.

The experiments highlight an interesting phenomenon: for a thick scale (in their configuration, >1.5μm), inter-cracks length does not change between the entry and the exit of the roll gap, contrary to thinner scales for which "**roll bite cracking**" obviously occurs.

They also show that the extrusion depends on the reduction. For a strip covered by a scale 15μm thick, a total extrusion is observed in the cracks for a reduction of 30% whereas it is only partial for a reduction of 10%.

VIII. CONCLUSION

In this first chapter, we have presented the industrial hot rolling process in order to better introduce our study on rolled-in scale defects initiated in the last part of the process: the finishing mill.
The thermomechanical description of the finishing mill as well as an isolated stand have shown the complexity of the rolled-in scale problem. In addition to the deformation involved in such a process, thermal cycles are also extremely critical.

Thermal phenomena in hot rolling have to be observed both at a macroscopic and a microscopic level. In the first case, cold work-rolls are mainly concerned: their contact with the hot strip increases their temperature, which decreases again by conduction as soon as the contact is finished. These variations of temperature promote rolls degradation.
At a microscopic level, the oxide scale plays the role of a thermal barrier if it is not damaged. The damage is also closely linked to its temperature. Thus, hot rolling mechanics has also to be studied with much care.

In terms of stress, two contributions have to be examined : thermal stresses in the interstand and mechanical stresses at the entry and inside the FM stands.

Two mechanisms are thought to be at the origin of scale embedding :

- cracking of the oxide layer at the entry of the roll bite followed by the metal extrusion under the rolls;
- the printing in the strip (due to work-roll roughness or residues embedding).

Tensile stresses at the entry of roll gaps remain the main cause of oxide scale damage. Compressive stresses seem to intervene mainly to turn damage (cracks) into the very detrimental embedding defect. This is why we have studied the oxide scale using several mechanical tests, to mimic mechanical solicitations (cf. chapter IV and V).

To realize the difficulty of the problem, several tendencies can already be noted:

- The roll surface state is closely linked to the friction coefficient at the scale-roll interface, itself linked to the stress magnitude at the entry of the roll gap which is at the origin of cracks initiation. It is therefore useful to decrease friction, submitted to the constraint that it must be sufficient to engage the strip inside the roll bite.
- Rolling at higher temperature decreases abrasion of the rolls by the oxide scale; it also causes lower stresses at the entry of the roll gap. In an opposite way, higher strip temperature means more roll heating, as well as a thicker oxide scale, which may generate more severe rolled-in scale defects.
- Stresses bring about scale damage but the initiation of detrimental defects is also a function of many parameters. It is also necessary to take into account the scale thickness at the entry of the roll bite. Indeed, for each steel grade, each reduction, each temperature… there exists a critical scale thickness below which cracks can be initiated, but **without forming** detrimental embedding.

All these parameters are thus closely linked. To better understand what is happening, it is **necessary** to get more data on the oxide scale physical and mechanical properties.

IX. REFERENCES

[Ber]   G.Béranger, G.Henry, G.Sanz, Le livre de l'acier, Tech. & Doc Lavoisier, Paris, (1994). *In french.*

[Betr]   G.Betremieux, Etude sur le defaut "gravelure" sur le train continu à chaud de Slooac Dunkerque, Rapport de stage, Université technologique de Compiègne / Sollac (Usinor). *In french.*

[Bey]   J.H.Beynon , Y. H. Li, M.Krzyzanowski, C. M. Sellars, Measuring, modelling and understanding friction in the hot rolling of steel, Metal forming 2000, Pietrzyk et al. (Eds), (2000).

[Boe]   R.Boelen, P.Curcio, M.Assefpou, Laboratory simulation of the effect of hot rolling on scale morphology, Proceedings of the 1st International Conference on descaling, London (UK), The Institute of Materials, (Octobre 1995).

[Cast]   E. de Castro, Etude des cinétiques d'oxydation des aciers au cours du laminage à chaud, rapport de stage IRSID, (juin 1998) ; Comportement cinétique et mécanique des couches d'oxydes formées au cours du laminage à chaud des aciers, rapport de stage IRSID, (septembre 1998). *In french.*

[Che]   J.L.CHENOT, Méthodes de calcul en plasticité. , technique de l'ingenieur M 595, (1991). *In french.*

[Chen]   W.C.Chen, I.V.Samarasekera, E.B.Hawbolt, Fundamental phenomena governing heat transfer during rolling, Met. Mat. Trans. A 24, (1993), pp.1307-1320.

[Col]   R.Colas, L.A.Leduc, Thermal evolution of low carbon steel strip, 34th MWSP conf. Proc., ISS-AIME, vol.XXX, (1993), pp.13-17

[Dev1]   C.Devadas, I.V.Samarasekera, E.B.Hawbolt, Thermal and metallurgical state of steel strip during hot rolling, Part I. Charactrization of heat transfert, Metall. Mater. Trans. A 22, (1991), pp.307-319.

[Dev2]   C.Devadas, I.V.Samarasekera., Heat transfert during hot rolling of steel strip, Ironmaking and steel making, vol13 n°6, (1986), pp.311-321.

[Fel]   E.Felder, Interactions cylindre-métal en laminage, rapport CESSID, Session laminage, Centre de Mise en forme des Matériaux, Ecole des Mines de Paris, (1985). *In french*

[Fos]   Sollac Fos internet Site: http://www.sollacmediterranee.com

[Garc]   M.Garcia-Villan, défaut calamine finisseur, Rapport de Stage Université de technologie de compiègne / Sollac (USINOR), (février 1998). *In french.*

[Jin]   D.Q.Jin, V.H.Hernandez, I.V.Samarasekera, Integrated process model for the hot rolling of plain carbon steel, in: J.H.Beynon, P.Ingham, H.Teichert, K.Waterson (Eds.), proceedings of the second international conference modeling of Metal Rolling Processes, London, UK, (December 1996), pp.36-58.

[Keu]   R.Keurgen, adaptation du modèle « metallurgical rolling force » (MRF) au train à chaud de Chertal,
in http://www.crm-eur.com/F-PUBLICATIONS/media/MRF_CHERTAL.pdf

[Kob]   S.Kobayashi, S.I.Oh, T.Altan, Metal forming and the Finite-Element Method, Oxford University press, New York, (1989), p119

[Krzy] M.Krzyzanowski, J.H.Beynon, C. M. Sellars, Analysis of secondary oxide-scale failure at entry into the roll gap, Metallurgical and Materials Transactions B, vol.31B, (december 2000), pp.1483-1490.

[Lagr] J.Lagergen, friction evaluation in hot strip rolling by direct measurement in the roll gap of a model duo mill, Journal of materials processing technology 70, (1997), pp.207-214.

[Lant] V.Lanteri, C. Thomas, F. Geffraye
"Défauts d'embedding calamine secondaire au Train à Bandes", Synthèse des mécanismes et perspectives, IRSID groupe USINOR, (décembre 1998).
Document réservé aux destinataires nommément désignés. In french.

[Le]   H.R.Le, M.P.F.Sutcliffe, P.Z.Wang, G.T.Burstein, Surface oxide fracture in cold aluminium rolling, Acta materialla 52 (2004), pp911-920

[Len]   J.G.Lenard, An examination of the coefficient of friction, in Metal forming science and practice, a state of the art volume in honour of Pr J.A.Schey's 80th birthday, edited by J.G.Lenard, (2002), pp85-114

[Li1]   Y. H. Li, C. M. Sellars, Effects of scale deformation pattern and contact heat transfer on secondary scale growth, in: Proc. 2nd Int. Conf. On Hydraulic Descaling in Rolling Mills, London, the institute of materials, (1997).

[Li2]   Y H Li, C M Sellars, Comparative Investigations of Interfacial Heat Transfer Behaviour during Hot Forging and Rolling of Steel with Oxide Scale Formation, Journal of Materials Processing Technology, Vol 80-81, (1998), pp.282-286.

[Li3]   Y. H. Li, C. M. Sellars
"Modelling deformation behaviour of oxide scales and their effects on interfacial heat transfer and friction during hot steel rolling", Proc. 2nd Int. Conf Modelling of Metals Rolling Processes, London, Institute of Materials, UK, (1996), pp.192-201.

[Li4]   Y H Li, C M Sellars, Modelling Surface Temperatures during Hot Rolling of Steels, in Proc 3rd Int Conf on Modelling of Metal Rolling Processes, ed J H Beynon et al., London, Institute of Materials, UK, (1999), pp.178-186.

[Li5]   Y.H. Li, C.M. Sellars, Modelling deformation behaviour of oxide scales and their effects on interfacial heat transfer and friction during hot steel rolling, 2nd Int Conf on Modelling of Metal Rolling Processes, The Institute of Materials, (December 1996), pp.192-201.

[Li6]   Y.H.Li, C.M.Sellars, Evaluation of interfacial heat transfer and friction conditions and their effects on hot forming processes, 37th MWSP CONF. PROC., ISS, vol. XXXIII, (1996), pp.385-393

[Li7]   Y. H. Li, M.Krzyzanowski, J.H.Beynon, C. M. Sellars, physical simulation of interfacial conditions in hot forming of steels, Acta metallurgica sinica, vol.13 n°1, (February 2000), pp.359-368.

[Li8]   Y.H.Li, C.M.Sellars, behaviour of surface oxide scale before roll bite in hot rolling of steel, Materials science and technology vol.17, (december 2001), pp.1615-1623.

[Mon1]   P.Montmitonnet, Laminage − Objectifs et modélisation, technique de l'ingenieur M3065, (2002). *In french.*

[Mon2]   P.Montmitonnet, Laminage à chaud − Théorie du laminage, technique de l'ingenieur M7840, (1991). *In french.*

[Mor]   G. Moreas, H. Uijtdebroeks, On-line roughness measurement of hot rolled strips, Publication CD European Communities, ISBN 92-894-3671-9, (2002).

[Munt]   A.Munther, J.G.Lenard, A study of friction during hot rolling of steels, Scandinavian Journal of Metallurgy 26, (1997), pp.231-240.

[Oka]   H. Okada, Effect of scale deformation at hot rolling on strip surface, CAMP-ISIJ, Vol. 9, (1996), p340

[Paw]   O.Pawelski, Berechnung der Wärmedurchgangszahl für das Warmwalsen und Schmieden, Arch. Eisenhüttenwes. 40 (10), (1969), pp821-827.

[Sam]   I.V.Samarasekera, 1990, The Importance of Characterizing Heat Transfer in Hot Rolling of Steel Strip, Int. Symp. on Mathematical Modelling of Hot Rolling of Steel, 26-29 Aug., pp.148-167.

[Schw]   K.Schwerdtfeger, S.Zhou, a contribution to scale growth during hot rolling of steel, Steel Research 74 n°9 (2003), pp.538-548

[Ste]   P.G. Stevens, K.P. Ivens, P. Harper, Increasing work roll life by improving roll cooling practice, J. Iron Steel Inst. (Jan. 1971) pp. 1-11

[Til]   J.B.Tiley, J.G.Lenard, Y.Yu, Roll bite deformation of the thin scale layer on a plain carbon steel during hot rolling, 42nd MWSP CONF. PROC., ISS, vol.XXXVIII, 2000, pp.215-220.

[Tom]   K.Tominaga, Prevention of secondary scale defect at H.S.M in Mizushima Works, Camp Isij vol.8, (1995), pp.1242. *In japanese.*

[Uijt2]   H. Uijtdebroeks, R. Franssen, G. Sonck, A. Van Schooten, On-line analysis of the work roll surface deterioration, *la revue de métallurgie-CIT*, (1998), pp.789-799.

[Uijt1]   H.Uijtdebroeks, R.Franssen,, D.Vanderschueren, P.M.Philippe, Integrated on-line work roll surface observation at the SIDMAR HSM, 44 th MWSP Conference Proceedings, Orlando, September 2002, Vol. XL, (2002), pp. 899-908.

[Wang]   S.R.Wang, A.A.Tseng, Macro and micro modelling of steel coupled by a micro constitutive relationship, I&SM 23 (9), (1996), pp.49-61

[Yu]   Y.Yu, J.G.Lenard, Estimating the resistance to deformation of the layer of scale during hot rolling of carbon steel strips, Journal of materials processing technology 121, (2002), pp.60-68

[Zhou]   S.X. Zhou, an integrated model for hot rolling of steel strips, J. Mater. Process. Tech.134 (2003) pp.338-351

Oxide scale properties

Observations MEB in situ de la croissance d'oxyde sur une éprouvette d'acier extra doux (900°C – atmosphère humide). Les quatre étapes sont (de haut en bas) : l'acier froid non oxydé, la formation du film polycristallin à 900°C, la formation de germes épitaxiaux et leur croissance latérale et verticale (8 min à 900°C).

Une représentation graphique est donnée Figure II-2.
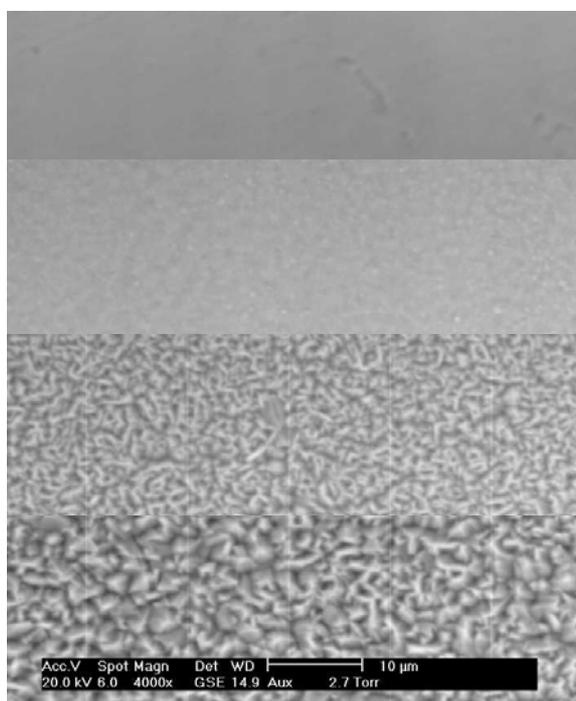
In situ ESEM observations of oxide growth on extra-low carbon steel specimen (900°C - wet atmosphere). The four steps are (from top to bottom): the cold non-oxidized steel, the formation of a polycrystalline film at 900°C, the formation of epitaxial germs and their lateral and vertical growth (8 min at 900°C).

A graphic representation is given on Figure II-2.

Résumé

Dans le chapitre I, le procédé complexe de laminage à chaud a été décrit, et plus particulièrement le but de notre étude : les différents mécanismes d'initiation de défauts d'incrustation dans le finisseur. Nous avons mis en évidence la nécessité d'étudier les propriétés physiques et mécaniques de la calamine dans une cage du finisseur, afin de mieux comprendre ce qu'il se passait exactement.

Dans le chapitre II, nous nous concentrons sur les paramètres critiques en terme de défaut de calamine incrustée, et sur la détermination de critères d'endommagement.

Plusieurs observations industrielles montrent que l'usure des cylindres des cages F1 et F2 du finisseur est la plus rapide. Dans ces cages, les températures et les réductions sont les plus élevées. Un lien direct a été fait avec l'existence d'une épaisseur critique de calamine de 20μm à partir de laquelle les défauts apparaissent.

Afin d'éviter la formation de ces défauts, une étude des mécanismes de croissance d'oxyde (sous des conditions chimiques et thermiques aussi proches que possible de celles rencontrées dans le finisseur) a été réalisée. Comme les cinétiques d'oxydation sont liées à la température, il est possible de déterminer pour chaque nuance d'acier, une température maximale de brame à l'entrée du finisseur. Les limites d'opération du train à bande sont alors exprimées en fenêtre de températures (autour de 900-1000°C), étroitement liées à l'épaisseur de calamine.

L'étude bibliographique réalisée ensuite sur le comportement mécanique des couches d'oxyde montre que dans la gamme de température du finisseur, la calamine se déforme plastiquement.
Néanmoins, les observations sont souvent faites sous des conditions de déformation et de vitesse de déformation très différentes du laminage.

Beaucoup de données existent sur l'endommagement des couches d'oxyde. Tous les types d'endommagement ont été étudiés (fissure, délamination, spallation), mais les résultats existants utilisent souvent les mécanismes de fissuration élastique linéaire au lieu du comportement plastique de la calamine. De plus, les valeurs critiques sont souvent obtenues en traction et exprimées en déformation globale. En conséquence, elles ne peuvent être appliquées pour d'autres tests expérimentaux ou pour des procédés industriels. Nous avons besoin de critères locaux. Tous les critères bibliographiques sont donc uniquement utilisables dans les conditions expérimentales des auteurs, très différentes des conditions de laminage.

Des tests expérimentaux reproduisant de manière la plus proche possible les conditions chimiques et thermomécaniques d'un finisseur industriel sont donc nécessaires.

I. INTRODUCTION

In chapter I, we have described the complex hot rolling process and more particularly the aim of our study: the different mechanisms of rolled-in scale defects initiation in the finishing mill (FM). We have also highlighted the necessity to study physical and mechanical properties of the oxide scale in a finishing mill stand, in order to better understand what happens exactly.

In chapter II, we are now going to focus on the critical parameters in terms of **rolled-in scale damage**, and on the **determination of damage criteria**.

Several industrial observations show that work-roll wear on the FM is fastest in F1 & F2. In these stands, temperature and reduction are highest. A direct link has been made with the critical scale thickness of 20μm above which rolled-in scale defects are initiated.
In order to control and avoid defects initiation, a study of the oxide growth mechanisms has to be made, under chemical and thermal conditions as close as possible to the FM ones : this is the aim of the first part. As the oxidation kinetics is linked to the temperature, it is possible to determine, for each steel grade, a maximal slab temperature at the entry of the FM.
In the second part, the mechanical oxide scale behavior is investigated. Starting from the fracture mechanics theory, we will explain several damage criteria available in the literature, more or less adaptable to our process.

II. PHYSICAL PROPERTIES

II.1. Oxidation growth

II.1.1. Bibliography

On clean surfaces, atomic bonds are not saturated. Such surfaces are therefore thermodynamically unstable, and present a high reactivity with external environment. Metal surfaces will thus create electrovalence in particular with oxygen : one speaks of **chemical adsorption** or **chemisorption** of the oxygen on the metal.
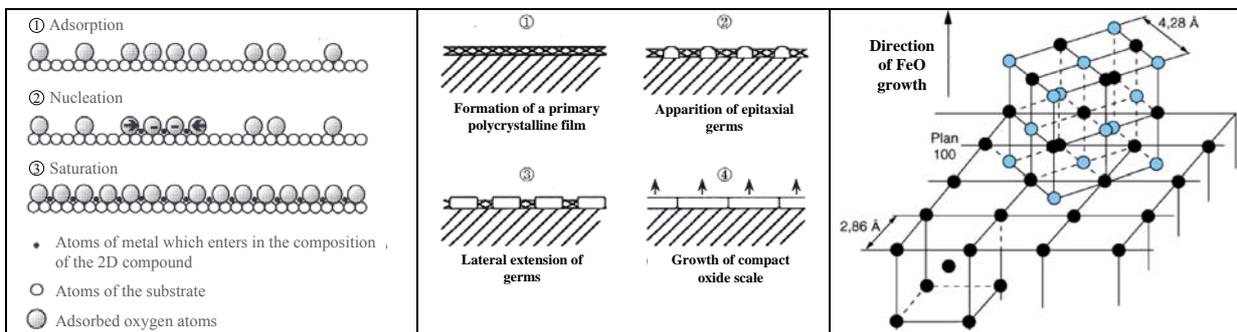
Figure II-1: Mechanism of surface saturation [Bar]

Mécanisme de saturation de surface [Bar]

Figure II-2: Growth of epitaxial nucleus [Ben].

Croissance des germes épitaxiaux [Ben].

Figure II-3: Epitaxial formation of FeO on Fe-α(001) face [Ber].

Formation épitaxiale de FeO sur la face Fe-α(001) [Ber].

Once the surface is saturated, an oxide nucleus appears and grows laterally (Figure II-1). When the surface is totally covered, growth continues perpendicularly at the expense of the substrate thickness (Figure II-2). The surface reactivity strongly depends on the crystalline orientation of the metal: the oxidation is influenced by grain orientation [Ver]. This is true only in the first stages of the reaction, when the film is less than 1µm thick. Afterwards, crystallographic orientation has no more influence on the oxidation velocity, because the growth is perpendicular to the surface (Figure II-3).

A double diffusion phenomenon of anions (oxygen ions) and cations (metallic ions) governs the oxide growth. Both of them migrate through the interstitial sites and gaps, from the metal-oxide interface to the surface for cations and in the opposite way for anions. But oxides are polycrystalline, and grain boundaries represent preferential diffusion paths. In the same way, other defects such as dislocations, porosity and cracks can enhance diffusion.

Three kinds of oxide may exist on iron (Figure II-4)**:**
- For T>570°C: wüstite (FeO), magnetite (Fe_3O_4) and hematite (Fe_2O_3).
- For T<570°C: only Fe_2O_3 and Fe_3O_4 exist. FeO is not stable.

The oxide scales formed on iron during isothermal high temperature heating (between 700°C and 1200°C) and are made up of a superposition, from the surface to the substrate, of hematite Fe_2O_3 (1% of the scale thickness), magnetite Fe_3O_4 (4%) and wüstite FeO (95%) [Païl]. The equilibrium diagram predicts this order with the iron richest oxide closest to the metal. Reaching the steady state takes more than one hour at 700°C, a few minutes at 1000°C.

The thickness of consumed metal (iron) can be calculated from mass conservation law. Indeed, the iron atoms present in the oxide scale are not anymore in the substrate. Thus:

$$m_{Fe} = m_{Fe/FeO} + m_{Fe/Fe_3O_4} + m_{Fe/Fe_2O_3}$$

eq. II-1

$m_{Fe/FeO}$, m_{Fe/Fe_3O_4} and m_{Fe/Fe_2O_3} represent the iron mass in each iron oxide type. $m = \rho.S.h$, where ρ is the material density, S its surface and h its thickness. For a same surface S of consumed metal and oxide, and for the oxide scale composition described previously:

$$\frac{h_{Fe-consumed}}{h_{scale}} = \left[0.95\frac{\rho_{FeO}}{\rho_{Fe}}\left(\frac{M_{Fe}}{M_O + M_{Fe}}\right) + 0.04\frac{\rho_{Fe_3O_4}}{\rho_{Fe}}\left(\frac{3M_{Fe}}{4M_O + 3M_{Fe}}\right) + 0.01\frac{\rho_{Fe_2O_3}}{\rho_{Fe}}\left(\frac{2M_{Fe}}{3M_O + 2M_{Fe}}\right) \right]$$
eq. II-2

Introducing $\rho_{Fe} = 7.86 g/cm^3$, $\rho_{FeO} = 5.5 g/cm^3$, $\rho_{Fe_3O_4} = 5.18 g/cm^3$, $\rho_{Fe_2O_3} = 5.24 g/cm^3$, $M_O = 16 g/mol$, $M_{Fe} = 56 g/mol$ (M: molar mass) leads to:

$$h_{Fe-consumed} = 0.54.h_{scale}$$

eq. II-3a

For a layer of pure FeO, the result is quasi-identical: $h_{Fe-consumed} = 0.545.h_{FeO}$.

eq. II-3b

When cooling is performed from temperatures higher than 570°C, Fe_3O_4 precipitates within FeO by a germination-growth mechanism: $4FeO \rightarrow Fe + Fe_3O_4$, as seen by [Schm] during *in situ* high temperature oxidation and cooling of iron by ESEM (Environmental Scanning Electron Microscope). Precipitations, which are explained by the form of the wüstite existence domain (Figure II-4), occur all the more easily as FeO is richer in oxygen. Thus,

precipitates are formed in the external part of the FeO layer. They also strongly depend on the cooling speed of the oxide scale (Figure II-5).
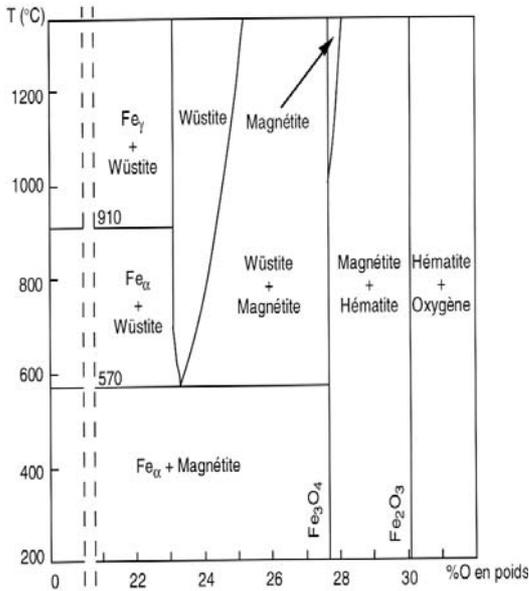
Figure II-4: Equilibrium Fe-O diagram.

Diagramme d'équilibre Fe-O.
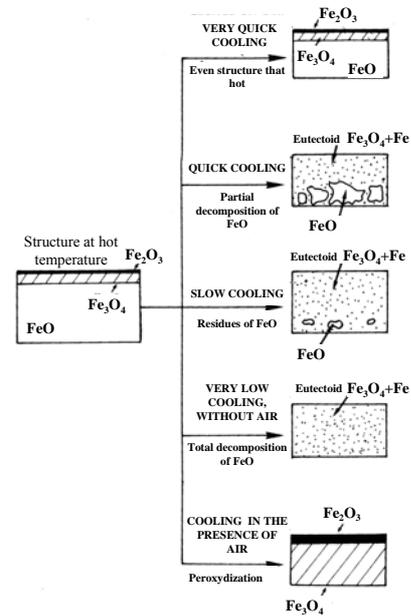
Figure II-5: Oxide decomposition depending on cooling speed.

Décomposition de l'oxyde en fonction de la vitesse de refroidissement.

The structure of iron oxides is:

FeO: NaCl structure (FCC: Face-centered cubic). Wüstite is a non-stœchiometric oxide noted $Fe_{1-x}O$ due to its iron deficiency (vacancy) in its crystalline structure. The value of x increases with the substrate/oxide interface distance.

Fe_3O_4: spinel structure containing iron vacancies but in weak concentration.

Fe_2O_3 : exists in two forms, a stable one α-Fe_2O_3 (CC: centered cubic) and a metastable one γ-Fe_2O_3 (FCC).

II.1.2. Oxidation kinetics – Scale thickness

The knowledge of the growth kinetics of oxide layers is essential to predict their thickness during rolling. Indeed, critical scale thickness is closely linked to the steel grade and to product elaboration conditions. Given its largely predominant percentage, **we will take into account FeO only in the following.**

Oxide scale growth mechanism on iron is well known and controlled by diffusion (Figure II-6) [Ber] :
- The diffusion of Fe^{2+} ions in wüstite in the form of cationic vacancies;
- The diffusion of iron in magnetite bringing into play the ferrous ions Fe^{2+}, ferric ions Fe^{3+} and implying the tetrahedral and octahedral sites;
- The diffusion of oxygen ions through the hematite layer.
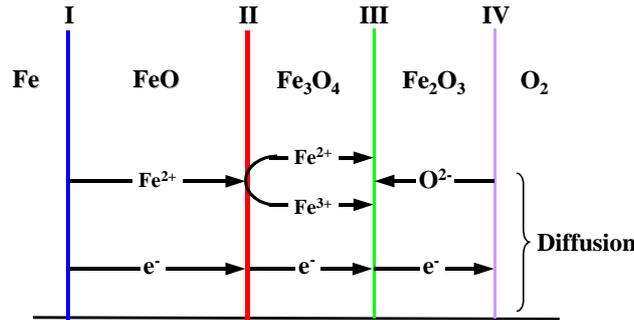
Figure II-6: Diffusion mechanisms of iron oxidation at T>570°C.

Mécanismes de diffusion de l'oxydation du fer à T>570°C.

A model of oxide scale growth (limited to the formation of FeO) was established by using the point defects theory and the heterogeneous kinetics calculation principles [Lan1]. The application to the isothermal oxidation of the extra low carbon steels in N_2+O_2 atmospheres highlights three stages of oxidation:

- The first moments of oxidation are governed by the oxygen diffusion in the gaseous boundary layers (the oxide scale formed is too thin to hinder the flow of the iron vacancies towards the surface). The oxidation kinetics has a linear time variation and the oxidation constant depends on the partial oxygen pressure P_{O_2} at the power 1. The gas flow in this case has an important influence (the oxidation constant is proportional to the flow at the power ½) because it affects the gaseous layer. The higher the temperature of treatment is, the longer this stage is. **During linear scale growth, hematite and magnetite are missing** [Sac]**.**

- After this initial stage, as soon as the oxide layer becomes sufficiently thick, the kinetics follows a first **parabolic law** as a function of time. A transport process (Fe^{+2} ions diffusion) represents the limiting stage of the oxidation reaction. The parabolic oxidation constant depends on the oxygen partial pressure at the power ¼ and is independent on the gas flow. In most cases, this stage governs the major part of the oxidation time.

- A second parabolic mode can occur when the oxidation time is long enough. Then, there is delamination or cracking of the oxide coating, causing a diffusion barrier at the metal-oxide interface.

Mathematically, the oxidation laws corresponding to the modes described above are (Figure II-7):

Linear law:

$$X = k_l.t \qquad \text{and} \qquad k_l = k_{lo}.P_{O_2}.\exp(-\frac{Q}{RT}) \qquad \text{eq. II-4}$$

with X the oxide scale thickness (cm), k_l and k_{lo} respectively the kinetic constant (cm.s^{-1}) and the pre-exponential constant (cm.s^{-1}) of linear mode, t the time (s), P_{O2} the oxygen percentage (in volume), Q the activation energy of the reaction mechanism (J.mol^{-1}), R the perfect gas constant (8.314 Jmol^{-1}.K^{-1}) and T the temperature (K).

Parabolic law:

$$X^2 = k_p.t \qquad \text{and} \qquad k_p = k_{po}.P_{O_2}^{\frac{1}{2}}.\exp\left(-\frac{Q}{RT}\right) \qquad \text{eq. II-5}$$

with k_p the kinetic constant (cm².s^{-1}) and k_{po} the pre-exponential constant (cm².s^{-1}) of the parabolic mode.

The transition from one mode to the other is a complex function of the temperature, time, steel grade, gas flow and oxygen partial pressure. **Moreover, it must be specified that the oxidation time is short in the FM. The linear growth stage cannot be neglected.** Mathematically, the linear and parabolic curves must be connected with a continuous tangent (Figure II-8).
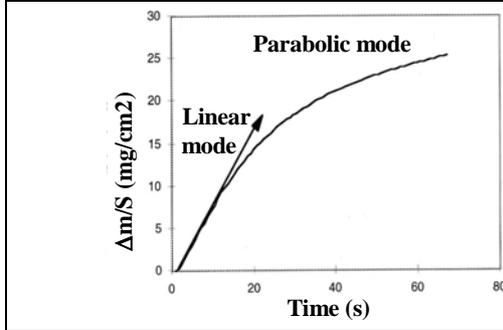
Figure II-7: Δm/s=f(t) curve for a DDS steel oxidized at 950°C in a N_2-20%O_2-15%H_2O atmosphere.

Courbe Δm/s=f(t) pour un acier DDS oxydé à 950°C dans une atmosphère de N_2-20%O_2-15%H_2O.
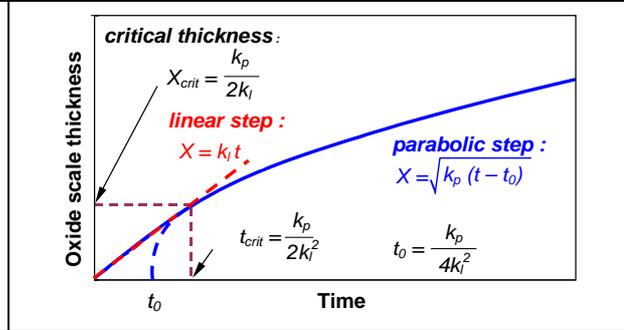
Figure II-8: Mathematical representation of the transition between the linear and the parabolic step.

Représentation mathématique de la transition entre l'étape linéaire et parabolique.

Thus, to a first approximation, the law can be written as:

$$t = t_0 + \frac{X}{k_l} + \frac{X^2}{k_p} \qquad \text{or} \qquad X = \frac{1}{2}\left[-\frac{k_p}{k_l} + \sqrt{\left(\frac{k_p}{k_l}\right)^2 + 4k_p\left(t - t_0\right)} \right] \qquad \textbf{eq. II-6}$$

For an oxidation at 900°C of DDS (deep-drawing steel), we obtain a transition time t_{crit} between 3 and 4s.

This mathematical model is correct if steel and scale are well in contact. Porosity, cracks or accumulation of addition elements at the interface modify this ideal law. Indeed, diffusion mechanisms depend on the quantity of defects present in the oxide scale, and thus on its compactness.

The Pilling-Bedworth factor F_{PB} determines the oxide scale protective capability, indicating if it is compact or porous. It is an expansion factor that takes into account the density of an oxide and its metallic substrate:

$$F_{PB} = \frac{V_{ox}}{V_m} = \frac{M_{ox} \cdot \rho_{ox}}{M_m \cdot \rho_m} \qquad \textbf{eq. II-7}$$

with V the molar volume, M the molar mass and ρ the density.

- If $F_{PB} > 1$: the film is protective;
- If $F_{PB} < 1$: The film is in tension and loses its protective role (micro-cracks occur).

Values for iron oxides are all greater than 1 (Fe/FeO: 1.69; Fe/Fe_3O_4: 2.10; Fe/Fe_2O_3: 2.15). They are therefore considered as protective layers.

<u>Oxidation parameters determination</u>

- *For Iron*

Païdassi [Paï2] has determined the oxidation parabolic constant of pure iron in air between 700°C and 1200°C for the 3-oxides scale.

$$k_p\left(cm^2.s^{-1}\right) = 6.03 \exp\left(-\frac{169300}{RT}\right) \quad \Rightarrow \quad X(\mu m) = 24550.\exp\left(-\frac{84650}{RT}\right).\sqrt{t} \qquad \textbf{eq. II-8}$$

Each oxide layer (FeO, Fe_3O_4, Fe_2O_3) follows the law $X_i^2 = k_i.t$ and the total thickness of the scale is then equal to

$$X^2 = \sum X_i^2 = \sum k_i.t \qquad \textbf{eq. II-9}$$

Kinetics of oxidation are principally studied by thermo-gravimetry tests. Thus, all previous growth parameters are more often expressed in terms of mass increase per unit surface (*Δm/S*), instead of the scale thickness *X*. Both parameters are linked [Cast]:

$$X(\mu m) = 7.78 \frac{\Delta m}{S}\left(mg/cm^2\right) \qquad \textbf{eq. II-10}$$

- *For steel*

Additional elements
Oxidation of steels is more complex than iron. Their oxide scales are mainly constituted of iron oxide but their structures change with the presence **of addition elements**, which can be oxidized too [Chan,Lan2]. The Ellingham diagram, representing the enthalpy of oxide formation in function of temperature, enables to roughly classify elements compared to iron (in term of oxide formation enthalpy). Several elements, easier to oxidise than iron (P, Mn, Cr, Si, Al) can react with iron oxide to form solid solutions (e.g. Mn gives MnO, Mn_3O_4, Mn_2O_3), or mixed oxides (Al gives spinel $FeAl_2O_4$; Si gives fayalite Fe_2SiO_4). They are, in most cases, localized at the metal-oxide interface under an oxide form or not, depending on their affinity with oxygen.

The presence of these thin oxide layers at the interface, often harmful for pickling, **influences the oxidation characteristics previously seen as well as the mechanical properties.**

Atmosphere of oxidation
In all our studies, the atmosphere of oxidation was chosen to best reproduce the entry of FM roll bite. Water jets operate along the HSM in order to cool rolls. The air is then saturated with water. Identification of air composition was performed several years ago by IRSID on an ARCELOR industrial FM : N_2-20%O_2-15%H_2O , with a dew point at ~50°C.
Thermo-gravimetry has also been performed [Cast] under these conditions on different steel grades having rolled-in scale defects. Results are presented in Table II-1, Table II-2 and Figure II- 9.

	C	Mn	P	S	Si	Al	Ni	Cr	Cu	Nb	Ti	N
DDS	1.6	210	8.5	11	5.1	32.4	17.8	19	10	0.2		2.6
Re-Nitrided	69.4	306	11	8.5	8.8	13.4	16.4	21.7	6.7	0		14.4
Dual Phase	81	521	72	3	287	42	134	522	274			56
Re-Phosphorized	60	654	33.7	12.7	87.7	46.1	17.6	18.1	11.8	0.2	3	3.9

Table II-1: Steel grades composition (in 10^{-3}% in weight) tested by thermo-gravimetry

Composition des nuances (en 10^{-3}% en masse) testées par thermo-gravimétrie

	Scale thickness (µm) with Linear law		Scale thickness (µm) with Parabolic law
	T < 1000°C	T > 1000°C	
DDS	$15.10^3.\exp\left(-\dfrac{89600}{RT}\right).t$	$22.6.\exp\left(-\dfrac{20300}{RT}\right).t$	$2.4.10^4.\exp\left(-\dfrac{85000}{RT}\right).\sqrt{t}$
Re-Nitrided	$18.5.10^3.\exp\left(-\dfrac{91700}{RT}\right).t$	$20.5.\exp\left(-\dfrac{19300}{RT}\right).t$	$1.85.10^4.\exp\left(-\dfrac{76000}{RT}\right).\sqrt{t}$
Dual Phase	$4.2.10^3.\exp\left(-\dfrac{87500}{RT}\right).t$	$3.9.\exp\left(-\dfrac{12400}{RT}\right).t$	$10.4.10^5.\exp\left(-\dfrac{125200}{RT}\right).\sqrt{t}$
Re-Phosphorized	$9.5.10^3.\exp\left(-\dfrac{91700}{RT}\right).t$	$4.3.\exp\left(-\dfrac{12600}{RT}\right).t$	$7.6.10^5.\exp\left(-\dfrac{120400}{RT}\right).\sqrt{t}$

Table II-2: Oxidation kinetics [Cast]

Cinétiques d'oxydation[Cast]
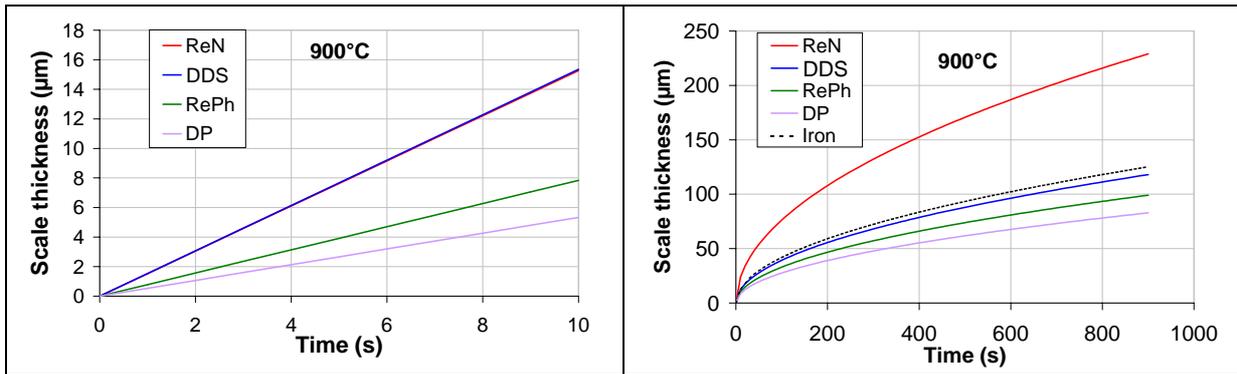
Figure II- 9a: Linear growth at 900°C for the four steel grades.

Cinétique de croissance linéaire à 900°C pour les quatre nuances d'acier.

b: Parabolic growth at 900°C for the four steel grades.

b: Cinétique de croissance parabolique à 900°C pour les quatre nuances d'acier.

Oxide scale constitution

In oxidizing pure iron in air, other researchers [Sac,Dav] found the same proportions as Païdassi [Paï1] for the 3-oxide scale constitution, (Figure II-10a). Figure II-10b shows the results of authors [Bern,Blaz] who worked on mild steels. These graphs only give a tendency and differences of oxidation between iron and steel. They cannot be applied for all steel grades, under all conditions (porosity, interface defects, atmosphere…).

We focus on temperatures of oxidation in the FM, after the secondary descaling, between 900 to 1000°C. For mild steel we can see (Figure II-10b) that at 900°C, oxide scale is only composed of FeO and Fe_3O_4 in a proportion of respectively 96% and 4%. Above this temperature, the diagram changes completely, probably with the phase transformation of the steel substrate into austenitic steel. This temperature of transformation depends on many parameters like steel grade, oxidation atmosphere or holding temperature, time…
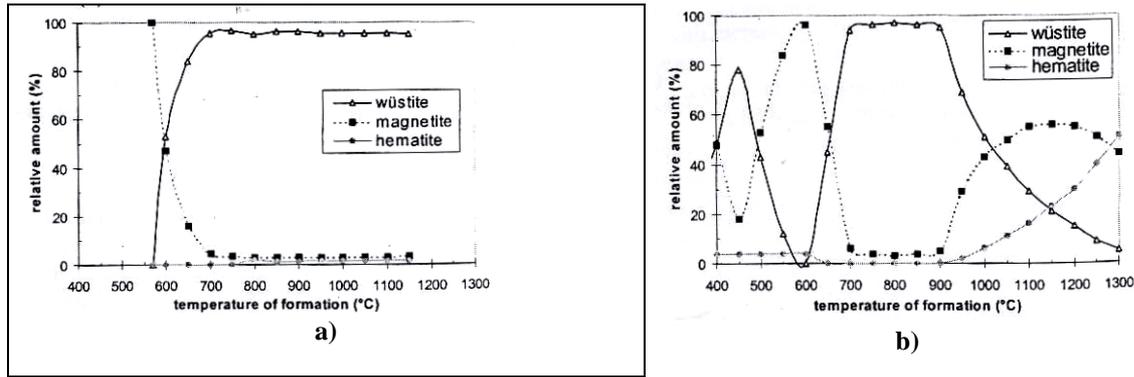
Figure II-10: a) Païdassi representation for pure iron   b) Blazevic's representation for Mild steel.

a) Représentation de Païdassi pour le fer pur   *b) Représentation de Blazevic pour l'acier doux.*

II.2. Oxide scale morphology in the finishing mill

Direct observations of industrial oxide layers are impossible. Indeed, the rare available pictures or micrographs were taken after an accidental stop of the FM. Strips covered by oxide scales were then cooled in ambient air, which may induce a modification of their structures and compositions, and thermal damage (Figure II-5).

II.2.1. Adapted thermal cycle and oxidation atmosphere

At the entry of the FM (after secondary descaling), secondary scale is formed on steel strips between 900 and 1000°C.

Previously studied layers do not precisely represent the usual morphology and structure of oxide layers in the FM. Indeed:

- Strip oxidation is performed at temperatures close to 900°C and in a few seconds, which is not long enough to reach a steady state during which previous results were obtained.
- Strip oxidation atmosphere is wet. The proportion of FeO formed under this condition is higher [Ben].
- Scale composition in the roll bite should not differ from the entry. Its abrupt cooling (at the time of contact under the work-rolls) is extremely quick and thus does not allow FeO decomposition (Figure II-5).
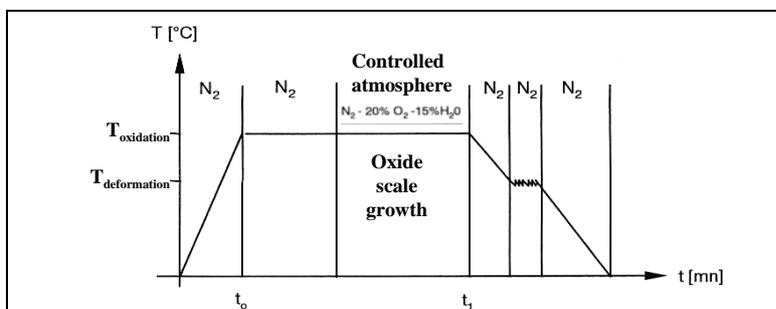
Figure II-11: Thermal cycle used for mechanical tests, mimicking those in the FM.

Cycle thermique utilisé pour les tests mécaniques, imitant celui d'un finisseur.

In order to respect these three conditions, a thermal cycle was developed to observe and test the oxide scale closest to the rolling conditions (Figure II-11):

- heating under nitrogen in order to make sure that oxidation does not begin before the chosen temperature;
- formation of the oxide layer at 900°C, under a wet controlled atmosphere (N_2-20%O_2-15%H_2O with a dew point at around 50°C);
- cooling under nitrogen to preserve the scale structure.

II.2.2. Preparation and microscopic observations of the oxide layer

Preparation:

Preparation of specimens covered by oxide scale is extremely delicate due to its hardness and brittleness. After a mechanical test, each specimen studied is cut in two equivalent pieces using a wire-saw not to weaken the oxide scale. The first half is observed **from the top,** to see possible cracks network, and the second in the **cross-section.** In the last case, the preparation involves several stages. Specimens are hot-coated in thermo-setting resins (epoxy) which are known to have a low shrinkage. Cold-coated ones were also used with equivalent results. Our experiments have shown that these resins adhere well, but although low, their shrinkage is sufficient to induce decohesion of the oxide scale when the **interface with the metal is weak** (Figure II-12). Thus, it is sometimes difficult to estimate the part of damage occurring during the experiment and due to preparation of sample for examination.
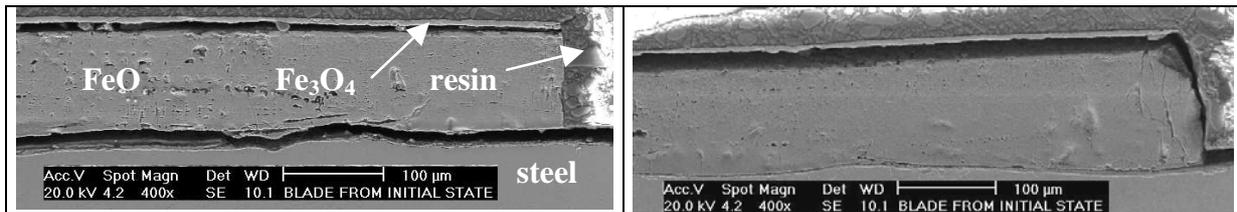
Figure II-12: Decohesion induced during the specimen preparation. Resin shrinkage.

Décohésion pendant la préparation des échantillons. Retrait de résine.
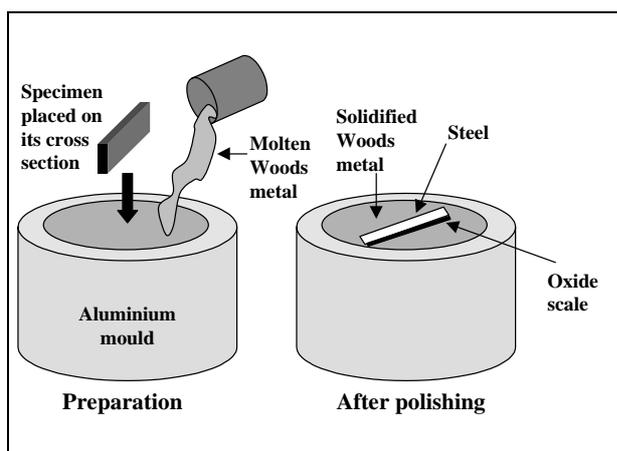
Figure II-13: Method described in [Hig1] for EBSD analysis.

Méthode décrite dans [Hig1] pour l'analyse EBSD.

For EBSD analysis, we have used a method proposed by Higginson et al. [Hig1] (Figure II-13). Specimens are placed in a small aluminium mould and covered with warm molten Woods metal (melting point around 80°C). After its solidification, the sample is polished as usual. This method is extremely interesting in terms of conductivity (micrograph quality) and preservation of the scale: no compression and no retraction. Indeed, the oxide was in a better state after this preparation than with resins. Nevertheless, preparation is significantly longer and more difficult.

Coated samples are then ground using 120 to 4000 grit polishing paper corresponding to respectively 125 and 5µm grain size. Finishing is performed with diamond pastes 3 and 1µm to obtain a mirror polish.

In the case of EBSD, results are extremely difficult to obtain due to the extreme surface hardening during mechanical polishing. Thus, before the observation, samples undergo OPS polishing for a long time (at least 15min). An electrolytic polishing can be applied on specimens with the usual preparation for non-alloyed steels.

In [Hig1,Hig2], authors used colloidal silica for final polishing and samples are lightly etched in 0.5%-Nital for 2 s.

Microscopic observations:
Undeformed specimen cross-sections, covered by an oxide scale 100µm thick and having undergone the thermal and chemical cycle seen in Figure II-11, have been observed. A predominant clear grey oxide layer appears in the middle, with two dark grey layers at the extreme surface (2µm thick) and at the steel/scale interface (1µm thick). Segregates, with the same dark grey colour, are present in the clear thick layer near the dark external layers (Figure II-14). From all that has been written previously, this oxide is probably constituted of a dominant FeO layer (light grey), of external Fe_3O_4 layers (dark grey), plus dark grey segregates suggesting a possible FeO decomposition into Fe_3O_4 during cooling, probably due to imperfect protection against oxidation. The interface layer could also be a segregation of addition elements.
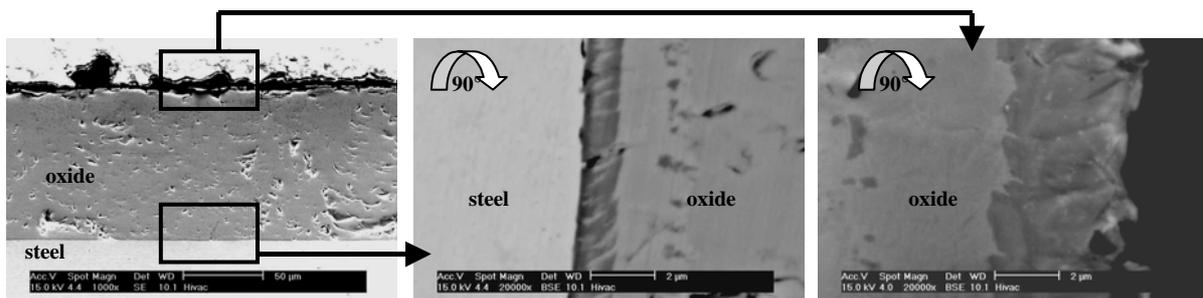
Figure II-14: SEM micrographs of specimen cross section. Presence of two different phases in scale.

Micrographie MEB de coupes d'échantillons. Présence de deux phases différentes dans la couche.

During cooling, the inert gas flow is stopped in the chamber around 350°C. It is also possible that the decomposition starts at this time. It can involve the formation of a magnetite film at the metal / oxide interface, depending on the temperature and the cooling rate. The formation conditions are not clearly established but several studies suggest curves representing the film existence domain [Che].

Structural observation is possible with adapted acid etching revealing grains. For scale, we used a hydrochloric solution in ethanol at 3% in volume. Sample is immersed ~4s in **Chloral** and abundantly rinsed in water to stop the reaction. With this attack, Fe_2O_3 is coloured in white, Fe_3O_4 in clear grey and FeO in dark grey. The steel substrate structure is revealed by an etching of a few seconds in **Nital** (5% nitric solution in ethanol).

II.2.3. Composition using X-rays diffraction analysis (XRD)

X-ray studies of surfaces and interfaces were considerably developed these last years. We have used this technique to confirm the scale composition assignments done in connection with Figure II-14.

Considering a coherent X-photon diffraction and supposing a periodic atom distribution in the crystal, the electromagnetic waves diffused by these atoms cause a phenomenon of constructive interference if they are in phase. This X-ray diffraction phenomenon by a crystal is described by the Bragg relation in the direct lattice [Gui]:

$$2d \sin \theta = n\lambda \qquad \qquad \text{eq. II-11}$$

The observation of a diffraction peak direction at 2θ from the incident X beam is thus characteristic of the presence of a family of {hkl} planes with interreticular distance d_{hkl}. Using a sufficient number of diffraction peaks, it is possible to determine the material crystallographic structure.

Penetration depths calculation

Analyses were made on the top of a non-deformed specimen (but on the uncut and uncoated half part). Three grazing incidence angles have been chosen (1°, 5° and 20°), corresponding to three penetration depths.

Figure II-15: Incident and diffracted beam.

Rayon incident et diffracté.
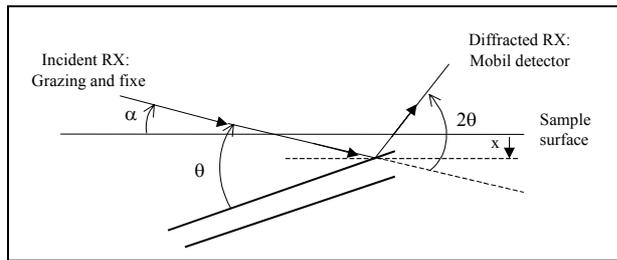
These depths are estimated from the beam path and the diffracted intensity (Figure II-15):

$$\text{Path} = x\left(\frac{1}{\sin \alpha} + \frac{1}{\sin(2\theta_i - \alpha)}\right) = A_i.x \qquad \text{eq. II-12}$$

A_i is a variable depending on the incident fixed angle α and on the diffraction angle θ of the considered peak i.

$$I_i(x, \alpha) = I_i(\infty).[1 - \exp(-\mu_i A_i x)] \qquad \qquad \text{eq. II-13}$$

$I_i(\infty)$ is the total diffracted intensity and $I_i(x, \alpha)$ is the diffracted intensity from a depth x. Considering 90% of the diagram intensity, so $1 - \exp(-\mu_i A_i x) = 0.9$, the explored depth is:

$$X = \left|\frac{1}{\mu_i A_i} Ln(0.1)\right| = \frac{2,3}{\mu_i A_i} \qquad \qquad \text{eq. II-14}$$

μ_i is the linear absorption coefficient in cm^{-1} ($\frac{1}{\mu_{FeO}} = 5.38$; $\frac{1}{\mu_{Fe_3O_4}} = 5.75$; $\frac{1}{\mu_{Fe_2O_3}} = 5.95$) [Crx].

The table below (Table II-3) gives the beam penetration depth as a function of the incident angle.

Incidence angle	1°	5°	20°
Depth (µm)	0.2	1	1.8

Table II-3: The penetration depth function of the incidence angle.

Profondeur de pénétration fonction de l'angle d'incidence.

Analyses results

Analyses are performed for an angle 2θ between 20° and 65° (diffraction zone of the different iron oxides phases FeO, Fe_3O_4 and Fe_2O_3).
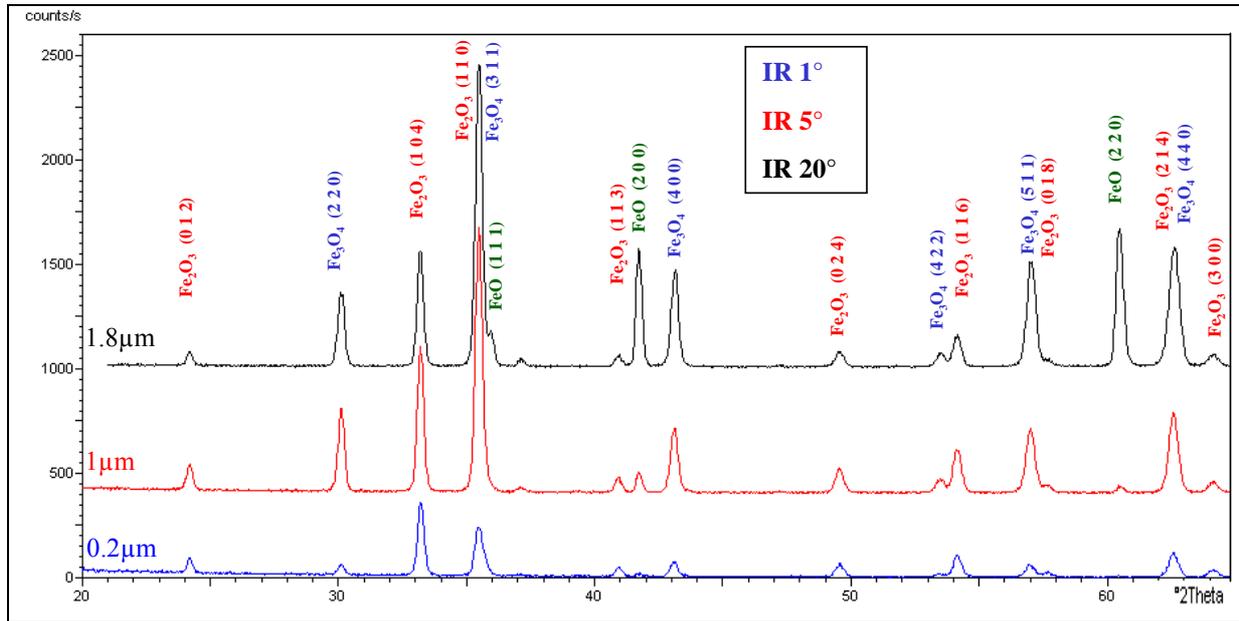
Figure II-16: XRD spectra superposition in grazing incidence. Angle between the beam and the oxide scale surface is 1°, 5° and 20°.

Superposition des spectres DRX en incidence rasante. Angle formé avec la surface de la couche d'oxyde : 1°, 5° et 20°.

The superposition of spectra presented in Figure II-16 gives some indications:

- Spectrum **IR 1°** highlights the presence of **Fe_2O_3 and Fe_3O_4 in extreme surface**.
- Spectrum **IR 5°** shows the initiation of a FeO peak, but principally shows that if Fe_2O_3 peaks remain approximately the same, the intensity of the Fe_3O_4 main peaks considerably increases. One can say that Fe_2O_3 is present only in the extreme surface, localized on a Fe_3O_4 layer and prolonged by a mixed FeO / Fe_3O_4 layer.
- Spectrum **IR 20°** validates this successive stacking of layers. This time, FeO peaks are fully developed.

Figure II-17: Schematic representation based on the results obtained in XRD.

Représentation schématique basée sur les résultats obtenus en DRX.

II.2.4. Other analyses

Several analytical techniques have been used to confirm the structure and the constitution of the oxide scale, such as:

- **WDS:** An electron micro-probe is a SEM equipped with wave dispersion spectrometers (WDS) and provided with current regulation. This equipment is dedicated to X-ray microanalysis of solid materials: this non-destructive technique determines the concentration of the elements present in a ~1 μm^3 volume. A quantitative X-ray microanalysis in WDS is always done by comparison with a reference specimen. Their applications are the phase analysis identification of elements, composition profiles, analysis of thin and multi-layer coatings, mapping of elements. WDS has been performed on the sample in Figure II-14, at the Center of Materials, EMP, at Evry by G. Frot. It has confirmed that the thickest layer is FeO, and that the dark grey layer at the extreme surface is Fe_3O_4. The interfacial dark layer has not been clearly identified but seems to be also a Fe_3O_4 layer (Figure II-18).
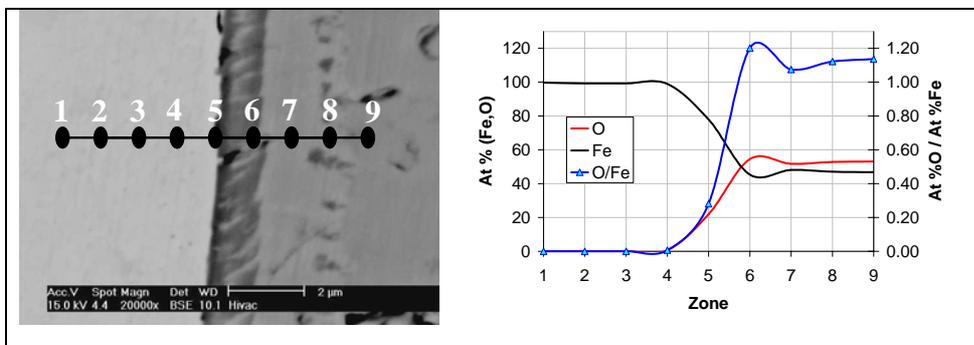
Figure II-18: WDS interface line scan. The % of O increases at the interface.

Profil de concentration à l'interface en WDS. Le % de O augmente à l'interface.

- **EBSD:** Higginson et al. [Hig1,Hig2], using EBSD analyses, disclose the complex crystallographic relationship existing between oxide scales. At the same time, they identify their composition (Figure II-19a). We have reproduced the experiments to reveal the grain structure of FeO. Grains cross the whole scale thickness (Figure II-19b). The differences with [Hig1] are principally due to the oxidation temperature and time.
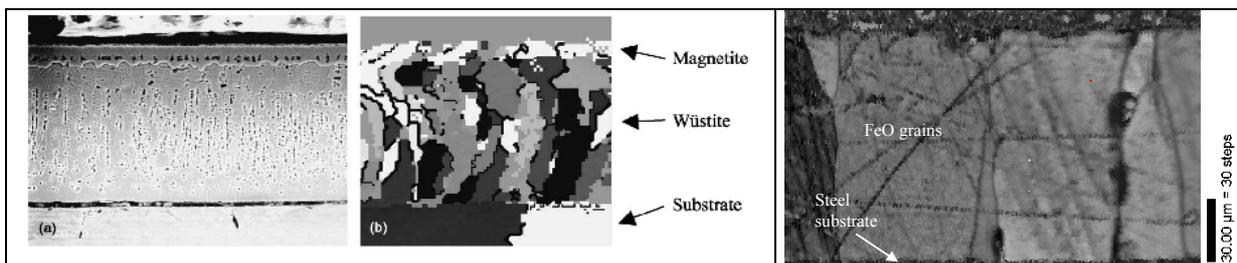
Figure II-19a) An electron micrograph of the oxide scale (70µm thick, T_{ox}=760°C, t_{ox}=2h) grown on an IF steel substrate and its EBSD map showing the different oxides [Hig1].

b) Oxidized specimen: T_{ox}=900°C, t_{ox}=8 min. Through-thickness grains.

a) Micrographie électronique de la calamine (épaisseur : 70µm, T_{ox}=760°C, t_{ox}=2h) sur un acier IF et sa carte EBSD montrant les différents oxydes [Hig1].

b) Eprouvette oxydée : T_{ox}=900°C, t_{ox}=8 min. Grains traversant l'épaisseur.

II.3. <u>The temperature: a key point for surface quality</u>

Results of previous studies as well as several **industrial observations** show that, at the entry of the roll bite, **the oxide scale thickness has to be less than 20μm to avoid rolled-in scale defects**. F1 and F2 seem to be the most critical stands.

Several parameters influence the defect formation: the secondary descaling efficiency, the steel grade, the rolling process (reduction, velocity…) and the work-roll degradation. However, two variables seem to be sufficient to qualify the apparition of defects:
- The thickness of the oxide scale at the entry of the FM;
- The energy dissipated by friction during rolling.

The energy dissipated by friction cannot be predicted. It is obtained from the rolling results. But, as long as the rolls are not degraded, the dissipated energy remains sufficiently low not to be a problem.
Thus, **the scale thickness at the entry of the FM is the first point to keep under control**.

II.3.1. The first parameter: the slab temperature

The scale thickness at the entry of the F1 stand results from the addition of **two terms**:
- The **residual scale** after the secondary descaling operation;
- The scale **thickness** formed during **slab transfer** between the descaling and the entry of the F1 stand.

During these two stages, the surface temperature is the influential parameter. As scale thickness increases with temperature, at a critical scale thickness corresponds a **critical temperature** not to exceed in order to avoid defects initiation. This limitation is stronger for the slab head, which is **the hottest part.** On the opposite, the coldest slab part is its tail, which waits more time before reaching the roll bite.
On the other hand, a higher temperature makes it easier to roll (the metal is softer, the oxide is more ductile). This oxide thickness constraint is thus quite unfortunate.
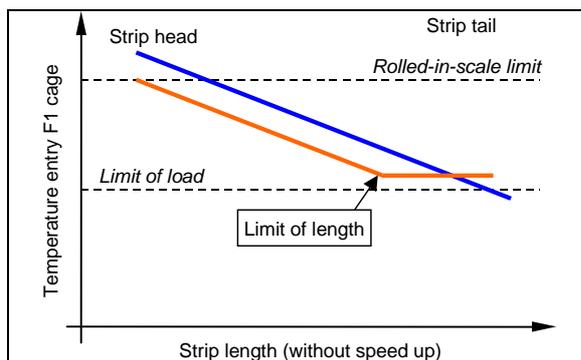
Figure II-20: Temperature at the FM entry.

Température en entrée de finisseur.

Thus, the temperature should not be too high, in order to avoid rolled-in scale defects, nor too low, to allow rolling. **These HSM operation limits** are expressed as a **temperature window** or as a **maximal strip length** (Figure II-20).
It is interesting to determine the maximum temperature for two different steel grades:
- the DDS, which is not particularly hard, but the oxide scale of which grows quickly;
- the DP600, which has a high yield strength.

II.3.2. Thickness of the oxide layer after the secondary descaling

The residual thickness at the descaling exit was determined by a study on a pilot mill at Irsid. Correlations were built by linking the scale thickness at the exit with the process parameters. For the descaling, the water impact pressure is 0.265 MPa (2.65 bar) and the flow rate 0.83 10^{-3} $m^3.s^{-1}$ (50 l / min). Using the HSM standard conditions, the thickness in Table II-4 is obtained:

Dunkerque HSM	T surface exit descaling (°C)	Scale thickness (µm)
DDS	920	12.8
	940	14.1
	950	14.6
DP 600	950	7.3
	1000	11.0
	1050	16.3

Table II-4: The importance of temperature effects on the scale thickness at the exit of descaling for DDS steel grade. DP 600 scale thickness is clearly lower.

Les effets importants de la température sur l'épaisseur de la couche en sortie de décalaminage pour une nuance DDS. Les épaisseurs de calamine sur le DP600 sont beaucoup plus faibles.

For DDS steel grade, the remaining layer is rather thick (between 12.8 and 14.8µm) compared to the limit size of 20µm. The variation of 2µm within 30°C is also significant.
Thickness obtained for **DP 600** steel **is twice as low**. For this kind of high alloy steel, scale is less plastic, so that the secondary descaling is more effective at "low temperature".

II.3.2.1.Scale growth between descaling and finishing mill entry

The scale growth between descaling and the entry of roll gap was calculated using the "**DECOX"** model developed by IRSID. It simulates the oxide layer growth on a steel surface. The model needs three inputs:
- the gas atmosphere ;
- kinetic constants;
- the thermal cycle.

On the mill, the gas atmosphere is a mixture of air and steam (dew point: 50°C). Kinetic constants are obtained, for these two steels, from thermo-gravimetry tests performed under characteristic **industrial mill conditions** and for a **"parabolic oxidation"**. For calculations, transfer is considered isotherm, even if there is in reality a slight temperature loss.
The parameter to take into account is the duration of the transfer. It depends on the descaling stand - F1 distance and on the slab speed. The latter varies from one strip to another. Two cases are simulated corresponding to real speeds: 40 m/min and 55 m/min (Table II-5).

V slab (m/min)	Distance (m)	Time (s)
40	2.9	4.3
55	2.9	3.2

Table II-5: Transfer time between descaling and F1 stand on Dunkerque HSM.

Temps de transfert entre le décalaminage et la cage F1 du TAB de Dunkerque.

For DDS steel, the layer thickness increase during transfer (Table II-6) varies from a minimum of 4.5µm to a maximum of 7.8µm (DDS oxide growth kinetics is rather fast). This is not negligible for a rolled-in scale defect because of the low critical thickness (20µm).

	Surface temperature, descaling exit (°C)	Scale thickness, descaling exit (µm)	Scale thickness, entry F1 (µm)	
			40m/mn	55m/mn
DDS	920	12.8	19.0	17.3
	940	14.1	21.3	19.3
	950	14.6	22.4	20.2
DP 600	950	7.3	10.33	9.57
	1000	11.0	14.81	13.85
	1050	16.3	20.92	19.73

Table II-6: Scale growth between descaling and F1 for two kinds of steel (DDS / DP600) and two velocities (40 / 55m/min).

Croissance d'oxyde entre le décalaminage et la cage F1 pour deux types d'acier (DDS / DP600) et deux vitesses (40 / 55m/min).

It is now possible to estimate the steel surface limit temperature corresponding to the critical scale thickness of 20µm at the entry of the F1 stand.

II.3.3. Effects on the acceptable maximum temperatures

Generally, the surface temperature is not a convenient parameter. On the other hand, the **slab average temperature** is used to determine the rolling force to apply. Surface temperatures are then converted into strip average temperature considering that the temperature profile is parabolic, with a heart / top-face difference of 150°C ($T_{heart}=T_{top}+150$) and a top-face / bottom-face difference of 40°C ($T_{bottom}=T_{top}+40$). These variations have been measured during a campaign on site. Conversions give the following graphs (Figure II-21), which links the strip head temperature to its scale thickness. In the Dunkerque HSM case, the maximal temperature of a DDS slab is 1015°C for an engagement speed of 55m/mn and 995°C if the speed is reduced to 40m/mn.
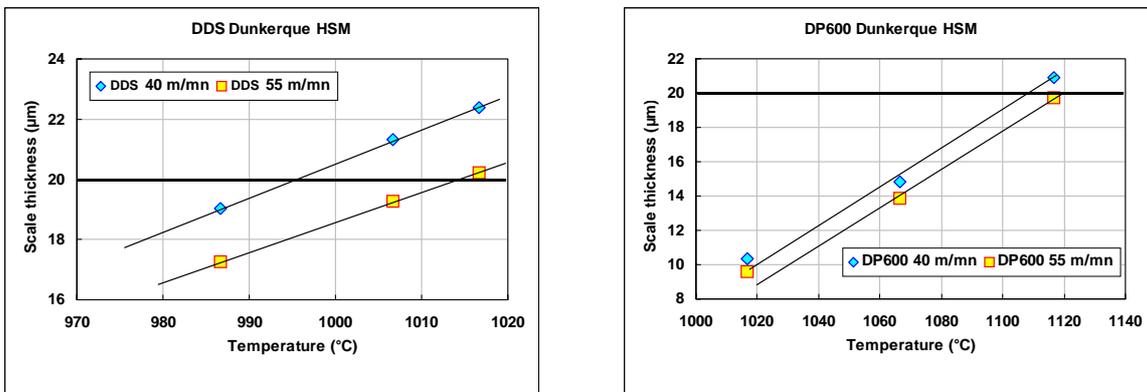
Figure II-21: A low maximal slab temperature to avoid rolled-in scale defect for DDS steel.

Une température maximale de bande faible pour éviter la formation du défaut d'incrustation pour l'acier DDS..

Maximal temperatures obtained for DDS are rather low (Figure II-21,Table II-7); they are rather close to usual rolling temperatures, which can make the process control more difficult. DDS steel is not classified among hard steels, therefore these low temperatures are not really a problem even if we consider the temperature of the strip tail.

Dunkerque	DDS	DP 600
40 m/mn	995	1109
55 m/mn	1014	1119

Table II-7: Critical temperature of engagement to avoid rolled-in-scale defect.

Température critique d'engagement pour éviter le défaut de calamine incrustée.

In the case of more alloyed steels (DP 600), calculated limit temperatures are relatively high, definitely higher than those used on the Dunkerque HSM. Then, considerations related to the scale thickness should not be a stringent constraint for these steels.

II.3.4. The true limit can be on the F2 stand

In the previous sections, we have assumed that the F1 stand was the most critical one in terms of rolled-in scale defect. This is not always the case because the oxide scale continues to grow between the stands and can reach the critical thickness in another stand. Thus, DECOX simulations of scale growth in the finishing mill were performed (in the Dunkerque HSM configuration). For calculations, diagrams of rolling (reductions-temperatures) were extracted from industrial data and inter-stand times were recomputed from the rolling speeds.

Dunkerque	Temperature entry F1	
	40 m/min	**55 m/min**
DDS	987	1003
DP600	1016	1016

Table II-8: Parameters list for DECOX calculation.

Liste des paramètres pour le calcul DECOX.
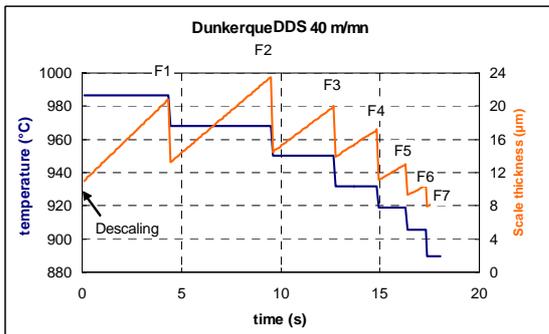
Figure II-22: DDS steel: Maximal scale thickness in stand F2.

Acier DDS : épaisseur maximale de calamine dans la cage F2.
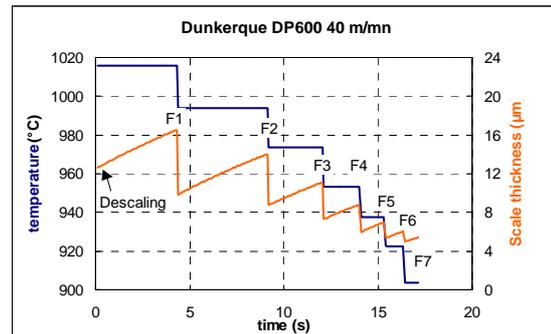
Figure II-23: DP 600 steel: Maximal scale thickness in stand F1.

Acier DP 600 : épaisseur maximale de calamine dans la cage F1.

For DDS steel, the selected starting temperatures are close to the maximal ones calculated previously. This is not the case for the DP 600, the temperature of which is fixed at 1016°C

(maximum in the available database). In both simulations of the DDS steel rolling (at 40 and 55m/min), the thickness of the layer is maximal in the F2 stand (Figure II-22). The difference with the F1 stand is not very large (22µm instead of 20µm). **However, we see that previous calculated temperatures were slightly optimistic. It would perhaps be relevant to limit the F2 stand reduction**. This maximal thickness obtained in stand F2 or F3 has already been evoked in chapter 1 with the oxide scale growth model of Li and Sellars (chapter I-Figure I-16b).

For the alloyed steel however, simulations predict a maximal scale thickness in F1 (Figure II-23).

Figure II-24 represents an experimental thermal profile for an industrial strip, and points out the influence of temperature on defect initiation. Defects are more localized in the strip head (hot zones), which has been cooled for a shorter time.
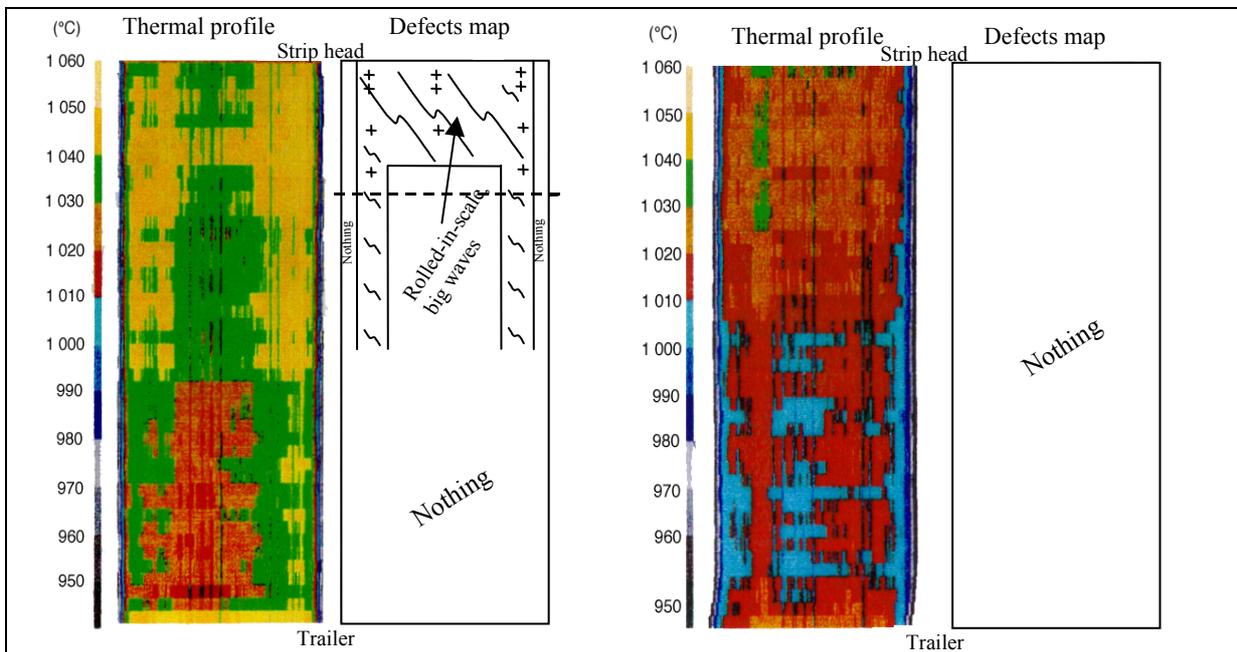
Figure II-24: Defects initiation in hot zones

Initiation des défauts dans les zones chaudes.

III. OXIDE SCALE MECHANICAL PROPERTIES

III.1. Thin scale coating

It is very difficult to characterize the mechanical behaviour of a substrate / ceramic coating (a few micrometers thick) couple. Felder et al. [Fel] have classified several experimental tests with their rheological or mechanical advantages (Figure II-25).

Qualitative
• Peeling by adhesive bands after scratches
• Abrasion

Quantitative
• Wrenching (normal and tangential) (after gluing)
• Peeling by laser impact, ultracentrifugation…
• Cleavage by bending, tension
• Indentation: normal or interfacial
• Stripe
• Spontaneous separation by additional deposit

Table II-9: Mechanical methods to estimate thin coatings adherence.

Méthodes mécaniques pour estimer l'adhérence des revêtements fins.

Figure II-25: Mechanical characterization tests.

Tests de caractérisation mécanique.

Concerning the adherence of thin coatings, tests can be classified in two categories: qualitative and quantitative ones (Table II-9).

An important complement of adherence tests is described in [Dup,Oll]. They are divided in three groups depending on their results (Figure II-26):
• Measurement technique of decohesion threshold (a);
• Continuous measurement of the interface crack energy (b);
• The assessment of initiation and fracture energy (c).
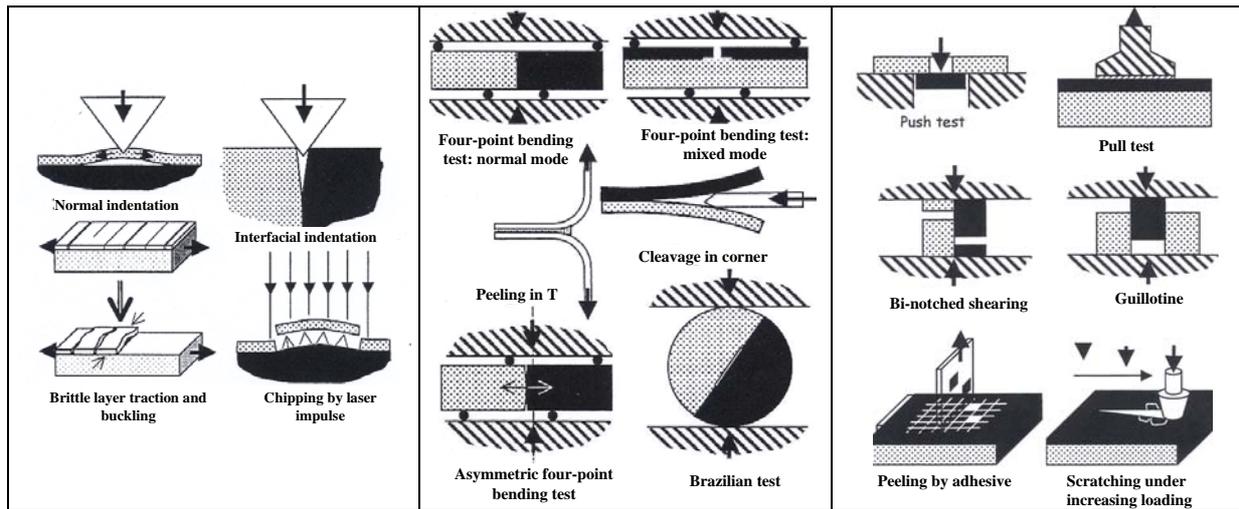
Figure II-26 a) Measurement of decohesion threshold.

a) Mesure du seuil de décohésion.

b) Continuous measurement of interface crack energy.

b) Mesure continue de l'énergie de fissure interfaciale.

c) Initiation and fracture energy.

c) Energie d'initiation et de rupture.

Among all these tests, several ones do not simulate adequately hot rolling conditions, or seem to be difficult to perform with our materials. We have chosen for our study the 4-point hot bending test and the hot tensile test, for reasons precisely explained in chapters IV and V.

III.2. Mechanical properties

Adherence of iron oxides

Oxide scale adherence remains a poorly known phenomenon, extremely difficult to measure at high temperature. Results obtained from adherence tests at high temperatures are often contradictory.
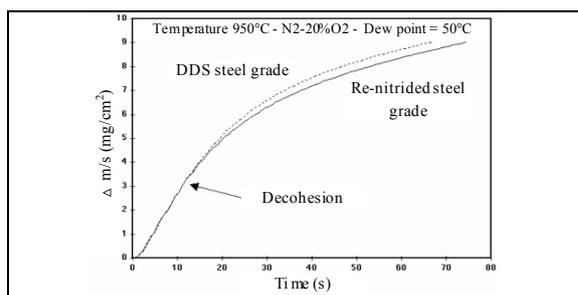
Figure II-27: Evaluation of adherence loss by thermo-gravimetry : the ReN grade is less adherent than the DDS ones.

Evaluation de la perte d'adhérence par thermo-gravimétrie : la nuance ReN est moins adhérente que la DDS.

Qualitatively, thermo-gravimetry represents an easy test to evaluate the adherence. Figure II-27, obtained by the isothermal oxidation of two steel grades in HSM atmosphere, shows that the oxide scale grown on a DDS steel is more adherent than on a Re-Nitrided steel. This means that oxide scale formed on different steel grades have different rheological behaviors and thus intrinsic mechanical properties.

The adherence is a determinant factor regarding the oxide scale behaviour in the FM:
- outside the roll gap under thermal stress effects;
- in the roll gap: the scale adherence reflects its resistance to fracture (fracture appears in the more brittle zone). Shearing appears at the interface or in the volume of the oxide depending on which one is the toughest.

It is possible to enumerate some general tendencies such as:
- FeO is the most adherent iron oxide;
- The adherence decreases when the scale thickness increases;
- The scale adherence increases when the oxidation is performed in the presence of steam.

The additional elements have of course an important impact on the adherence. The interface with the steel substrate is different according to the alloy elements.
- Chromium and aluminium can form an external layer (Cr_2O_3, Al_2O_3) which protects the alloy at high temperature. They also slow down the oxidation.
- Sulfur is mostly present in the furnaces and its action is counterbalanced by an increase of the oxygen content. If it is in the steel, the manganese content must be taken into account, because it slows down the oxy-sulfide formation.
- Phosphorus, as copper or sulfur, is concentrated at the interface. Once its low melting point (960°C) is reached, it wets the grain boundaries which it embrittles.
- Manganese oxide is miscible with wüstite. It hardens significantly the oxide scale and makes it more brittle.
- Silicon usually protects the metal from oxidation (in the FM temperature range). Fayalite is more adherent than FeO and reduces the oxidation kinetics.

Hardness of iron oxides

	Vickers hardness (Hv)	Shore hardness (ShC)
FeO	270 to 350	40 to 51
Fe_2O_3	1030	>97
Fe_3O_4	420 to 450	60 to 64
* roll	450 to 740	60 to 85

 * roll: Cast iron high Cr content: skin grade of first stands

Table II-10: Hardness at ambient temperature
Dureté à température ambiante.

Rolls are clearly harder than FeO (Table II-10). The latter can also have a lubricating action during contact with the work-roll, depending on the temperature.
In an opposite way, Fe_2O_3 and Fe_3O_4 are harder than the rolls, will abrade them and increase friction.
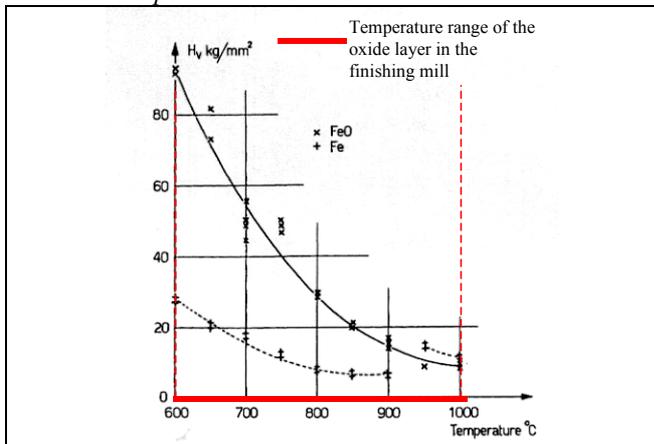
Figure II-28: FeO and Fe Vickers hardness vs. temperature

Dureté Vickers du FeO et Fe en fonction de la température

Vagnard and Manenc [Vagn] performed creep tests in order to determine the FeO hardness. Figure II-28 shows their FeO Vickers hardness measurements vs temperature. In the FM temperature range, oxide is harder than iron except for temperatures higher than 950°C. This value corresponds to the α-Fe/γ-Fe transition temperature. In the austenitic temperature regime, wüstite can also act as a hot rolling lubricant. Under 600°C, the values cannot be compared due to eutectoid decomposition.

III.3. <u>Oxide scale behavior</u>

<u>Elastic part</u>

The iron oxide behaviour is generally considered as elastic and brittle. Thus, most models simulating the oxide scale deformation only use its elastic parameters (Young's modulus E_{ox}, its Poisson coefficient v_{ox}) coupled with a fracture or a decohesion criterion. These data are available in the literature. Additional data are given in the **APPENDIX 1.**

Schütze proposes [Sch1] iron oxides scale Young's modulus expressions depending on the temperature, and originally determined by Morrel [Mor]:

$$E_{ox} = E_{ox}^0 \left(1 + n(T - 25)\right) \qquad \text{eq. II-15}$$

where E_{ox}^0 is the Young modulus at 25°C (240Gpa), T the temperature in °C and n a constant depending on the oxide. For iron oxide scale, $n = -4.7.10^{-4}$.

From the iron oxides shear modulus G_{ox}^0 at 25°C and melting point value T_M, we obtain their Young modulus:

$$G_{ox} = G_{ox}^0 \left(1 + \frac{T - 27}{T_M} \frac{T_M}{G_{ox}^0} \frac{dG}{dT}\right) \quad \text{and} \quad G_{ox} = \frac{E_{ox}}{2(1 + v_{ox})} \qquad \text{eq. II-16}$$

For FeO: $\qquad v_{ox} = 0.36$, $G_{ox}^0 = 55.7 GPa$, $T_M = 1643K$ and $\frac{T_M}{G_{ox}^0}\frac{dG}{dT} = -0.3$

Thus: $\qquad E_{ox} = 151.504\left(1 - \frac{T - 27}{5476.66}\right) \qquad \text{eq. II-17}$

For Fe$_2$O$_3$: $\qquad v_{ox} = 0.29$, $G_{ox}^0 = 88.2 GPa$, $T_M = 1840K$ and $\frac{T_M}{G_{ox}^0}\frac{dG}{dT} = -0.2$

Thus: $\qquad E_{ox} = 209.916\left(1 - \frac{T - 27}{9200}\right) \qquad \text{eq. II-18}$
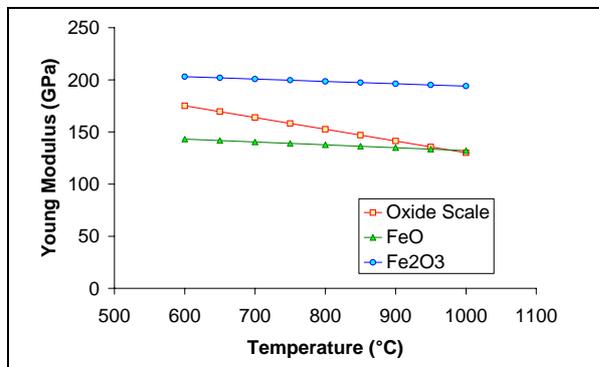
Figure II-29: Temperature dependence of iron oxides Young modulus [Sch1].

Dépendance du module d'Young des oxydes de fer à la température [Sch1].

Figure II-29 shows the temperature dependence of the iron oxides Young's modulus. The Young's modulus of FeO depends less on temperature than that of Fe$_2$O$_3$.

The oxide **porosity** effect can be represented using various equivalent semi-empirical formulas [Rob]:

$$E_{ox} = E_{ox}^0 \left(1 - p\right)^3 \qquad \text{eq. II-19a}$$

or

$$E_{ox} = E_{ox}^0 \exp(-bp) \qquad \text{eq. II-19b}$$

where E_{ox}^0 is the modulus of the fully compact solid and p is the porosity ($b \approx 3$).

Plastic part

Iron oxide plastic deformation is one of the most important issues in the FM. Indeed, it is difficult to know how the oxide scale accommodates the deformations induced by the different stress sources. As we have specified before, in most cases, the selected mechanism in the literature is the damage of a brittle elastic layer. However, several authors have shown that iron oxides could be plastically deformed.
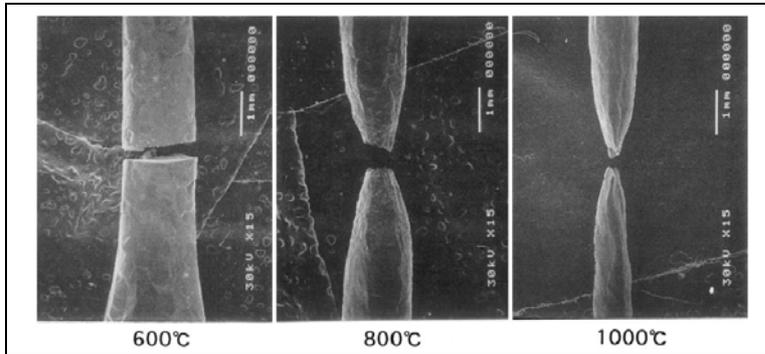
Figure II-30: Scanning electron micrographs (SEM) of FeO specimens after tensile tests at 2.10^{-4}s^{-1} and at various temperatures.

Micrographies MEB d'éprouvettes FeO après tests de traction à 2.10^{-4}s^{-1} et à différentes températures.
.

For example, Hidaka et al. have performed tensile tests of virtually pure FeO, γ-Fe$_3$O$_4$ and α-Fe$_2$O$_3$, under controlled atmosphere (H$_2$, H$_2$O, O$_2$, N$_2$), between 600°C and 1200°C and at strain rates between 2.10^{-3} s^{-1} and 6.7.10^{-5}s^{-1}.

Iron oxide tensile specimens were prepared by the complete oxidation of pure iron specimens [Hid1, Hid2].

Authors clearly prove the plastic deformation of FeO and γ-Fe$_3$O$_4$ above respectively 700°C and 800°C, contrary to α-Fe$_2$O$_3$, which does not show ductility (fracture by cleavage) (Figure II-30, Figure II-31). From Figure II-31 a), a superplastic behavior can even be noted at 1150°C.

Figure II-31: a) FeO behavior at various strain rate b) FeO behavior at various temperature and at 2.10^{-4}s^{-1} c) Elongation of iron oxides in function of the temperature at 2.10^{-4}s^{-1}.

a) Comportement du FeO à différentes vitesses de déformation b) à différentes températures et à 2.10^{-4}s^{-1} c) Elongation de l'oxyde en fonction de la température à 2.10^{-4}s^{-1}.

Ashby distinguishes six ways to deform plastically a crystalline material while preserving its crystallinity [Ash1]:
- The defect-less flow, which exceeds the theoretical shear strength even in a defect-free crystal;
- The glide motion of dislocation;
- The dislocation climb (dislocation creep) at high temperature;
- Nabarro-Herring creep and Coble creep: The stress applied is too low to trigger dislocation movements. At a microscopic scale, the stress application to a piece of matter induces tensile stress at the grain boundary along a direction. An atomic diffusional movement is then initiated to the grain boundaries (Coble creep) or across the grains (Nabarro-Herring creep);
- Twinning, which only supplies a limited amount of deformation.

These phenomena are highly dependent on the deformation temperature and the strain rate.

Ashby reports deformation-mechanism maps for $Fe_{1-x}O$ [Ash2] (Figure II-32) and Fe_3O_4 [Sch2].
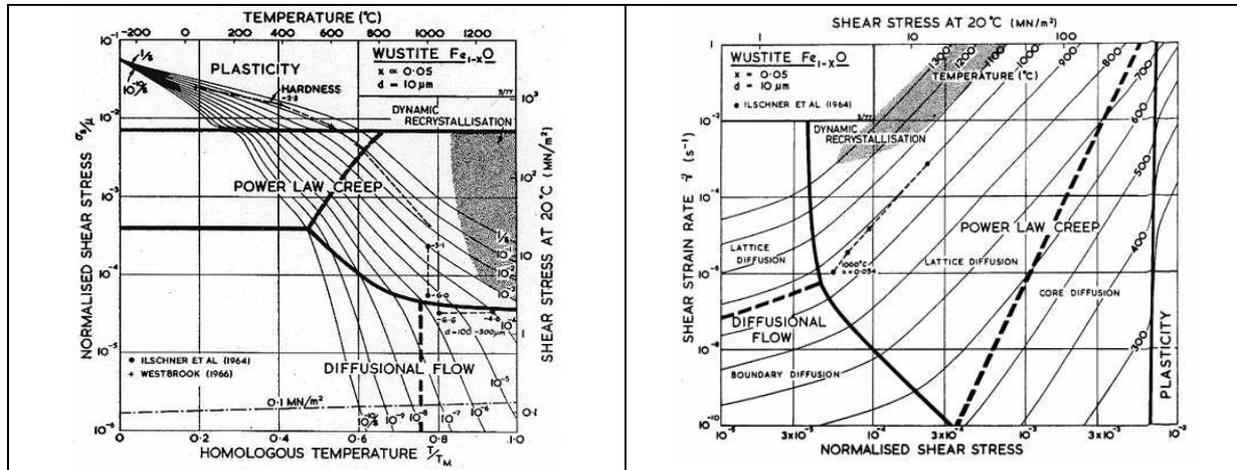
Figure II-32: $Fe_{1-x}O$ deformation-mechanism map [Ash2].

Carte des mécanismes de déformation du $Fe_{1-x}O$ [Ash2].

In their experiments, Hidaka et al. observe two types of plasticity:

- Type I: accompanying the work hardening (for FeO at 700-900°C and for γ-Fe_3O_4 at 800-1100°C); it corresponds to the dislocation glide or the grain boundary sliding. The Bürgers vectors of the dislocations are determined.

- Type II: notified as "steady-state" deformation (for FeO at 1000-1200°C and for γ-Fe_3O_4 at 1200°C). Type II of plasticity is associated to dislocation climb (dislocation creep) or diffusion creep (Nabarro-Herring creep, Coble creep).

It is rather easy to find articles studying the oxide scale plastic deformation **at low strain rate**, in the creep deformation range. However, how do mechanisms involved at strain rates of 10^{-5} s^{-1} –10^{-3} s^{-1} compare with these reached in a rolling stand (at ~10 s^{-1})? At such a strain rate, is it possible for plastic mechanisms to be initiated?

III.4. Stresses evaluation and damage criteria

To understand what the scale undergoes in a FM (in terms of damage), it is primordial to do a detailed assessment of the different stresses and the damage criteria available in the literature. This part is divided in three sections:

- The interstand: the strip mainly undergoes thermal stresses. In a first case, the scale is in tension: cohesive failure is then initiated (**through thickness cracks**), followed sometimes by interfacial cracks (**delamination**) and the total **decohesion** of scale rafts (spallation). The delamination can be due to interfacial shear stresses connected with interfacial sliding. The second case corresponds to the spallation under compressive stresses: two ways are possible, depending on the interface strength. In a strong interface case, the spallation is initiated from cohesive cracks in the scale. For a weaker interface, buckling mode is reached first.

- <u>The entry of the roll bite</u>: mechanical tensile stresses are high in this area. Indeed work-rolls put the skin in tension by their rotational movements. Similar behaviours to the interstand (tension part) are observed. Nevertheless, an additional contribution is the scale bending at the entry of the roll bite.
- <u>Under the rolls</u>: What occurs under the rolls is quite mysterious. In the following developments we will only focus on through-thickness crack initiation and the extrusion of soft steel within them.

III.4.1. Fracture mechanics theory
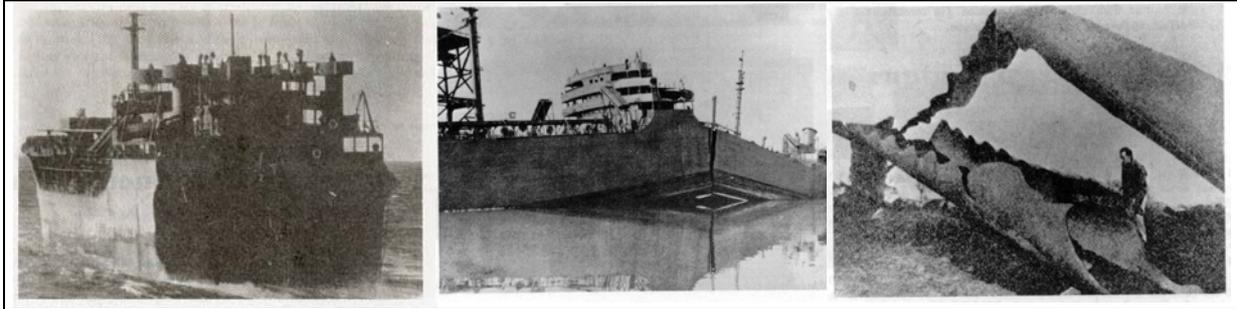
Figure II-33: Example of construction accident

Exemple d'accident de construction

In 1920, Griffith understood that accidents happened for applied stresses very much lower than **theoretical** fracture strength of **elastic** materials (=E/10 [Rob]) (Figure II-33). He pointed out the existence of a local stress concentration, near a **defect** (inclusion, micro-porosity, crack, grain boundary…) or a geometrical material singularity.

Then, he introduced the notion of **local stress concentration** σ_y:

$$\sigma_y = K_t \sigma \qquad \text{eq. II-20}$$

where σ is the global applied stress and K_t the **stress concentration factor**.

In the case of an initial ellipsoidal defect (radius: a and h), the relation between the local stress and the global one is:

$$\sigma_y = \sigma\left(1 + 2\frac{a}{h}\right) \text{ with } K_t = 1 + 2\frac{a}{h} \qquad \text{eq. II-21}$$
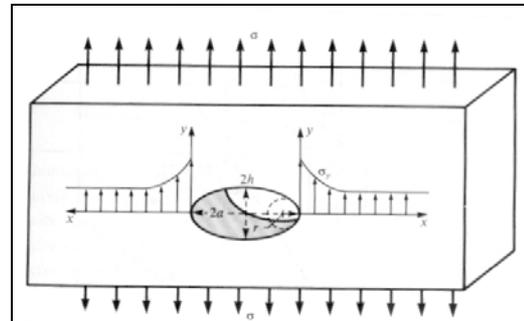
Figure II-34: Stress concentration zone for an initial ellipsoidal defect.

Zone de concentration de contrainte pour un défaut initial ellipsoïdal.

In **linear elastic fracture mechanics LEFM** (for elastic material), the initial defects are sharp cracks. Two approaches are available: local or global (or energetic).

The local approach
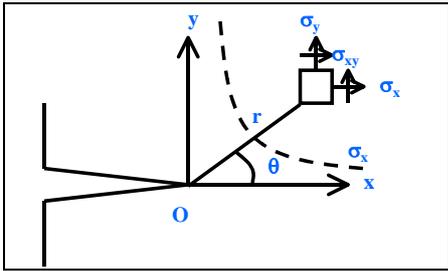
Figure II-35: Crack tip singularity.

Singularité en pointe de fissure.

It is based on the local description of mechanical fields at crack tips.

Irwin defined in 1957 the notion of **stress intensity factor** (SIF), which characterizes the force of the stress field singularity at the crack tip. The SIF is defined from the elastic stress field equations for a stressed element near the tip of a sharp crack under biaxial (or uniaxial) loading in an infinite body (Figure II-35).

Stress and strain fields are singular at the crack tip. We can analytically describe these fields using the SIF K_I, K_{II} and K_{III}, which corresponds respectively to modes I, II and III (mode I: opening-cleavage – mode II: plane shear– mode III: anti-plane shear: Figure II- 36).
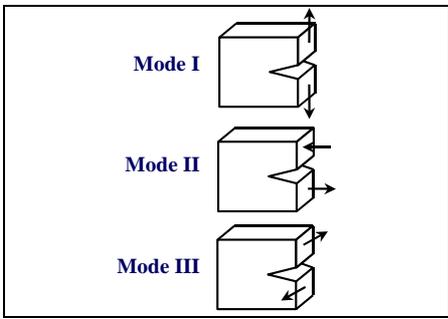
Figure II- 36: Fracture modes.

Modes de rupture.

$$\begin{cases} \sigma_{ij} = K_\alpha \dfrac{1}{\sqrt{2\pi r}} f_{ij}^\alpha(\theta) \\[2mm] \varepsilon_{ij} = K_\alpha \dfrac{1}{\sqrt{2\pi r}} g_{ij}^\alpha(\theta) \end{cases} \qquad \text{(Figure II-35).} \qquad \textbf{eq. II-22}$$

where α=1, 2, 3; i and j are the x and y coordinates; r and θ are the polar coordinates of the vicinity of the crack tip.

These SIF depend on the distribution of the exterior loads and the crack geometry. To study the initiation or the propagation of a crack, the SIF is compared with a critical characteristic of the material: its **fracture toughness** noted K_{Ic} ($MPa\sqrt{m}$) when conditions of plane strain apply and K_c otherwise. Irwin postulated that fracture occurs when K reaches the value K_c.
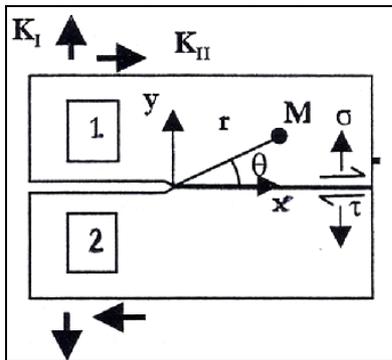
Figure II-37: Interfacial crack representation [Dup].

Représentation d'une fissure interfaciale [Dup].

An extension of the model is available for interfacial cracks in 2-D. Fracture mode I and II cannot be discussed independently, which explains the use of complex numbers for the SIF:

$$K = K_I + iK_{II} \qquad\qquad \textbf{eq. II-23}$$

For an interfacial fracture, θ=0 (Figure II-37). Normal and tangential stresses are thus coupled:

$$(\sigma + i\tau)_{r,\theta=0} = \frac{K.r^{i\varepsilon}}{\sqrt{2\pi r}} \qquad\qquad \textbf{eq. II-24}$$

ε is a constant depending on both materials [Dup,Dal] :

$$\varepsilon = \frac{1}{2\pi} \ln\left(\frac{1-\beta}{1+\beta}\right)$$

eq. II-25

In plane deformation, the Dundurs parameter β is defined as:

$$\beta = \frac{1}{2} \frac{\mu_o (1-2\nu_s) - \mu_s (1-2\nu_o)}{\mu_o (1-2\nu_s) + \mu_s (1-2\nu_o)}$$

eq. II-26

μ is the shear modulus and subscripts o and s point respectively to the oxide layer and the steel substrate.

Nevertheless, it is sometimes difficult to study the local stress fields at the crack tip. Since there are high stress gradients, it may be more relevant to study the crack propagation from an **energetic** point of view.

The global (energetic) approach

Crack propagation is an energy dissipative phenomenon. In 1920, Griffith introduced the notion of **strain energy release rate G**, which represents the total energy $W_{e,p}$ (elastic and potential) for an unitary crack propagation. If b is the crack width and c the crack length:

$$G = -\frac{1}{b} \frac{\partial W_{e,p}}{\partial c}$$

eq. II-27

The cohesion is characterized by the free energy γ per unit area of a solid surface. Just as K is compared to K_{IC}, G can be compared to a critical value $\mathbf{G_c}$. The crack is then propagated when G reaches G_c, equal to the energy 2γ required to create a corresponding material free surface (the factor 2 represents the two new surfaces created during the crack propagation) :

$$G = G_c = 2\gamma$$

eq. II-28

A link between local and global approaches

Both notions, local as well as global, can be used. Indeed, they are linked by the relation:

$$G = \frac{\left(K_I^2 + K_{II}^2\right)}{E'} + \frac{K_{III}^2}{2\mu}$$

eq. II-29

with $E' = E$ in plane stress; $E' = \dfrac{E}{1-\nu^2}$ in plane strain. E is Young's modulus, ν the Poisson coefficient and $\mu = \dfrac{E}{2(1+\nu)}$ is the shear modulus.

J-integral

Among numerous methods available to calculate G, the J-Integral (JI) is one of the most popular. This method, developed at the origin for elastic materials, can also be used in confined **plasticity** under particular conditions.

The stress field singularity near a crack tip can be investigated from a path-independent integral deduced from the energy conservation law. This integral has the specificity to be equal to the strain energy release rate, and to be independent of the integration path. One of the most used is the **Rice integral**, which considers a cracked bidimensional domain. The crack is supposed to be rectilinear. The contour C is open and oriented. Its ends are on the bottom and top faces of the crack (Figure II-38).

Figure II-38: Integration path

Contour d'intégration.
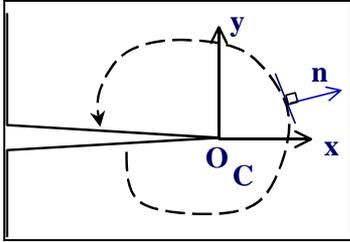
$$J = \int_C \left(W_e(\varepsilon)dy - \sigma_{ij}n_j \frac{\partial u_i}{\partial x} ds \right) = G = -\frac{1}{b}\frac{\partial W_{e,p}}{\partial c} \qquad \textbf{eq. II-30}$$

W_e is the energy density of elastic deformation with $\sigma_{ij} = \partial W_e / \partial \varepsilon_{ij}$. u is the displacement vector in a point of the path C with the outline normal n and σ is the stress field.

Under certain conditions (the principal being the analogy between elastoplastic and non-linear elastic behavior in the cases without unloading), the J integral allows to describe the stress and strain fields at the crack tip from the HRR analytical solution (Hutchinson-Rice-Rosengren [Hutc,Rice]).

The model can also be described for bimaterials. A new term corresponding to an integral over the interface is added to the previous expression of J.

$$J = \int_C \left(W_e(\varepsilon)n_1 - \sigma_{ij}n_j \frac{\partial u_i}{\partial x_1} \right)ds + \int_I \left\{ \left(W_{e1}(\varepsilon) - W_{e2}(\varepsilon)\right)n_1 - \sigma_{ij}n_j \left[\left(\frac{\partial u_i}{\partial x_1}\right)_1 - \left(\frac{\partial u_i}{\partial x_1}\right)_2 \right] \right\}ds \qquad \textbf{eq. II-31}$$

The J integral is theorically independent on the integration path, but in practice its value can be sensitive to the mesh or the integration path. For a better accuracy, surface integral methods such as the Gθ method [Bou] are preferable.

III.4.2. Interstand

III.4.2.1. Thermal stresses
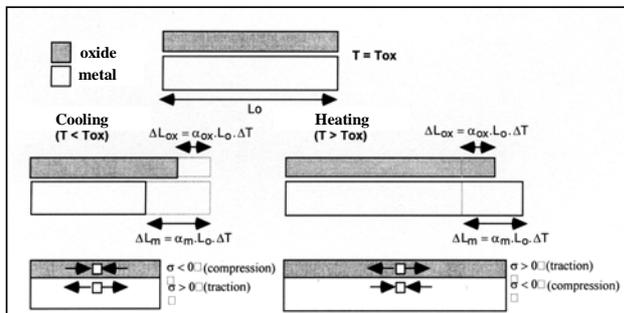
Figure II-39: Kind of stress obtained by differential dilatation.

Type de contrainte obtenue par dilatation différentielle.

During temperature changes, stresses are developed in a bimaterial due to the differential dilatation of each material (difference between the thermal expansion coefficients of metal α_m and oxide α_{ox}). Values of α_m are usually larger than the oxide ones. Tien and Davidson [Tien] give an expression of average thermal stress **for elastic materials**, later summarized by Evans [Evan]:

For the scale:
$$\sigma_{ox} = -\frac{E_{ox}.\Delta T.(\alpha_m - \alpha_{ox})}{(1-\nu)\left(1 + \dfrac{E_{ox}h_{ox}}{E_m h_m}\right)}$$
eq. II-32a

For the substrate:
$$\sigma_m = +\frac{E_m.\Delta T.(\alpha_m - \alpha_{ox})}{(1-\nu)\left(1 + \dfrac{E_{ox}h_m}{E_m h_{ox}}\right)}$$
eq. II-32b

with h_{ox} the oxide scale thickness, ΔT the temperature jump amplitude, h_m the substrate half-thickness, E the appropriate Young's modulus and ν the Poisson coefficient (assumed to be the same for both materials). The signs are inverted if the sample is heated over the oxidation temperature.
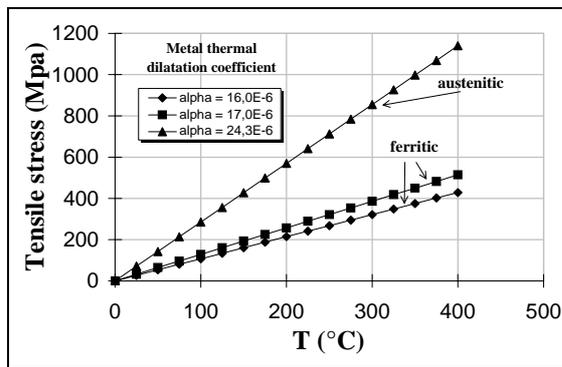
Figure II-40: Thermal stresses developed in FeO scale for different values of steel thermal dilatation coefficient. $E_{ox}=150Gpa$; $\alpha_{ox}=11.10^{-6}$; $\nu=0.3$.

Contraintes thermiques développées dans la couche de FeO pour différentes valeurs de coefficients de dilatation thermique. $E_{ox}=150Gpa$; $\alpha_{ox}=11.10^{-6}$; $\nu=0.3$.

Under the assumption, perfectly true in our case, that the oxide thickness is thin relative to the metal ($h_{ox} \ll h_{cal}$):

For the scale:
$$\sigma_{ox} = -\frac{E_{ox}.\Delta T.(\alpha_m - \alpha_{ox})}{(1-\nu)}$$
eq. II-33a

For the substrate:
$$\sigma_m = +\frac{E_m^2.\Delta T.h_{ox}.(\alpha_m - \alpha_{ox})}{(1-\nu).E_{ox}.h_m}$$
eq. II-33b

If $\alpha_m > \alpha_{ox}$, cooling induces compressive (negative) stresses in the oxide while heating induces tensile ones (Figure II-39).

Figure II-40 represents thermal stresses computed using eq. II-33. Even if the elastic materials condition is not totally respected, these expressions give an estimate of the thermal stresses.

III.4.2.2. Cohesive failure criteria under tensile stresses

- Elastic fracture

Hancock and Nicholls [Han] generalized the previous formula by adding a geometrical factor f depending on the original defect geometry:

$$\sigma_c = \frac{K_{1c}}{f\sqrt{\pi\overline{a}}}$$
eq. II-34

where f can take the value of 1.12 for a surface notch of infinite length, 1.0 for a buried defect and 0.64 for a semicircular notch of radius $\overline{a}$. $\overline{a}$ is the half-length of an embedded defect or the whole length of a surface defect (determined by the authors: Table II-11). They take into account the oxide porosity and the interactions between the different defects constituting the porosity.

K_{Ic} can also be calculated from the oxide surface fracture energy γ: $K_{Ic} = \sqrt{2\gamma E_{ox}}$ **eq. II-35**

Temp. [°C]	Strain .10⁴	Scale thickness [µm]	Young's Modulus [GPa]	Fracture stress [MPa]	$\overline{a}$ [µm]	K1c [MN.m⁻³/²]
570	2.1	35.,8	182	38	715	1,82
674	2.4	110.8	168	40	882	3,1 ± 1,4
743	1.9 2.8 4.4.	206.4	158	31 44 70	1642	3,5 ± 1,4
800	4.9 8.0	324.7	151	74 120	2584	7,7 ± 2,5
825	7.8 10.3	390.2	148	115 152	3105	11,7 ± 1,7

Table II-11: Data for Armco Iron [Han].

Données pour le fer Armco [Han].
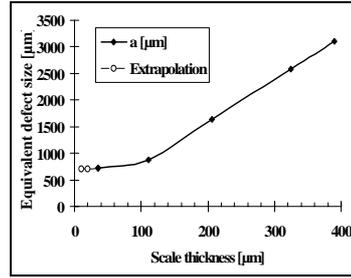
Figure II-41: Scale thickness influence on equivalent defects of size $\overline{a}$. Extrapolation to thin scales.

Influence de l'épaisseur de la couche sur la taille de défauts équivalents $\overline{a}$. Extrapolation aux épaisseurs fines.
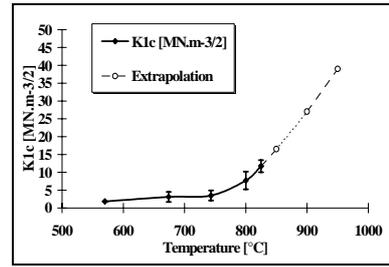
Figure II-42: Temperature influence on the toughness. Extrapolation to higher temperatures.

Influence de la température sur la dureté. Extrapolation aux hautes températures.
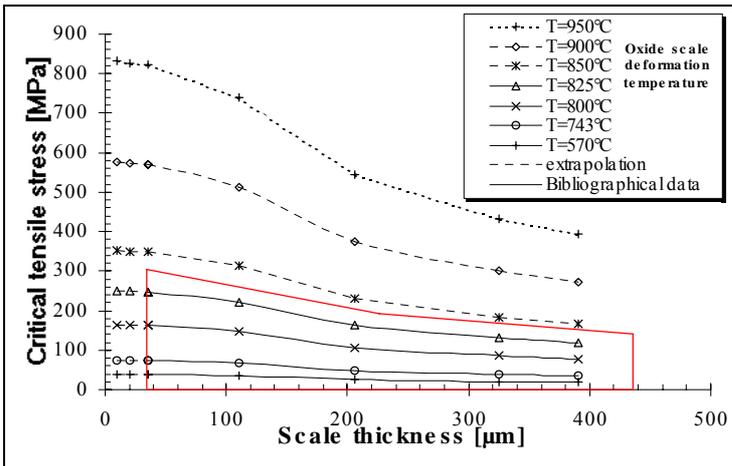
Figure II-43: Critical tensile stress depending on scale thickness and temperature.

Contrainte critique de traction en fonction de l'épaisseur de calamine et de la température.

Graphical extrapolations of equivalent defect size values for thinner scales and of critical stress intensity factor for higher temperatures are shown Figure II-41 and Figure II-42.

Introducing data from Table II-11, we obtain the critical tensile stress depending on the scale thickness and temperature (Figure II-43).

Extrapolations to high temperatures are extremely subject to caution due to the plastic deformation.

The **oxide scale is then tougher when the temperature is higher and the thickness smaller.**

Due to the elastic assumption, it is easy to transform a critical stress σ_c into a critical strain ε_c:

$$\varepsilon_c = \frac{\sigma_c}{E_{ox}} = \frac{K_{1c}}{f E_{ox} \sqrt{\pi \overline{a}}} = \sqrt{\frac{2\gamma}{f^2 E_{ox} \pi \overline{a}}}$$ **eq. II-36**

Results from the formula in [Han] (Figure II-44-left) are compared with experiments (Figure II-44-right) [Nag1].
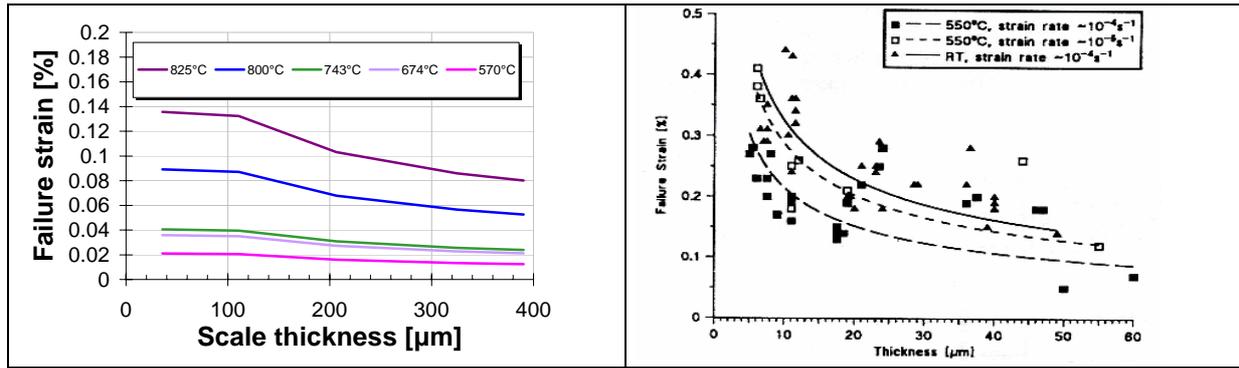
Figure II-44: Critical strain as a function of scale thickness. Left: [Han]; Right: [Nag1]

Déformation critique en fonction de l'épaisseur de calamine. Gauche: [Han]; Droite: [Nag1]

On Figure II-44-right [Nag1], the failure strains obtained on a 4-point bending jig are represented. Comparing figure a) and b) we remark that results are significantly different. For a 35µm-thick scale, at around 550°C, a) gives a failure strain of 0.02% vs 0.15% in b). This important difference may be due to the deformation mode or more probably to the strain rate (not given in [Han]), which has a high influence as shown in graph b). Indeed, lower strain rates lead to a deformation accommodation by creep, which delays the material fracture. This assumes that the strain rate used in a) is higher than in b).

Schütze tackles the oxide scale plastic deformation problem above a limit thickness. A scale thicker than h_c does not fail by cracking but in a ductile manner:

$$h_c = \frac{2.8\gamma_0 E_{ox}}{\sigma_y^2}$$

eq. II-37

where σ_y is the plastic oxide yield stress.

Distance between cracks:

Bruns et al. introduce crack density [Brun]. They propose a damage evolution model depending on the increase of the deformation. In a first stage, when the deformation reaches a critical value ε_c, cracks are initiated. At higher deformation $\varepsilon_{c,del}$, a lattice of equidistant cracks is formed (distance L_c). Once a saturation crack density has been reached, i.e. a crack number per unit length, no through-thickness cracks are formed, they are replaced by the initiation of a delamination process, starting from the cracks (Figure II-47).
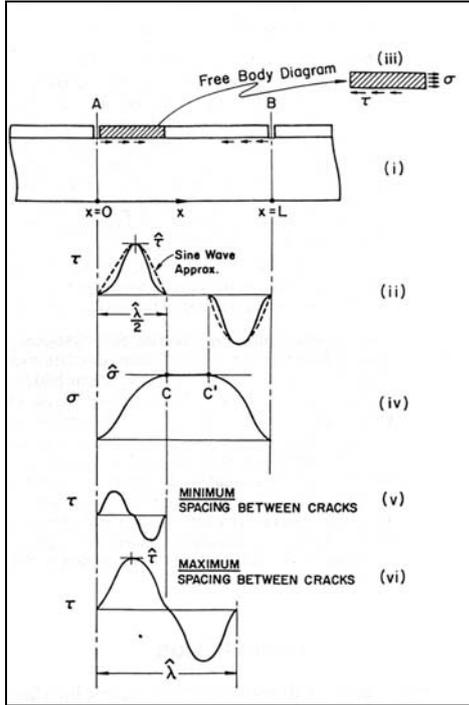
Figure II-45: Determination of critical crack spacing L_c. [Agr]

Détermination de la distance critique interfissure L_c. [Agr]

Agrawal and Raj give an expression of this critical length [Agr]. They schematically represent two cracks A and B (Figure II-45) distant of L (i). Distribution of shear and tensile stresses are represented in (ii-iv). The free body equilibrium condition applied between A and B imposes a shear stress integral equal to zero in this zone. They assume that the shear stress has a sinusoidal form:

$$\tau = \hat{\tau}\sin\frac{2\pi x}{\hat{\lambda}} \qquad \text{for} \qquad 0 \leq x \leq \frac{\hat{\lambda}}{2}$$

and **eq. II-38**

$$\tau = -\hat{\tau}\sin\frac{2\pi}{\hat{\lambda}}\left[x - \left(L - \frac{\hat{\lambda}}{2}\right)\right] \text{ for } \left(L - \frac{\hat{\lambda}}{2}\right) \leq x \leq L$$

$\hat{\lambda}$ is the maximum crack spacing. As for the axial stress (iv):

$$\sigma \propto \hat{\sigma}\sin^2\frac{\pi x}{\hat{\lambda}} \qquad\qquad \textbf{eq. II-39}$$

They finally find that: $\hat{\tau} = \dfrac{\pi h}{\hat{\lambda}}\hat{\sigma}$ **eq. II-40**

The critical length is comprised between two values (v, vi) $\dfrac{\hat{\lambda}}{2} \leq L_c \leq \hat{\lambda}$, so that :

$$\frac{\pi h}{2\hat{\tau}}\hat{\sigma} \leq L_c \leq \frac{\pi h}{\hat{\tau}}\hat{\sigma} \qquad\qquad\qquad \textbf{eq. II-41}$$

In [Nag1,Tien] another expression of L_c is given for a purely linear elastic situation. In this case, the shear stress decreases linearly from the maximum value at the interface next to the through-thickness cracks.
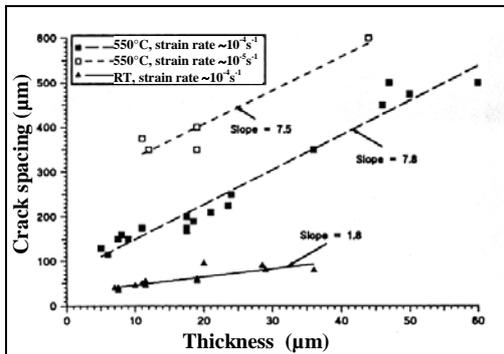
Figure II-46: Crack spacing vs. scale thickness.

Espacement de fissure en fonction de l'épaisseur de calamine.

$$L_c = \frac{kh\hat{\sigma}}{\hat{\tau}} \quad (\hat{\sigma} = \sigma_c \text{ and } \hat{\tau} = \tau_c) \qquad \textbf{eq. II-42}$$

The ratio $r = \sigma_c/\tau_c$ determines the slope of the curve (Figure II-46). This slope seems to be independent of the strain rate. The crack spacing increases when strain rate decreases. This is due to an additional creep that allows for more plastic deformation. For the authors, the factor k depends on the oxide behaviour : it stands between 2 (for an ideal plastic behavior) and 4 (for an elastic behavior).

Interfacial damage:
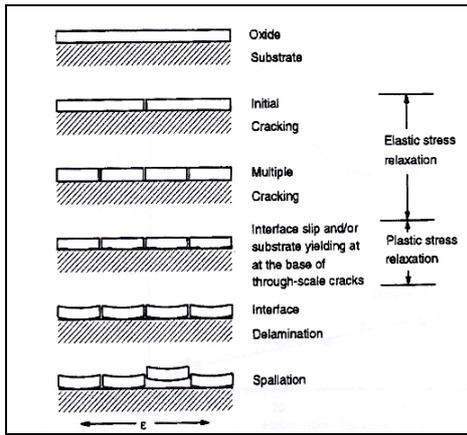
Figure II-47: Delamination and spallation [Nag2]

Délamination et spallation [Nag2]

Figure II-48: Strain causing cracks and spallation vs. scale thickness. Tests at room temperature [Nag2].

Déformation causant fissures et spallation en fonction de l'épaisseur de calamine. Température ambiante [Nag2].

As mentionned before, at further deformation $\varepsilon_{c,del}$, stress relaxation by through-thickness cracks is replaced by a delamination process, starting from these cracks:

$$\varepsilon_{c,del} = \frac{K_{1c}}{f\sqrt{\pi c_g}} \frac{(1+r/h)(1+\nu)}{2E_{ox}}$$ **eq. II-43**

where c_g is the half-length of the interfacial physical defect, $f \approx 1$, r is the interfacial roughness amplitude, h the oxide scale thickness and ν the Poisson ratio of the oxide.

Finally, when deformation reaches $\varepsilon_{c,spall}$, delamination leads to spalling (Figure II-49c).

We will see in chapter V that we have observed this succession of events during hot tensile tests.

Spalling is characterized by the equation:

$$\varepsilon_{c,spall} = \frac{2\gamma_i}{hE_{ox}(1-\nu)}$$ **eq. II-44**

where $2\gamma_i$ represents the fracture energy of the oxide / metal interface. The interfacial roughness can be taken into account by replacing γ_i by γ_r:

$$\gamma_r = \gamma_i\left(1 + \frac{0.1E_{ox}}{2\gamma_i} \cdot \frac{r}{\lambda}\right)$$ **eq. II-45**

r is the interfacial roughness height and λ is the interfacial roughness wave length [sch1].

Figure II-48 represents the experimental results of Figure II-49.
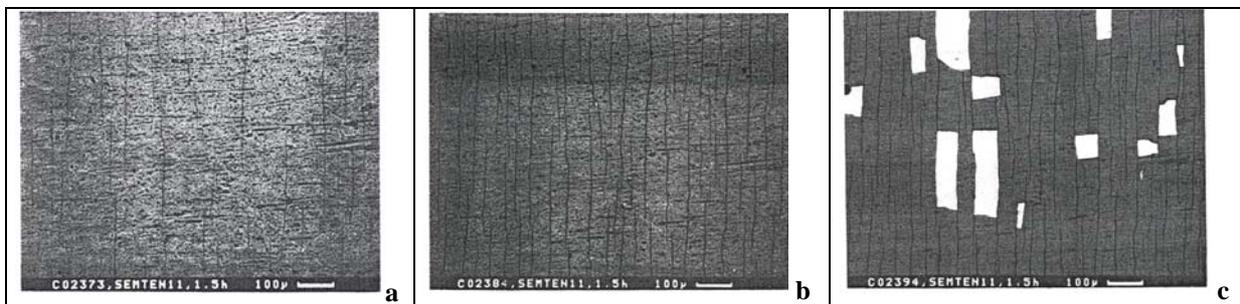
Figure II-49: SEM micrographs showing through-thickness cracks during tensile tests at room temperature. Scale thickness: 9.5µm. Strains: a) 0.54% b) 1.21% c) 2.3% [Nag3].

Micrographies MEB montrant les fissures transverses pendant des tests de traction à température ambiante. Epaisseur de calamine: 9.5µm. Déformation: a) 0.54% b) 1.21% c) 2.3% [Nag3].

III.4.2.3.Compressive damage

In compression, two mechanisms can lead to the oxide spallation (Figure II-50) [Nag4,Sch2] :

- **In mechanism I**, the oxide / metal interface is strong. In a first stage, failure occurs by shear cracking, followed by the interfacial crack propagation and the spallation of a scale fragment (Figure II-50-2a).
- **In mechanism II**, (Figure II-50-2b,c), the oxide / metal interface is weak. In this case, spallation results from interfacial decohesion, followed by buckling and tensile cracks initiation (due to a critical curvature of the scale).
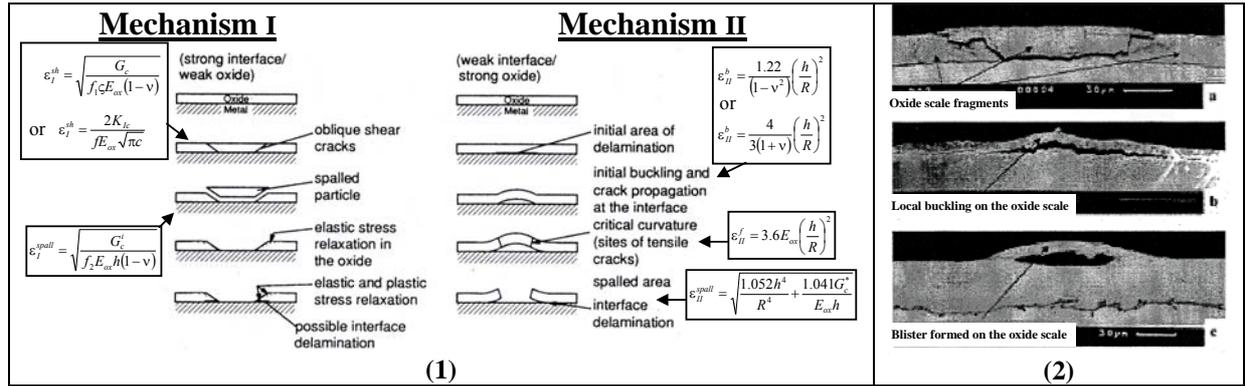
Figure II-50: 1) Schematic diagram of compressive failure mechanisms [Nag4] 2) SEM images illustrating decohesion on compression side of steel rod during bending [Krz1] a) cracked oxide scale b) buckling c) blister formed during oxidation

1) Diagramme schématique des mécanismes de fissuration en compression [Nag4] 2) Images MEB illustrant la décohésion sur le côté comprimé d'une tige d'acier en flexion [Krz1] a) Couche d'oxyde fissurée b) boursouflure c) gonflement formé pendant l'oxydation.

We have seen before that the failure through the oxide could be explained from the energy release rate $G_c = 2\gamma$, γ representing the oxide fracture surface energy. For the interfacial delamination, the energy release rate becomes [Nag4] :

$$G_c^i = \gamma + \gamma_m - \gamma_i \qquad \text{eq. II-46}$$

γ_m and γ_i are respectively the fracture surface energy of the metal and the energy released on removal of a unit area of interface.

Mechanism I:

- The shear failure of length ς is obtained by [Nag4] :

$$\varepsilon_I^{sh} = \sqrt{\frac{G_c}{f_1 \varsigma E_{ox}(1-\nu)}} \qquad \text{eq. II-47}$$

where f_1 (<<1) is a factor related to the fraction of the energy used for the fracture process of the layer and ς is the shear crack length. Spallation can begin only when the crack reaches the interface. Another expression of the critical shear strain is given in [Sch1]. It corresponds to twice the critical tensile deformation:

$$\varepsilon_I^{sh} = \frac{2K_{Ic}}{f E_{ox} \sqrt{\pi c}} \qquad \text{eq. II-48}$$

- The spallation is initiated when [Nag4] :

$$\varepsilon_I^{spall} = \sqrt{\frac{G_c^i}{f_2 E_{ox} h(1-v)}}$$

<div align="right">eq. II-49</div>

where h is the oxide thickness, f_2 (≈ 1) the proportion of the energy in the volume $\zeta^2 h$ used in the fracturing process.

Mechanism II:

This weak interface mode is initiated by buckling at a strain:

$$\varepsilon_{II}^b = \frac{1.22}{(1-v^2)}\left(\frac{h}{R}\right)^2 \qquad \text{[Nag4]}$$

<div align="right">eq. II-50</div>

or $\varepsilon_{II}^b = \frac{4}{3(1+v)}\left(\frac{h}{R}\right)^2 \qquad \text{[Wel]}$

<div align="right">eq. II-51</div>

$2R$ is the initial decohesion diameter. A failure strain ε_{II}^f is established to represent the start of crack deflection, on the perimeter of the buckled zone, from the interface towards the surface ; [Sch1] gives:

$$\varepsilon_{II}^f = 3.6 E_{ox}\left(\frac{h}{R}\right)^2$$

<div align="right">eq. II-52</div>

but this expression of the failure strain ε_{II}^f indeed has the dimension of a **stress** (it should probably read $\varepsilon_{II}^f = 3.6\,(h/R)^2$). Spalling finally occurs at a strain ε_{II}^{spall} :

$$\varepsilon_{II}^{spall} = \sqrt{\frac{1.052 h^4}{R^4} + \frac{1.041 G_c^*}{E_{ox} h}}$$

<div align="right">eq. II-53</div>

G_c^* is selected depending on the delamination localization.

All these results are summarized in Figure II-50-1.

III.4.2.4. Sliding

Beynon and Krzyzanowski [Krz2] highlight, above a critical temperature, a sliding behavior of the oxide scale along the interface during tensile tests. They use a theory that H. Riedel [Rie] had exploited before them to describe the behavior of a thin secondary-phase layer on an arbitrarily shaped solid. The initial hypothesis is an adherent oxide layer containing through-thickness cracks, and in which tangential viscous sliding is allowed. For linearly viscous behavior the shear traction τ transmitted from the substrate to the scale is:

$$\tau = \eta v_{rel} \quad \text{if} \quad \eta v_{rel} \geq \tau_s^c$$

<div align="right">eq. II-54</div>

η is the viscosity coefficient and v_{rel} the relative velocity between scale and steel surface. Slipping occurs if the critical stress τ_s^c is exceeded. Values of η depend on stress-directed diffusion around irregularities at the oxide/metal interface.

Linear viscous sliding is treated as grain-boundary sliding in high temperature creep. Raj and Ashby [Raj] have shown that, if the interface roughness has a periodicity of wavelength λ and an amplitude $p/2$ (Figure II-51), the viscosity coefficient has the form

$$\eta = \frac{kTp^2}{8\Omega(\delta Ds + \lambda Dv/4\pi)} \qquad (T \in 873.15 - 1373.15K) \qquad \textbf{eq. II-55}$$

Ω is the atomic volume, k the Boltzman constant, T the temperature (K), Dv the volume diffusion coefficient ($m^2.s^{-1}$), δDs the surface diffusion coefficient along the interface metal / scale ($m^3.s^{-1}$).

$$\delta D_s = \delta D_{os}.\exp(-Q_s/RT)$$
$$\delta D_{os} = 1.1.10^{-10} m^3.s^{-1}, \ Q_s = 220 KJ.mole^{-1}, \ R = 8.314 J.mole^{-1}.K^{-1}$$

$$D_v = D_{ov}.\exp(-Q_v/RT)$$
$$D_{ov} = 1.8.10^{-4} m^2.s^{-1} \ ; \ Q_v = 159 KJ.mole^{-1}$$
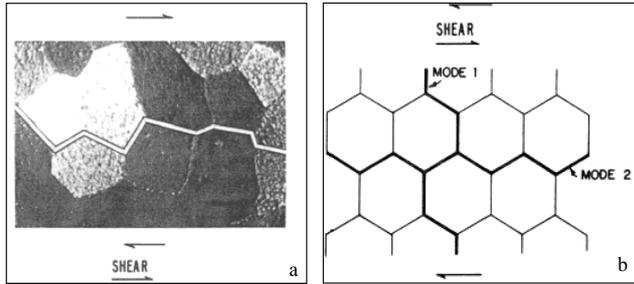
Figure II-51: a) crystals formation   b)Idealized representation of the crystals by regular hexagons.

a) Formation de cristaux   b) Représentation idéalisée des cristaux par des hexagones réguliers.

It could be argued that interface irregularities can also be avoided by dislocation creep in addition to diffusional flow of atoms. The non-linear form of sliding law for dislocation creep is:

$$v_{rel} = \frac{1}{\eta_c}|\tau|^{k-1}\tau \qquad \textbf{eq. II-56}$$

where vertical bars denote the absolute value and k is of the order of the creep-stress exponent, i.e. $k \approx 4$.

The use of such friction laws to explain hot rolling process requires a real in-depth investigation. Indeed, the basic theory concerns creep, which, as mentioned before, seems to be very far from the oxide behavior in the FM, would it be only by the strain rate order of magnitude.

III.4.3. Roll gap entry

At the entry of the roll bite, the scale undergoes tensile stress (substrate plastic flow due to the reduction and traction of the surface skin due to the rolls rotation) and bending (strip reduction). The former has been investigated just before with the **tensile**, **interfacial** and **sliding** damages. The latter consists in the **scale bending** when it starts to contact the roll. Using the critical energy release rate of a system, and considering that we are in plane deformation and that the predominant mode of deformation is a mixed one (bending and tension), the expression of the complex stress intensity factor is [Zhou]:

$$|K| = \frac{2\cosh\pi\varepsilon}{\sqrt{\left(\dfrac{1-\nu_o}{\mu_o} + \dfrac{1-\nu_s}{\mu_s}\right)}}\sqrt{G_c}$$

<div align="right">eq. II-57</div>

where $|K|$ is the stress intensity factor norm, μ_o and μ_s are respectively the shear modulus of the oxide scale and the steel substrate, ν_o and ν_s their Poisson coefficients and ε the constant defined in eqs. II-25 and II-26 (Figure II-37).

[Zhou] describes the energy release rate G_c of an interface cracking in bending from the Suo-Hutchinson formula [Suo]:

$$G_c = \frac{1-\nu_o}{4\mu_o}\left[\frac{P^2}{Ah} + \frac{M^2}{Ih^3} + 2\frac{PM}{h^2\sqrt{AI}}\sin\gamma\right]$$

<div align="right">eq. II-58</div>

A, I and the angle γ are non-dimensional parameters defined in [Zhou]. P and M are the load and the moment.

III.4.4. Under the rolls
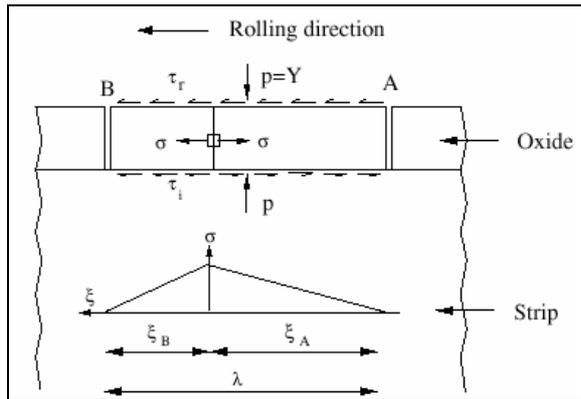
Figure II-52: Model of roll bite oxide fracture due to extension of the substrate metal during rolling [Le]

Modèle de fissuration de calamine due à l'extension du substrat (métal) pendant le laminage [Le]

Le et al. have developed a model for the oxide scale cracking under the rolls [Le]. They use the existing "shear lag" models, which predict the composite materials fiber cracking (Figure II-52). Contact with the roll is given by a Coulomb friction τ_r ($\tau_r = \mu p$). Compared to the previous interstand case, this surface friction influences the position of the next crack. As before, it is initiated where the shear strength sign at the oxide / metal interface τ_i changes. The overall balance of lateral forces gives:

$$\xi_A(\tau_i - \tau_r) = \xi_B(\tau_i + \tau_r)$$

<div align="right">eq. II-59</div>

$\xi_A + \xi_B = \lambda$ is the initial crack space, and the local "neutral point" is located at:

$$\xi_B = \frac{\lambda}{2}\left(1 - \frac{\tau_r}{\tau_i}\right)$$

<div align="right">eq. II-60</div>

and the maximal tensile stress σ_c is: $\qquad \sigma_c = \frac{\xi_B}{h}(\tau_i + \tau_r)$

<div align="right">eq. II-61</div>

This model is interesting but, as all the others, it does not deal with the possible scale fragmentation under vertical compression. In our case, this is really important because the

scale can be cooled under the rolls down to ≈ 600°C. At such temperatures, it is extremely brittle.

A second effect of roll pressure, studied by the same authors, is the extrusion of the soft steel in the opening cracks.
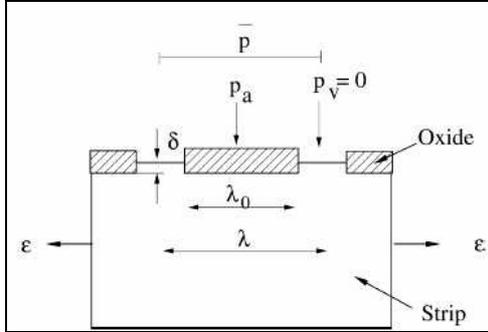
Figure II-53: Metal extrusion through the oxide cracks [Le]

Extrusion du métal à travers la couche d'oxyde [Le]

Assuming that the oxide scale is inextensible, they give the area ratio A_c (Figure II-53) as a function of bulk strain ε:

$$A_c = \frac{\lambda}{\lambda_0} = 1 - \varepsilon \qquad \text{eq. II-62}$$

They consider the problem as oxide fragments indentation into a bulk deforming substrate. They define a non-dimensional extrusion rate W:

$$W = \frac{2v_f}{\lambda\dot{\varepsilon}} \qquad \text{eq. II-63}$$

where $v_f = d\delta/dt$ is the extrusion velocity and $\dot{\varepsilon}$ is the bulk strain rate.

Both equations are combined to give the variation with the bulk strain ε of the extrusion height δ, normalized by the oxide film thickness t_c:

$$\frac{d(\delta/t_c)}{d\varepsilon} = \frac{(1+\varepsilon)\lambda_0 W}{2t_c} \qquad \text{eq. II-64}$$

The non-dimensional extrusion rate depends on A_c and the pressure difference Δp between the scale and the extruded material normalized by the substrate yield strength Y:

$$\frac{\Delta p}{Y} = \frac{\bar{p}}{YA_c} \qquad \text{eq. II-65}$$

At the end of the extrusion process, when metal reaches the roll, pressures on oxide and metal become equal.

Specifying that most of the bulk deformation occurs before the neutral point, the authors use Johnson's solution to evaluate the contact pressure on the surface $\bar{p}$ at the entry zone [John]

$$\frac{\Delta p}{Y} = \left(1 + \frac{\Gamma_1}{\Gamma_2} - \Gamma_1\right)e^{\Gamma_2(1+x/b)} - x\frac{\Gamma_1}{b} - \frac{\Gamma_1}{\Gamma_2} \qquad \text{eq. II-66}$$

where x is the distance from the entry, b the roll bite length, $\Gamma_1 = b/\mu R$ and $\Gamma_2 = 4\mu b/(t_1 + t_2)$ with t_1 and t_2 the inlet and exit strip thickness.

Other micro-extrusion models exist in the literature, such as the **Bay / Wanheim** models [Bay1,Bay2,Bay3].

IV. CONCLUSION

The scale thickness at the entry of the roll bite seems to be a **key parameter** to control rolled-in scale defects. Oxidation growth kinetics of steel have thus been investigated under conditions as close as possible to the finishing mill. **HSM operation limits** have been expressed as a **temperature window** (around 900-1000°C), closely linked to the scale thickness.

The bibliography on the oxide scale mechanical behavior has emphasized that in the finishing mill temperature range, the oxide scale seems to be plastically deformed. Nevertheless, observations are often done under strain and strain rate conditions very different from rolling.

Many data exist on the oxide scale damage. All kinds of damage have been studied (crack, delamination, spallation), but the existing results often used **linear elastic fracture mechanics** despite the **plastic behavior** of the oxide scale. Moreover, critical values are often obtained using tensile stress and are expressed as a global deformation. Thus, they cannot be applied for other experimental tests or industrial processes. We need local criteria.

It is therefore probable that all these criteria from the literaturemay be used only in their limited experimental range, very different from the rolling conditions. **Experimental tests reproducing as close as possible chemical and thermomechanical conditions of an industrial finishing mill stand are therefore necessary.**

V. REFERENCES

[Agr]   D.C.Agrawal, R.Raj, Measurement of the ultimate shear strength of a metal-ceramic interface, Acta metallurgica vol.37 n°4, (1989), pp.1265-1270.

[Ash1] M.F.Ashby, A first report on deformation-mechanism maps, Acta metallurgica, vol20, (july 1972), pp.887-897.

[Ash2] http://thayer.dartmouth.edu/~defmech/
        Web version of: Deformation-Mechanism Maps, The Plasticity and Creep of Metals and Ceramics, by Harold J Frost, Dartmouth College, USA, and Michael F Ashby, Cambridge University, UK.

[Bar]   N. Barbouth: Corrosion sèche des métaux et alliages, Techniques de l'ingénieur, M170-1 (1979). *In french.*

[Bay1] N.Bay, Cold welding - Part 1 – Characteristics, bonding mechanisms, bond strength, Metal construction, (June 1986), pp.369-372.

[Bay2] N.Bay, Cold welding - Part 2 – Process variants and applications, Metal construction, (August 1986), pp.486-490.

[Bay3] N.Bay, Cold welding - Part 3 – Influence of surface preparation on bond strength, Metal construction, (October 1986), pp.625-629.

[Ben]   J.Bénard, l'oxydation des métaux, Tome I, Processus fondamentaux, Ed. Gauthier-villars & Compagnie éditeur – Paris (1962). *In french.*

[Ber]   G.Béranger, G.Henry, G.Sanz
        "Le livre de l'acier", (1994). *, Tech. & Doc Lavoisier, Paris, 1994. In french.*

[Bern] J.Bernard, O.Coquelle, Nouvelles recherches sur l'oxydation du fer aux températures élevées par la méthode micrographique, compte rendus 222, (1946), p796.

[Blaz] D.T.Blazevic, Tertiary rolled in scale-the hot strip mill problem of the 1990's, in: 37th Mechanical Working and Steel Processes Conf. Proc., vol. 33, Hamilton (Canada), (1995), Iron and steel society, Warrendale, (1996), pp.33-38.

[Bou]   P.O.Bouchard, Contribution à la modélisation numérique en mécanique de la rupture et structures multimatériaux, PhD Thesis, Ecole nationale supérieure des Mines de Paris, (september 2000), *In french.*

[Brun] C.Bruns, M.Schütze, Investigation of the mechanical properties of oxide scales on Nickel and TiAl, Oxidation of metals, vol.55, Nos.1/2, (2001), pp.35-67.

[Cast]   E. de Castro, Etude des cinétiques d'oxydation des aciers au cours du laminage à chaud, rapport de stage IRSID, (juin 1998) ; Comportement cinétique et mécanique des couches d'oxides formées au cours du laminage à chaud des aciers, IRSID report, (september 1998).

[Chan]   Y.N.Chang, F.I.Wei, High temperature oxidation of low alloy steels, Journal of Materials science 24, (1989), pp.14-22.

[Chen]   R.Y.CHEN, W.Y.D.YUEN - A study of the scale structure of hot rolled steel strip by simulated coiling and cooling - Oxidation of metals, vol 53, 5-6, (2000) pp.539-560.

[Crx]   http://www-cxro.lbl.gov/optical_constants/atten2.html

[Dal]   D. Dalmas, Adhérence et propriétés mécaniques de dépôts obtenus par projection thermique: application de l'émission acoustique à l'étude des modes d'endommagement, UTC Compiègne, (July 2001).

[Dav]   M.H.Davies, M.T.Simnad, C.E.Birchenall, on the mechanism and kinetics of the scaling of iron, Journal of Metals (1951), pp889-896.

[Dup]   M. Dupeux, Mesure des énergies de rupture interfaciale : problématique et exemples de résultats d'essais de gonflement-décollement. Ecole de Mécanique des Matériaux, Aussois (Jan. 2002)

[Eva1]   H.E.Evans, stress effects in high temperature oxidation of metals, International Materials Reviews vol.40 n°1, (1995), pp.1-40.

[Eva2]   H.E.Evans, Spallation of oxide from stainless steel AGR nuclear fuel cladding: mechanisms and consequences, Materials Science and technology vol. 4, (May 1988), pp415-420.

[Eva3]   H.E.Evans, R.C.Lobb, Conditions for the initiation of oxide-scale cracking and spallation, Corrosion Science vol. 24 n°3, (1984), pp209-222.

[Fel]   E. Felder, C.Angelelis, M. Ducarroir, M. Ignat, P. Mazot, Propriétés mécaniques des films minces : problématique et moyens de mesure, Ann. Chim. Mat., 1998, 23, pp. 791-819.

[Gui]   A.Guinier, Théorie et techniques de la radiocristallographie, Ed.Dunod, Paris, (1964).

[Han]   P.Hancock, J.R.Nicholls, Application of fracture mechanics to failure of surface oxide scales, Material Science and technology vol. 4, (May 1988), pp398-406.

[Hid1]   Y.Hidaka, T.Anraku, N.Otsuka, Deformation of iron oxides upon tensile tests at 600-1250°C, Oxidation of metals, vol 59, 1-2, February 2003.

[Hid2]   Y.Hidaka, T.Anraku, N.Otsuka, Deformation of FeO oxide scales upon tensile tests at 600-1200°C, Materials Science Forum Vols 369-372 (2001), pp. 555-562

[Hig1]   R.L.Higginson, R.Roebuck, E.J.Palmiere, Texture development in oxide scales on steel substrates, Scripta Mater. 47 (2002), pp 337-342

[Hig2]   D.P.Burke, R.L. Higginson, Characterization of multicomponent scales by electron back scattered diffraction (EBSD), Scripta Mater. 42, (2000), pp277-281.

[Hutc]   J.W.Hutchinson, Singular behaviour at the end of the tensile crack in a hardening material, J.Mech.Phys.Solids, Pergamon Press, vol.16, (1968), pp.13-31.

[John]   K.L.Johnson, Contact mechanics. Cambridge, UK: Cambridge university press, (1985), in [Le].

[Krz1]   M.Krzyzanowski, W. Yang, C.M.Sellars, J.H.Beynon, Analysis of mechanical descaling: experimental and modelling approach, Materials Science and Technology vol.19, january 2003, pp.109-116.

[Krz2]   M.Krzyzanowski, J.H.Beynon, Modelling the boundary conditions for thermo-mechanical processing – oxide scale behaviour and composition effects, Modelling & Simul. Mater. Sci. Eng. 8, (2000) pp.927-945.

[Lan1]   V.Lanteri, C. Thomas, F. Geffraye
         "Défauts d'incrustation calamine secondaire au Train à Bandes", Synthèse des mécanismes et perspectives, IRSID groupe USINOR, (décembre 1998) *(confidential documen, In French)*.

[Lan2]   V.Lanteri, Les réactions de surface des aciers au cours des traitements thermiques. In [Ber] pp.559-581. *In French.*

[Le]   H.R.Le, M.P.F.Sutcliffe, P.Z.Wang, G.T.Burstein, Surface oxide fracture in cold aluminium rolling, Acta Mater. 52 (2004), pp.911-920

[Mor]   R. Morrel: Handbook of properties of technical and engineering ceramics, HSMO, London, (1987).

[Nag1]   M.M.Nagl, W.T.Evans, D.J.Hall, S.R.J.Saunders, The failure of iron oxide scales at growth temperature under tensile stress, Journal de Physique (1994IV, colloque C9, Journal de Physique III suppl., volume 3, (décembre 1993), pp.933-941.

[Nag2]   M. M. Nagl, S. R. J. Saunders, W. T. Evans, D. J. Hall, The tensile failure of nickel oxide scales at ambient and at growth temperature, Corrosion Science, Vol. 35, 5-8, (1993), pp.965-969.

[Nag3]   M.M.Nagl, W.T.Evans, D.J.Hall, S.R.J.Saunders, an in-situ investigation of the tensile failure of oxide scales, (1994).

[Nag4]   M.M.Nagl, W.T.Evans, S.R.J. Saunders, D.J.Hall, Investigation of failure of brittle layers under compressive stresses using acoustic emission, Materials Science and Technology vol.8, (november 1992), pp.1043-1049.

[Oll]   H. Ollendorf, D. Schneider, A Comparative study of adhesion test methods for hard coatings, Surface and Coatings Technology 113, (1999), pp.86-102.

[Païl]   J.Païdassi, Sur la cinétique de l'oxydation du fer dans l'air dans l'intervalle 700-1250°C. Acta Metallurgica 6, (1958), pp.184-194.

[Paï2]   J.Païdassi, Monographie sur l'oxidation du fer, in [Ber]. *In French.*

[Raj]   R.Raj, M.F.Ashby, On grain boundary sliding and diffusional creep, Metallurgical Transactions, vol2, (april 1971), pp.1113-1127.

[Rice]   J.R.Rice, G.F.Rosenberg, Plain strain deformation near a crack tip in a powerlaw hardening material, J. Mech. Phys. Solids, vol.16, (1968), pp.1-12.

[Rie]   H. Riedel, Deformation and cracking of thin second-phase layers on deforming metals at elevated temperature, Metal Science vol 16, (december 1982), pp.569-574.

[Rob]   J.Robertson, M.I.Manning, Limits of adherence of oxide scales, Materials Science and Technology vol.6, (january 1990), pp.81-91.

[Sac]   K. Sacks, C.W. Tuck, Surface oxidation of steel in industrial furnaces, Proc. Conf. On Reheating for Hot Working, The Iron and Steel Institute, London, (1967), pp.1-17.

[Schm]   B.Schmid, N.Aas, O.Grong, R.Odegard, High-temperature oxidation of iron and the decay of wüstite studied with in-situ ESEM, Oxidation of metals, vol 57, 1-2, (February 2002), pp.115-130.

[Sch1]   M. Schütze: Mechanical properties of oxide scales, Oxid. Met. 44 n°1-2, (1995) pp.29-60.

[Sch2]   M. Schütze, plasticity of protective Oxide scales, Materials Science and Technology, vol 6, (Jan. 1990), pp.32-38.

[Tien]   J.K. Tien, J.M. Davidson, in "stress effects and the oxidation of metals", ed. J.V. Cathcart, New York, AIME, (1975), pp.200-219.

[Vagn]   G.Vagnard, J.Manenc, Etude de la plasticité du protoxyde de fer et de l'oxyde cuivreux, Mémoires Scientifiques Revue Métallurgie, LXI, n°11, (1964), pp.768-776. *In French.*

[Ver]   C.Vergne, Analyse de l'influence des oxydes dans le frottement d'une fonte pour outil de travail à chaud, PhD thesis, Ecole nationale supérieure des Mines de Paris (2001), *In French.*

[Wel]   C.H.Well, P.S.Follansbee, R.R.Dils: in Proc. Symp. On 'stress effects and the oxidation of metals', (ed. J.V.Cathcart), Pittsburg, PA, AIME, (1975), p220.

[Yu]   Y.Yu, J.G.Lenard, Estimating the resistance to deformation of the layer of scale during hot rolling of carbon steel strips, Journal of Materials Processing Technology 121, (2002), pp.60-68.

[Zhou]   Y.C.Zhou, T.Tonomori, A.Yoshiba, L.Liu, G.Bignall, T.Hashida, Fracture characteristics of thermal barrier coatings after tensile and bending tests, Surface and Coating Technology 157, (2002), pp.118-127.

Numerical developments

Résumé

L'intérêt de la simulation numérique est de nos jours complètement reconnu. Dans l'industrie, elle devient de plus en plus utile pour améliorer la production, diminuer les temps d'élaboration, pour les études préliminaires ou de faisabilité, ou encore pour le dimensionnement des presses… Finalement, la majorité des industries de mise en forme l'utilise pour des raisons économiques.

Le logiciel éléments finis utilisé et développé dans cette étude est Forge2®. Ce code éléments finis 2D développé conjointement par le CEMEF et TRANSVALOR S.A depuis la fin des années 80, est spécialisé dans la simulation numérique des procédés de mise en forme des métaux et des grandes déformations. Récemment, une version spéciale du logiciel a été développée pour modéliser les matériaux multicouches.
La méthode éléments finis est utilisée pour résoudre les équations d'équilibre thermique et mécanique. Dans ce chapitre, ces équations sont décrites, ainsi que leurs discrétisations et la méthode de résolution dans Forge2®.

Le problème que nous voulons modéliser requiert des développements spécifiques qui concernent la gestion du contact dans les directions normale et tangentielle.
Pour le contact normal, il est maintenant possible de passer d'un contact bilatéral à un unilatéral (décohésion).
Pour le contact tangentiel, un contact initialement collant peut maintenant devenir glissant au cours du calcul.
Les changements de contact sont basés sur des critères simples :

- *Décohésion: si $\sigma_n \geq \sigma_n^c > 0$, transition d'un contact bilatéral à un contact unilatéral.*

- *Glissement : si $\tau \geq \tau_s^c > 0$, transition d'un contact collant à un glissant.*

Un couplage a également été réalisé pour prendre en compte l'influence croisée du comportement tangentiel et normal.

Une autre modification majeure a été développée dans Forge2® pour simuler la fissuration d'un corps fin sur toute son épaisseur. Le critère d'apparition d'une fissure implémenté est basé sur une contrainte critique : la fissure s'initie quand $\sigma_{tension} \geq \sigma_{crit}$.

Toutes ces modifications permettent maintenant de simuler les différentes étapes de l'endommagement de la calamine telles que sa décohésion, son glissement sur son substrat en acier et l'apparition de fissures transverses.

I. INTRODUCTION

The interest of numerical simulation is nowadays fully recognized. In industry, it becomes more and more useful to improve products, decrease time-to-market, for preliminary or feasibility studies, for tool dimensioning… Finally, most metal forming industries use it mainly for economical reasons.

The FEM software used and developed in our study is Forge2®. This 2D finite element code developed jointly by CEMEF and TRANSVALOR S.A since the late 80's, specializes in the numerical simulation of metal forming processes and large deformation. The materials behavior can be elastic, elastoplastic, viscoplastic or elastic-viscoplastic… An automatic remesher is available to prevent element distortion during large deformation. Plane strain and axi-symmetrical configurations are allowed. The mesh is based on three-node triangular elements.
Recently a specific version of the software was developed to model multi-layered materials. Such systems are used increasingly in industry (automobile, aeronautical, aerospace…) to improve aesthetic, chemical, thermal and mechanical properties.

In this chapter, the Forge2® software is described through the equations of Mechanics and their numerical solution. The contact management is then particularly detailed. Specific developments implemented in order to simulate the oxide scale damage under hot rolling conditions (crack initiation, interfacial decohesion or sliding) are also described, with several examples showing their efficiency.

II. The Equations of Mechanics

It is important to summarize the mechanical expression of a forming process, with its basic equations.

II.1. <u>Mechanical formulation</u>

The hot metal is assimilated to a continuous domain. During forging, its flow is modeled from the fundamental principles of **continuum mechanics**. Thus the material verifies:
- the mass conservation
- the conservation of momentum

Mathematically, these principles are written:

- equation of continuity $\qquad \dfrac{\partial \rho}{\partial t} + div(\rho v) = 0$ **eq. III-1**

- equation of mechanical equilibrium $\qquad \rho \dfrac{\partial v}{\partial t} - div\sigma = 0$ **eq. III-2**

where t represents the time, v the velocity of a material particle, σ the stress tensor and ρ the density.

In the case of hot metal forming, it is usual to consider the following assumptions:

- the material is supposed to be completely viscoplastic: the elastic deformation is neglected with respect to the plastic deformation

- plasticity is incompressible
- the gravity and inertia forces are neglected with respect to the viscous forces.

In this restrictive framework, the conservation laws simplify :

$$\begin{cases} div\sigma = 0 \\ divv = 0 \end{cases}$$

<div style="text-align:right">**eq. III-2**</div>

Notations used in the following to define spaces and boundaries are schematically represented on Figure III-1.
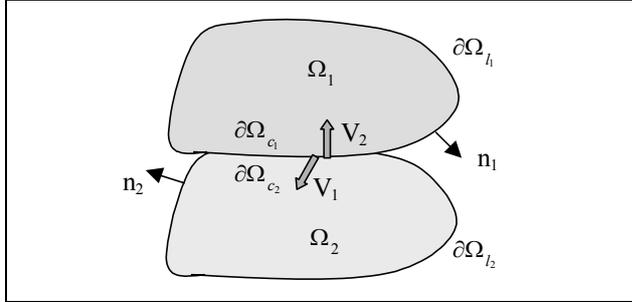
Figure III-1: Notations.

Notations.

II.2. Constitutive modelling

Here, a more general Elastic-viscoplastic law is used (Figure III-2).

0 to A: reversible linear elastic behaviour

$$\sigma = E\varepsilon$$

<div style="text-align:right">**eq. III-3**</div>

A to C: viscoplastic behavior (non-linear and irreversible) :

$$\sigma = K\bar{\varepsilon}^{n}\dot{\bar{\varepsilon}}^{m}$$
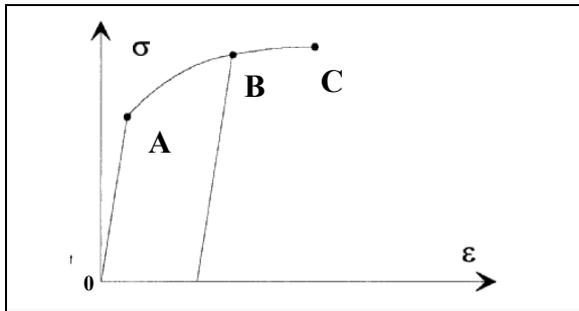
<div style="text-align:right">**eq. III-4**</div>

Figure III-2: Elasto-viscoplastic behavior.

Comportement élasto-viscoplastique..

This experimental behavior is expressed in a tensorial form, using the Prandtl-Reuss constitutive equations, as implemented in Forge2®:

$$\begin{cases} \dot{\varepsilon} = \dot{\varepsilon}^{el} + \dot{\varepsilon}^{vp} \\[2mm] \dot{\varepsilon}^{el} = D^{el^{-1}}\dot{\sigma} \\[2mm] \dot{\varepsilon}^{vp} = \dfrac{\sqrt{3}}{2}\dfrac{s}{\bar{\sigma}}\left\{\dfrac{\left\langle \bar{\sigma} - \sqrt{3}K_s\left(T,\bar{\varepsilon}\right)\right\rangle}{\sqrt{3}K(T)\left(\varepsilon_0 + \bar{\varepsilon}\right)^n}\right\}^{1/m} \qquad \left\langle x \right\rangle = x \ if \ x \geq 0; \ else \ \left\langle x \right\rangle = 0 \\[3mm] f\left(\sigma,\bar{\varepsilon},\dot{\bar{\varepsilon}},T\right) = \bar{\sigma} - \left\{\sqrt{3}.K_s\left(T,\bar{\varepsilon}\right) + \sqrt{3}.K(T)\left(\varepsilon_0 + \bar{\varepsilon}\right)^n\left(\sqrt{3}\dot{\bar{\varepsilon}}\right)^m\right\} = 0 \end{cases}$$

<div style="text-align:right">**eq. III-5**</div>

where $\dot{\varepsilon}$ is the strain rate tensor decomposed into its elastic and viscoplastic components respectively $\dot{\varepsilon}^{el}$ and $\dot{\varepsilon}^{vp}$. $f(\sigma, \overline{\varepsilon}, \dot{\overline{\varepsilon}}, T)$ is the Von Mises plasticity criterion, $\overline{\sigma}$ the equivalent Von Mises stress, s the deviatoric part of the stress tensor and $\overline{\varepsilon}$ the equivalent plastic strain in the sense of Von Mises. $K(T)$ is the material consistency, $K_s(T, \varepsilon)$ represents its elasticity threshold, m its strain rate sensitivity coefficient and n its strain hardening coefficient. To avoid infinite derivatives at $\overline{\varepsilon} = 0$, a regularization parameter ε_0 is added.

D^{el} is the elasticity matrix (4th order tensor), defined by Hooke's law for isotropic materials :

$$D_{ijkl}^{el} = 2\mu\delta_{ik}\delta_{jl} + \lambda\delta_{kl}\delta_{ij} \quad \text{with} \quad \begin{cases} \mu = \dfrac{E}{2.(1+\nu)} \\ \lambda = \dfrac{E.\nu}{(1+\nu).(1-2\nu)} \end{cases}$$

eq. III-6

μ and λ are the Lamé coefficients, E the Young's modulus and ν the Poisson coefficient. The equivalent stress is defined by:

$$\overline{\sigma} = \sqrt{\frac{3}{2} s : s}$$

eq. III-7

where s is the deviatoric stress: $s = \sigma - \dfrac{1}{3} Trace(\sigma)I = \sigma + pI$

and the equivalent strain rate is: $\dot{\overline{\varepsilon}} = \sqrt{\dfrac{2}{3} \dot{\varepsilon}^{vp} : \dot{\varepsilon}^{vp}}$

with p the hydrostatic pressure and I the identity tensor.

<u>Particular case:</u>   For elastic-viscoplastic law without a threshold: $K_s=0$

If large rotations occur in a process, the small strain formulation, derived from the material derivative of the stress tensor, is no longer appropriate because it violates the mechanical principle of objectivity. A new form of the stress tensor differentiation must be introduced to satisfy objectivity; for isotropic solid materials, the Jaumann derivative is the most often used [Chen]. It is defined by the formula:

$$\frac{d_j\sigma}{dt} = \frac{d\sigma}{dt} + \omega\sigma - \sigma\omega$$

eq. III-8

where the material derivative of the stress tensor is used in the right-hand side of the above equation, and ω is the rate of rotation skew-symmetrical tensor, the components of which are:

$$\omega_{ij} = \frac{1}{2}\left(\frac{\partial v_i}{\partial x_j} - \frac{\partial v_j}{\partial x_i}\right)$$

II.3. <u>Boundary conditions</u>

Contact and friction management implies two different items: enforcement of the non-penetration condition (normal direction) and friction law (tangential condition).

II.3.1. In the normal direction of an interface between two bodies

The non-penetration condition writes:

$$(V_2 - V_1).n_1 \geq 0 \qquad \text{on } \partial\Omega_c$$

<div align="right">**eq. III-9**</div>

where **n** is the normal to the surface (outward from body 1. See Figure III-1), V_1 and V_2 the velocity vectors of the coinciding points of body 1 and 2, respectively. **Bilateral contact** means that once in contact, bodies 1 and 2 cannot be separated anymore, so that (Figure III-3):

$$(V_2 - V_1).n_1 = 0 \qquad \text{on } \partial\Omega_c \qquad\qquad \text{for bilateral contact}$$

<div align="right">**eq. III-10**</div>

On the contrary, **unilateral contact** means that separation may occur if and only if the normal stress $\sigma_n = (\sigma.\mathbf{n}).\mathbf{n} = 0$ (σ is Cauchy stress tensor), which is written as Signorini's inequation condition :

$$(V_2 - V_1).n_1 \geq 0, \quad \sigma_n \leq 0, \quad [(V_2 - V_1).n_1]\sigma_n = 0 \qquad\qquad \text{on } \partial\Omega_c$$

<div align="right">**eq. III-11**</div>
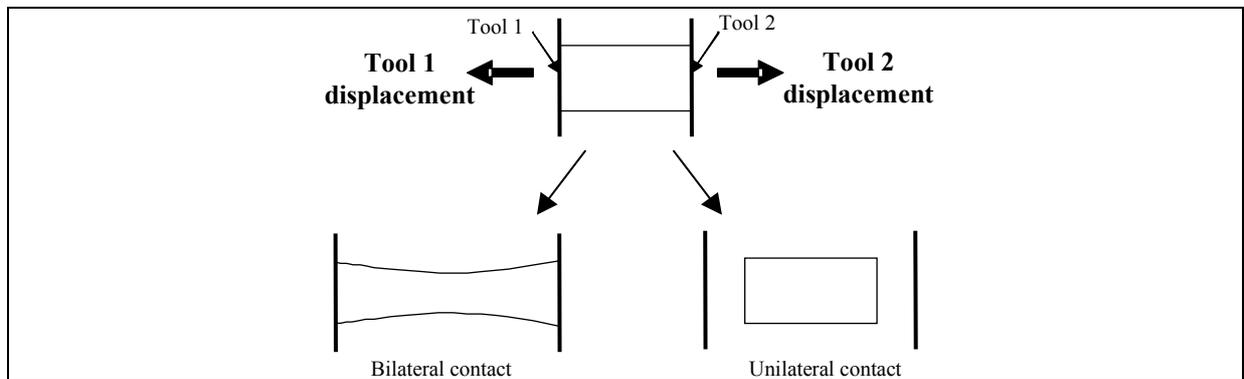
Figure III-3: Unilateral and bilateral contact.

Contact unilatéral et bilatéral.

The free surface condition writes:

$$\sigma.n = 0 \qquad \text{on } \partial\Omega_l$$

<div align="right">**eq. III-12**</div>

II.3.2. In the tangential direction

In the tangential direction, friction is a threshold phenomenon, so that :

$$\begin{cases} \tau = (\sigma.n).t \le \tau_c(a_i) & \Rightarrow & (V_2 - V_1).t = 0 & (stick) \\ \tau = (\sigma.n).t = \tau_c(a_i) & \Rightarrow & (V_2 - V_1).t \ne 0 & (slip) \\ \tau = (\sigma.n).t > \tau_c(a_i) & & impossible \end{cases}$$

or $\tau - \tau_c(a_i) \le 0, \quad [\tau - \tau_c(a_i)][(V_2 - V_1).t] = 0$ on $\partial\Omega_c$ **eq. III-13**

τ_c is the critical friction stress (sliding criterion) depending on external (σ_n, V_2-V_1, Temperature) and internal (sliding length, roughness, lubrication…) variables a_i. For instance for Coulomb friction, $\tau_c = \mu. \sigma_n$ (μ is the Coulomb friction coefficient).

Alternatively, contact may be considered as blocked in the tangential direction ("sticking contact"), in which case $(V_2$-$V_1).t = 0$ is imposed whatever the values of a_i.

II.3.3. Standard implementation

In the standard implementation of Forge2®, two features are of prime importance. First, the inequalities and threshold conditions in Signorini and free surface equations are relaxed and treated by a penalty technique and a regularisation method respectively:

If penetration occurs so that a point of body 2 gets inside body 1 by a distance *d*, a repulsive force is generated:

$$F_p = -K_p. < d - d_0 >^+$$

eq. III-14

d_0 is a tolerance factor, and $<x>^+$ means that the force is generated only if x>0. K_p must be large enough not to let penetration drift too far from *d=0*. As all bodies are deformable, a "master / slave" strategy is enforced to avoid spurious oscillations (Figure III-4) [Pich,Four].
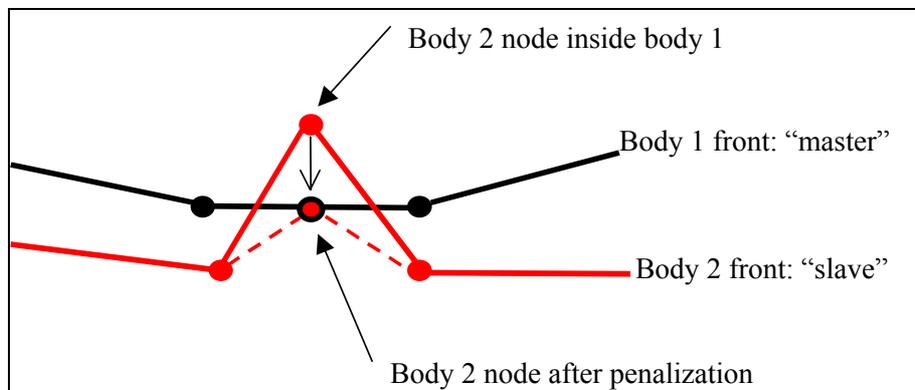
Figure III-4: Illustration of the master-slave version.

Illustration de la version maître-esclave.

Similarly for friction, a velocity regularization is used :

$$\tau = \tau_c(a_i).F\big[(V_2 - V_1).t\big]$$

<div align="right">**eq. III-15**</div>

where F is a continuous and differentiable function such that $F(0) = 0$, $F'(0) \neq \infty$ and $F \to 1$ as $\big[(V_2 - V_1).t\big] \to \infty$ – and in fact reaches this asymptote quickly enough. For instance

$$F(x) = x/\sqrt{K_r^2 + x^2}$$

<div align="right">**eq. III-16b**</div>

where K_r is a small regularisation parameter.

Avoiding non-differentiability in $(V_2-V_1).t = 0$ eliminates infinite terms in the stiffness matrix. The stick-slip transition does not exist any more strictly speaking, although an adequate choice of K_r preserves it in practical terms.

Secondly, unilateral and bilateral contact options are available; similarly, sliding or sticking contact options exist. The two notions can be crossed, i.e. four cases are available: bilateral sliding (relative displacement in the tangential direction only), bilateral sticking (no relative displacement at all), unilateral sliding, unilateral sticking (only normal separation is possible).

Finally, contact and friction conditions, once chosen, are valid for a whole interface between two bodies and all along the simulation: if "sticking bilateral contact" is selected for the interface between bodies i and j, no point of i on the i/j interface will be allowed to slide along j, nor will it be allowed to move away from the interface.

II.4. __Strong formulation of the mechanical problem__

On a domain Ω, taking into account equations of conservation, boundary conditions and the material flow, we obtain the strong formulation equation system of the mechanical problem.

$$\begin{cases} div\,\sigma = 0 & on\ \partial\Omega \\[2mm] div\,v = -\dfrac{\dot{p}}{K} & on\ \partial\Omega \\[2mm] \sigma.n = 0 & on\ \partial\Omega_l \\[2mm] (V_2 - V_1).n_1 \geq 0 & on\ \partial\Omega_c \\[2mm] \tau - \tau_c(a_i) \leq 0,\ \big[\tau - \tau_c(a_i)\big]\big[(V_2 - V_1).t\big] = 0 & on\ \partial\Omega_c \end{cases}$$

<div align="right">**eq. III-16**</div>

($K = (3\lambda+2\mu\ /\ 3)$). Then, we realize a temporal discretization using an explicit Euler scheme. This leads, at each increment, to the resolution of a non-linear stationary problem by the Finite Element Method.

III. Variational formulation

III.1. Continuous form of the weak formulation

The material domain is Ω. Let $L^2(\Omega)$ be the Lebesgue space of square-integrable functions, associated to the scalar product $(.,.)$ and to the norm $\|.\|_0$.

The velocity pressure formulation consists in looking for a solution (v,p) in $\vartheta \times P$ with:
$$\vartheta = \left\{ v \in \left[H^1(\Omega)\right]^2 \mid (V_2 - V_1).n_1 \geq 0 \quad on \ \partial\Omega_c \right\}$$
$$P = L^2(\Omega)$$

H^1 is the Hilbert space: $H^1(\Omega) = \left\{ v \in L^2(\Omega); \dfrac{\partial v}{\partial x_i} \in L^2(\Omega) \quad \forall i = 1,2 \right\}$

The weak formulation is obtained from conservation laws and boundary conditions equations, using the virtual work principles:

$$\int_\Omega \sigma : \dot{\varepsilon}^* + \int_\Omega \rho g v^* - \int_{\partial\Omega_c} T.v^* = 0 \qquad \forall v^* \ a \ test \ function \in \vartheta \qquad \textbf{eq. III-17}$$

with $\dot{\varepsilon}_{ij}^* = \dfrac{1}{2}\left(\dfrac{\partial v_i^*}{\partial x_j} + \dfrac{\partial v_j^*}{\partial x_i} \right)$, $T_i = \sigma_{ij} n_j$, n_j being the normal surface.

The Cauchy stress tensor σ can be decomposed into its deviatoric and spherical parts:
$$\sigma = -p\mathrm{I} + s \qquad \textbf{eq. III-18}$$
with $Tr[\sigma] = -3p$

The final, mixed variational formulation follows :

$$\begin{cases} \int_\Omega s : \dot{\varepsilon}^* - \int_\Omega p\,div(v^*) - \int_{\partial\Omega_c} T.v^* + \int_\Omega \rho g v^* = 0 \\ \int_\Omega p^*\left(div(v) - \dfrac{\dot{p}}{K} \right) = 0 \end{cases} \qquad \forall v^* \in \vartheta, \ \forall p^* \in P \qquad \textbf{eq. III-19}$$

with the boundary conditions including contact.

v and p are the unknowns of the problem and $K = \dfrac{E}{3(1 - 2\mu)}$ is the bulk elastic modulus.

III.2. Finite element spatial discretization

Let two vector spaces ϑ_h and P_h be created to approach ϑ and P. These spaces define polynomial functions of $d° \leq 1$ by parts.

$\vartheta_h \subset \vartheta,\ P_h \subset P / \lim\limits_{h \to 0} \vartheta_h = \vartheta$ and $\lim\limits_{h \to 0} P_h = P$

The problem consists in finding (v_h, p_h) belonging to $\vartheta_h \times P_h$ such as, $\forall v^* \in \vartheta,\ \forall p^* \in P$:

$$\begin{cases} a(v_h, v^*) + b(p_h, v^*) = \langle f, v^* \rangle \\ \int_\Omega p^* \left(div(v_h) - \dot{P}_h \big/ K \right) = 0 \end{cases} \qquad \text{with} \qquad \begin{cases} a(v_h, v^*) = \int_\Omega s : \dot{\varepsilon}^* + \int_\Omega \rho g.v^* \\ b(p_h, v^*) = -\int_\Omega p_h div(v^*) \\ \langle f, v^* \rangle = \int_{\partial \Omega_c} Tv^* \end{cases} \qquad \textbf{eq. III-20}$$

Thereafter one will note v and p the discretized unknowns instead of v_h and p_h for the sake of legibility. The finite element discretization is based on the triangular mini-element, the unknowns of which are the pressure and the components of velocity at nodes.

Figure III-5: P1$^+$/P1 triangular element.

Figure III-5 : Elément triangulaire P1$^{+/}$P1.
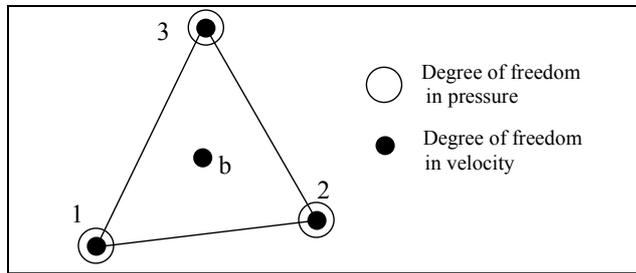
The discretization of the geometry is performed using (P1$^+$/P1) three-node triangular elements in 2D, which means that the velocity and the pressure are interpolated linearly (Figure III-5).

The "+" exponent means the use of an additional degree of freedom at the center of the element for velocity interpolation. Element P1$^+$/P1 can thus satisfy the **Brezzi-Babuska relation** [Arno] between interpolation spaces of velocity and pressure. The interpolation function of the additional velocity degree of freedom is equal to 1 at the element center and 0 on its border.

The spatial discretization of the velocity field v and pressure p can be expressed:

$$v(x) = \sum_{k=1}^{Nbnoe} N_k^l(x) V_k + \sum_{j=1}^{Nbelt} N_j^b(x) B_j$$

$$p(x) = \sum_{k=1}^{Nbnoe} N_k^l(x) P_k$$

$\textbf{eq. III-21}$

N_k^l is the linear interpolation function associated to node k and N_j^b that of bubble element j. B_j is the bubble function associated to the element j. *Nbnoe* and *Nbelt* are respectively the numbers of nodes and elements of the whole mesh.

III.3. Temporal discretization

- **Incremental formulation**

This incremental formulation is only necessary in the case of an evolution problem (if not, only one increment is sufficient to solve the system). We use an updatedv Lagrangian formulation with a forward Euler temporal integration scheme. $\Omega(t=0)$ is a system at an initial instant which undergoes a deformation $\Omega(t)$ (Figure III-6):
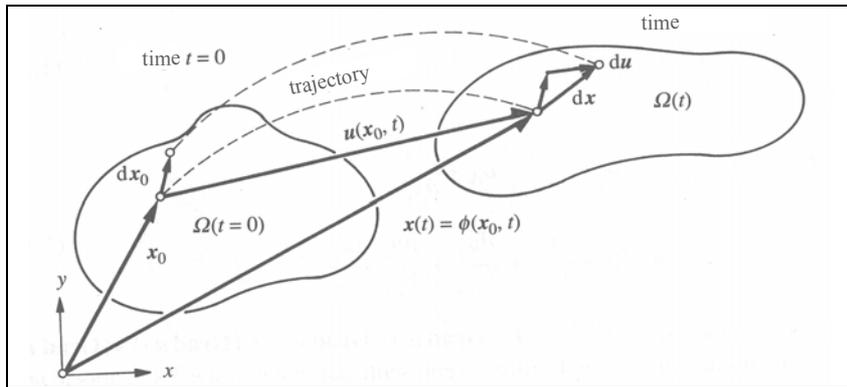
Figure III-6: Updated Lagrangian small time steps.

Petits pas de temps : Lagrangien actualisé.

At time $t+\Delta t$, one seeks $v^{t+\Delta t}$ and $p^{t+\Delta t}$ such as:

$$v^{t+\Delta t}=v^t +\Delta v^t$$
$$p^{t+\Delta t}=p^t+\Delta p^t$$

At each increment of time, the velocity-pressure system is expressed as:

$$\begin{cases} \int_{\Omega^t} s^{t+\Delta t} : \dot{\varepsilon}* - \int_{\Omega^t} p^{t+\Delta t} div(v*) - \int_{\partial\Omega^t_c} T^{t+\Delta t}.v* + \int_{\Omega^t} \rho g v* = 0 \\ \int_{\Omega^t} p*\left(div(v^{t+\Delta t}) - \frac{p^{t+\Delta t}}{K} \right) = 0 \end{cases} \qquad \forall v* \in \vartheta, \ \forall p* \in P \qquad \textbf{eq. III-22}$$

The integration on Ω^t is an approximation of $\Omega^{t+\Delta t}$ to avoid non-symmetric terms in the matrix.

- **Incremental resolution of the mixed problem**

The system obtained is non-linear. It is solved in an iterative way by the Newton-Raphson algorithm:

1) At the increment $t+\Delta t$, one initializes $(v_0^{t+\Delta t}, p_0^{t+\Delta t}) = (v^t, p^t)$ (for the sake of clarity, we will not specify the increment: $(v_0^{t+\Delta t}, p_0^{t+\Delta t})=(v_0, p_0)$)

2) (v_k, p_k) is supposed to be known. One seeks (v_{k+1}, p_{k+1})

3) Let $v_{k+1} = v_k + \delta v_k$ and $p_{k+1} = p_k + \delta p_k$

4) velocity and pressure residuals Rv and Rp can be written at iteration k:

$$R_v(v_k, p_k) = \int_\Omega s_k : \dot{\varepsilon}^* - \int_\Omega p_k div(v^*) - \int_{\partial\Omega_c} T_k.v^* + \int_\Omega \rho g v^*$$

$$R_p(v_k) = \int_\Omega p^* \left(div(v_k) - \frac{p_k}{K} \right)$$

eq. III-23

At iteration k+1, we can write:

$$\begin{cases} R_v(v_{k+1}, p_{k+1}) = R_v(v_k, p_k) + \dfrac{\partial R_v}{\partial v}(v_k, p_k)\delta v_k + \dfrac{\partial R_v}{\partial p}(v_k, p_k)\delta p_k + O((\delta v_k)^2, (\delta p_k)^2) \\[2em] R_p(v_{k+1}) = R_p(v_k) + \dfrac{\partial R_p}{\partial v}(v_k)\delta v_k + O((\delta v_k)^2) + \dfrac{\partial R_p}{\partial p}(v_k)\delta p_k + O((\delta p_k)^2) \end{cases}$$

eq. III-24

Imposing:

$$\begin{cases} R_v(v_{k+1}, p_{k+1}) = 0 \\ R_p(v_{k+1}, p_{k+1}) = 0 \end{cases}$$

The velocity / pressure Newton-Raphson correction is obtained by solving the system:

$$\begin{pmatrix} \delta v_k \\ \delta p_k \end{pmatrix} = - \left(\begin{pmatrix} \dfrac{\partial R_v}{\partial v} & \dfrac{\partial R_v}{\partial p} \\[1em] \dfrac{\partial R_p}{\partial v} & \dfrac{\partial R_p}{\partial p} \end{pmatrix}(v_k, p_k) \right)^{-1} \begin{pmatrix} R_v(v_k, p_k) \\ R_p(v_k) \end{pmatrix}$$

eq. III-25

IV. GENERALISATION OF CONTACT MANAGEMENT IN FORGE2®

IV.1. <u>Our objective</u>

In our study, the objective is to take into account the interface damage like sliding or decohesion in Forge2®. In a first part, we will describe how it is possible to obtain the interface failure via the modification of existent laws, the occurrence of decohesion and finally, both phenomena simultaneously.

A priori, an adherent scale is represented by a bilateral (impossible separation) and sticking (impossible slipping) contact. The possibility of separation means that we must define a criterion to switch from bilateral to unilateral contact (the latter being the standard of Forge2®). Moreover, the layer must be able to slip along the interface. It is thus necessary to define a simple criterion for the transition between sticking and sliding friction, both options being available in the software.

The criteria can be formulated simply:

- Slipping: if $\tau \geq \tau_s^c > 0$,   transition from sticking to sliding contact.
- Decohesion: if $\sigma_n \geq \sigma_n^c > 0$,   transition from bilateral to unilateral contact.

IV.2. **A CZM approach**

The extensions made in Forge2® are quite similar to Cohesive Zone Models (CZM). CZM are used in fracture Mechanics to model crack propagation on the basis of a traction-separation law at the crack tip. This technique is almost systematically used in numerical simulation of coating delamination [Abdu,Chan] (Figure III-7).
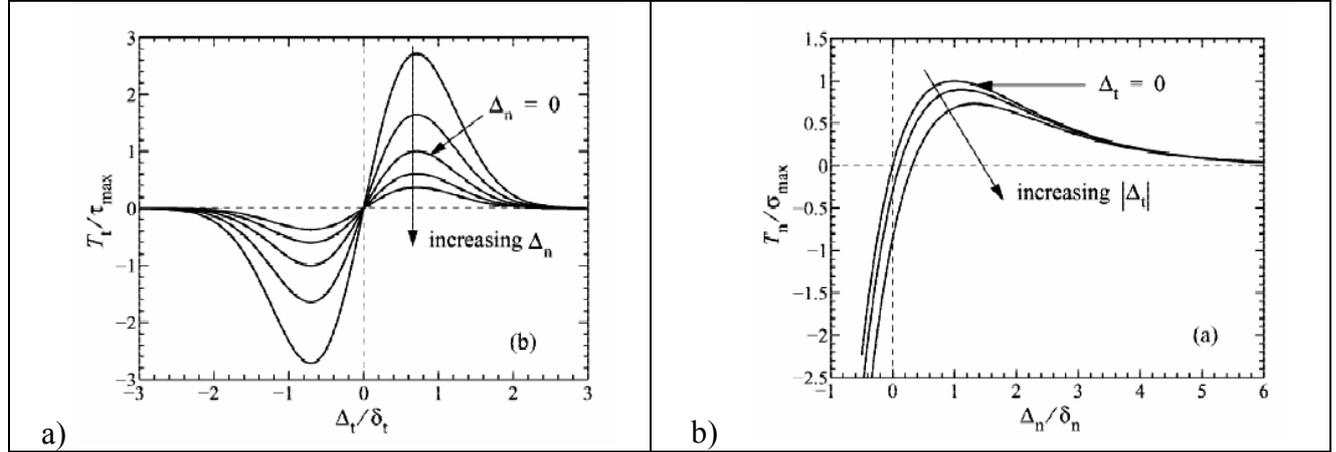
Figure III-7: illustration of the normal (a) and tangential (b) stress – displacement relations. (a,b): CZM-like model of [Abdu]: damage by sliding in the tangential direction decreases adhesion in the normal direction, and vice-versa.

Illustration des relations contraintes normale (a) et tangentielle (b) – déplacement. (a,b) modèle CZM [Abdu].
(b) : l'endommagement par glissement tangentiel diminue l'adhésion dans la direction normale, et vice-versa.

In order to make our model more realistic, a coupling between normal and shear strength relations has been carried out. Some authors like Abdul-Baqi and Chandra [Abdu,Chan] did it within a CZM approach.

In the description of the interface as a cohesive surface, a small displacement jump Δ is allowed between the film and the substrate, with normal and tangential components Δ_n and Δ_t respectively. The interfacial behavior is specified in terms of a constitutive equation for the corresponding traction components T_n and T_t at the same location.

As the bulk constitutive law adopted by these authors is reversible elastic, the only energy dissipation comes from the normal and tangential separation law. This dissipative interfacial behaviour derives from a potential Φ which reflects the physics of the bimaterial. Φ is given by Needleman [Need] as a combination of frictional (tangential) and adhesive (normal) terms:

$$\Phi = \Phi_n + \Phi_n \exp\left(\frac{\Delta_n}{\delta_n}\right)\left\{\left(1 - r + \frac{\Delta_n}{\delta_n}\right)\frac{1-q}{r-1} - \left[q + \left(\frac{r-q}{r-1}\right)\frac{\Delta_n}{\delta_n}\right]\exp\left(-\frac{\Delta_t^2}{\delta_t^2}\right)\right\} \qquad \textbf{eq. III-26}$$

with $q = \dfrac{\Phi_t}{\Phi_n}$; $r = \dfrac{\Delta_n^*}{\delta_n}$. Φ_n and Φ_t represent the works of normal and shear separations respectively; Δ_n and Δ_t are normal and tangential displacement jumps respectively; δ_n and δ_t are characteristic lengths of the interface ; Δ_n^* is the value of Δ_n after complete shear separation, i.e. when normal traction becomes zero : $T_n = 0$.

T_n and T_t are determined by: $T_\alpha = \dfrac{\partial \Phi}{\partial \Delta_\alpha}$ $(\alpha = t,n)$, giving:

$$T_n = -\frac{\Phi_n}{\delta_n}\exp\left(-\frac{\Delta_n}{\delta_n}\right)\left\{\frac{\Delta_n}{\delta_n}\exp\left(-\frac{\Delta_t^2}{\delta_t^2}\right) + \frac{1-q}{r-1}\left[1-\exp\left(-\frac{\Delta_t^2}{\delta_t^2}\right)\right]\left[r-\frac{\Delta_n}{\delta_n}\right]\right\}$$

$$T_t = 2\frac{\Phi_n}{\delta_n}\left(\frac{\delta_n}{\delta_t}\right)\frac{\Delta_t}{\delta_t}\left\{q+\left(\frac{r-q}{r-1}\right)\frac{\Delta_n}{\delta_n}\right\}\exp\left(-\frac{\Delta_n}{\delta_n}\right)\exp\left(-\frac{\Delta_t^2}{\delta_t^2}\right)$$

eq. III-27

Maximums of normal and tangential stresses are reached respectively at a separation of $\Delta_n = \delta_n$ and $\Delta_t = \dfrac{\delta_t}{\sqrt{2}}$ (Figure III-8). From this, the works of normal and tangential separations are related to σ_{max} and τ_{max} , respectively by:

$$\Phi_n(\Delta_n = \delta_n, \Delta_t = 0) = e.\sigma_{max}.\delta_n$$

$$\Phi_t\left(\Delta_n = 0, \Delta_t = \delta_t\middle/\sqrt{2}\right) = \sqrt{\left(\frac{e}{2}\right)}.\tau_{max}.\delta_t$$
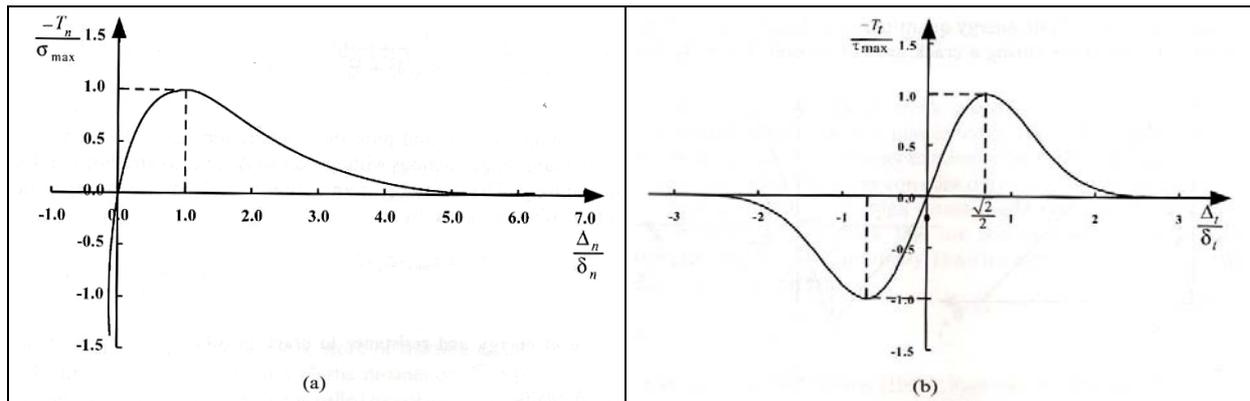
Figure III-8: a) Variations of normal traction, T_n, with Δ_n for Δ_t =0   b) Variations of shear traction, T_t, with Δ_t for Δ_n =0.

a) Variations de la traction normale (T_n) avec Δ_n pour Δ_t =0   b) Variation du cisaillement (T_t) avec Δ_t pour Δ_n =0.

Using these two equations together with the relation $q = \dfrac{\Phi_t}{\Phi_n}$, the uncoupled normal and shear strengths can be related through:

$$\boxed{\sigma_{max} = \frac{1}{q\sqrt{2e}}\frac{\delta_t}{\delta_n}\tau_{max}}$$

eq. III-28

IV.3. Extension of contact management in Forge2®

At the beginning of each simulation, bilateral sticking contact is selected (the oxide scale is adherent). A transition has been introduced, for each node individually.

IV.3.1. Tangential direction

Sticking and sliding friction are based on a tangential critical stress τ_{crit}. Sticking contact (regularized by a large elastic spring constant) breaks down at $\tau = \tau_{crit}$, bringing about a fall of the tangential stress to the level given by the friction law, which is itself regularized (hence $(V_2\text{-}V_1).t = 0 \Leftrightarrow \tau = 0$); if separation has occurred ($\delta_n > 0$), friction disappears of course ($\tau = 0$).

There are 3 friction laws in Forge2®: Coulomb, "viscoplastic" and "Tresca" laws. Two parameters are required to express these laws:
− a critical shear stress τ_c at which sliding with friction occurs;
− a sliding relative velocity v_g, the tangential part of the relative velocity of the two bodies in contact.

- Coulomb's law:

$$\tau_c = \mu\sigma_n \qquad \qquad \text{eq. III-29}$$

with σ_n the normal stress to the interface and μ the Coulomb friction coefficient.

$$\begin{cases} \|\tau\| < \tau_c \Rightarrow V_g = 0 \\ \|\tau\| = \tau_c \Rightarrow \exists \lambda \geq 0, \qquad V_g = -\lambda\dfrac{\vec{\tau}}{\|\vec{\tau}\|} \\ \|\tau\| > \tau_c \qquad \qquad prohibited \end{cases} \qquad \text{eq. III-30}$$
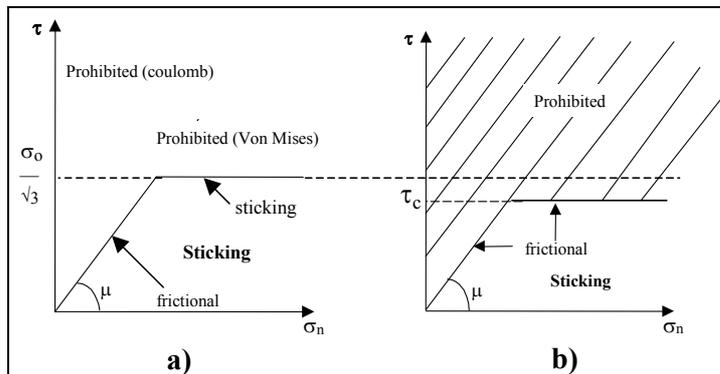
Figure III-9: Representation of Coulomb's law with von Mises plasticity limit :

Représentation de la loi de Coulomb avec la limite de plasticité de von Mises :

a) $\tau_c = \mu\sigma_n$ **and** $\tau < \sigma_0 / \sqrt{3}$

b) $\tau_c = Min\ (\mu\sigma_n; \sigma_0 / \sqrt{3})$

If one of the bodies in contact is plastic incompressible, its plasticity criterion limits the shear critical stress. For a von Mises body, we have $\tau_c \leq \dfrac{\sigma_0}{\sqrt{3}}$ (Figure III-9).

- Norton's law (or viscoplastic law) :

It is a law without a threshold ($\tau_c = 0$).

$$\tau = \alpha \frac{\sigma_0}{\sqrt{3}} \left(\frac{\|V_g\|}{\|V_{ref}\|} \right)^{pf}$$

eq. III-31

with α the Norton friction coefficient, *pf* the velocity-sensitivity and V_{ref} a reference velocity for adimensionalization.

- Tresca's law:
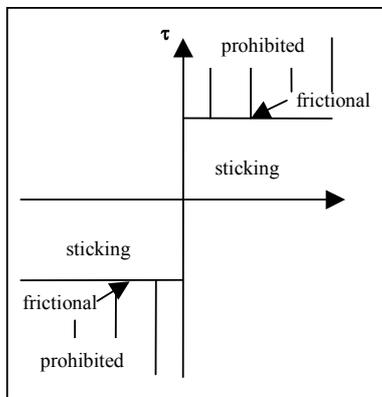
Figure III-10: Representation of Tresca's law with plastic relation: $\tau_c \leq \dfrac{\sigma_0}{\sqrt{3}}$

Représentation de la loi de Tresca avec la

relation plastique $\tau_c \leq \dfrac{\sigma_0}{\sqrt{3}}$

The yield criterion in shear $\tau_c \leq \dfrac{\sigma_0}{\sqrt{3}}$ can be expressed by (Figure III-10) :

$$\tau_c = \overline{m} \frac{\sigma_0}{\sqrt{3}} \qquad \text{with} \qquad 0 \leq \overline{m} \leq 1$$

eq. III-32

($\overline{m}$: Tresca's friction coefficient, or friction factor)

$$\tau < \tau_c \Rightarrow V_g = 0$$
$$\tau = \tau_c \Rightarrow \exists \lambda \geq 0, \qquad V_g = -\lambda \tau$$
$$\tau > \tau_c \quad prohibited$$

Underlined_Implementation

In our case, the friction factor has to be replaced by the viscosity factor η expressed in chapter II (paragraph III.4.2.4).

The first step consists in selecting each border sides of the piece mesh and to flag them with a value 0 or 1 ; 0 means sticking contact, 1 enforces sliding contact. Once the shear stress of the node in contact (calculated at each integration point) exceeds the critical value, the flag initially equal to 0 is set to 1.

Concerning friction, we only have to introduce the viscosity expression from the stress τ ($\tau = \eta.v_{rel}$). Indeed, τ intervenes in the multiplicative factors both in the **stiffness matrix** and the **residual vector**, and consequently on the velocity calculated at each node.

Figure III-11 compares a CZM model (a) with the present strategy (b) in terms of the $\tau(\delta_t)$ curves.
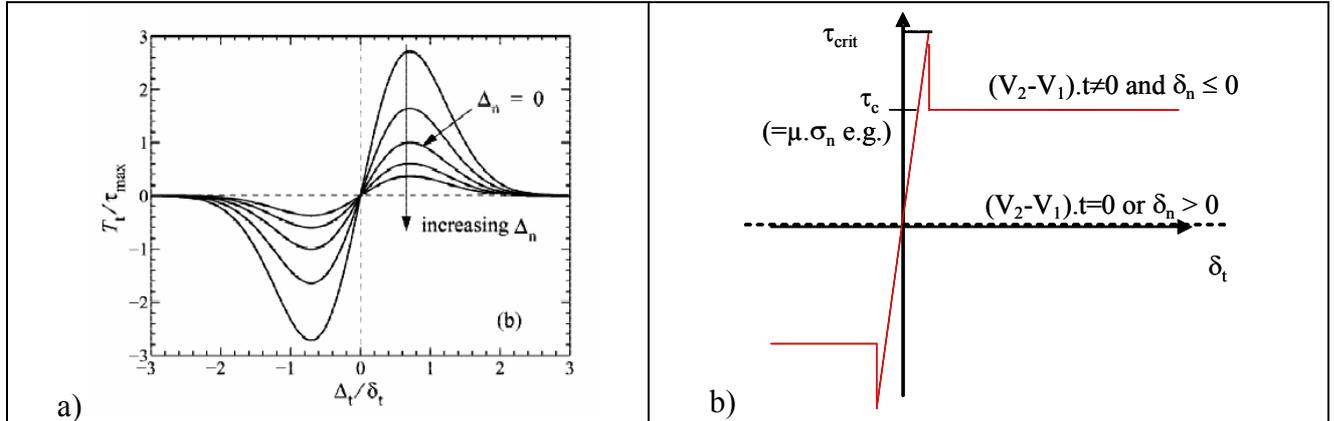
Figure III-11: Illustration of tangential stress – displacement relations. (a): CZM-like model of [Abdu]. (b) : present strategy, with contact penalty associated with stress-based transitions.

Illustration des relations contrainte tangentielle – déplacement. (a) modèle CZM [Abdu].
(b) : stratégie implémentée, le contact pénalisé étant associé à des transitions basées sur les contraintes.

IV.3.2. Normal direction

In the normal direction, the transition from bilateral to unilateral contact (based on a critical stress criterion σ_{adh}) is equivalent to unilateral contact with adhesion:

$$(V_2 - V_1).n \geq 0, \quad \sigma_n \leq \sigma_{adh}(a_i), \quad [(V_2 - V_1).n][\sigma_n - \sigma_{adh}] = 0 \qquad \text{eq. III-33}$$

The transition is reversible, i.e. if the contact is resumed later (with compressive stress), bilateral contact is imposed again until $\sigma_n > \sigma_{adh}$ once more. This supposes that diffusion is quick enough to rebuild adherence on a time scale much smaller than the time step.

Implementation

First, those interfaces where decohesion will be allowed are selected. Their nodes are flagged with the value 0 for those interfaces starting in bilateral contact, or 1 for unilateral contact. Later on, the flag for a given node is switched from 0 to 1 (i.e. from a bilateral to a unilateral contact ensuring decohesion) when the stress normal to the interface at that node exceeds the critical normal stress.

Figure III-12 compares CZM (a) with the present strategy (b) in terms of the $\sigma_n(\delta_n)$ curves.
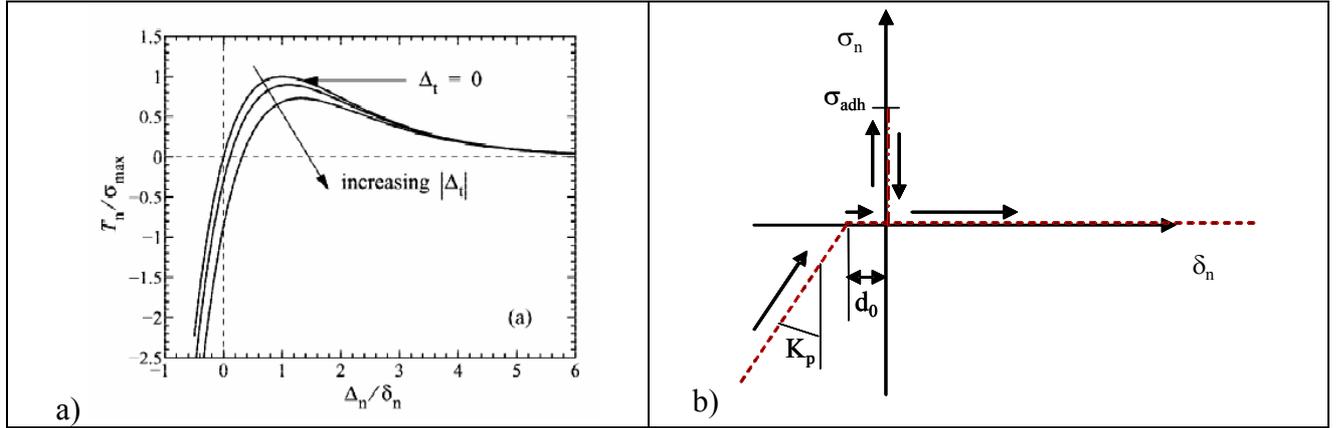
Figure III-12: illustration of the normal stress – displacement relations. (a): CZM-like model of [Abdu] (b) : present strategy, with contact penalty associated with stress-based transitions. In (b): standard contact penalty technique and the added bilateral to unilateral transition; arrows follow a typical separation process.

Illustration des relations contrainte normale – déplacement. (a) modèle CZM [Abdu]. (b) : stratégie implémentée, le contact pénalisé étant associé à des transitions basées sur les contraintes. Dans le cas (b) : Technique standard de pénalisation du contact additionnée à la transition bilatéral-unilatéral. Les flèches suivent le processus typique de séparation.

IV.3.3. Comparison between our extensions and the CZM model

Significant differences appear between [Abdu] and the present implementation:

- transitions are quite abrupt, whereas CZM are made precisely to smooth out discontinuities. This might result in a more difficult convergence; however, no major convergence problems have been observed yet in our tests.
- CZM models are characterized by a fracture energy; whereas Figure III-12b) shows no dissipation when the crack propagates; dissipation may occur later on if friction remains, i.e. if normal separation ($\delta_n > 0$) has not taken place.

IV.3.4. Coupling

Instead of the coupling expression seen in the bibliographic paragraph (IV-2), we prefer a less global relation between the two critical stresses. The normal critical stress and the level of friction are related, whenever the critical shear strength is exceeded, i.e. whenever sliding occurs. This is done on a node-by-node basis. The rationale is that interfacial sliding means that the interface weakens, which makes normal separation easier.

Thus, one needs a law which takes into account the progressive decrease of the normal critical stress the relative velocity between the two bodies is high, which should also mean that friction is low. We have therefore modified the critical stress using the relative velocity v_{rel}:

$$\boxed{\sigma_{nc} = \sigma_{nc0} - \alpha.v_{rel}}$$

eq. III-34

σ_{nc} is the normal critical stress evolving along the computation from its initial value σ_{nc0} (in sticking contact, i.e. when $v_{rel} = 0$); α is a constant depending on interface properties, with the constraint $0 \leq \alpha \leq \dfrac{\sigma_{nc0}}{v_{rel}}$ to avoid negative values of σ_{nc}. In the sticking case, $v_{rel} = 0$ throughout so that the normal critical stress does not evolve during calculation.

IV.4. Test examples

IV.4.1. Interfacial sliding

A simple tensile test simulation leads to a better view of the criterion. A plane specimen is cut in two parts in its middle and covered by a continuous thin oxide layer. Both parts of the substrate move apart with a constant velocity (Figure III-13).

The critical shear stress is 100 MPa and the friction factor is 0.3. At the beginning, the oxide layer is in sticking contact (no relative sliding), so that all the deformation is concentrated near its central "crack". Sliding initiates in the central area, which is exposed to the highest interface shearing, then propagates outwards along the interface. A stress concentration is visible at the meeting of the sliding and the sticking zones (marked with the green arrow). We have followed the history of node 223, located on the surface of the oxide scale.
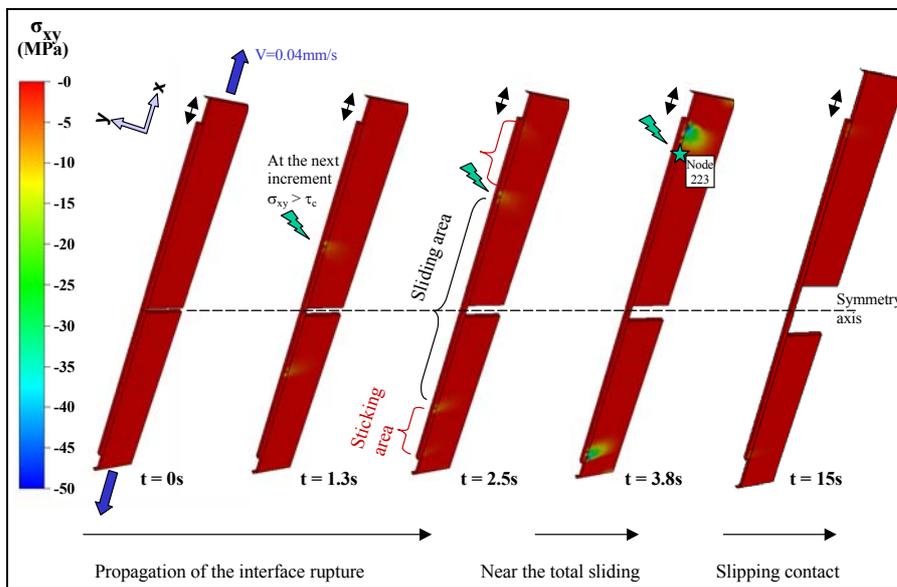
Figure III-13:

τ_c=100 MPa ; η=0.1

(3-d representation of a 2-d computation).

(représentation 3-d d'une simulation 2-d).

It is interesting to see on the two graphs below (Figure III-14 ; Figure III-15) the influence of the friction viscosity for a constant critical shear stress value (100 MPa). They represent the shear stress evolution and the displacement of the node 223 as a function of time.
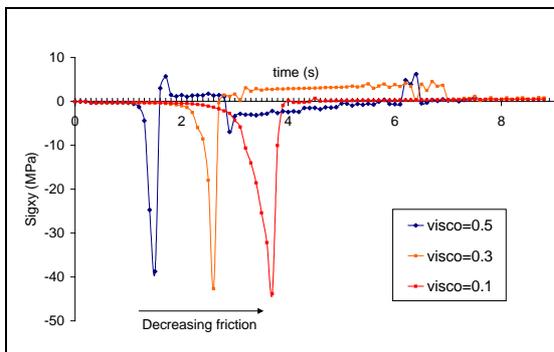
Figure III-14: Shear stress for node n°223.

Contrainte de cisaillement du nœud 223.
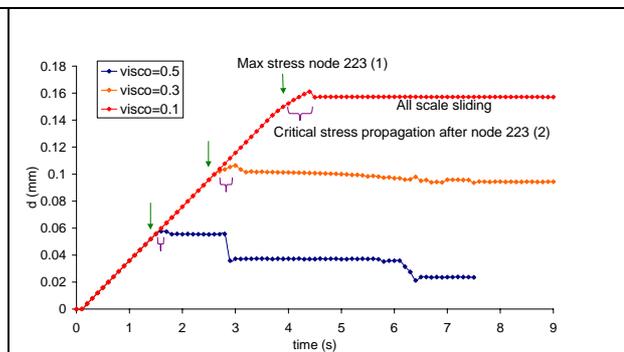
Figure III-15: Displacement of node n°223 along x-axis.

Déplacement du nœud n°223 le long de l'axe des abcisses.

As long as its neighbouring nodes are in a sticking contact, node 223 moves with the tool (i.e. the central part of the oxide layer elongates), without undergoing any shear stress. When nearby nodes are relaxed (after 3 sec of calculation if η = 0.1), the shear stress at node 223 increases ; after 3.8s, the shear stress of node 223 reaches the critical value : the stick / slip transition is reaching this point. But (Figure III-15) the node continues to follow the substrate because its external neighbours are still in sticking contact. Finally, when the stick / slip transition has reached the end of the oxide layer, all the scale slides on the substrate.
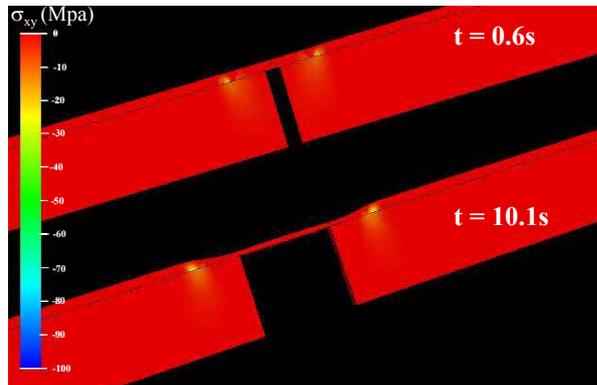
Figure III-16: shear stress field at two different time steps and for τ_c=150MPa and η=0.1

Contraintes de cisaillement à deux incréments de temps, pour τ_c=150MPa et η=0.1.

The higher the friction coefficient (η), the quicker the relaxation of the surface. But if the critical shear stress is higher, like in Figure III-16 (150Mpa), it is reached only in the middle. In this case, all the deformation is performed by thinning the central part of the oxide layer.

IV.4.2. Decohesion

Figure III-17 presents an example of cleavage. All contact types between bodies are different in order to test all the developments implemented. Some interfaces are in unilateral contact, allowing separation if the normal stresses is higher than the critical value ; other interfaces are in bilateral contact. Critical normal stresses are written on each interface.
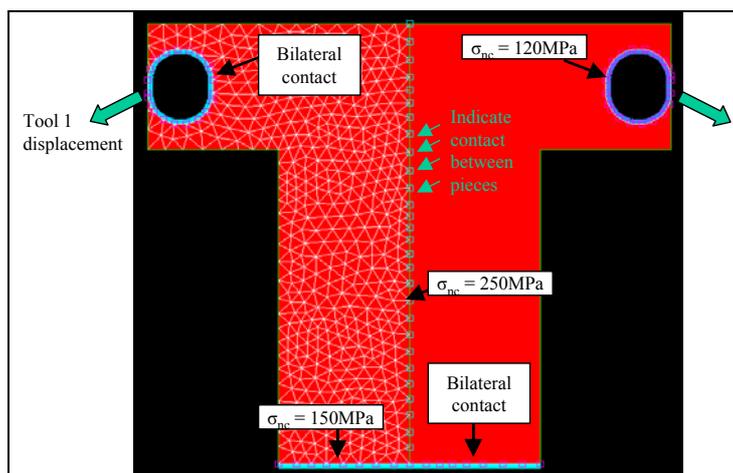
Figure III-17: Cleavage simulation with interface-dependent type of contact condition.

Simulation d'un cas de clivage avec différents types de contact entre chaque corps.

We can see on Figure III-18 that unilateral interfaces indeed get separated, whereas they remain perfectly adherent when a bilateral contact has been imposed for the whole simulation. The "crack propagation" is smooth and regular, CZM-like smooth force - displacement relations do not seem to be necessary here (Figure III-18; see discussion of Figure III-7).
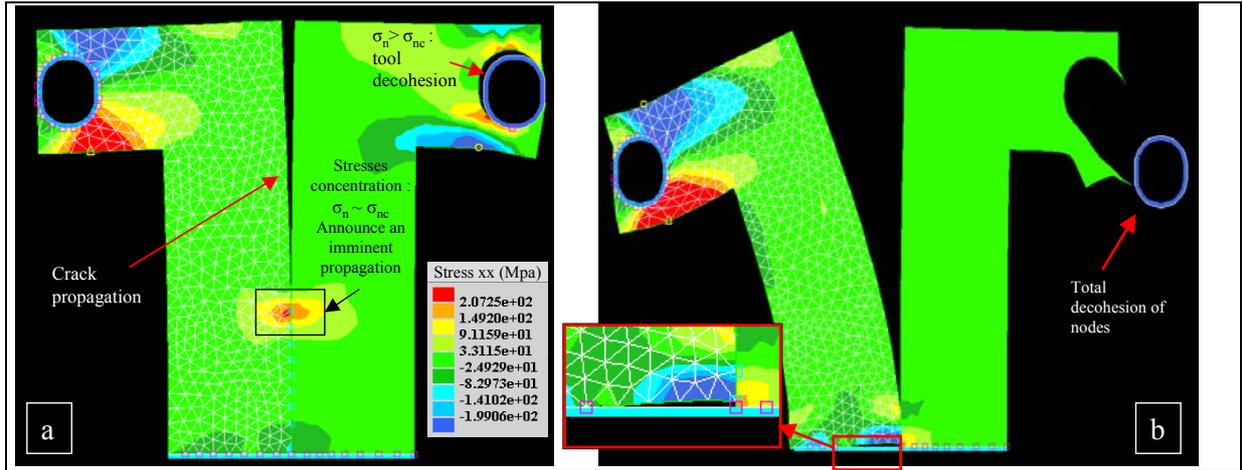
Figure III-18: Simulation at different calculation times.

Simulation à différents instants du calcul.

IV.4.3. Sliding and decohesion coupling

Effect of coupling on a bimaterial indentation test

To illustrate the influence of coupling on the interface behavior, we represent results obtained with simulations of indentation tests on a bimaterial.

After a while, decohesion appears near the indentor. The length **d** of the delaminated zone is measured and used as a damage characteristic parameter (Figure III-19).
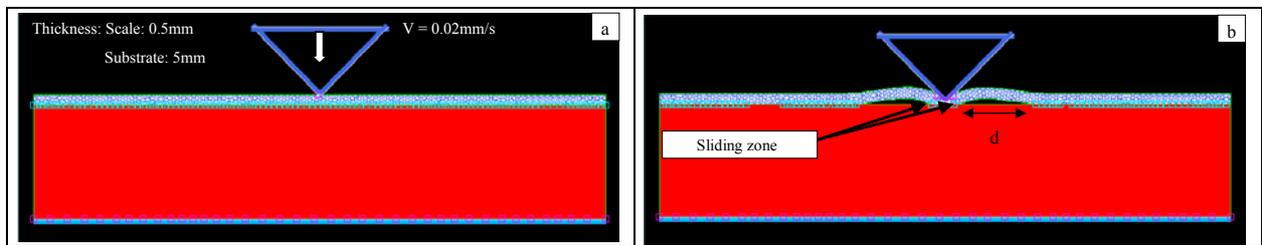
Figure III-19: Indentation simulation.   a) Initial configuration: d=0mm   b) d=3,28mm: decohesion

Simulation d'indentation : a) configuration initiale : d=0mm   b) d=3,28 : décohésion.

Figure III-19 represents a simulation without coupling between the normal separation criterion and the sliding one (α=0). Distance **d** stagnates after a 0.0246mm penetration of the rigid tool. Only the bulge height increases slowly afterwards. Similar simulations, but with coupling are presented Figure III-20 and Figure III-21 (critical normal strength decreases proportionally to the sliding velocity, eq. III-35). They highlight the coupling effect, with a larger decohesion zone, and in one case a total spallation of the scale layer.
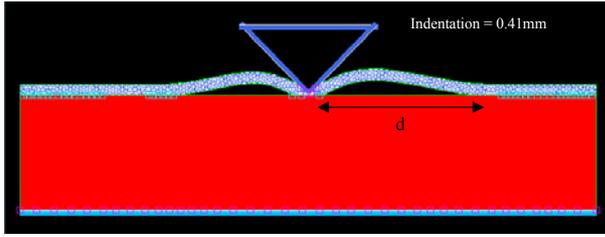
Figure III-20: d = 7,51mm. Low coupling: σ_{nc} decreases by 10% of its original value σ_{nc0}.

d = 7,51mm. faible couplage : σ_{nc} décroît de 10% de sa valeur initiale σ_{nc0}.
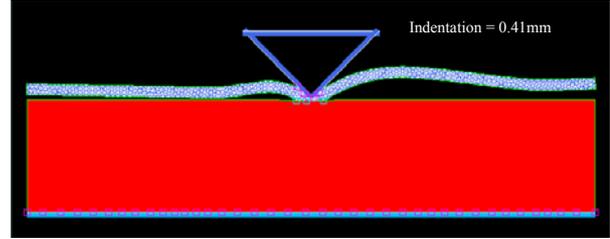
Figure III-21: Descaling; Strong coupling: σ_{nc} decreases by 40% of its original value σ_{nc0}.

Délamination ; couplage fort : σ_{nc} décroît de 40% de sa valeur initiale σ_{nc0}.

The length of delaminated zone has been compared for different coupling coefficients α (Figure III- 22), as a function of several displacement values. The expected evolution is obtained, by which an increase of *d* results when coupling strength α increases.
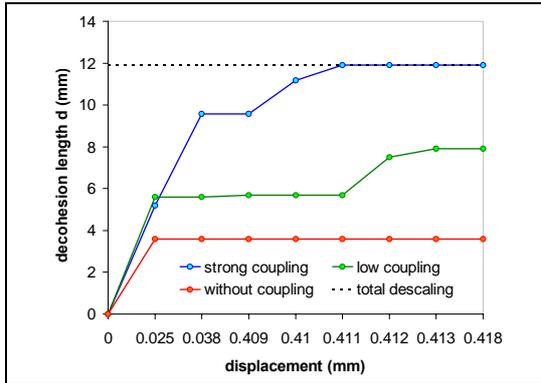
Figure III- 22: Influence of coupling on interface decohesion.

Influence du couplage sur la décohésion interfaciale.

V. TRANSVERSE CRACKS

Another key point concerning the scale damage during hot rolling is the numerical modeling of transverse cracks in the scale layer. When they are observed, they always extend through the whole oxide layer. In its initial version, Forge2® does not allow any crack propagation modeling. A simple stress-based fracture criterion has been implemented:

$$\boxed{\sigma = \sigma_{crit}(T)}$$

eq. III-36

V.1. Pre-existing cracks

A first simple technique to study steel extrusion through oxide scale cracks is to insert pre-existing cracks in the initial geometry of the scale. Figure III-23 represents such a rolling simulation of a steel slab covered by an oxide scale.
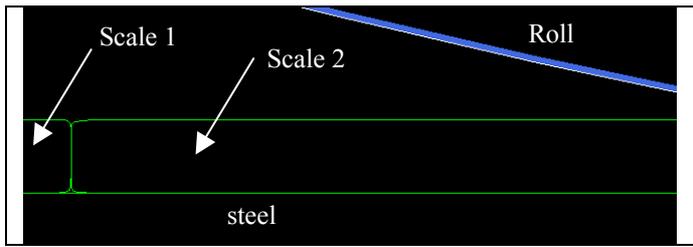
Figure III-23a: Two parts of scales in sticking bilateral contact.

Deux morceaux de calamine en contact bilatéral collant.

To simulate through-thickness cracks, two pieces of scale are put in a sticking bilateral contact (Figure III-23a). After each increment, principal tensile stresses of nodes belonging to scales interfaces are checked and compared to the critical tensile stress beforehand entered in the data file by the user (here 200 MPa). Figure III-23b shows an increment just before crack opening. The maximal stress value, marked by a triangle, exceeds the critical one (220MPa > 200MPa).

b) Critical-cracking stress reached in a node of the interface of two scale pieces.

b) Contrainte critique de fissuration atteinte en un nœud de l'interface entre les deux morceaux.
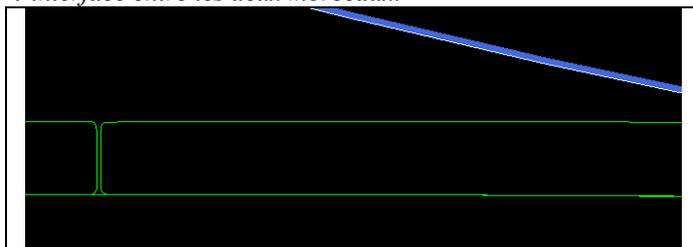
c) Separation of the crack lips.

c) Séparation des lèvres de la fissure.

At the next increment, the contact of the entire vertical interface is switched to unilateral, which results in the separation of the two lips of the crack due to the tensile stresses (Figure III-23c).
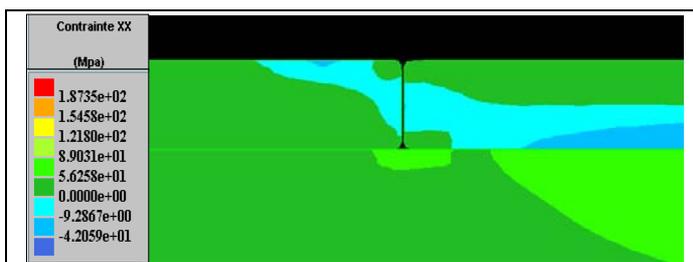
d) Relaxation of stresses

d) Relaxation des contraintes.

This change of contact conditions triggers stress relaxation (Figure III-23d).
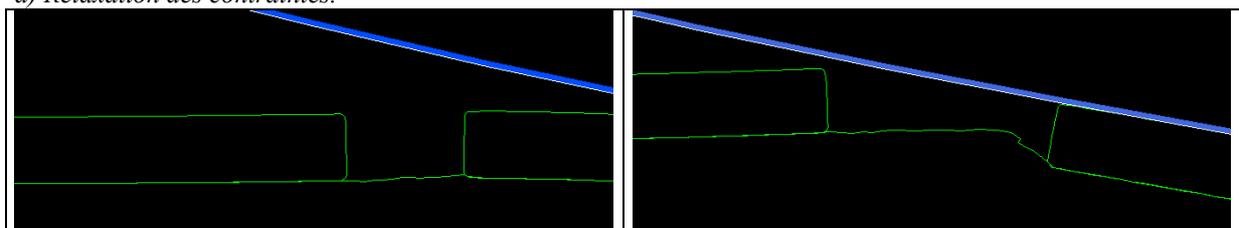
e) Opening of crack   **f) Scale embedding**

e) Ouverture de la fissure.   *f) Incrustation de la calamine.*

119
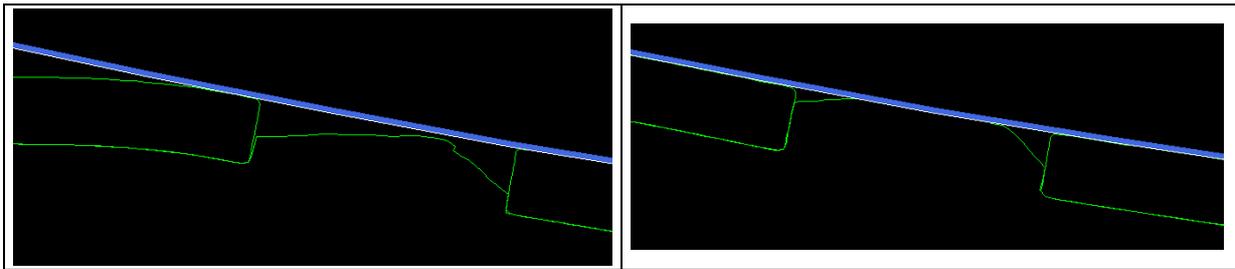
g) Extrusion of steel   **h) Contact between steel and roll**

g) Extrusion de l'acier.   *h) Contact entre l'acier et le cylindre.*

The final pictures show the opening of the fracture lips, the right piece of scale being strongly drawn by the roll (Figure III-23e) ; the embedding of scale in steel (Figure III-23f) and finally the extrusion of steel in the gap in the oxide layer (Figure III-23g,h).

V.2. <u>A more realistic model</u>

The previous model suffers from two main limitations:
- The number of cracks can be very large during a hot rolling simulation. Then it is necessary to create at least the same number of oxide part, which is extremely long and even impossible, the number of parts being limited in Forge2®.
- The creation of interfaces between two scale pieces induces a stress concentration which distorts the results.

Consequently, a more realistic model has been developed to simulate more precisely the occurrence of cracks. The implementation of this numerical technique in Forge2® can be decomposed in five steps (Figure III- 24):
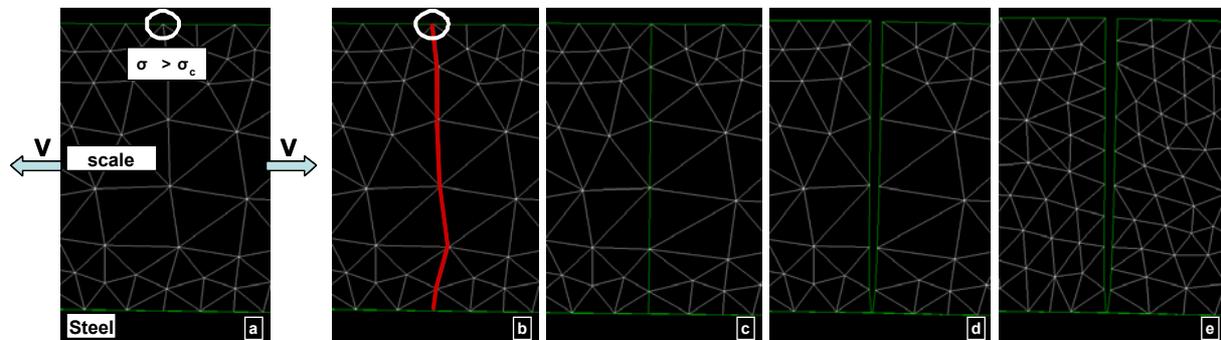
Figure III- 24: Successive steps for through thickness crack creation in Forge2®

Etapes successives pour la création d'une fissure transverse dans Forge2®

Critical stress: figure a

We make the assumption that cracks initiate at the surface. At each increment of calculation, every boundary node is checked for the critical principal stress criterion. If, at a node, the tensile stress σ_{xx} is higher than the critical value σ_c, a "crack" flag is set to 1 to trigger the creation of a crack. If several nodes overtake the critical value, only the one with the highest stress is selected.

Only one crack opening is allowed per increment. Short enough time steps must therefore be selected.

<u>Nodes belonging to the crack: figure b</u>

At the next increment, the nodes nearest to the perpendicular of the surface between the surface and the interface (starting from the critical node), are selected to constitute the through-thickness crack.

<u>Rectilinear crack: figure c</u>

From literature and experimental observations, we can reasonably assume that this kind of crack appears instantaneously (without propagation) and is rectilinear. Thus, nodes are tangentially projected on the normal line issued from the crack starting point, along its previously calculated normal.

<u>Duplication of nodes and re-creation of elements: figure c and d</u>

Nodes are duplicated to allow opening of the crack and relaxation of tensile stresses. A re-numbering of elements belonging to the crack is necessary.

<u>Remeshing: figure e</u>

Sometimes remeshing is necessary when elements are too distorted. As there is a sticking contact at the bimaterial interface, the crack opening is larger at the external surface.

This technique is now fully automatic and can be used with success to model the failure of an oxide scale during bending tests (see chapter IV), tensile tests (see chapter V) or hot rolling (see chapter VI).

VI. CONCLUSIONS

In this chapter, we have described the mechanical equations of a metal forming problem, their discretization and the resolution method used in Forge2®.

The problem we want to model needed specific developments in the contact management in normal and tangential directions.

For the normal contact, it is now possible to switch from a bilateral contact to a unilateral one (decohesion). For the tangential contact, an initially sticking contact can now become sliding. This is done on a node-by-node basis, using local, simple criteria:

- Decohesion: if $\sigma_n \geq \sigma_n^c > 0$ transition from bilateral to unilateral contact.
- Sliding: if $\tau \geq \tau_s^c > 0$ transition from sticking to sliding contact.

A coupling has also been introduced to take into account the crossed influence of tangential and normal behavior (for example, when sliding initiates, the decohesion is easier due to interfacial damage).

Another major modification has been developed into Forge2® to simulate a thin body cracking through its entire thickness. The fracture criterion implemented is simply based on a critical stress: a crack initiates where $\sigma_{tension} \geq \sigma_{crit}$.

All these modification now allow the different steps of the oxide scale damage to be simulated: oxide scale decohesion, sliding on steel substrate and initiation of through thickness cracks.

VII. REFERENCES

[Arno]   D.N.Arnold, F.Brezzi and M.Fortin, A stable finite element for Stokes equations, Calcolo, 21, (1984), pp.337-344.

[Chen]   J.L.Chenot, R.H.Wagoner "metal forming analysis", Cambridge University Press, (2001).

[Pich]   E.Pichelin, K.Mocellin, L.Fourment and J.L.Chenot, An application of a master-slave algorithm for solving 3D contact problems between deformable bodies in forming processes, European Journal of Finite Elements, 10, n°8, (2001), pp.857-880.

[Four]   L.Fourment, J.L.Chenot and K.Mocellin, Numerical Formulations and algorithms for solving contact problems in metal forming simulation, Int. J. of Num. Meth. in Engrg., 46, (1999), pp.1435-1462.

[Chan]   H.Li, N.Chandra: Analysis of crack growth and crack-tip plasticity in ductile materials using cohesive zone models, International journal of plasticity 19, (2003), pp.849-882.

[Abdu]   A.Abdul-Baqi, E.Van der Giessen: Numerical analysis of indentation-induced cracking of brittle coatings on ductile substrates, International journal of Solids and Structures 39, (2002), pp.1427-1442.

[Need]   A.Needleman, An analysis of decohesion along an imperfect interface, Int. J. Fract. 42, (1988), pp.21-40.

CHAPTER III. Numerical developments

The 4-Point Hot Bending Test

Résumé

Le test de flexion 4 points à chaud (F4P) a été choisi pour reproduire le comportement mécanique de la calamine en entrée d'emprise d'une cage de finisseur. Dans les deux cas, les couches d'oxydes sont sollicitées en flexion, induisant des contraintes de traction à l'intérieur de la calamine.

Une procédure expérimentale a été établie pour être aussi proche que possible des conditions du finisseur. Les cycles thermiques et mécaniques ont été choisis identiques pour tous les tests après l'observation de leurs influences sur le comportement des matériaux. Les tests ont été réalisés avec plusieurs nuances d'aciers, à différentes températures, déformations et vitesses de déformation, et avec des épaisseurs de calamine comprises entre 70 et 100μm.

Le comportement de l'acier pendant la F4P a été étudié par analyse inverse. Les résultats de détermination de leurs modules d'Young en F4P sont intéressants car il n'existe que peu de données pour les aciers disponibles dans cette gamme de températures (600°C-1000°C). La F4P, telle qu'elle est réalisée à l'IRSID, est donc un très bon outil pour la caractérisation mécanique des aciers à haute température et pour des très petites déformations.

Le comportement de la calamine déterminé peut être divisé en deux catégories :
- *<u>A basse température</u>, la calamine est fragile malgré son comportement plastique. L'interface entre elle et son substrat en acier est forte. Pendant la déformation, des fissures transverses apparaissent, perpendiculaires à la direction de sollicitation. Les fissures intergranulaires se propagent à travers la profondeur de l'échantillon.*
- *<u>A haute température</u>, la calamine est plus plastique et peut se déformer sans fissuration. Néanmoins, l'interface semble beaucoup plus faible et des décohésions interfaciales peuvent être observées.*

L'influence de plusieurs paramètres est mise en évidence par une combinaison de nombreux essais de F4P, d'observations microscopiques et de cartes de fissurations : la déformation, la vitesse de déformation, l'épaisseur de la calamine, la nuance d'acier. L'évolution de la densité de fissures en fonction de ces paramètres est également étudiée. Globalement, on se rend compte que la densité de fissure augmente lorsque la calamine devient plus dure et plus fragile.

Afin de simuler le comportement de la calamine, plusieurs étapes ont été nécessaires :
- *Le montage de F4P a été instrumenté avec de l'émission acoustique. Cette technique nous a permis de mieux comprendre ce qui se passait au cours des essais ;*
- *Les équations constitutives de l'acier et de la calamine ont été déterminées par une méthode d'analyse inverse pour les éprouvettes non endommagées ;*
- *Les équations constitutives pour les éprouvettes endommagées ont été déterminées par extrapolation des résultats précédents ;*
- *Les contraintes critiques ont été déterminées (par couplage entre les résultats des simulations numériques et d'émissions acoustiques).*

La dernière partie de ce chapitre concernant la simulation numérique d'essais de F4P montre l'efficacité de l'approche présentée précédemment. En effet, les simulations reproduisent très bien les résultats expérimentaux.

Néanmoins, l'interprétation des résultats de F4P est à prendre avec beaucoup d'attention. La F4P imite parfaitement la flexion en entrée d'emprise de finisseur. Mais cette flexion ne représente en laminage qu' une part de la déformation du système acier-calamine.
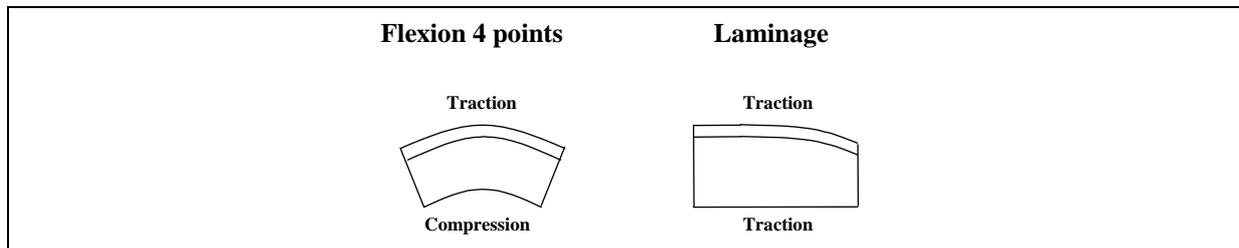
La plus grande partie des contraintes de traction engendrées dans la zone critique est due à la rotation des cylindres qui mettent fortement en tension la peau de la bande. De plus, les essais de F4P mettent en évidence la très forte influence de la vitesse de déformation sur le comportement de la calamine. Or il existe une très grande différence de ce point de vue entre la F4P (entre $7.10^{-5}s^{-1}$ et $1.4.10^{-2}s^{-1}$) et le laminage ($\sim 10s^{-1}$).

Des doutes peuvent alors être justifiés sur l'utilisation de tous les résultats de F4P pour les simulations de laminage. Le meilleur argument est le fait que l'on obtient des défauts dans le finisseur à des températures auxquelles ils ne sont pas apparus en F4P (entre 850 et 1000°C).

Malgré les nombreux avantages de la F4P, cet essai mécanique ne s'avère donc pas suffisant. Des essais de tractions à chaud sont donc réalisés pour compléter notre jeu de données nécessaire pour simuler numériquement le comportement de la calamine en laminage à chaud.

I. INTRODUCTION

The four-point hot bending test (4-PHBT) has been chosen for the rheological study of the oxide scale. Its principal interest is to involve mechanical solicitations, very close to those initiated at the entry of the roll gap. Indeed, in both cases, materials undergo a mixture of bending and tension.

A first step consists in testing non-oxidized steel specimen to obtain the mechanical contribution of the substrate. Specimens constituted of steel covered by an oxide scale are then tested. The comparison between the mechanical behavior of oxidized and non-oxidized steel specimens leads to the identification of the oxide scale mechanical characteristics.

The mechanical equations of the 4-PBT are not summarized in this manuscript, but can be found in the different references given in the next bibliographic part (in most cases, these equations are given for elastic material). Indeed our interest concerning the 4-PHBT is not the computation of stresses or the localization of the bimaterial neutral fiber: all these data are given by the numerical simulation (Forge2®). We want to understand the mechanical behavior of oxides, when they undergo a mixture of bending and tension, to be able in the end to simulate the oxide scale behavior in 4-PHBT.

Fundamental questions are:
What is the oxide scale behavior regarding such a deformation: is it **plastically deformed** or does it yield by **cracking**? What are **the influencial parameters**? Is it possible to determine **behavior laws** and scale **damage criteria**? Last, but not least: is it possible to **explain** the oxide scale mechanical behavior in a **rolling stand** from the **4-PHBT results**?

This chapter is divided in four parts:

- In a first part, recent bibliographic 4-PBT results are briefly summarized, when the focus is close to ours.
- The second part is devoted to the presentation of our experimental device, our process parameters and to the description of additional instrumentation used, namely the acoustic emission.
- Experimental results are then described. The influence of the different test parameters on the oxide scale behavior is investigated as well as the significant contribution of the acoustic emission technique.
- Simulations of several experimentally obtained examples are given in the last part. They are obtained using the identified behavior laws for the steel substrate / oxide scale bimaterial, and the determined damage criteria. These simulations show the efficiency, the accuracy and the different capabilities of the developed numerical model.

II. BIBLIOGRAPHY

Several researchers have investigated the oxide scale mechanical properties using 4-PBT. This test gave them a better knowledge of the oxide scale behavior during the hot rolling process. They all have the same objective: describe the scale damage during the deformation and determine the critical values for its initiation.
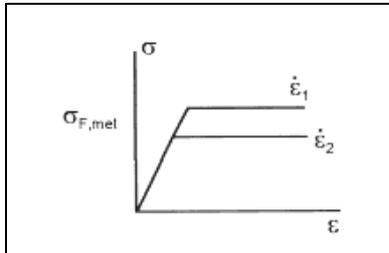
Figure IV-1: Ideal elastic-viscoplastic behavior [Echs].

Comportement élasto-viscoplastique idéal [Echs].

Nevertheless, before showing the oxide damage, it is interesting to give general ideas on the mechanics of the 4-PBT. In [Echs], the authors take the example of a ductile material assuming an ideal elastic-viscoplastic behavior (ideal means that the stress remains constant whatever the strain; the stress level depends however on the strain rate: Figure IV-1). During a 4-PBT, the specimen has a symmetric behavior under tensile and compressive loading (Figure IV-2).
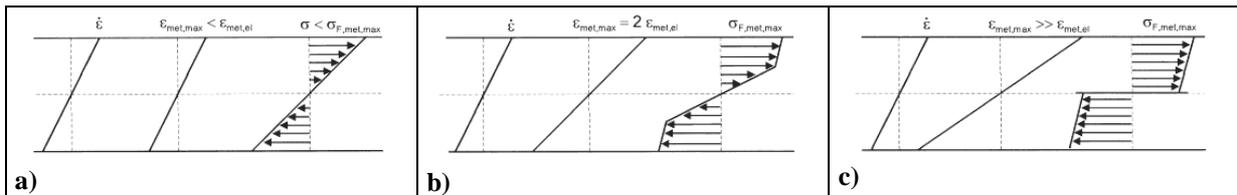
Figure IV-2: Stress-strain dependence during the 4-PBT [Echs].

Dépendance contrainte-déformation pendant la flexion 4 points (f4p) [Echs].

First, the specimen is elastically deformed until the stress in the outer fiber reaches the flow stress $\sigma_{F,met,max}$ for a given strain rate (Figure IV-2a). The specimen is then deformed plastically in the outer fiber. The maximum stress in the outer fiber then remains constant and the elastically deformed area in the cross section shrinks with increasing deflexion (Figure IV-2b,c). An identical example has been simulated using Forge2®. Results are represented in Figure IV-3 and Figure IV-4.
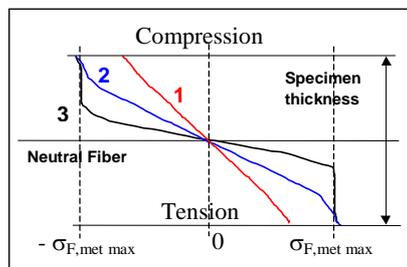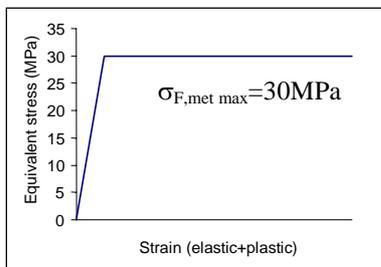
Figure IV-3: Computation using Forge2®. Left: Ideal plastic behavior. Right: Stress-strain dependence during the 4-PBT.

Simulation Forge2®. A gauche : comportement plastique idéal. A droite : Dépendance contrainte-déformation pendant la f4p.

(1)   (2)   (3)
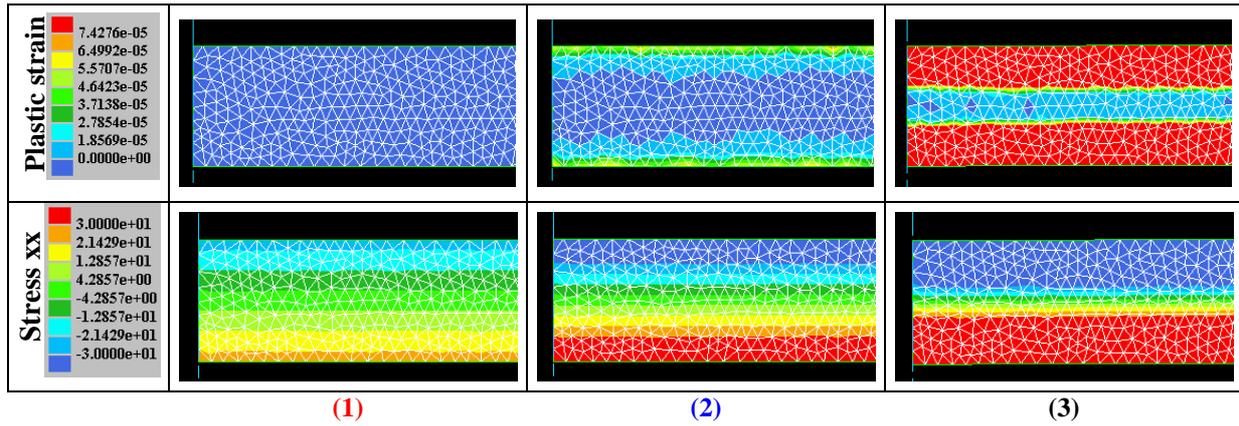
Figure IV-4: 4-PBT simulation of a steel specimen using Forge2®. Visualization of plastic strain and tensile stress (xx) at the three stages of the simulations of Figure IV-3.

Simulation d'un essai de f4p d'une éprouvette en acier avec Forge2®. Visualisation des déformations plastiques et des contraintes de traction (xx) à trois instants des simulations correspondant à ceux de la figure IV-3.

We find the same stages of specimen deformation as [Echs]: when the plastic strain is equal to zero, all the material is elastically deformed (σ_{xx}<30Mpa). At a given elastic strain (corresponding to the material yield strength), the specimen start to be plastically deformed from the outer fibers (σ_{xx}<30Mpa) toward the neutral fiber.

Figure IV-6 and Figure IV-5 show the influence of a scale that covers the specimen. A shift of the neutral zone is observed.
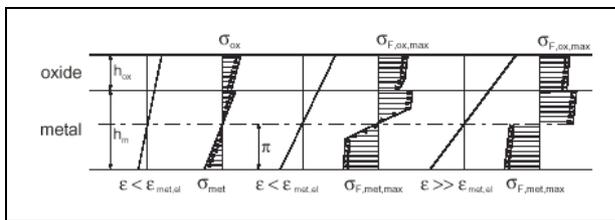
Figure IV-5: Schematic Stress-strain distribution in the cross section of an oxidized bent bar [Echs].

Distribution schématique contrainte-déformation dans une coupe d'une éprouvette de flexion oxydée [Echs]
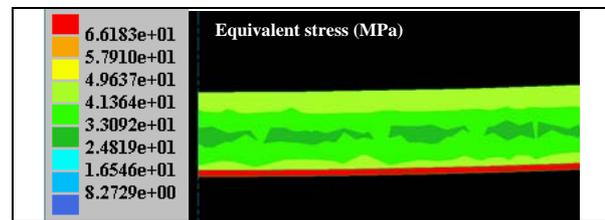
Figure IV-6: 4-PBT simulation using Forge2® of a steel specimen covered by a thin oxide scale on its lower side.

Simulation Forge2® d'une éprouvette de f4p en acier couverte sur sa partie inférieure d'une fine couche d'oxyde.

Zhou et al. [Zhou]

4-PB experiments were conducted by Zhou et al. on stainless steel (SUS304) and carbon steel (S45C) substrates, covered with two types of ceramic thermal barrier coatings: a two-layer coat system (a bond coat and a much larger top coat) or a functionally graded material coating.
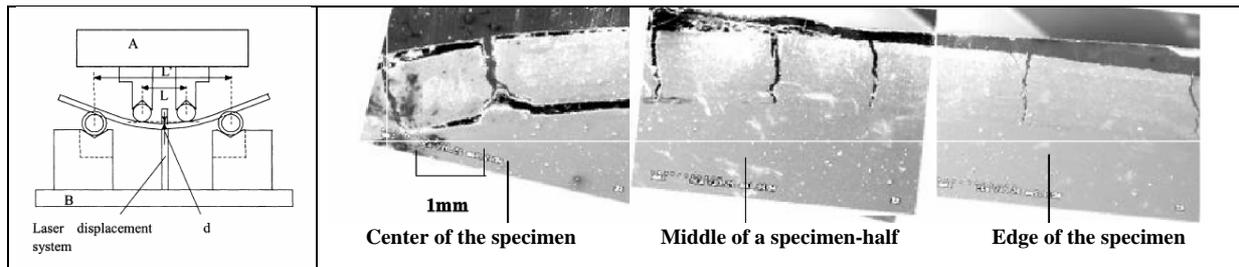
Figure IV-7: SEM cross section of functionally graded material specimens in four-point bending test [Zhou]

Coupe MEB d'éprouvettes de f4p en matériau d'une nuance fonctionnelle [Zhou]

The authors observe that vertical cracks appeared first on the surface layer, perpendicularly to the load axis. When the crack tip reaches the interface, cracks can also kink to propagate along the interface, leading sometimes to the layer spallation.

Schütze et al. [Schü, Brun, Echs]

These authors have studied the damage behavior of the oxide scale on nickel and TiAl in 4-PBT coupled with acoustic emission (AE) (Figure IV-8). Indeed, the different fracture modes, among other factors, are liable to cause important variations on AE parameters values (Table IV-1). The AE technique is detailed in **APPENDIX 3**.

	Favorable factors for high amplitude	Favorable factors for low amplitude
Mechanical properties	high yield strength	low yield strength
Structure	Anisotropy, defects, heterogeneity, martensitic transformation, large grain size	Isotropy, no defects, homogeneity, diffusion transformation, low grain size
Rupture mode	Crack propagation	Plastic deformation
Loading mode	Large deformation	Low deformation
Geometry	Large thickness	Low thickness
Environment	Low temperature	High temperature

Table IV-1: Factors that influence AE detectability from Dunegan and Green [Dune].

Facteurs influençant la détectabilité de l'émission acoustique (EA) d'après Dunegan et Green [Dune]

For nickel, tests have been performed at room temperature due to its extremely low high-temperature strength. The tests on TiAl have been performed at room temperature, 700°C and 900°C.
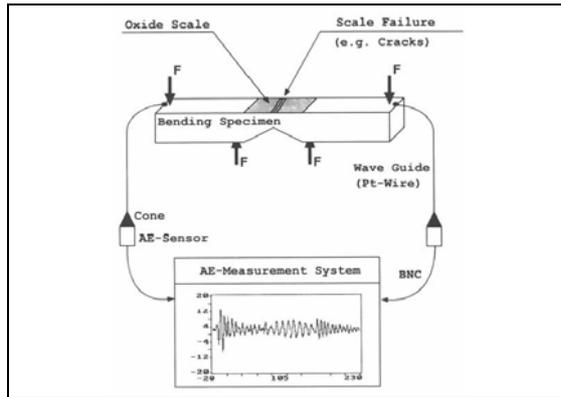
Figure IV-8: Schematic of the test arrangement. The V-shape focuses the deformation in the specimen center [Brun].

Schéma du montage. La déformation est concentrée au centre de l'éprouvette [Brun].
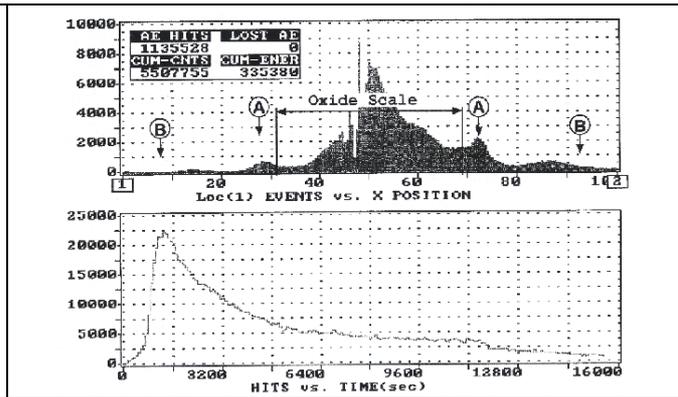
Figure IV-9: Results from AE measurements for a Nickel specimen oxidized at 900°C in air for 50 hours and deformed at room temperature. A and B are the rolls positions [Brun].

Résultats de mesures d'EA d'une éprouvette de Nickel oxydée à 900°C à l'air pendant 50 h et déformée à température ambiante.
A et B représentent les positions des rouleaux [Brun].

- **Nickel**

Figure IV-10: SEM image (BSE) of through-scale cracks in the oxide scale on Nickel substrate. Same test as Figure IV-9. Strain is 1.6% in the specimen center.

Image MEB d'une couche d'oxyde fissurée d'une éprouvette en Nickel oxydée (test de la figure IV-9). La déformation est de 1,6% au centre de l'éprouvette.
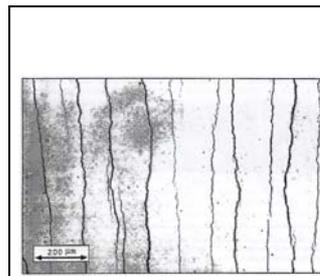
Figure IV-11: Crack densities in the oxide represented just above.

Densité de fissures dans la couche d'oxyde représentée ci- dessus.
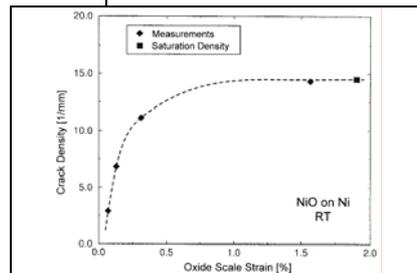
The deformation of the 4-PBT specimen leads to the formation of a quasi-equidistant through-scale crack network. These cracks are perpendicular to the specimen axis and in most cases run over the whole width (Figure IV-10).

The number of cracks increases with the strain until a saturation value above which the density of through-scale cracks remains the same (Figure IV-11). For the authors, this saturation strain also corresponds to the crack branching to interfacial cracks, leading to the start of a delamination process.

The AE resulting from the previous tests are represented on Figure IV-9. The use of two sensors (see Figure IV-8) allows spatial discrimination of signals. The AE is focused on the centre of the specimen due to the increase of damage events in the highest deformation zone. The peaks observed at the positions of the rolls A result from friction noise.

The AE events correspond to the scale damage. Indeed, tests without oxidation did not reveal any AE event.

The second graph of Figure IV-9 represents the number of hits versus time.

- **TiAl**

A typical example of the cracks appearing during deformation is represented on Figure IV-12. In addition to the through-scale cracks, large spalled areas can also be observed.
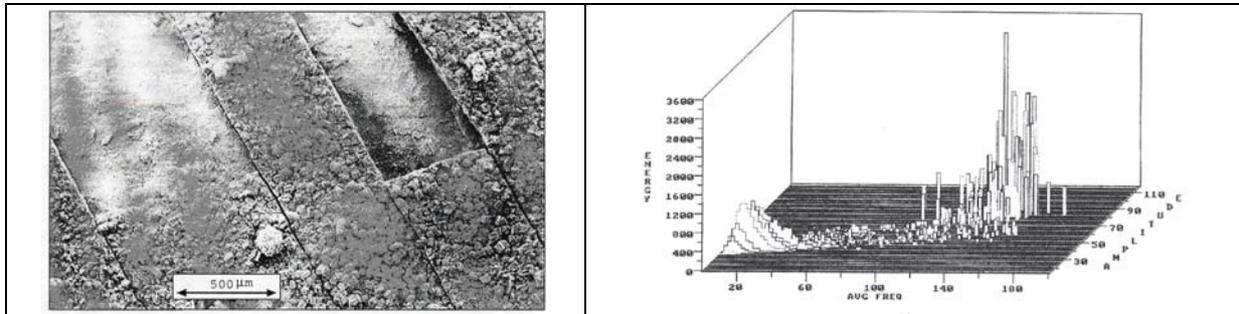
Figure IV-12: SEM micrograph of cracks and spalled areas in the oxide scale on TiAl after oxidation and deformation at 900°C. Pre-oxidation time: 75 hours.

Micrographie MEB de fissures et de zones délaminées dans une couche d'oxyde sur du TiAl après oxydation et déformation à 900°C. Temps de pré-oxydation : 75 h.

Figure IV-13: Analysis of the AE signals of the oxide scale on TiAl after oxidation and deformation at 900°C with respect to cumulative energy, average frequency and signal amplitude. Pre-oxidation time: 25 hours.

Analyse de signaux d'EA de la couche d'oxyde sur l'éprouvette en TiAl oxydée et déformée à 900°C, en fonction de l'énergie cumulée, la fréquence moyenne et l'amplitude. Temps de pré-oxydation : 25 h.

In this case, there is already significant AE for the unoxidized specimens due to dislocation movement, twinning and possible microcracks formation in the TiAl substrate.

The different tests performed by the authors are not precisely described ; detailed results are lacking, e.g. the AE difference between through-scale cracks and delamination. Nevertheless, they obtain interesting results concerning the importance of the average frequency in AE or the fracture toughness of the scales and the interfaces.

An example showing the frequency dependency is given on Figure IV-13. The substrate contribution is in a frequency range of [0-60Hz] (highlighted by tests on unoxidized specimens). The frequency range of events in the coating is [100-160Hz].

Moulin et al. [Dalm, Mou1, Mou2]

An interesting collaboration has been initiated during this thesis with the Technical University of Compiègne (UTC) and more particularly with Pr. Moulin, on the oxide scale behavior during 4-PHBT. Indeed, the UTC has a 4-PHBT machine instrumented with AE and [18]O marking. Iinjected during the test just after the deformation, the latter enables cracks to be marked. It is thus possible to distinguish cracks coming from thermal dilatation/contraction and from mechanical deformation.

Preliminary studies have been undertaken on the characterization of adherence and cracking within a WC-CO coating on a steel substrate (

Figure IV-14**)** [Dalm]. These studies have been performed at **room temperature**, using an **acoustic emission device.**

Figure IV-14: 4-PBT experimental device [Dalm]

Montage expérimental de f4p [Dalm].
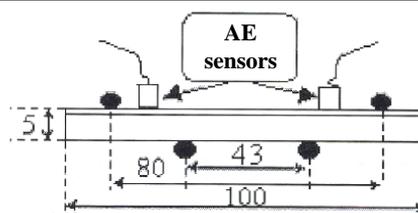
Figure IV-15: Load-displacement curves of specimens covered by two coatings of different thickness [Dalm].

Courbes force-déplacement d'éprouvettes couvertes de deux couches d'épaisseurs différentes [Dalm].
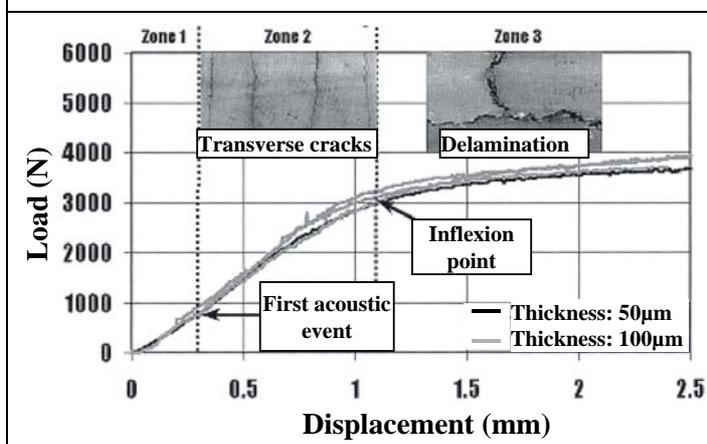
Interesting results have been obtained: a correspondence between the coating damage during deformation and characteristic AE signals has been observed. On Figure IV-16, the AE amplitude is represented during the deformation. A first part, without any signal, represents the elastic deformation of the bimaterial. The second stage is no more elastic, and through-scale cracks initiate. Finally, the last zone represents the delamination stage (Figure IV-15), characterized by large amplitude events. These different stages can also be observed by plotting the absolute energy of the AE events as a function of their amplitude. Each damage type has a specific signature. Thus, the authors describe two types of signatures A and B, which correspond respectively to the coating cracking and to its delamination.
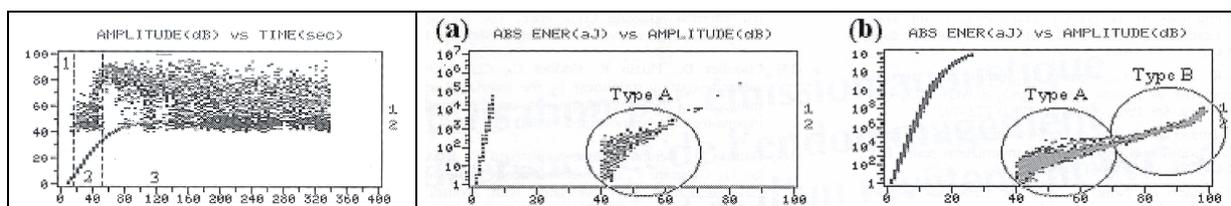
Figure IV-16: Amplitude of events (dB) vs. time (s) + associated load curve (in arbitrary scale) [Dalm].

Amplitude des événements (dB) en fonction du temps (s) + courbe de force associée (échelle arbitraire) [Dalm].

Figure IV-17: Absolute energy of events (1 aJ=10⁻¹⁸ J) vs. amplitude (dB) for two levels (a and b) of load. The associated load curve is plotted also (in arbitrary scale) [Dalm].

Energie absolue des événements (1 aJ=10⁻¹⁸ J) en fonction de l'amplitude (dB) pour deux niveaux (a et b) de force + courbe de force associée (échelle arbitraire) [Dalm].

Then, Moulin started a study completely similar to ours (Figure IV-18). Indeed, to compare in a best possible way their results with ours, the same material were used (provided by IRSID) as well as the same thermal and chemical cycles for the tests.
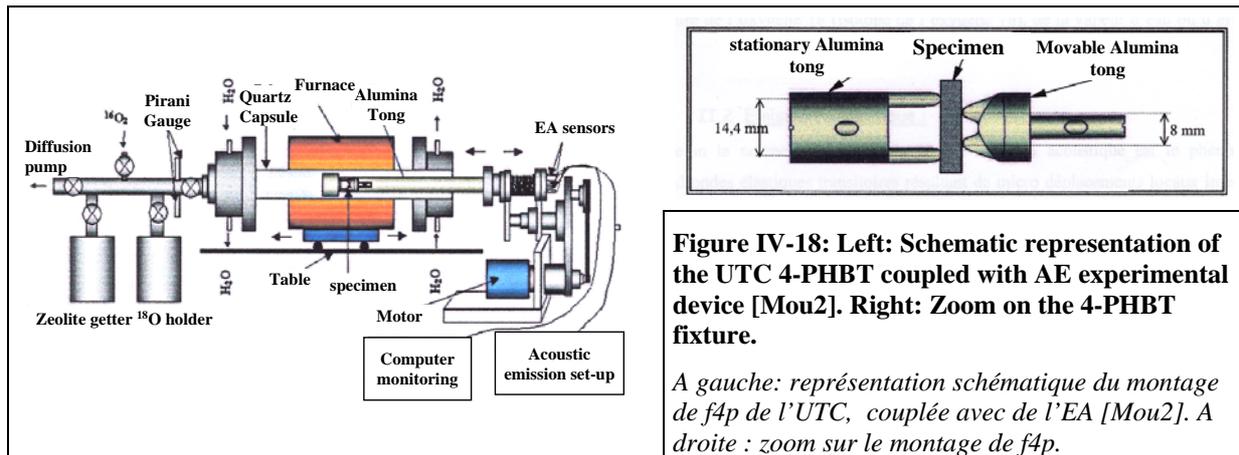
Figure IV-18: Left: Schematic representation of the UTC 4-PHBT coupled with AE experimental device [Mou2]. Right: Zoom on the 4-PHBT fixture.

A gauche: représentation schématique du montage de f4p de l'UTC, couplée avec de l'EA [Mou2]. A droite : zoom sur le montage de f4p.

Tests are performed between 650°C and 900°C. A general behavior is observed:

- At temperatures lower than 750°C, equidistant cracks initiate (Figure IV-19), perpendicular to the loading direction, starting from the specimen sides and propagating toward the centerline. As the distance from the middle of specimen increases (in the length direction), the propagation decreases.
- At temperatures higher than 750°C, there are no more cracks. The oxide scale is plastically deformed (Figure IV-20).

They also observe a sensitivity to the strain rate with the apparition of cracks at higher temperature when the tool velocity increases.
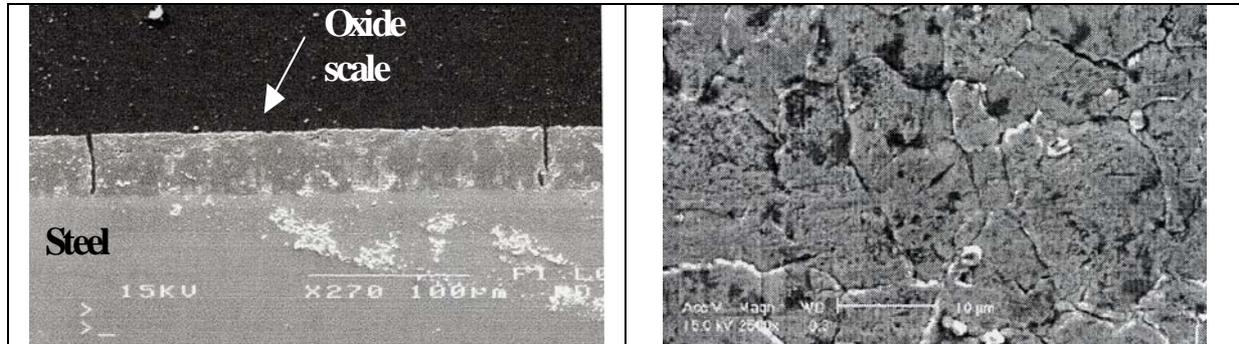
Figure IV-19: Micrograph of specimen oxidized in air at 900°C and deformed at 650°C [Mou2].

Micrographie d'une éprouvette oxydée à l'air à 900°C et deformée à 650°C [Mou2].

Figure IV-20: Oxide scale granular morphology: Micrograph of specimen oxidized in air at 900°C and deformed at 800°C [Mou1].

Morphologie granulaire de la calamine : micrographie d'un échantillon oxydé à l'air à 900°C et déformé à 800°C [Mou1].

Relaxation tests after the deformation confirm this oxide behavior. At 700°C, no stress relaxation is found. The material has eliminated its internal stresses by opening cracks. At higher temperature, the relaxation is important because all stresses have been accommodated by plastic deformation and thus not totally relaxed.

^{18}O detects the formation of cracks *during* the test. The authors remark that its surface concentration is lower when cracks are present because in this case, ^{18}O diffuses toward the interface of the bimaterial.

Concerning AE, the authors have succeeded in measuring AE at high temperature of deformation with a steel substrate covered by an oxide scale. The number of events is high when cracks are present, whereas plastic deformation is characterized by a low emission level. Several assessments are given on different parameters allowing the number of cracks to be measured ; although they are not really justified in the present state of our knowledge, the study seems to be promising. An example of cracking with AE *during cooling* is briefly mentioned, but not detailed.

Conclusion on bibliography

The bibliographic study has highlighted the general behavior of coatings covering ductile substrates during 4-PBT. At room temperature or in a range in which the coating is brittle, equidistant through-scale cracks are observed, perpendicular to the loading direction. These cracks can propagate along the bimaterial interface if the deformation increases enough. Interestingly, strain rate sensitivity has also been observed.

Several authors use the AE technique to complete their 4-PBT results. Indeed, this technique is a strong tool to detect damage initiation, or possible cracking due to thermal stresses.

Promising results have been obtained at high temperature (where the emission is significantly lower). Specimens with cracks are clearly identified from the number of AE events, their amplitude or their signature in frequency or in energy.

Motivated by the preliminary results obtained by experiments at UTC, we have instrumented our 4-PHBT with AE. This choice has also been motivated by difficulties in interpreting "accidents" on our experimental load-deflection curves. This will be explained in details in the following.

III. THE FOUR POINT HOT BENDING TEST OF IRSID (4-PHBT)

The 4-PHBT have been performed at IRSID. A temperature and humidity cycle is imposed to mimic the conditions encountered in the finishing mill. The experimental device of the 4-PHBT is placed under controlled atmosphere and installed on a Zwick 1474 tension-compression machine (Figure IV-21).

Figure IV-21: General presentation of the Zwick 1474 machine.
1. ZWICK machine
2. PYROX resistance furnace
3. ZWICK electronic (measurement and command)
4. REGULEST Wet gas generator
5. PYROX furnace Command

Présentation général de la machine Zwick 1474.
1. machine ZWICK
2. four à résistance PYROX
3. électronique ZWICK (mesure et commande)
4. générateur d'air humide REGULEST
5. commande du four PYROX

The atmosphere control is obtained using a **REGULEST** atmosphere controller and the specimen heating by a **PYROX** (HMO type) resistance furnace, all controlled by a PC. The interactive **tXpert 6.01** program guides the operator during the test.

III.1. Test preparation

Both top tools are connected by a load pin to the fixed frame of the machine, via a load cell (0-200N +/-0.01N). A support tube connects the bottom tools to the mobile crosshead. In this tube, a measuring pin is connected to a LVDT displacement transducer -5/+5mm (+/- 50µm) measuring the deflection at the specimen center (Figure IV-22).
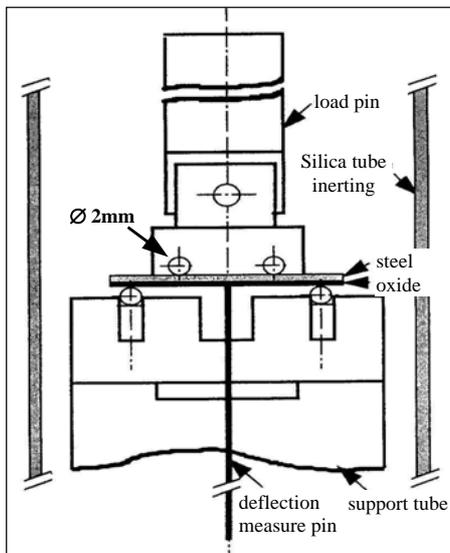
Figure IV-22: Schematic representation of the 4-point bending test device.

Représentation schématique de la machine de f4p.

Figure IV-23: Opened Pyrox Furnace.

Four Pyrox ouvert.

Figure IV-24: Specimen installation in the silica tube.

Installation de l'échantillon dans le tube en silice.

The 4-PHBT fixtures were manufactured in alumina because of its high temperature strength and its excellent hardness. All the pieces are mobile.

The horizontal distance is 40mm between the two bottom tools, and 20mm between the two top tools (Figure IV-22, Figure IV-24).

The entire device is confined in a silica tube and heated by a resistance furnace placed around (Figure IV-23).

A K-thermocouple is placed close to the specimen. Its indication is available on a high precision universal measuring AOIP device.

Gaseous joints ensure the air-tightness between the tube and the mobile part of the device (load pin and carrying device tube). This system gives an accurate load measurement resolution by avoiding all friction on the load pin.

III.2. <u>The heating system</u>

The heating system is composed of a PYROX furnace (Figure IV-23) and a command. The PYROX furnace is fixed to the ZWICK machine and positioned for an optimal specimen heat. The heat is provided by silicon carbide resistances distributed in three independent heat zones with type S-thermocouples. It is equipped with an opening system along a median plane. The furnace is controlled in « manual » or « programmer » mode via a controller / programmer EUROTHERM 902P.

III.3. <u>Wet atmosphere generator</u>

A wet atmosphere generator provides the chamber with gas. This generator allows regulating the injected gas dew point temperature ($30°C < DP < 65°C$). In order to prevent condensation, the gas is conducted from the atmosphere controller to the test chamber by a heated line.
The generator has 4 gas entries and 3 exits:

Gas entries:
- The compressed air used to pilot the oxidizing gas supply controller;
- The inlet of $N_2 + O_2$ in the humidifier;
- N_2 or CO_2 which can be mixed to the wet gas, after its humidification;
- Dry N_2 used here as inert gas for the gaseous joints and during the non-oxidized phases.

Gas exits:
- The wet gas used for the specimen oxidation; this is a heated line;
- The open air, where wet gas excess is sent;
- Dry N_2 used for the gaseous joints and the furnace inerting.

The water humidifier temperature is adjusted from a JUMO controller. The dew point is measured by a SIEMENS humidity probe. The rack containing the probe is heated and its temperature adjusted by a second JUMO controller. Supplies are fixed at 100 l/h.

III.4. <u>Specimens preparation</u>

The steel has two origins:
- The first tests were performed with specimens machined from hot rolled slabs. They have been tested in the two cutting directions (transversal and longitudinal): no difference has been observed.
- Others directly came from little ingots obtained by laboratory casting performed in a melting furnace at IRSID.
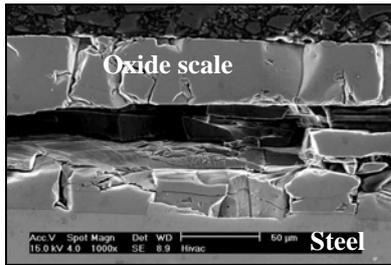
Figure IV-25: Preparation problem for cast extra low carbon steel specimen.

Problème de préparation avec un échantillon d'ExDx.

Little difference has been observed between these two origins of steel specimens. We have recently noted that the preparation of cast extra-low carbon steel was more difficult than from rolled steel, because the oxide scale of the former sometimes breaks during the preparation (Figure IV-25).

Several such assessments on scale structure, adherence or plasticity are made but without any certainty.

Dimensions of all specimens are 50mm x 8mm x 1mm.

The oxide layer (predominantly FeO) is built only on the lower side, which is in tension during the test. The other side is protected by a deposited Cr / Cr_2O_3 layer around 1-2µm thick. The face to oxidize is beforehand ground with a 1200 grit paper and washed with ethanol.

III.5. <u>Experimental procedure</u>

The thermo-mechanical cycle undergone by all samples is displayed in Figure IV-26. Controlled oxidation is performed for a given time at a prescribed temperature (900°C) in a controlled atmosphere, simulating the thermo-chemical history of the strip in the rolling mill. Then the sample is brought to the mechanical testing temperature (between 600°C and 1000°C, which is judged typical of the surface temperatures in the hot finishing mill). For each temperature, two different kinds of tests are performed: systematically, a reference test is performed on a non-oxidized sample (air +H_2O is *not* introduced), then tests using the oxidized samples.

The material is heated in N_2 up to 900°C. Then air with 15% H_2O is introduced for 4 to 8 minutes, then N_2 is flooded again while the material is brought down to the test temperature, then deformed. Time, crosshead displacement, deflection and load are continuously recorded during the test (Figure IV-27).
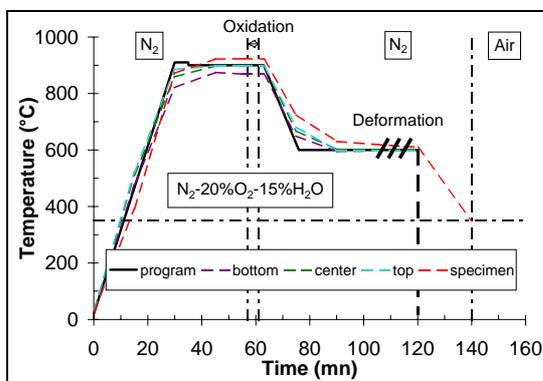
Figure IV-26: Samples thermal cycle of 4-PHBT.

Cycle thermique des échantillons de f4p.
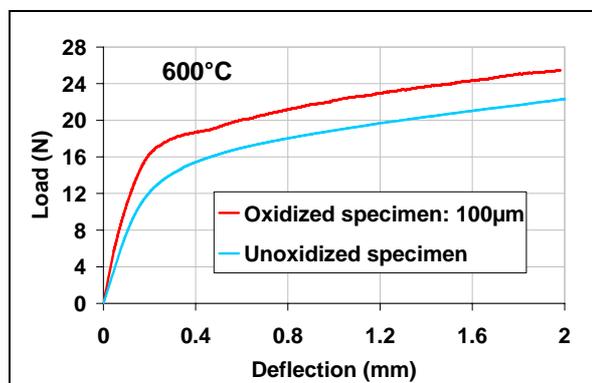
Figure IV-27: Example of curves obtained during unoxidized and oxidized tests at 600°C.

Exemple de courbes obtenues pendant des tests oxydés et non oxydés à 600°C.

During the temperature increase, the specimen is just placed on the bottom tool-rolls to avoid any loading due to both specimen and tools dilatation. Just before the test, the specimen undergoes a pre-load at 0.5 N. Then, the LVDT transducer is put in contact with the specimen oxidized face, by turning a wheel placed on the mobile crosshead.

The studied steel grades are the **Ex-LC** extra-low carbon steel (in 10^{-3} % in weight: C=45/55; Mn=230/270 ; S=11 ; Si=15 ; Al=30/40), the **DDS** deep drawing steel, the **ReN** re-nitrided steel, the **DP** dual-phase steel and the **ReP** re-phosphorized steel. Composition of the four latter steels has been given in chapter II (part II.1.2).
Nevertheless the major part of the 4-PHBT study has been performed with the Ex-LC steel grade.
The oxide scales are 70 to 100µm thick, which is larger than on the finishing mill, but is judged necessary to detect a measurable effect in bending tests. In addition, shorter oxidation times would lead to a non-homogeneous oxide growth.

The crosshead velocities are 0.0167 mm.s^{-1} (1mm/min), 0.333 mm.s^{-1} (20mm/min), 0.833 mm.s^{-1} (50mm/min) and 3.33 mm.s^{-1} (200mm/min), corresponding respectively to strain rates of 7.10^{-5}s^{-1}, $1.4.10^{-3}$s^{-1}, $3.5.10^{-3}$s^{-1} and $1.4.10^{-2}$s^{-1}.

In most cases, the deflection imposed during the test is 2mm, giving a strain of ~ 0.5%. To estimate the relevance of this strain level, we decided to determine the amount of plastic bending strain before bite entry in rolling.
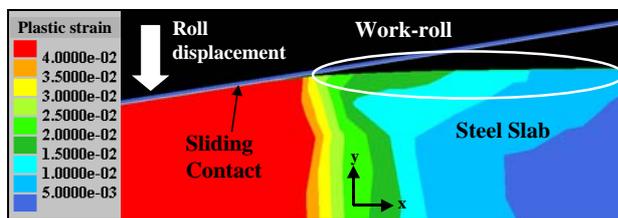
Figure IV-28: Compression test under hot rolling conditions.

Test de compression dans des conditions de laminage à chaud.

For simplicity, a strip compression simulation under hot rolling conditions (same dimensions, velocity of the roll = component V_y of the rolling tangential velocity, reduction: 45%) is represented on Figure IV-28. The strain induced by bending in the zone of crack initiation, due to the thickness reduction in the rolling process, is between 0.5 and 3%.

The 4-PHBT can therefore be considered to impose plastic strain of the same order of magnitude.

Test exploitation

The deformed oxide scale is first observed from the top to study its general aspect (crackling, cracks, oxide grains type). When damage is observed, a crack mapping is reproduced.
In a second stage, specimens are cut, coated and polished to be observed in their cross-section (see Chapter II – specimens preparation).

III.6. <u>The acoustic emission instrumentation</u>

Two channels for AE hits reception have been installed in our tests. A piezoelectric sensor, a pre-amplifier and the AE computer compose each line. The software used is MISTRAS. Both lines are exclusively devoted to acquisition of AE data.

Parameters like minimum and maximum AE wave duration have to be fixed properly because they may be responsible for an incorrect individualization, or a false monitoring, of events.

Hardware and software settings used in the tests, are all saved in the data directory.

At the beginning of each test, it is of great importance to check the quality of wave transfer between the sensor and the test specimen surface to avoid serious losses of signal. The interposition of *Silicon Grease* on the entire contact surface is crucial to improve transmission.
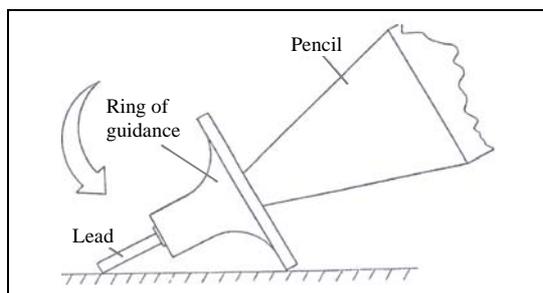
The instrument that allows checking wave transmission quality through the interface is the HSU-Nielsen test (Figure IV-29). It consists of cracking a pencil lead (hardness 2H, diameter 0.5, length 3 mm) on the sample's surface to have a standardized AE source. Reception must be checked. High amplitude hits have to be registered (close to 80-90 dB).

Figure IV-29: Hsu-Nielsen test

Test de Hsu-Nielsen

The AE transducers are firmly installed on a piece carrying the alumina pin of the deflection measurement (Figure IV-30).

The position of this piece allows it to be in a cold area and isolated from spurious vibrations of the machine frame, while being mechanically connected to the deformed specimen.

As the background noise closely depends on surrounding conditions, the threshold is changed for each test. It varies from 23 to 27dB.
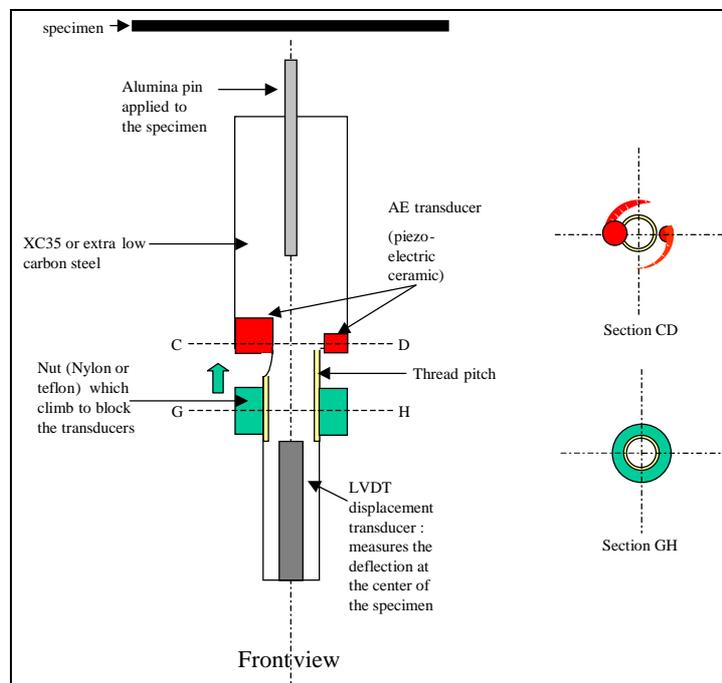
Figure IV-30: Device modifications to fix the AE transducers.

Modifications du montage pour fixer les capteurs d'EA.

IV. 4-PHBT RESULTS

IV.1. General behavior of non-oxidized specimens

Unoxidized steel specimens are first deformed in order to obtain the mechanical behavior of the steel substrate. This **reference test** is used later on to evaluate the oxide scale behavior. The measured load-deflection curves are smooth. Nevertheless, several remarks can be done concerning the steel behavior during hot deformation.

The importance of the thermal cycle

When the thermal cycle changes, the observed load levels are significantly different. Figure IV-31 represents load-deflection curves obtained with two distinct thermal cycles. The first one, called **direct**, directly reaches the temperature of deformation. The second one is our **standard** cycle previously described (Figure IV-26) : heating up to 900°C before reaching the temperature of deformation. The strong difference is mainly due to the grain size (Figure IV-32), which has a major impact on the mechanical behavior of the samples. The longer the high-temperature dwell, the larger the grain size, and bigger grains decrease the yield stress of the metal (the grain boundaries hinder plastic deformation by stopping dislocation glide) (Figure IV-31).
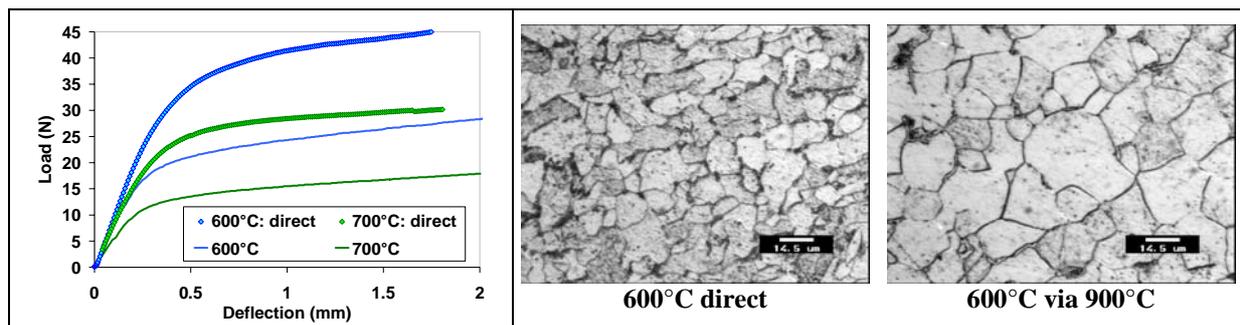
Figure IV-31: Thermal cycle influence on load-deflection curves.

Influence du cycle thermique sur les courbes force-flèche.

Figure IV-32: Optical micrographs of Ex-LC steel – Nital etching. Grain size difference depending on the heat treatment.

Micrographies optiques d'aciers extra doux (ExDx). Attaque au Nital. Différence de taille de grains en fonction du traitement thermique.
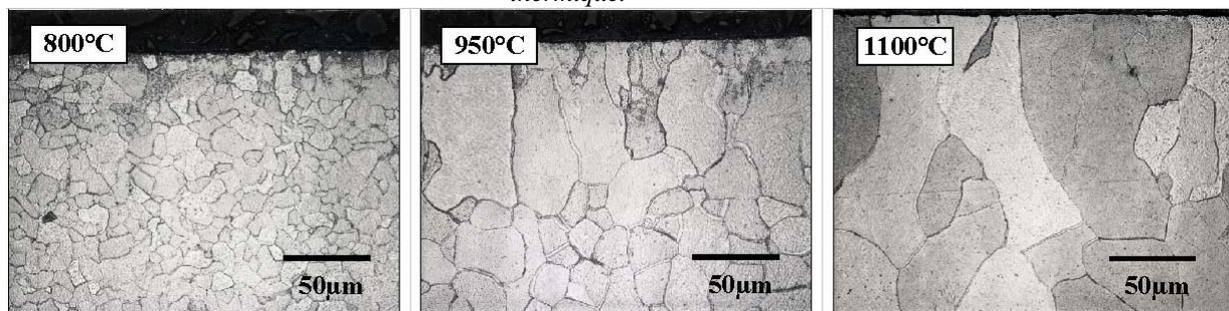
Figure IV-33: Optical micrographs of Ex-LC steel. Grain size difference depending on the high temperature dwell (idem for dwell time). Nital etching.

Micrographies optiques d'un acier ExDx. Différence de taille de grains en fonction de la température de maintien (ainsi que du temps de maintien). Attaque au Nital.

With our standard thermal cycle, the steel remains ferritic. Figure IV-33 shows the grain growth when steel goes though austenitic transformation (micrographs at 950 and 1100°C).

The time spent at this temperature is very important as well. Indeed, grains tend to grow as long as the specimen is maintained at high temperature. Thus, after less than two hours at 800°C, one grain covers the whole thickness of the specimen (1mm).

These observations have lead us to impose a strictly identical thermal cycle between oxidized and non-oxidized tests. This is necessary for "really comparable" tests and finally to determine the oxide scale behaviour by subtracting the steel behaviour.

Only the temperature of deformation, the strain rate and the chemical cycle (injection of oxidizing gas for oxidized samples) change from test to test.

General behavior and influence of creep

Load-deflection curves of steel specimens deformed at high temperature present two parts (Figure IV-34):
- A linear domain, which corresponds to the elastic deformation of the specimen;
- A second domain in which the load increases in a parabolic way with the deflection. It corresponds to the plastic deformation of the specimen.
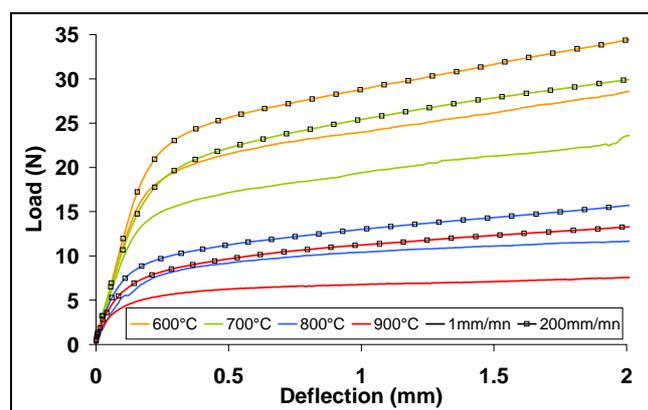
Figure IV-34: Curves of DDS non-oxidized steel tests

Courbes des tests avec acier DDS non oxydé.

The curves represented on Figure IV-34 show the temperature dependence of the material strength. The required load to deform a steel specimen is all the higher as the temperature is low. The steel also shows a strain rate dependency (hardening of the material when strain rate increases). In addition, the shape of the plastic part of the curves reminds of kinematic hardening [Bruh].

The curves obtained for tests performed at 1 and 200mm/min are quasi-parallel. This reflects an identical mechanism of plastic deformation.

Nevertheless, the curve corresponding to the test performed at 900°C and 1mm/mn is more flattened than the others. The deformation mechanism is probably different. For such a strain rate value and at high temperature, creeping phenomena perhaps occur in the deformation of the material, as suggested by the defromation maps of Figure IV-35). Indeed, several mechanisms are available at extremely low strain rate, whereas they do not have enough time to initiate at higher strain rate.

This kind of behavior is also found with the other steel grades tested at 1mm/min. It is sometimes initiated at lower temperature (800°C), as for the DP, Ex-LC and ReP steels.
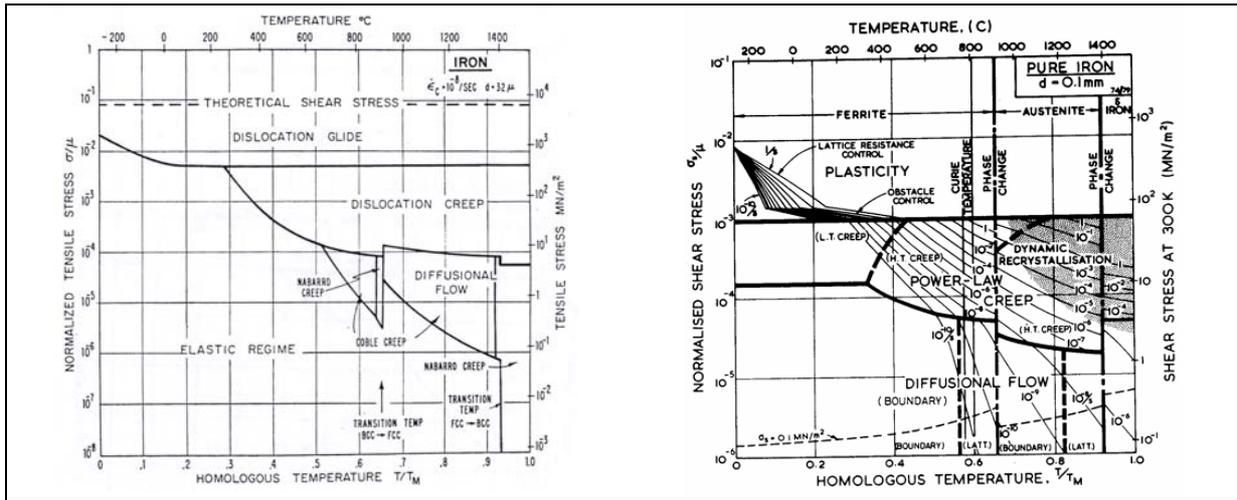
Figure IV-35: Iron deformation map [Ashby].

Carte de déformation du fer [Ashby].

Remarks on Young's modulus

1 - To validate the Young's modulus measurements, a stainless steel had been previously tested at IRSID in 4-PHBT and tension-compression test (T-CT). The chemical composition and measured Young's moduli are reported in Figure IV-36. Results obtained in 4-PHBT are in good agreement with those of T-CT.

C	Mn	P	Si	Ni	Cr	Mo	Nb	Ti	N
0.013	0.47	0.02	0.55	0.09	16.76	0.02	0.461	0.16	0.019
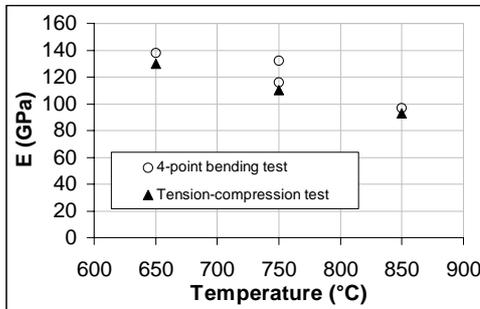
Figure IV-36: Stainless steel chemical composition (in 10^{-3}% in weight) and Young's modulus measured on specimens tested on 4-PHBT and tension-compression test at several temperatures.

Composition chimique d'un acier inoxydable (en 10^{-3}% massique) et module d'Young pour des échantillons testés en f4p et en traction-compression à différentes températures.

The Young's modulus can be directly calculated from the load-deflection curves thanks to the **beam theory**:

$$E = \frac{11.p.L^3}{768.I} [MPa] \qquad \textbf{eq. IV-1}$$

p is the load-deflection curve slope at the origin, L the distance between bottom tools and I the moment of inertia of the beam.

$$I = \frac{b.e^3}{12} [mm^4] \qquad \textbf{eq. IV-2}$$

where b is the width and e the thickness.

2 - Tests performed at low strain rate involve creep deformation, which decreases the apparent Young's modulus [Koz]. At higher strain rate creep has no time to occur. Thus the apparent Young's modulus is higher (Figure IV-37).

3 - We can also observe a difference of Young's modulus depending on the thermal cycle (slope of the curve at the origin, Figure IV-31).
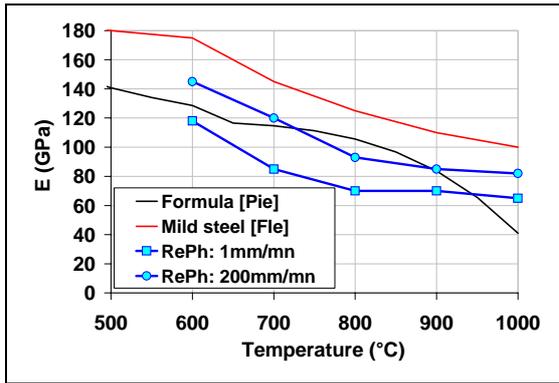
Figure IV-37: Strain rate influence.

Influence de la vitesse de déformation.

IV.2. <u>General behavior of oxidized specimens</u>

IV.2.1. Damage

Two kinds of behaviors have been identified for two temperature ranges. The critical temperature **Tc** (the limit between both behaviors) depends on many parameters such as the steel composition, the strain rate, the oxide thickness or the adherence and brittleness of the oxide scale (depending on the growth temperature, the oxidation atmosphere…).

- **For T < Tc:** The oxide-metal interface is very strong and even stronger than the oxide scale itself. In this case, damage occurs in the oxide scale, with the initiation of equidistant cracks (Figure IV-38).

a) ReN: deflection: 3mm -700°C-20mm/mn-oxide:80µm   b) Ex-LC: deflection: 2mm-600°C-20mm/mn-oxide:100µm   c) Ex-LC: deflection: 2mm-600°C-1mm/mn-oxide:100µm
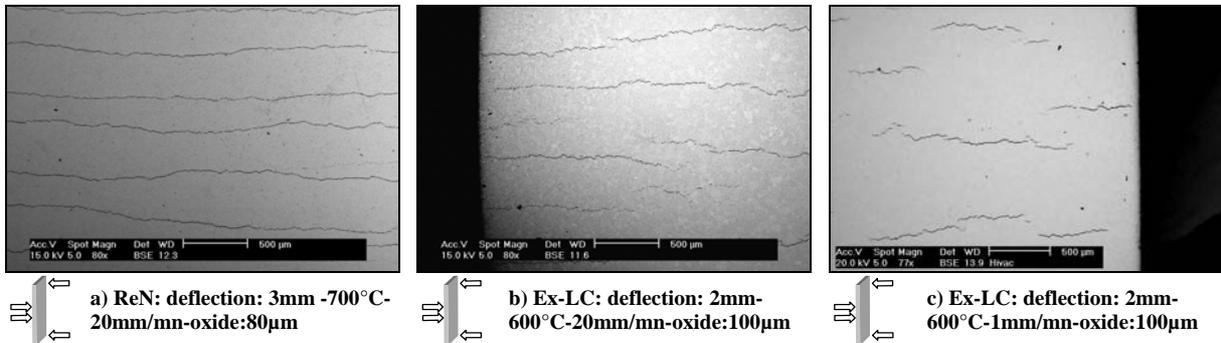
Figure IV-38: Equidistant crack network.

Réseau de fissures équidistantes..

Cracks propagate in the width direction of the specimen. In most cases, this propagation follows the oxide scale grains boundaries. This means that the stress relaxation in the oxide is performed by propagation of **intergranular cracks** (Figure IV-39).

a) Ex-LC: deflection: 2mm - 600°C -1mm/mn-oxide:70µm

b) Ex-LC: deflection: 2mm -700°C-20mm/mn-oxide:100µm
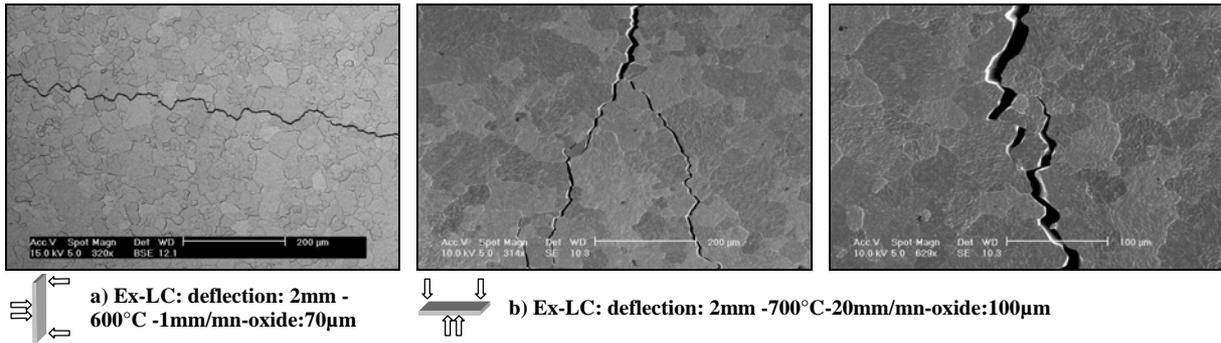
Figure IV-39: intergranular crack propagation.

Propagation de fissures intergranulaires.

a) Ex-LC: deflection: 1mm-600°C-1mm/mn-oxide:70µm

b) Ex-LC: deflection : 1mm-600°C-1mm/mn-oxide:70µm
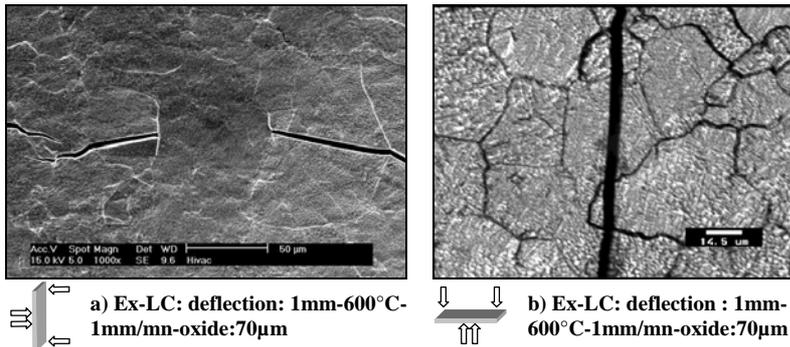
The propagation can be stopped by a perpendicular grain surface. In such rare cases, the crack propagates through the grain: transgranular propagation (Figure IV-40).

Figure IV-40: Transgranular cracks propagation.

Propagation de fissures transgranulaires.

Observations of specimens cross-sections confirms that cracks always cross the **entire** scale thickness. Indeed, post-deformation scale observations have never showed a crack interrupted in the middle of the scale thickness. They are therefore called **through-thickness cracks** or **through-scale cracks** in the following (Figure IV-41).
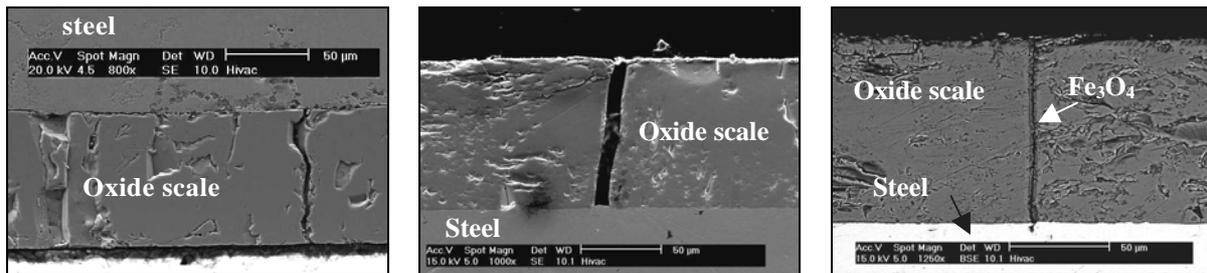
Figure IV-41: Micrographs of through-thickness cracks: Ex-LC: deflection: 2mm - 600°C -1mm/mn-oxide:100µm. Left and middle: micrographs in SE mode / Right: micrograph in BSE mode: FeO is decomposed in $Fe_3O_4 \Rightarrow$ mechanical crack.

Micrographies de fissures transverses : ExDx: flêche: 2mm - 600°C -1mm/mn-oxyde:100µm.
Gauche et milieu : micrographie en mode SE.
Droite : micrographie en mode BSE : FeO est décomposé en $Fe_3O_4 \Rightarrow$ fissure mécanique.

Through-thickness cracks can sometimes propagate from a crack tip along the interface (**interfacial crack**) (Figure IV-42). This phenomenon can lead to the total delamination of an oxide particle when the interfacial crack meets the neighbouring through-thickness crack.
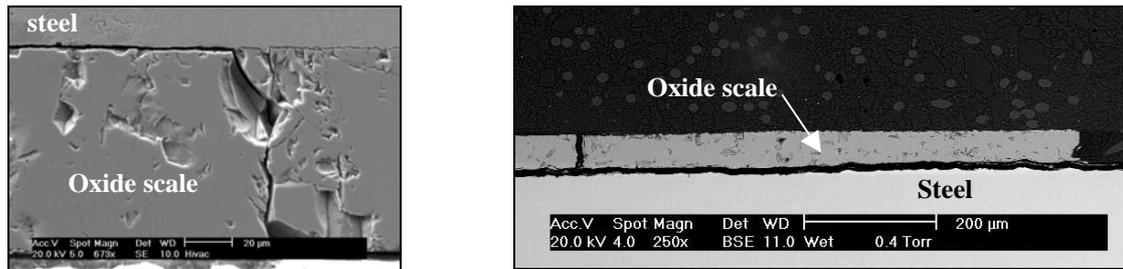
Figure IV-42: Micrographs of a through-thickness crack followed by an interfacial crack. <u>Left</u>: Ex-LC: deflection: 2mm-600°C-1mm/mn-oxide:100µm / <u>Right</u>: Rep: deflection:5mm-600°C-1mm/mn-oxide:60µm.

Micrographies de fissures transverses suivies de fissures interfaciales. <u>Gauche</u> : ExDx : fl:2mm-600°C-1mm/mn-oxyde:100µm / <u>Droite</u> : Rep: fl:5mm-600°C-1mm/mn-oxyde:60µm.

- **For T ≥ Tc:** Stress relaxation of the bimaterial occurs by plastic deformation of the oxide scale, without any transverse crack. A decohesion at the metal-oxide interface can also relax the stresses. In fact, the critical stress of decohesion is reached in this case before the failure of the oxide scale (Figure IV-43).
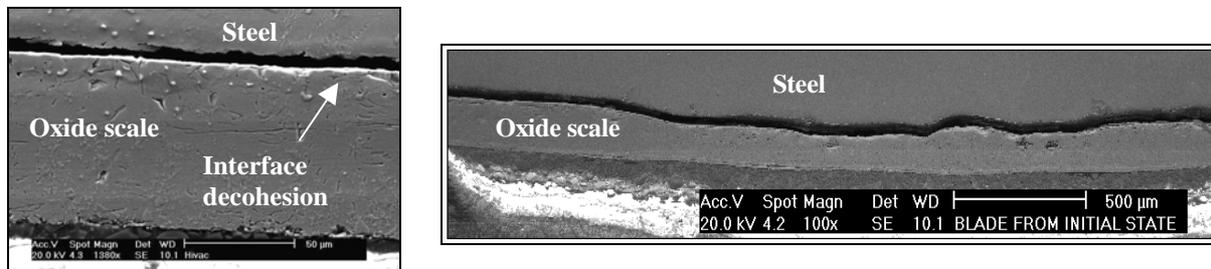
Figure IV-43: Decohesion at the metal-oxide interface. Ex-LC: deflection: 2mm - 1mm/mn-oxide:100µm. <u>Left</u>: 700°C / <u>Right</u>: 800°C.

Décohésion interfaciale métal-oxyde. ExDx: flèche : 2mm - 1mm/mn - oxyde:100µm.
<u>Gauche</u> : 700°C / <u>Droite</u> : 800°C.

Interfacial decohesion represented on Figure IV-43 were not visible before specimen cross-section observation : scales seemed to be adherent. It is thus possible, and even probable, that decohesion is due in these cases to the retraction of the resin coating during embedding of the specimens. Nevertheless, this phenomenon has been principally observed on samples deformed at high temperature. Thus, the crack-less, plastic deformation of the oxide scale seems to weaken the bimaterial interface.

IV.2.2. A granular structure

The oxide surface is made of grains, visible in Figure IV-39 or Figure IV-40. A similar crack pattern is often observed in brittle coatings on ductile substrates under biaxial tensile stress.
They are observed even on the non-deformed specimens (Figure IV-44a). In this case, the scale fragmentation in grains is due to the thermal stresses induced by the specimen cooling.
It is possible that the fragmentation only concerns the first, extreme surface oxide (Fe_3O_4). The delamination of the latter can be observed on Figure IV-44c.
Near the specimen edges, the grain size is divided by 2 (high deformation zone near a geometric singularity). Logically enough, in most cases cracks start from the sides, where the required energy to initiate an intergranular crack is lower.

a) Thermal cycle without any deformation.   b) defl:0.6mm - 700°C -1mm/mn.   c) defl:0.3mm - 600°C -1mm/mn.

d) defl:2.5mm - 600°C -1mm/mn.   e) defl:0.3mm - 600°C -1mm/mn.   f) defl:0.6mm - 600°C -1mm/mn.
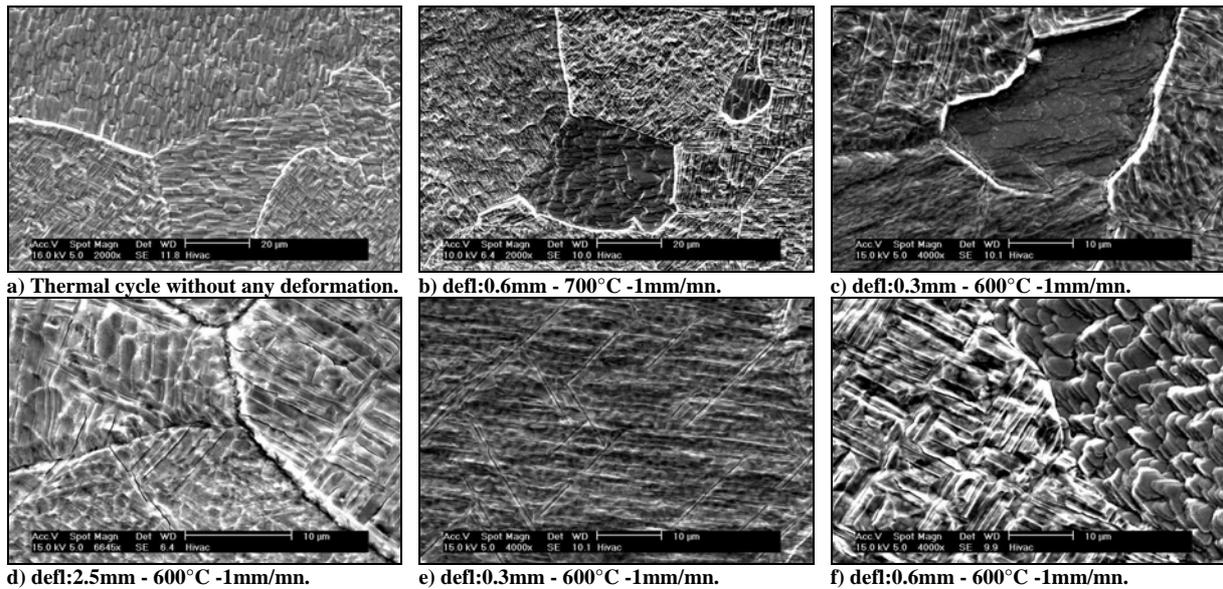
Figure IV-44: Ex-LC steel specimens: SEM micrographs of the oxide scale surface aspect. Oxide:100µm

Eprouvette d'ExDx: micrographies MEB d'aspects de surface de la calamine. Oxyde:100µm

A lot of information is available from the different micrographs represented in Figure IV-44 :

- All the grains are oriented differently (a,b,f).
- The fragmentation can lead to the delamination of the surface oxide scale (c).
- This delamination uncovers the FeO layer, which seems to be plastic.
- On the contrary, the Fe_3O_4 surface layer seems to be **brittle**. Indeed, observing with attention micrographs d), e) and f), many microcracks are visible inside grains. The micrograph e) suggests that they **follow the crystallographic network**. Indeed, the angles between the cracks are perfectly reproducible.
- Nevertheless, it is impossible to determine the nature of the oxide by this way. For example the angles of 60° formed by the cracks could be due to a CC grain structure oriented along a (111) plan. This oxide could be Fe_2O_3. The 90° angles on micrograph f) could confirm the nature of the oxide with an orientation of a Fe_2O_3 grain along a (110) plane for example. However these interpretations have to be done with much care, as the perspective effect makes any interpretation concerning the oxide nature quite dangerous.
- These microcracks have not been observed at high temperature (e.g. 900°C) due to the oxide plasticity at such high temperatures. However, the fragmentation is still present.

IV.2.3. Experimental load-deflection curves

An example of experimental curves is represented on Figure IV-45. They correspond to oxidized Ex-LC steel specimen (scale 100µm thick) deformed at 1mm/min, and temperatures between 600 and 900°C. The general shape of the curves seems quite similar to those from non-oxidized specimens, with a linear elastic part followed by a "parabolic" plastic part.

Nevertheless, a significant difference can be noted. Curves obtained from the tests on non-oxidized samples were smooth. Those from oxidized specimens reveal many accidents like small hooks (load drop), brutal load increase or oscillations. Figure IV-46 shows the load-deflection curves obtained with several tests performed at 700°C. They are different but superimpose at the end of the deformation.

At the beginning of the study, these accidents appeared in most cases for tests performed at low temperature. At higher temperature, the curves were more continuous. All curves discontinuities were then interpreted as crack initiations or interface delamination. The AE technique however suggested that it was not always the case, as will be detailed later in paragraph V.
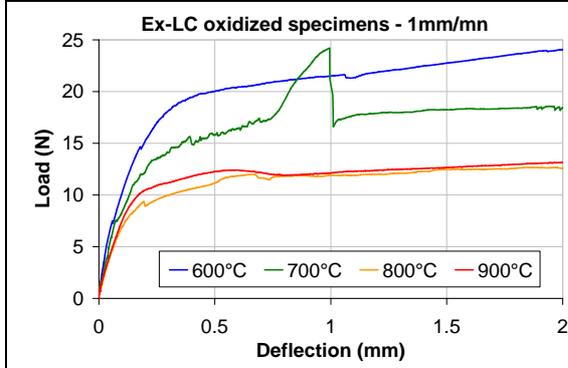
Figure IV-45: Load-deflection curves of oxidized Ex-LC steel. Oxide:100μm – 1mm/min

Courbes force-flèche d'aciers oxydés ExDx. Oxyde : 100μm – 1mm/mn
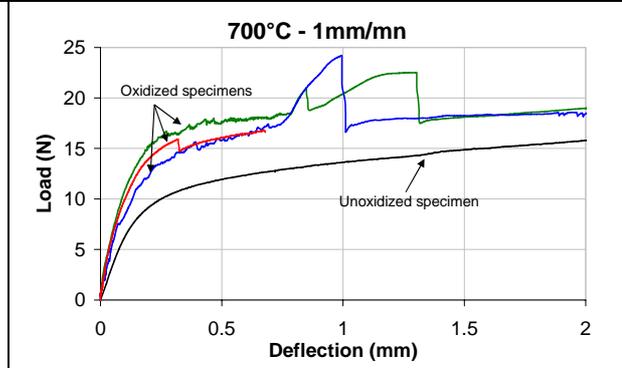
Figure IV-46: Several oxidized Ex-LC steel specimens deformed at 700°C. Oxide:100μm – 1mm/min

Plusieurs échantillons ExDx déformés à 700°C. Oxyde:100μm – 1mm/mn

IV.3. <u>Influence of the 4-PHBT parameters on scale damage</u>

IV.3.1. Temperature influence

The temperature effect on the oxide scale has been described previously. We have seen the oxide scale cracking at 600°C and at 700°C for sufficiently high strain rate. At higher temperature (800°C or 900°C), ductile deformation was experienced whatever the velocity.

Nevertheless, an interesting point: fracture is again observed during tests at 1000°C (Figure IV-47). These specimens have been oxidized under the same conditions as the others (at 900°C). All steel grades tested at such a temperature have shown this behavior.

The through-scale cracks network observed is certainly due to thermal stresses involved by the specimen heating between 900°C and 1000°C. Steel phase change (ferritic⇒austenitic) reinforce this phenomenon. Indeed, the high dilatation coefficient of austenite increases thermal stresses. In addition, the grains transformation as well as their growth has probably an influence on the bimaterial interface.
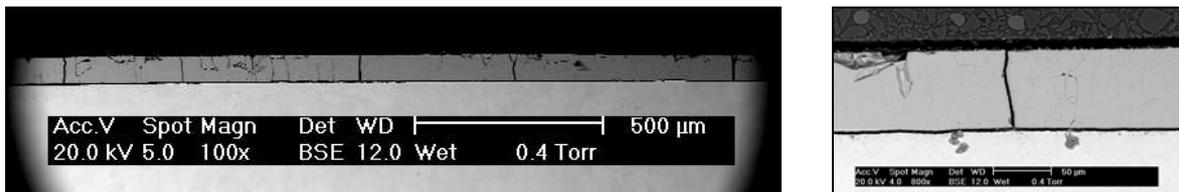
Figure IV-47: Micrograph of ReP specimen cross-section: defl: 3mm – 1mm/min – oxide: 70μm – 1000°C.

Micrographie d'une coupe d'éprouvette en ReP: flèche: 3mm – 1mm/mn – oxyde: 70μm – 1000°C.

IV.3.2. Strain influence
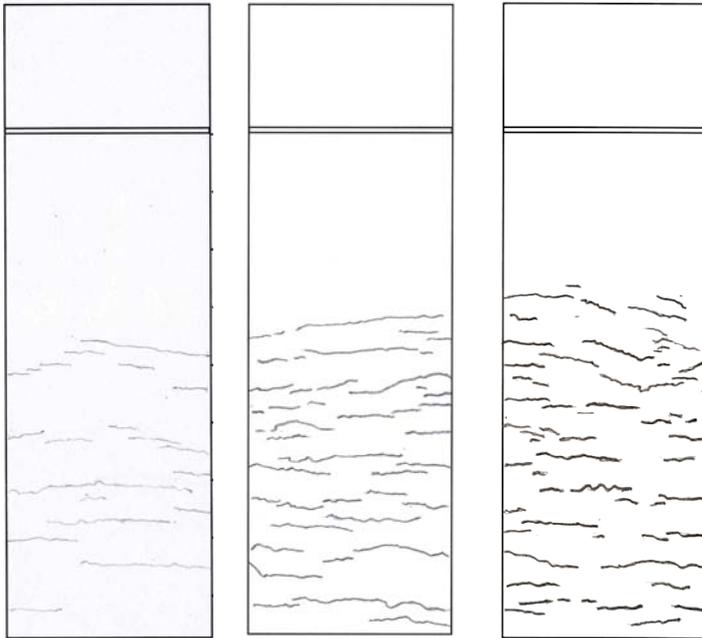
The number and the density of cracks increase with the deformation of the specimen. Cracks seem to be always equidistant, at each step of the deformation.

An extension of the crack network towards the outermost tool-rolls can be observed with the increase of the deformation.

For significantly higher strain, the mechanism of though-thickness cracks initiation is replaced by a delamination process. Thus, ReP steel specimens deformed at a deflection of 5mm have been totally delaminated.

Figure IV-48: Ex-LC deformed using 4-PHBT: 600°C - 1mm/min - oxide: 100µm. Crack mapping of oxidized half-samples; From the left to the right: deflection = 0.25 mm, 1.2 mm, 2 mm.

ExDx deformé en f4p : 600°C-1mm/mn-oxyde: 100µm. Cartographies de fissuration de demi-éprouvettes oxydées; De la gauche vers la droite : flêche=0.25 mm – 1.2 mm – 2 mm.

IV.3.3. Steel grade influence

Several steel grades have been studied. Fragile / ductile transitions are rather similar in a velocity / temperature diagram (Figure IV-55). However, strong ductility differences show up by the density and the nature (transverse / interfacial) of the cracks. Steel grades tested can be classified in two categories :

- The first group represents the steel grades which grow "**adherent**" oxide scales. Cross-sectional microscopic observation of deformed specimens has shown a strong cohesion between the steel substrate and the oxide scale. **Ex-LC** steel, **DDS** steel and **DP** steel belong to this category.
- The second group (**ReN** steel, **ReP** steel and finally the high-manganese steel **H-Mn**)show a much weaker adherence.

Figure IV-49 represents the load-deflection curves of ReP steel at 200mm/min. Figure IV-50 shows spallation of oxide parts - only at 600°C and 700°C. The existence of cracks on the semi-adherent oxide raft still present at the center of the specimen deformed at 700°C, confirms the assessment of a first initiation of through-thickness cracks, followed by interfacial cracks and spallation (Figure IV-50).

As a consequence, load-deflection curves of unoxidized specimens at 600°C and 700°C lie above those of oxidized specimen at the same temperature. The rason is that the steel

substrate is consumed during oxidation; thus, after oxide delamination (Figure IV-50), the remaining metal is thinner than non-oxidized specimens and therefore weaker.
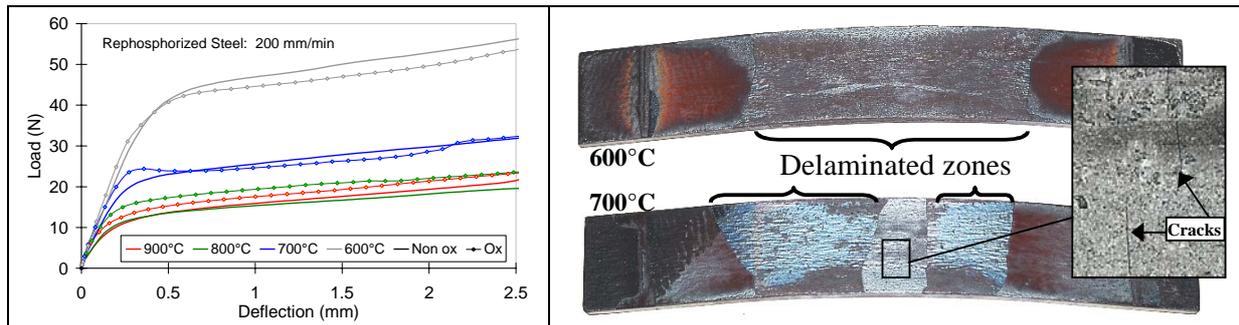
Figure IV-49: ReP: 4-PHBT curves obtained at 200mm/mn. deflection: 3mm - oxide:90µm

ReP: courbes de f4p obtenues à 200mm/mn. flêche: 3mm - oxyde: 90µm

Figure IV-50: ReP specimens corresponding to the curves at 600°C (top) and 700°C (bottom). Deflection : 3mm -200 mm/min - oxide: 90µm.

Eprouvettes ReP correspondant aux courbes à 600°C (haut) et 700°C (bas). flêche: 3mm – 200 mm/min - oxyde: 90µm.

The high-manganese H-Mn Steel is the best example of the influence of the steel grade on the oxide scale behavior. An ARCELOR development project on a high-manganese content austenitic steel (22% Mn - 0.6% C) has required to control the surface quality of this new product. We have therefore studied the H-Mn oxidation kinetics and the mechanical behavior of its oxide scale using 4-PHBT.

The oxidation kinetics is very slow compared to the other steel grades studied, due to the Mn additional element (oxidation time at 900°C for an oxide scale 100µm thick: ~13 min for H-Mn / ~8 min for the others).

The 4-PHBT has shown the brittleness of the oxide scale formed on the H-Mn steel and its **extremely weak adherence**. Indeed, the oxide scale on deformed specimens was completely spalled in most cases. Tests performed even **without any deformation** have shown that thermal stresses were sufficient to spall the scale.

Thus, it has been impossible to characterize the oxide scale of this steel grade.

IV.3.4. Scale thickness influence

4-PHBT have been performed with an oxide scale 90-100µm thick in most cases. In hot rolling, and more particularly in the finishing mill, its thickness is rather around 15-30µm.

The Irsid researchers thought at the beginning of the campaign that for such a scale thickness, it would be impossible to obtain the oxide scale mechanical behavior (and the behavior laws), because the oxide strength contribution would have been too small, the load-deflection curves of oxidized and unoxidized specimens almost superimposed. In addition, the oxidation system does not allow homogeneous thin scales to be built at too short oxidation times.

Nevertheless, several tests with thinner scales have been performed. An example is given Figure IV-51 with the Ex-LC steel grade. Two tests with oxide scale 70µm and 100µm thick are compared. For this steel grade as well as for the others, the observations have led to the conclusion that the number of cracks **slightly increases** when thickness decreases. At the same time, the **adherence also increases.**
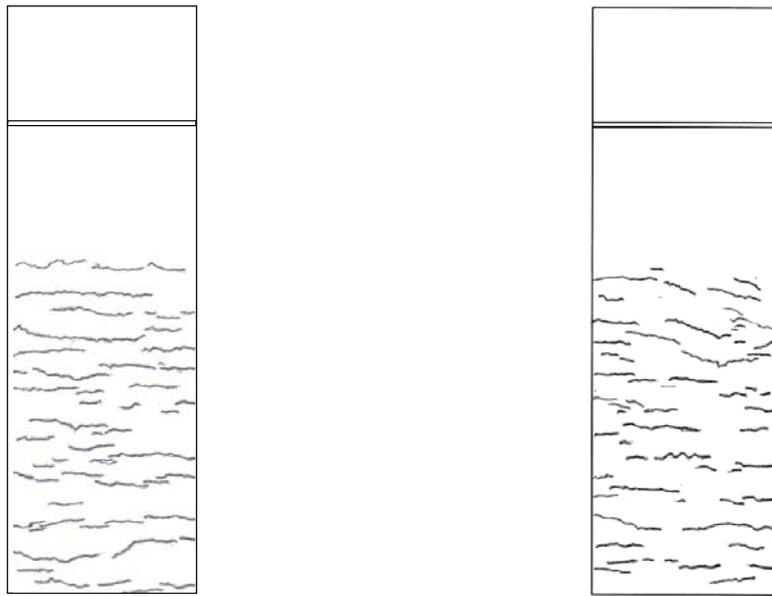
Figure IV-51: Ex-LC: 600°C-deflection = 2 mm - 1mm/min. <u>Left</u>: 70μm / <u>Right</u>: 100μm

ExDx: 600°C – flèche = 2 mm – 1 mm/min - <u>Gauche</u>: 70μm / <u>Droite</u>: 100μm

IV.3.5. Strain rate influence

DDS-700°C-50mm/mn
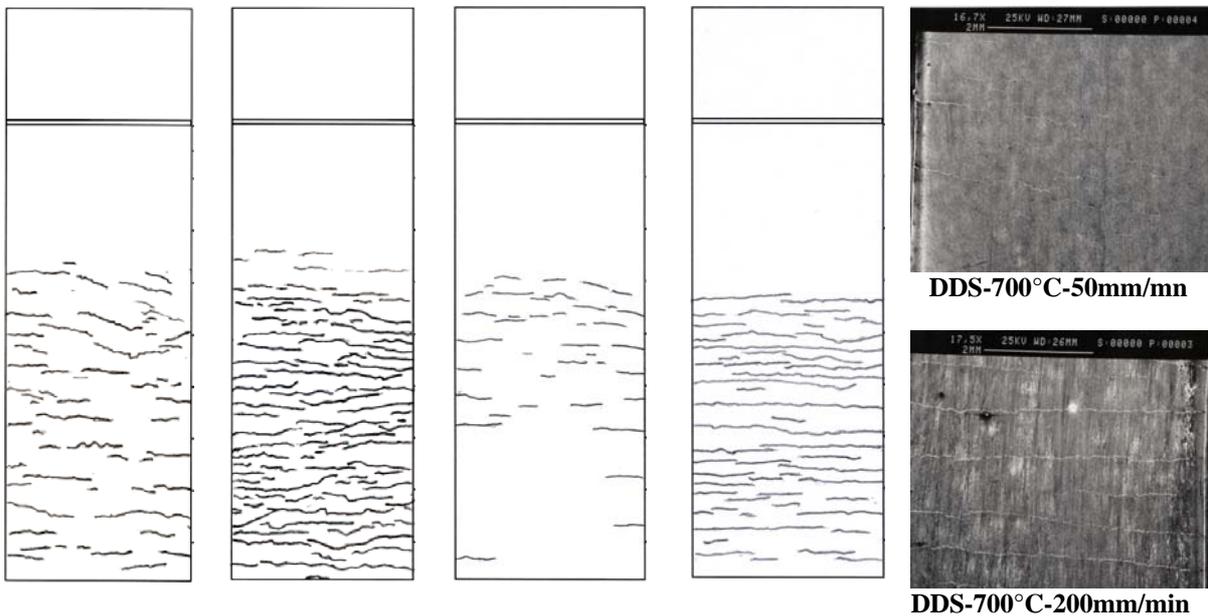
DDS-700°C-200mm/min

Figure IV-52: Ex-LC: 600°C-deflection = 2 mm - 100μm. <u>Left</u>: 1 mm/min ; <u>Right</u>: 20 mm/min

ExDx: 600°C-flêche=2mm - 100μm. <u>Gauche</u> : 1mm/mn ; <u>droite</u> : 20mm/mn

Figure IV-53: DDS: 700°C – deflection 3mm - 80μm. <u>Left</u>: 50 mm/min ; <u>Right</u>: 200 mm/min

DDS: 700°C-flêche 3 mm – 80 μm. <u>Gauche</u>: 50 mm/mn ; <u>droite</u> : 200 mm/mn

Figure IV-52 and Figure IV-53 emphasize the **high influence of the strain rate** on the oxide scale behavior and on its damage. This point is extremely important to conclude on the oxide viscoplastic deformation, even at low temperature such as 600°C. Indeed, an elastic material

152

has no strain rate sensitivity. In Figure IV-52, a significant increase of the crack number can be observed at 600°C for tests at 20 mm/min as compared to 1 mm/min. Figure IV-53, which represents a test at 700°C, confirms this trend. Indeed, cracks are totally absent from specimens deformed at 1mm/min ; they start to appear at 50 mm/min, and build a dense network at 200 mm/min.
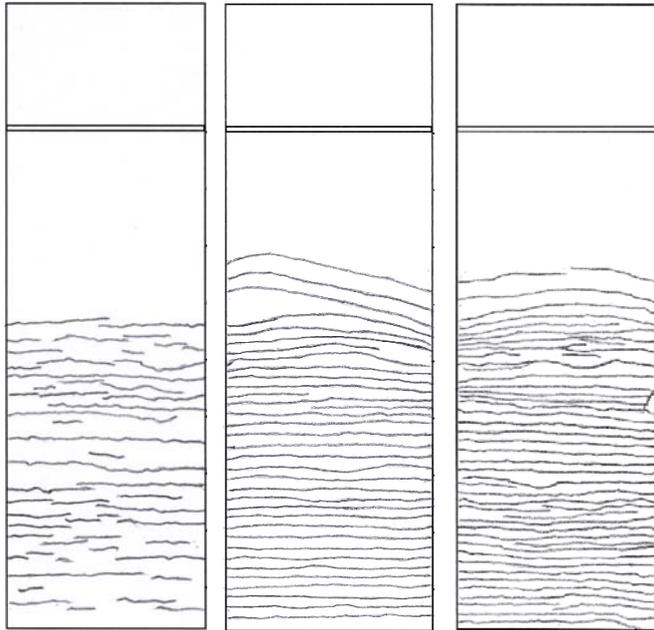
An additional effect of the strain rate influence is the crack propagation in the width direction of the specimen : at high strain rate, cracks cross all the specimen width (Figure IV-54).

It would be interesting to perform interrupted tests at such a strain rate, to see if cracks propagate smoothly or if they instantaneously cross the entire specimen after initiation.

Low temperatures reinforce this phenomenon. Indeed, at 600°C, the specimen seems to be more brittle than at 700°C (Figure IV-54).

Nevertheless, cracks always remain intergranular.

Figure IV-54: deflection =3 mm - 80μm – 200 mm/min. Left: DDS-700°C ; Middle: DDS-600°C ; Right: ReN-600°C

flêche=3 mm - 80μm – 200 mm/mn. Gauche: DDS-700°C ; Milieu: DDS-600°C ; Droite: ReN-600°C

IV.3.6. Summary of parameters influence
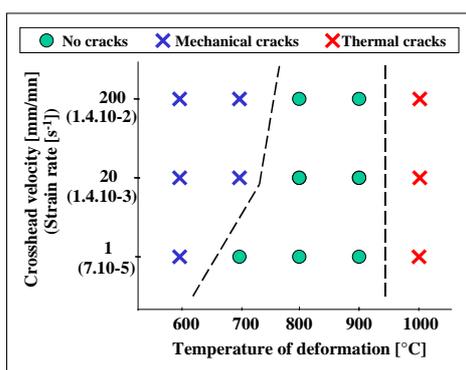
Figure IV-55: Schematic representation of oxide scale damage in 4-PHBT as a function of temperature and strain rate. Strain ~ 0.5%.

Représentation schématique de l'endommagement de la calamine en fonction de la température et de la vitesse de déformation. Déformation ∼ 0.5%.

Several parameters have an influence (more or less important) on the oxide scale behavior during 4-PHBT. The general behavior is given Figure IV-55:

- Strain: Cracks start to appear at a given deformation, which corresponds to a critical stress value. The number of cracks increases with strain until a dense network of equidistant cracks is formed. Distance between cracks decreases with a strain increase. A second effect of the strain increase is the propagation of cracks through the specimen width.
- Strain rate: a high strain rate sensitivity has been evidenced. Crack number significantly increases with strain rate. Cracks can also be initiated at higher temperature if the strain rate is high.

- Scale thickness: Two evolutions have been noted when thickness decreases: a slight increase of crack number and a better adherence of oxide scales on steel substrates.
- Steel grade: Steel grade has a major influence on the oxide scale behavior during 4-PHBT, mainly in terms of adherence at the bimaterial interface.

IV.3.7. Crack density

The influencing parameters in terms of crack density are the strain, the strain rate, the temperature and the steel grade. Crack density variations induced by thickness changes are too small to conclude on its influence (but the thickness range tested was also very narrow).
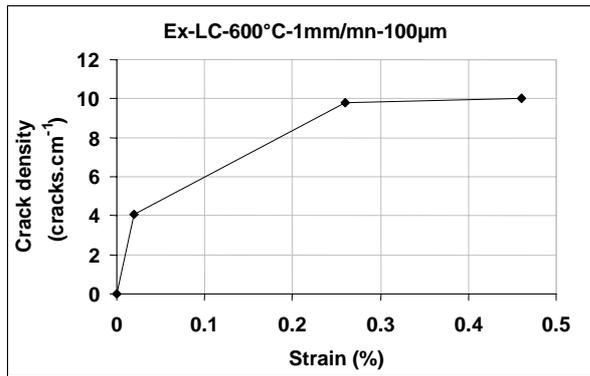
Figure IV-56: Crack density in the oxide scale as a function of strain for Ex-LC samples schematically represented in Figure IV-48.

Densité de fissures dans la calamine en fonction de la déformation pour les éprouvettes d'ExDx représentées schématiquement Figure IV-48.

Figure IV-56 describes the strain dependence of crack density. In [Brun], the authors obtain a similar curve shape with specimens constituted of NiO scales on Ni substrates deformed at RT. At high deformation, their curve, as ours, tends to a saturation value. Their observations show that this value corresponds to the beginning of the delamination process. In our study however, delamination appears only for ReP steel at significantly higher strain rate (0.014 s^{-1}). From Figure IV-57, the saturation crack spacing value from which delamination starts would be ~300-400µm (taking for ReP the maximal value of crack density reached).

Two phenomena can explain why delamination does not appear when crack density reaches a saturation value in our test:

- The first one is the propagation across the specimen width, which induces a stress relaxation.
- The second reason is the extension of the crack network towards the outmost rollers, which also allows relaxing the stresses sufficiently to avoid scale delamination.

Crack density evolution as a function of strain rate, steel grade and temperature is represented Figure IV-57. The crack density increases when temperature decreases (oxide scales is more brittle at low temperature). A logarithmic dependence on strain rate can also be observed. The slopes of the curves at 600°C and 700°C are quite similar. It would be perhaps interesting to estimate the crack density ρ_{cracks} by the expression below:

$$\ln \rho_{cracks}\left(h_{ox}, \varepsilon, \dot{\varepsilon}, T\right) = \alpha\left(h_{ox}, \varepsilon\right).\ln\left(\frac{\dot{\varepsilon}}{\dot{\varepsilon}_0}\right) + \beta\left(h_{ox}, \varepsilon\right).\frac{T}{T_{RT}} + \gamma\left(h_{ox}, \varepsilon, T\right) \qquad \textbf{eq. IV-3}$$

where $\alpha\left(h_{ox}, \varepsilon\right)$ is the strain-rate dependence of crack density (for an elastic material e.g., α=0), which depends on the scale thickness h_{ox} and the strain ε, $\beta\left(h_{ox}, \varepsilon\right)$ is the temperature

coefficient, and $\gamma(h_{ox}, \varepsilon)$ is a constant. This law could be refined to include steel grade dependence. T and T_{RT} are respectively the temperature of deformation and the room temperature. $\dot{\varepsilon}_0$ is the minimal strain rate used in tests.
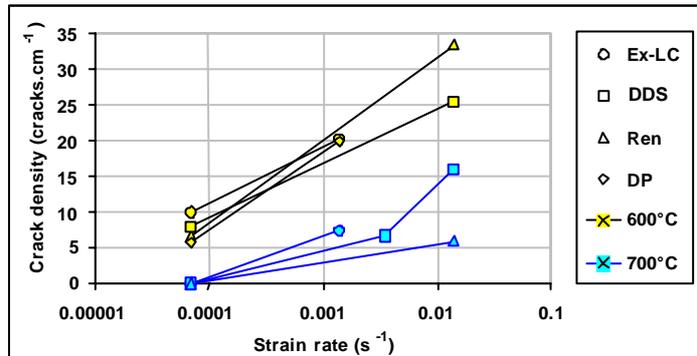
Figure IV-57: Evolution of several steel grades crack density versus strain rate at 600 and 700°C.

Evolution de densités de fissures de différentes nuances d'aciers en fonction de la vitesse de déformation à 600 et 700°C.

Evaluations of crack spacing versus scale thickness by Nagl et al. have been presented in chapter II (Figure II-45). At a strain rate of 10^{-4} s^{-1} and at 550°C, they obtained a crack spacing of 550µm for a 60 µm-thick oxide scale. Using their thickness dependence, an extrapolation for a 100 µm-thick scale gives a crack spacing of 800 µm. Under quasi-identical conditions (600°C instead of 550°C), we obtain a crack spacing of 1mm (Figure IV-57). Results are thus in reasonable agreement.

V. THE SIGNIFICANT CONTRIBUTION OF THE AE

Only the Ex-LC steel grade has been tested in 4-PHBT coupled with acoustic emission. [APPENDIX 4] presents the Acoustic Emission Technique.

V.1. First works

At the beginning of the study, the analysis of the oxide scale behavior was made by comparing the events visible on the load-deflection curves and the microscopic observations of the specimen after the test.

As has been explained previously, two kinds of behaviors have been identified for two ranges of temperature, with a critical temperature depending on many parameters :

- For T < Tc: damage occurs in the oxide scale, creating equidistant through-thickness cracks sometimes followed by interfacial cracks.
- For T ≥ Tc: stresses relaxation at the interface of the bimaterial occurs by plastic deformation without any transverse crack.

But these post-mortem observations were really insufficient to determine critical stresses for damage criteria. Misinterpretation of load-deflection curves lead us to false determinations of critical stresses. For example, we associated the first little hook visible on the curves with the first crack. The interest of AE lies in helping in the interpretation of this kind of events to determine critical stresses. Tests coupled with AE technique have therefore been undertaken.
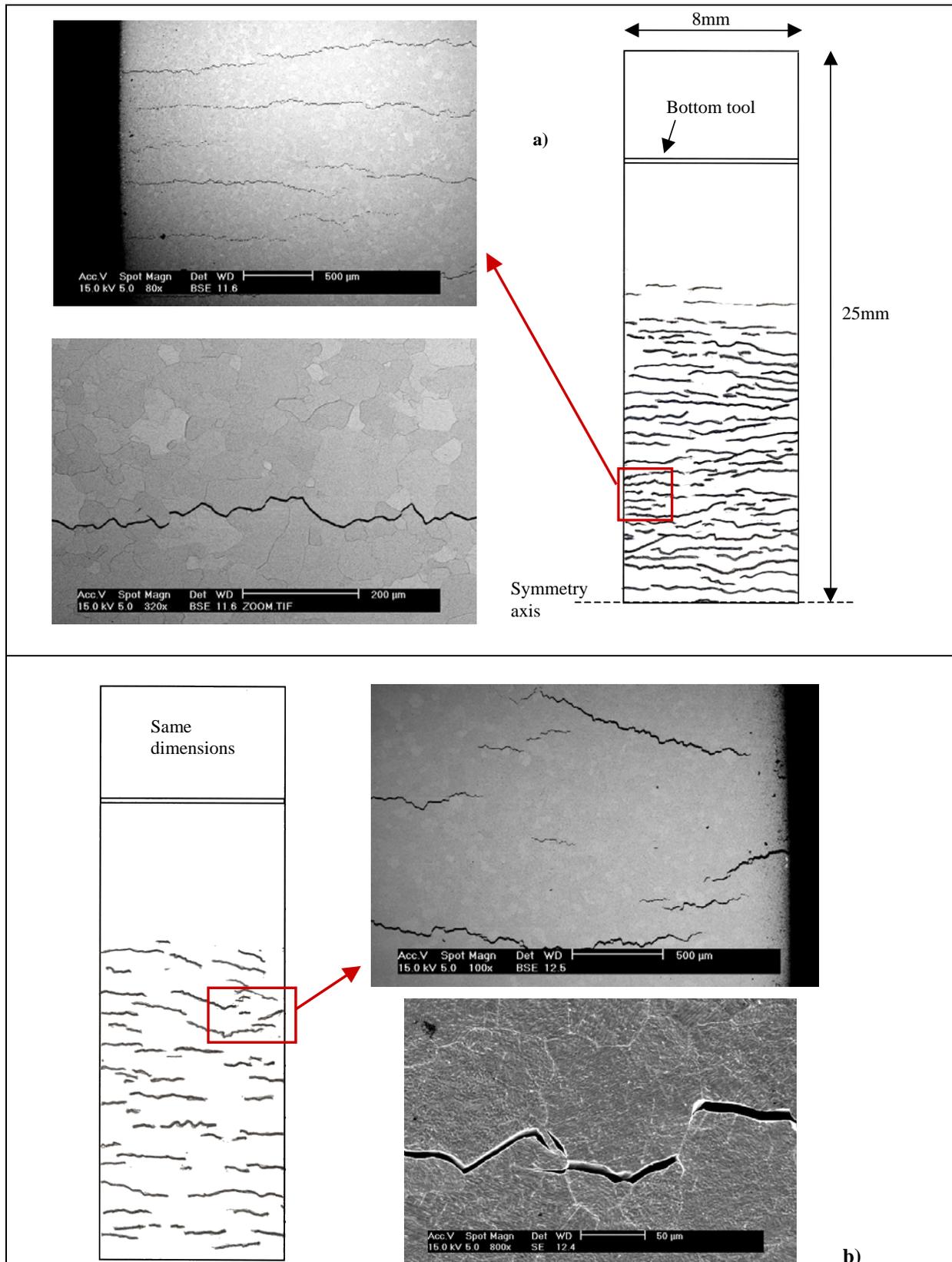
Figure IV-58: Crack maps of half specimens after deformation : T=600°C ; scale thickness = 100µm ; deflection=2mm   a) Test n°1 : v = 20 mm/min   b) Test n°2 : v = 1 mm/min

Cartes de fissures de demi-éprouvettes après déformation : T=600°C ; épaisseur de calamine = 100µm ; flèche =2mm   a) Test n°1 : v = 20 mm/min   b) Test n°2 : v = 1 mm/min

V.2. Crack initiation

It has been easy for us to determine the AE events connected to the oxide failure, and this for two main reasons:
- The test with only steel does not generate detectable signals;
- Most of the time, emissions caused by plastic deformation are below the threshold.

However, for T>Tc, with the extra low carbon steel Ex-LC, and in the range of strain rate and strain used for the tests, the post-mortem observations have shown that there was only plastic deformation and no delamination or interface sliding. These kinds of damage had been observed for other steel grades.

In conclusion, tests without scale made at high temperature (T > Tc) and those without cracks do not give any AE signal.

In Figure IV-59 and Figure IV-60, there are many events on the curves of tests n°1 and n°2 represented Figure IV-58. The number of bursts is approximately proportional to the population of cracks, but it is impossible to quantify them exactly, due to the occurrence of artifact events as we will see in the next paragraph.
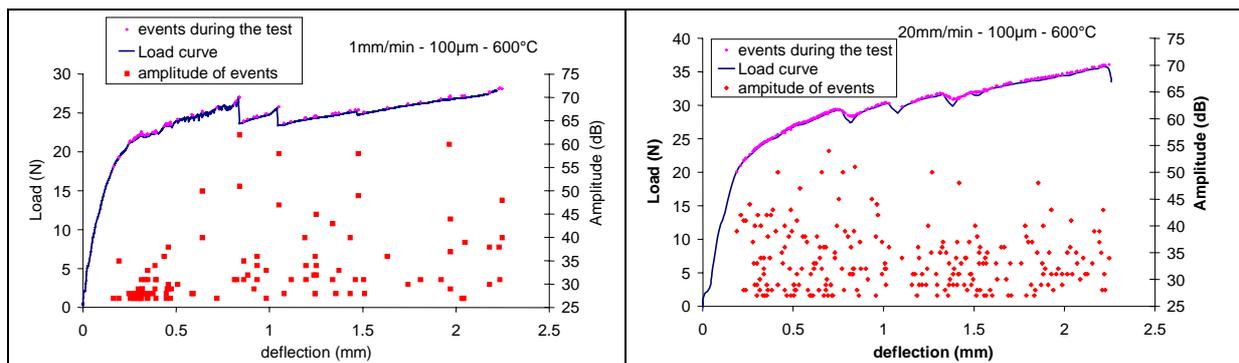
Figure IV-59: AE of test n°2 at 1 mm/min

EA du test n°2 à 1mm/min

Figure IV-60: AE of test n°1 at 20 mm/min

EA du test n°1 à 20mm/min

There are also large load drops, identified as cracking or interface damage before AE was used. But the observation of specimens has shown that there is nothing in the interface and that the number of cracks is much higher than the number of hooks on the curves. We thus concluded that our initial interpretation was wrong.

V.3. Identification of events

To understand how AE allows the identification of events, the simplest way is to take an example : three tests at 600°C, 1 mm/min (Figure IV-61):
- Steel-only specimen, deflection 2mm
- steel covered by 70µm of oxide, deflection 2 mm(test n°4)
- steel covered by 70µm of oxide, test interrupted at a deflection of 0.7 mm, i.e. before hooks (test n°3)
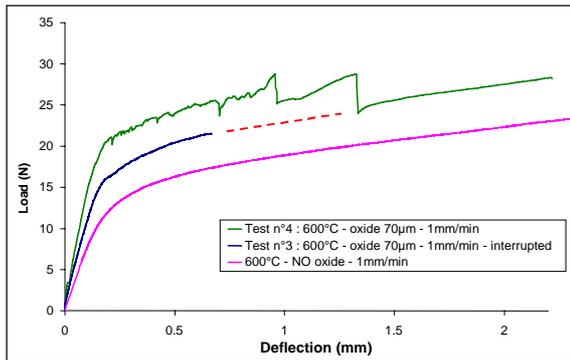
Figure IV-61: Two identical tests with different load-deflection curves. A prolongation of curve n°3 leads to a superposition with curve n°4.

Deux tests identiques avec différentes courbes force-flèche. Une prolongation de la courbe n°3 mène à une superposition avec la courbe n°4.

Normally, both oxidized test curves should be superposed; but this is not the case. Nevertheless, a prolongation of the interrupted curve seems to join the other in the end.
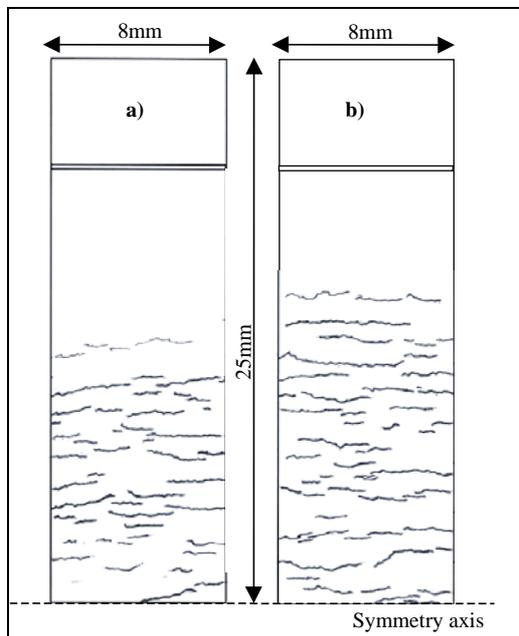
Figure IV-62: Crack maps of half-specimens after deformation : T=600°C ; scale thickness = 70μm ; v=1 mm/min   a) Test n°3 : deflection=0.7 mm   b) Test n°4 : deflection = 2 mm

Carte de fissuration de demi-éprouvettes après déformation : T=600°C ; épaisseur calamine = 70μm ; v=1mm/min   a) Test n°3 : flèche=0.7 mm   b) Test n°4 : flèche = 2 mm

The observation of specimen surfaces shows that there is approximately the same number of cracks on both (Figure IV-62). Thus, the major part of the opening of cracks appears in the first stage of deformation, before deflection reaches 0.7mm.

AE spectra of these two tests confirm this first observation :

- AE appears near **yielding** of the bimaterial (Figure IV-63-Figure IV-64).
- Events practically disappear between 0.6 and 0.9 mm (Figure IV-64).

Due to the attenuation of the surface wave, it is impossible to decide which amplitude range is typical of crack opening because amplitude depends significantly on the distance between the event location to the transducer (due to attenuation of the wave).

Thus, any single parameter is generally insufficient to conclude and identify the origin of a burst. Several parameters have to be examined together and correlated.
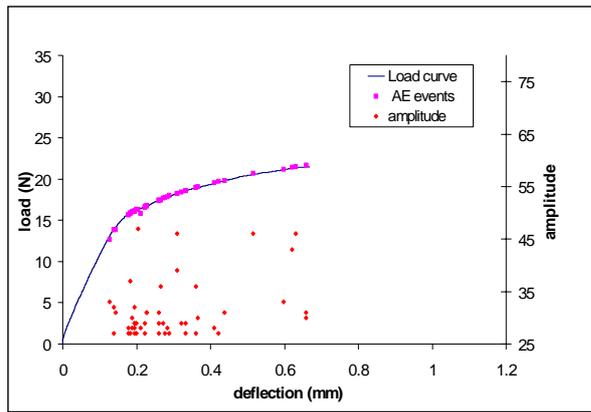
Figure IV-63: AE of test n°3 at 600°C – 1 mm/min – 100 µm – deflection = 0.7 mm

EA du test n°3 à 600°C - 1mm/min – 100µm – flèche=0,7mm
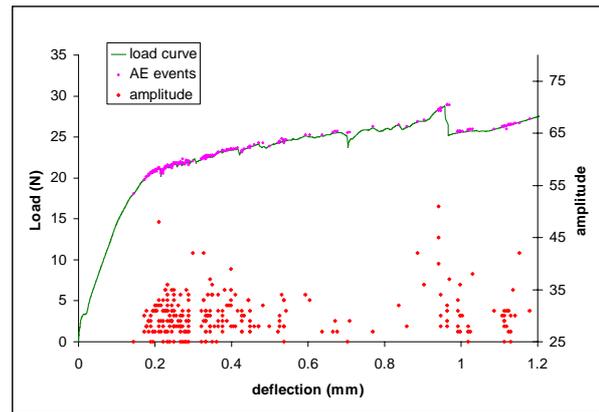
Figure IV-64: AE of test n°4 at 600°C – 1 mm/min – 100 µm – deflection = 2 mm

EA du test n°4 à 600°C - 1mm/min – 100µm – flèche=2mm
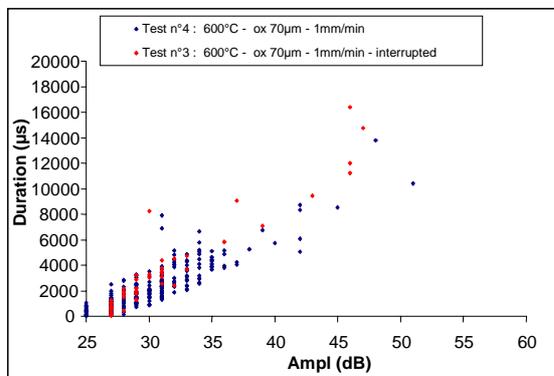
Figure IV-65: Superposition of acoustic signature for both oxidized sample tests. A correlation between the duration and the amplitude reveals a mechanical behavior: here, crack opening.

Superposition de la signature acoustique des deux tests avec éprouvettes oxydées. Une corrélation entre la durée et l'amplitude révèle le comportement mécanique : ici, l'apparition de fissures.

Correlation between parameters give the signature of an event like cracks, friction or plastic deformation... Drawing, for example, the duration of a burst versus its amplitude (Figure IV-65), one finds a **correlation, characteristic of a mechanical event**. Indeed, when there is an attenuation (due to the distance to transducers), the amplitude decreases but the duration too, because fewer bursts remain above the threshold.

Thus in Figure IV-65, the acoustic signatures of both tests superpose, proving their common origin: **through-thickness crack opening.**

Apart from such correlations, other parameters, like the frequency, independent from attenuation, could be representative of an event type as well. We have determined a frequency band between 60 and 100 MHz for cracks events. Although insufficient in itself to characterize a signature, this is a further guide for identification.

It is possible now to understand Figure IV-61. Before 0.7mm, in test n°4, the number of events is much larger than in test n°3, accompanied with oscillations of load curve, although surface observations count a very similar number of cracks. Furthermore, the duration / amplitude correlation (Figure IV-65) shows that all these events describe cracks.

In reality the additional AE events do come from cracks, but from **delaminating crackling** of scale at contacts with the bottom tools rather than the through-thickness tensile cracks. To prove this, we have examined also the energy parameter. High energy events (e.g. above 80

V.s in Figure IV-67) in close relationship with the significant drops of load observed on load curves (Figure IV-66, Figure IV-67) clearly betray a different type of damage. Microscopic observations of scale at the position of the bottom tools (Figure IV-68) do confirm they are due to **the interface cracks under tools** (hertzian contact damage) which are present in test n°4 and not in test n°3.
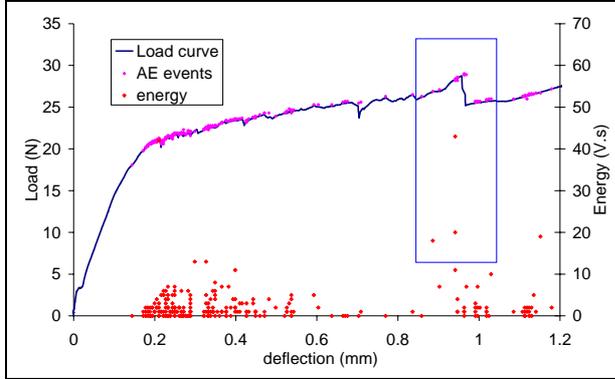
Figure IV-66: Test n°4. Highly energetic events near the load drop.

Test n°4. Evénements hautement énergétiques près de la chute de force.
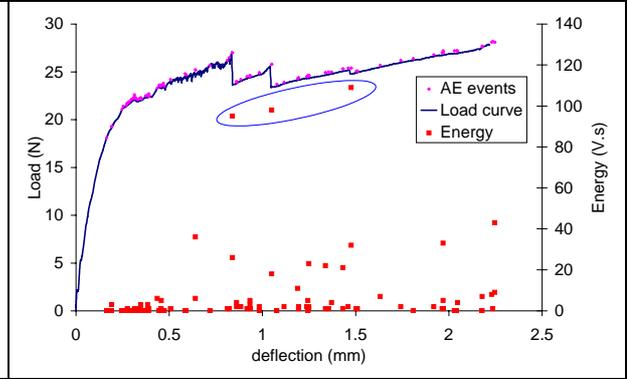
Figure IV-67: Test n°2. To each high energy event corresponds a load drop.

Test n°2. A chaque événement d'énergie élevée correspond une chute de force.
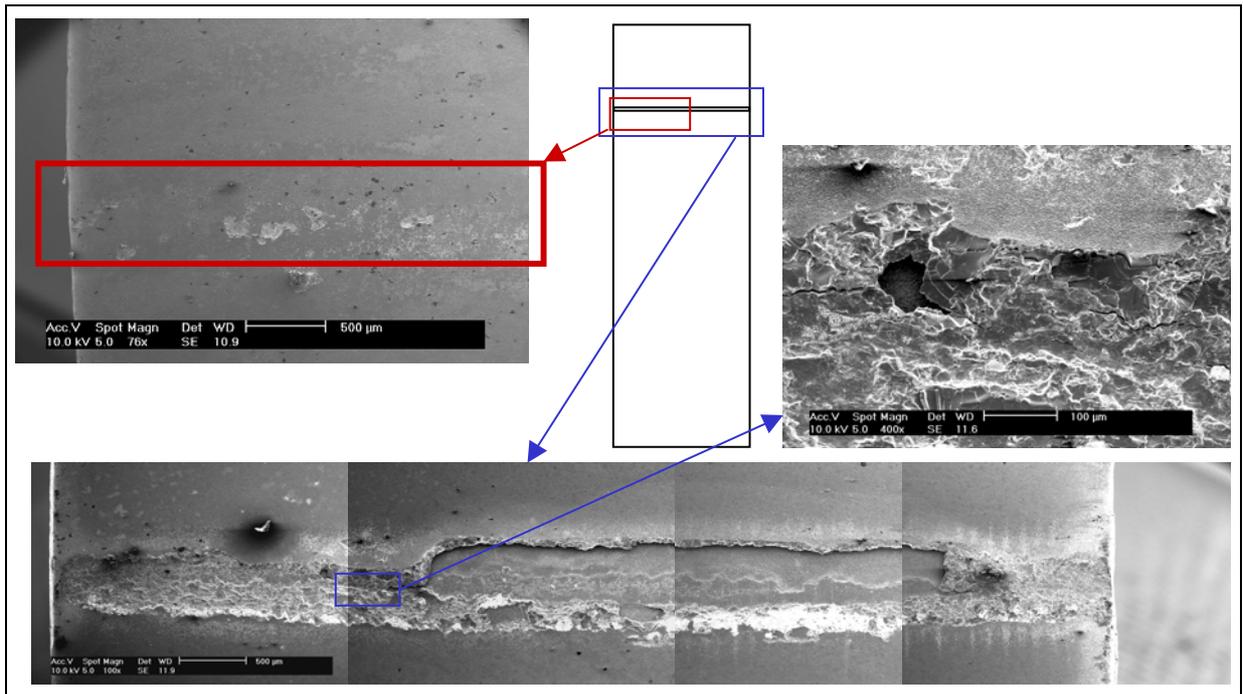
Figure IV-68: Red box: test n°3. Sliding contact between tools and scale : no damage.
Blue box: test n°4. Sticking contact: crackling and interface cracks.

Boite rouge : test n°3. Contact glissant entre les outils et la calamine : pas d'endommagement .
Boite rouge : test n°4. Contact collant : craquellements et fissures interfaciales.

In test n°4, the scale stuck to the bottom tools, resulting in a higher bending load. After crackling, interface cracks and delamination of a part of the scale completely relaxed the load. Sliding contact was thus resumed, and the load returned to the curve of the interrupted test, where low friction and sliding prevailed from the very beginning. After the last event, the curve was smooth, without oscillations (Figure IV-61), a sign of a sliding contact.

V.4. <u>Conclusion</u>

The AE technique appears to be very effective for the exploitation, interpretation and understanding of the 4-PHBT results. The simultaneous use of several parameters was found necessary to explain all the "accidents" on the test curves, and to distinguish the through-thickness, transverse crack opening events from parasite bursts principally due to the contact between the oxide scale and the tools.

A typical amplitude / duration curve betrays **crack opening in general**; some qualitative information on the number of cracks is thus obtained, but only specimen observation enables to determine the exact number of cracks. Furthermore, not all the cracks detected are significant for our purpose; **a high density of low amplitude** events has highlighted the **crackling** under the tools followed by the occurrence of **extremely energetic** events associated to the **wrenching** of parts of scale under the tools.

Eliminating these parasite bursts, it is now possible to know when the first cracks of interest open, and to determine exactly the critical tensile crack initiation stress.
The critical stress is found to be very close to the yield strength of the specimen, governed by the plastic deformation of the metal.

In the above-described analysis, we have focused on transverse, through-thickness cracks. However, tests with interface damage could also be very interesting, since delamination of scale under tools has been clearly detected thanks to the energy parameter: it seems to be possible to determine critical stresses for interface sliding and decohesion using the AE technique.

VI. DETERMINATION OF BEHAVIOR LAWS FOR STEEL AND SCALE

VI.1. <u>The inverse analysis [APPENDIX4, Pic1]</u>

The objective is to determine the parameters of constitutive equations for steel and oxide, from the experimental load-deflection curves obtained in 4-PHBT. This can be done using an automatic inverse method based on a FEM analysis. To interpret the curves correctly, a good understanding of the layer damage during the test is necessary, so that SEM observations of deformed specimens and AE have been performed.

The parameter identification module has been written at CEMEF, on another version of Forge2, for the identification of magnetic and thermal parameters for induction heating applications [Fav]. This program has been transferred on Forge2® and adapted for the identification of mechanical behaviors. The identification is fully automatic.

First, sensitivity tests are performed to evaluate the identification feasibility. From experimental results on non-oxidized specimens, we can identify the steel constitutive parameters. Finally, oxide scale mechanical characteristics are determined from the oxidized steel specimens results.

VI.2. <u>Steel parameters identification</u>

VI.2.1. Sensitivity study

As described in chapter III, the steel behavior is taken into account in Forge2® by the respective laws:

$$\sigma = E\varepsilon \qquad \text{for the elastic part} \qquad \qquad \textbf{eq. IV-4}$$

$$\overline{\sigma} = K\overline{\varepsilon}^{\,n}\dot{\overline{\varepsilon}}^{\,m} \qquad \text{for the viscoplastic part} \qquad \qquad \textbf{eq. IV-5}$$

A sensitivity study is very important to check the identification feasibility. It is necessary to evaluate the influence of the different parameters on the observables before the identification starts. Each parameter P_k (E, K and n) is successively perturbed by factor α. The sensitivity matrix [S] writes:

$$S_{ik} = S_i(P_k) = \frac{F_i^{\,c}(P_k + \alpha.P_k) - F_i^{\,c}(P_k)}{\alpha.P_k} \qquad \qquad \textbf{eq. IV-6}$$

$F_i^{\,c}$ represents the calculated observables (load and displacement). Components $S_i(P_k)$ of the sensitivity matrix must be sufficiently high to ensure good convergence of the parameter identification. Nevertheless, these values depend on the order of magnitude of the parameters. The sensitivities of all the parameters represented on Figure IV-69 are then balanced by their corresponding P_k values. The perturbation coefficient α is chosen equal to 1%.
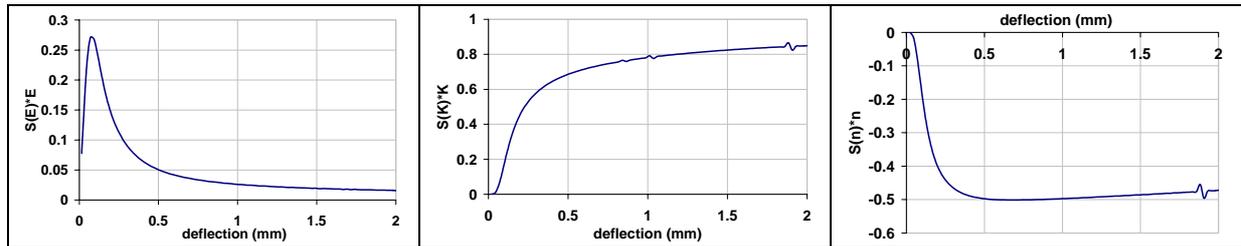
Figure IV-69: Sensitivity analysis of different parameters

Analyse de sensibilité par rapport à différents paramètres

a) $S_i(E)*E$ **b)** $S_i(K)*K$ **c)** $S_i(n)*n$

The identification is more precise when the matrix elements are high. Then, the identification of E and K will be probably more accurate.

It is also necessary to calculate the ratio between the different sensitivities, which is important for unicity of the solution. A constant value of the ratio all along the computation means that two parameters induces identical effects on the load-deflection curves. In this case, parameters cannot be dissociated : an infinity of solutions exists.

In our case (Figure IV-70), the sensitivity ratios change during the test. Inverse analysis identification seems to be possible. The parameter E is identified from the beginning of the curve, the rest is used for the identification of K and n.
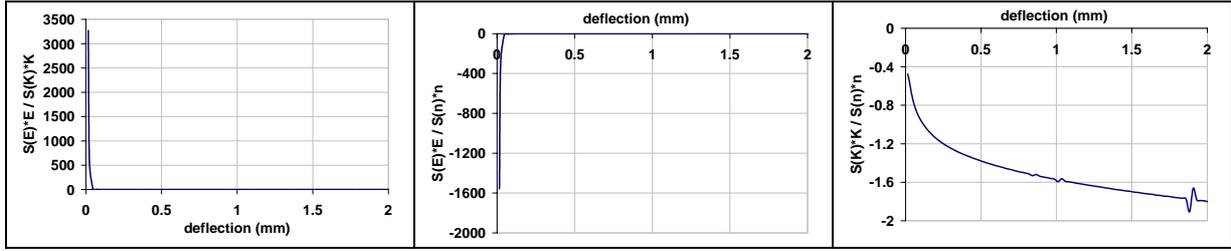
Figure IV-70 : Sensitivity ratios

Rapport de sensibilité entre les différents paramètres

a) $S_i(E)*E \big/ S_i(K)*K$ **b)** $S_i(E)*E \big/ S_i(n)*n$ **c)** $S_i(K)*K \big/ S_i(n)*n$

VI.2.2. Identification of steel mechanical parameters by inverse analysis

Experimental curves for deformed steel specimens are made out of a first linear part, which corresponds to its elastic behavior, and of a second flattened part corresponding to its viscoplastic behavior.

The elastic contribution is easily obtained by identifying the Young's modulus E. The viscoplastic part requires the identification of two parameters : the consistency K and the strain hardening coefficient n. The strain rate sensitivity coefficient is determined from tests performed at different crosshead velocities.

Equations below represent the viscoplastic behavior of two deformed identical steel specimens:

$$\sigma_1 = K_1(T)\varepsilon_1^{n_1(T)}\dot{\varepsilon}_1^{m_1(T)}$$ **eq. IV-7a**

$$\sigma_2 = K_2(T)\varepsilon_2^{n_2(T)}\dot{\varepsilon}_2^{m_2(T)}$$ **eq. IV-7b**

For two tests performed at the same temperature and at different strain rates, m is obtained at a given deflection ($\varepsilon_1 = \varepsilon_2$) by the relation:

$$\frac{\sigma_1}{\sigma_2} = \left(\frac{\varepsilon_1}{\varepsilon_2}\right)^n \left(\frac{\dot{\varepsilon}_1}{\dot{\varepsilon}_2}\right)^m \Rightarrow \frac{F_1}{F_2} = \left(\frac{V_1}{V_2}\right)^m \Rightarrow m = \frac{\ln\left(\dfrac{F_1}{F_2}\right)}{\ln\left(\dfrac{V_1}{V_2}\right)}$$ **eq. IV-8**

m is supposed to be constant whatever the temperature, due to the low calculated variations.

The contact management between the specimen and the cylindrical work-tools is a problem. Two options are available:

- **Frictional sliding contact** ; friction in Forge2® is calculated on an element basis : it needs at less two nodes in contact to declare that the corresponding element side in in contact ; otherwise, the friction force is zero. It is impossible in practice to have

several nodes in contact between a plane and a cylinder. Thus, in the present case, sliding contact is equivalent to frictionless, an unrealistic approximation.

- **sticking contact** ; it imposes *node-wise v_{rel}* =0 between the cylinder and the specimen: point contact is sufficient. But this stringent condition overestimates the frictional restraint and therefore induces too high loads.

The user chooses an initial set of parameters to start the identification process (the first full load-deflection curve simulation). The identification is then performed by successive iterations. Figure IV-71 represents parameters evolution at each iteration for three different initial sets. The corresponding cost function (Q) evolution is also plotted. This identification is performed on an experimental curve obtained by an Ex-LC steel specimen deformed at 600°C and 1 mm/mn.
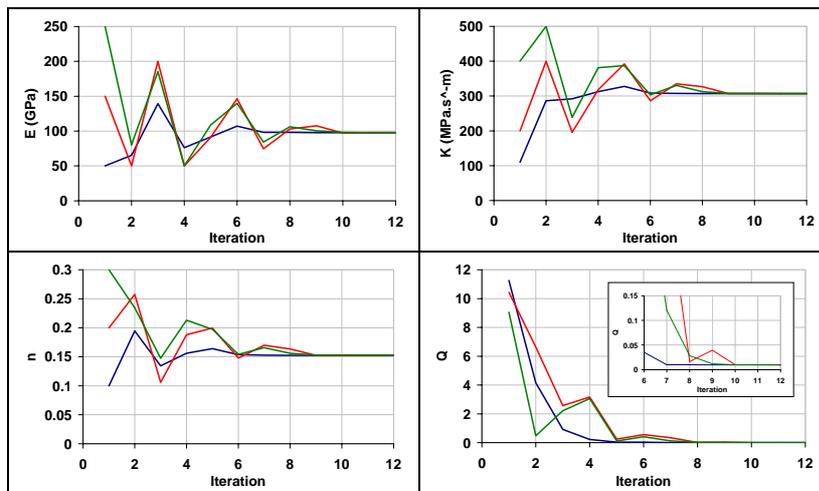
Figure IV-71: Parameters identification on load-deflection curve of Ex-LC steel deformed at 600°C and 1 mm/mn. Three different initial parameters sets (three different colors).

Identification des paramètres sur la courbe force-flèche d'un acier ExDx déformé à 600°C et 1mm/mn. Les trois couleurs correspondant à trois jeux différents de paramètres initiaux.

The three parameters sets have been chosen very different from one another. Each of them generates a high initial cost function value (~10: the curve obtained with initial set is very far from the experimental one).
All three initialisations givve the same, final, identified parameter set. The associated cost function values are very low (~10^{-2}).

The identification has been performed for each temperature of deformation. Curves obtained by simulation using identified parameters are plotted on Figure IV-72 and compared to experiments.

The identification is very good, with a quasi-perfect superposition of experimental and numerical load-deflection curves.
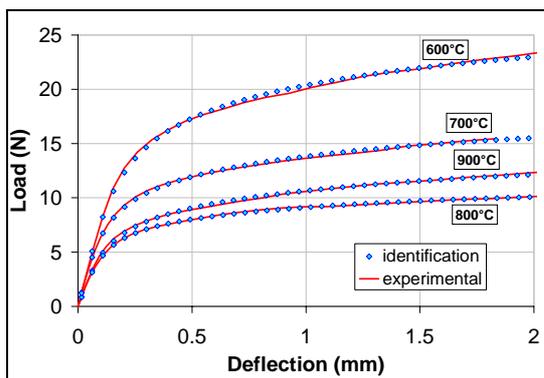
Figure IV-72: Ex-LC load-deflection curves. Superposition of experimental and numerical curves.

Courbes force-flèche ExDx. Superposition des courbes expérimentales et numériques.

The identified parameters are summarized in Table IV-2 and Figure IV-73.

T (°C)	600	700	800	900
Eapp (GPa)	98	92	63	68
K (MPa)	307	213	124	155
n	0.152	0.159	0.139	0.164
m	0.1	0.1	0.1	0.1

Table IV-2: Table of Ex-LC steel identified parameters.

Tableau des paramètres identifiés pour l'acier ExDx.

Figure IV-73: Graphical representation of Ex-LC steel identified parameters evolution vs. temperature.

Représentation graphique de l'évolution des paramètres identifiés de l'acier ExDx en fonction de la température.
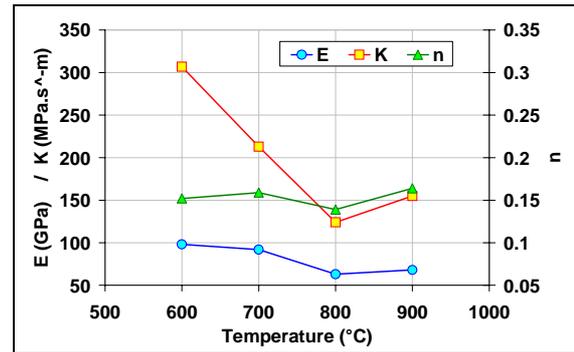
The drawback of this kind of inverse method is the possible convergence to local minima (Figure IV-71: iterations 3 and 5 for the red parameter set). To validate the solution, it is necessary to confirm that the method has converged to a global minimum. To eliminate this problem, identification is stopped before the end only if the cost function becomes lower than an extremely low value (see APPENDIX 4). Else, the identification continues during a maximum of 12 iterations, which has been found sufficient (after many tests) to make sure that the global minimum has been reached.

The identified Young's modulus can be compared to those obtained from beam theory (BT):
$$E_{BT}(600°C) = 104GPa ; E_{BT}(700°C) = 104GPa ; E_{BT}(800°C) = 63GPa ; E_{BT}(900°C) = 67GPa$$
These values are almost equal to the automatically identified ones.

A significant computation time can be saved calculating the Young modulus from the BT or identifying it before the other parameters (only with the linear part of the curve). Indeed, as shown in Figure IV-74, identification is quicker for two parameters than for three. In the former case, only 3-4 iterations (~ 15 min) are necessary instead of 9-10 iterations (50 min) for the latter. This phenomenon is explained by Figure IV-70 a) and b): the identification of the Young's modulus is only possible in the first part of the test; afterward sensitivity ratios become constant and make the identification difficult.
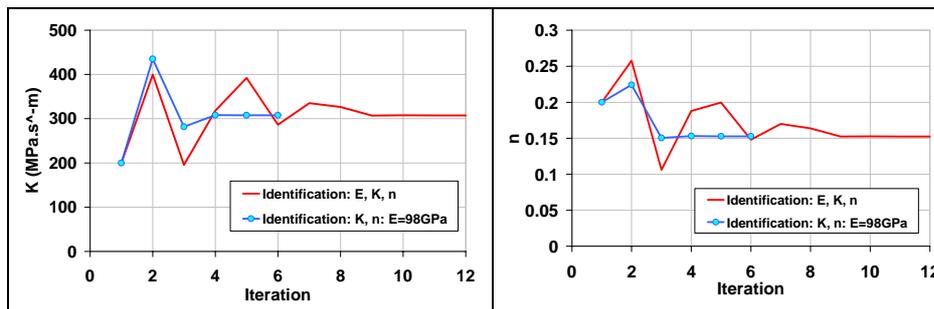
Figure IV-74: Identification of *K* and *n* with or without the identification of *E*.

Identification de K et n avec ou sans l'identification de E.

Identification results are verified by using them in simulations at higher strain rate. Thus, 4-PHBT Ex-LC steel deformed at 20 mm/mn are simulated with the identified parameters, and compared to the experimental load-deflection curves (Figure IV-75). Results are very good at 1 mm/mn, but constitutive laws identified at 1 mm/mn are slightly less accurate at higher strain rates, in particular at higher temperature (Figure IV-75). Perhaps this is due to creep being present at low strain rate, and progressively disappearing when velocity increases.

Such simple material laws cannot be effective under all conditions. Each law has a range of applicability. In the same way, large strain laws developed for hot rolling (APPENDIX 2) give totally wrong results in the case of 4-PHBT simulation.
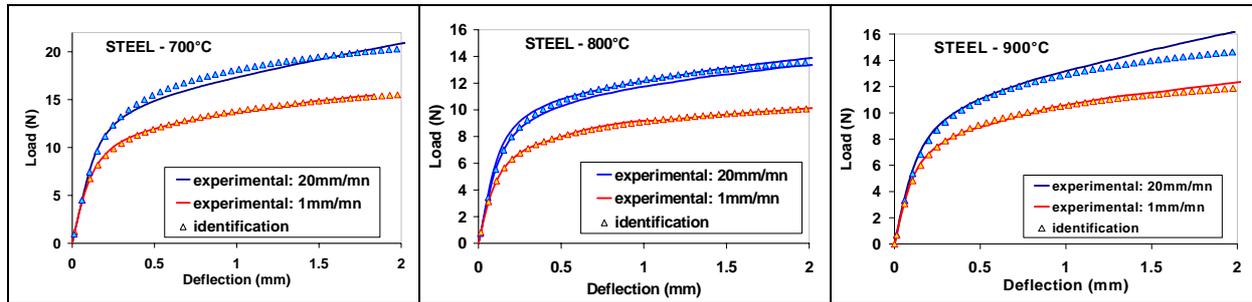
Figure IV-75: Comparison between simulated load-deflection curves (using the identified constitutive parameters) and the Ex-LC experimental curves.

Comparaison entre les courbes simulées (utilisant les lois de comportement identifiées) et les courbes expérimentales ExDx.

Parameters identification of the other steel grades has been performed. Results are summarized in Table IV-3 and Figure IV-76.

RePh	600	700	800	900	1000
E (GPa)	120	85	70	70	65
K (MPa)	411	188	107	173	120
n	0.154	0.121	0.121	0.166	0.149
m	0.1	0.1	0.1	0.1	0.1

ReN	600	700	800	900	1000
E (GPa)	122	90	84	78	55
K (MPa)	477	252	168	179	131
n	0.214	0.192	0.176	0.174	0.161
m	0.078	0.078	0.078	0.078	0.078

DDS	600	700	800	900	1000
E (GPa)	144	136	80	60	60
K (MPa)	236	168	91	47	62
n	0.16	0.144	0.148	0.111	0.131
m	0.05	0.05	0.05	0.05	0.05

Table IV-3: Parameters identification for three other steel grades. From left to right: ReP, ReN, DDS.

Identification des paramètres pour trois autres nuances d'acier : de gauche à droite : ReP ReN, DDS.
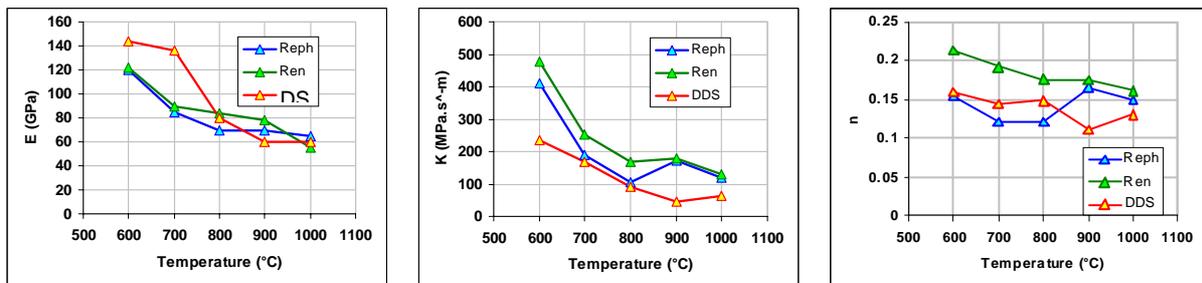
Figure IV-76: Graphical representation of parameters evolution with temperature for the three steel grades.

Représentation graphique de l'évolution des paramètres avec la température pour les trois nuances d'acier.

For all steel grades, Young's modulus E as well as consistency K logically decrease when temperature increases. The evolution of n is less clear. We can also observe that strain rate sensitivity is not the same for all steel grades. DDS steel seems to have a lower strain rate sensitivity.

VI.3. <u>Oxide scale constitutive equations</u>

The oxide scale parameters identification is performed using load-deflection curves of oxidized specimen. Constitutive parameters of steel identified previously are used for the simulation of oxidized samples aiming at oxide parameters identification.

Parameter identification of 4-PHBT in which **damage** is observed is **extremely difficult**. Indeed, even if each crack initiated on the specimen does not give a load drop on its corresponding load-deflection curve, cracking tends to **slow down the general load increase** required to deform the specimen (identification without any damage simulation). Identification is then performed from **undamaged specimens**.

The first step of the identification has been to analyse the elastic behaviour (characterized by the identification of a Young's modulus E). Due to the remaining problem of tool-rolls / oxide scale contact detailed in the AE section, the first identified Young's moduli were extremely high. We have therefore decided to adopt Morrel's values [Mor]. The oxide viscoplastic parameter identification then confirms that a pure elastic law cannot be used to simulate oxide scale behavior in 4-PHBT.

From specimens microscopic observations, the oxide scale plasticity as well as its strain rate sensitivity has been evidenced. Finally, an elastic-viscoplastic law has been selected.

VI.3.1. Young's modulus identification

A key-point for oxide scale parameters identification is the delimitation of the zone of the experimental curve that has to be studied : thus, the Young's modulus is fitted on the **initial elastic slope**. Identification is performed in 2 or 3 iterations. The Young's modulus is the only one parameter, which can be identified from all load-deflection curves, even those showing oxide damage. Indeed, damage appears only after the linear curve part, when the substrate enters the plastic state.
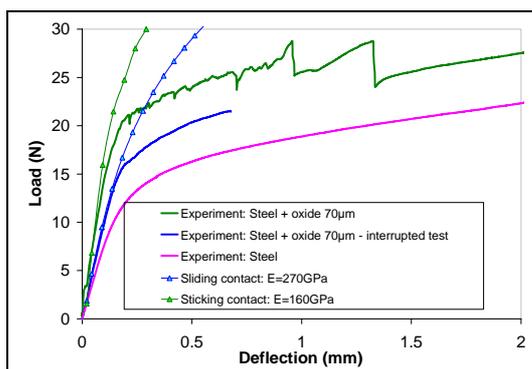
Figure IV-77: Young's modulus identification on experimental Ex-LC load-deflection curves (1mm/mn-600°C). Contact influence.

Identification du module d'Young sur les courbes force-flèche expérimentales (1mm/mn-600°C). Influence du contact.

Due to the tool-rolls / oxide scale contact (often close to sticking), the first identified Young's moduli were extremely high. Young's moduli values obtained at temperature between 600 and 900°C were sometimes higher than at room temperature!

An example is given Figure IV-77. With a sliding contact (µ=0) the identified E is 270 GPa for the blue interrupted test (curve) and 450 GPa for the green test. These values have no physical sense compared to 240 GPa at room temperature.

With a sticking contact, the identified value is 160GPa for the green test, which seems to be more realistic. In the case of the blue curve, the tool-rolls / oxide scale contact seems intermediate between the sliding and the sticking contact (friction).

Morrel gave a temperature dependence expression for oxide scale (See chapter II ; [Mor]):

$$E_{ox} = E_{ox}^0 \left(1 - p.(T - 25)\right)$$ **eq. II-15**

E_{ox}^0 is the Young modulus at 25°C (240 GPa), T the temperature in °C and p a constant depending on the oxide. For iron oxide scale, $p = 4.7.10^{-4}$:

$$E_{ox}(600°C) = 175GPa \; ; E_{ox}(700°C) = 164GPa \; ; E_{ox}(800°C) = 153GPa \; ; E_{ox}(900°C) = 141GPa$$

These values are in good agreement with our results. Young's modulus variations between several scales grown on different steel grades are not significantly different, and due to the identification difficulties sometimes encountered (due to unpredictable friction conditions)**, values from [Mor] are used in the following to simulate the elastic part of all scales**.

VI.3.2. Viscoplastic behavior (800°C-900°C)

In this section, we restrict the analysis to uncracked specimens (i.e. tests at 600°C as well as tests at 700°C and high strain rate are excluded for this reason).
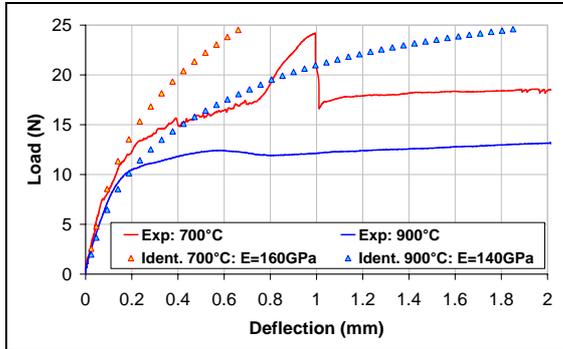
Figure IV-78 shows that **pure** elastic behavior is not suitable to simulate the oxide scale behavior in 4-PHBT.

Indeed, the numerical elastic load-deflection curves lie well above the experimental ones.

Figure IV-78: Superposition of experimental Ex-LC load-deflection curves (1mm/mn) and numerical curves obtained from purely elastic oxide scale behaviour.

Superposition des courbes force-flèche expérimentales (1mm/mn) et numériques obtenues pour un comportement d'oxyde purement élastique.

From specimens observations, the oxide scale plasticity as well as its strain rate sensitivity has been described. To simulate the inflexion of the curve that a pure elastic law is unable to reproduce, elastic-viscoplastic constitutive equations have finally been identified:

$$\overline{\sigma}_{ox} = K_{ox}\left(\dot{\overline{\varepsilon}}\right)\varepsilon^{n_{ox}}$$ **eq. IV-9**

$K_{ox}\left(\dot{\overline{\varepsilon}}\right)$ is the oxide consistency, which depends on the strain rate.

The identification of the viscoplastic part is more difficult. Several points have to be considered:

- The identification is performed using undamaged specimens.
- Contact problems: despite a random behaviour due to friction, all curves are superimposed for high deflection values (Figure IV-77, Figure IV-80-700°C). In these cases, the identification can be performed using the last part of the curves.

The identification of parameters has been performed. The method was tedious because oxide scale parameters must be identified separately for each temperature, each strain rate and for each steel grade. Moreover the identification is significantly longer in the case of an oxidized specimen than for an unoxidized one (direct computation is longer for a bi-material than for a mono-material).

In the following, we propose a simple useful technique to identify these parameters, which gives **results quasi-identical** to those obtained from the identification of parameters by inverse analysis. The observation of experimental load-deflection curves shows that "oxidized" and "non-oxidized" curves are parallel after the initial linear elastic slope. This means a quite identical strain dependence for scale and for steel. The strain hardening coefficient n can therefore be chosen identical for axide and steel (Figure IV-80; Figure IV-81) :

$$\overline{\sigma}_{ox} = K_{ox}.\dot{\varepsilon}^{m_{ox}}.\varepsilon^{n_{steel}} = K_{ox-app}.\dot{\varepsilon}^{m_{steel}}.\varepsilon^{n_{steel}} \quad \text{with} \quad K_{ox-app} = K_{ox}.\dot{\varepsilon}^{m_{ox}-m_{steel}} \qquad \textbf{eq. IV-10}$$

K_{ox-app} represents an **apparent oxide consistency**.

It is possible to do this because all tests are performed at constant strain rate. This method reduces the identification to a single parameter, the **hardness ratio H** between oxide scale and steel :

Steel: $\overline{\sigma}_{steel} = K_{steel}.\dot{\varepsilon}^{m_{steel}}.\varepsilon^{n_{steel}}$ Oxide: $\overline{\sigma}_{ox} = K_{ox-app}.\dot{\varepsilon}^{m_{steel}}.\varepsilon^{n_{steel}}$

Hardness ratio: $H = \dfrac{Hv(ox)}{Hv(steel)} = \dfrac{\sigma_{0\_ox}/\sqrt{3}}{\sigma_{0\_steel}/\sqrt{3}} = \dfrac{\sigma_{0\_steel}}{\sigma_{0\_ox}} = \dfrac{K_{ox-app}.\dot{\varepsilon}^{m_{steel}}}{K_{steel}.\dot{\varepsilon}^{m_{steel}}} = \dfrac{K_{ox-app}}{K_{steel}}$ **eq. IV-11**

And $\boxed{\overline{\sigma}_{ox} = H.\overline{\sigma}_{steel}}$ **eq. IV-12**

Hardness ratios obtained for different steel grades from the identification of the apparent consistency are represented Figure IV-79 and compared to the ratio between FeO and Fe determined by Vagnard and Manenc using Vickers hardness testing [Vagn].

Remark: A good approximation of the hardness ratio can be obtained geometrically from the experimental curves of non-oxidized and oxidized specimens. Knowing the respective thickness of steel and oxide, H is found by dividing the mechanical contribution of the oxide (load), by the thickness ratio between the scale and its steel substrate:

$$\boxed{H = \left(L_{s+ox}\left(d^*\right) - L_s\left(d^*\right)\right)\frac{h_s}{h_{ox}}}$$ **eq. IV-13**

where the first term represents the load values difference between an oxidized (*s+ox*) and a non-oxidized (*s*) specimen. *h* is the thickness.
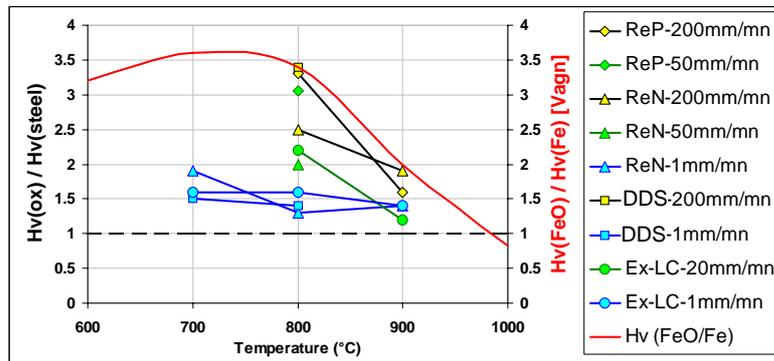
Figure IV-79: hardness ratio between oxide scales and their respective steel. Evolution as a function of steel grade, temperature and strain rate.

Rapport des duretés entre les couches d'oxydes et leurs substrats respectifs. Evolution en fonction de la nuance d'acier, la température et la vitesse de déformation.

Figure IV-79 represents the evolution of the ratio, for different steel grades, temperatures and strain rates.

Results are extremely interesting because they display three useful tendencies:

- The ratio does not depend too much on the steel grade. This method based on ratios thus seems to be effective to identify constitutive parameters.
- The strain rate dependence is clearly represented: the hardness ratio increases with strain rate. Oxides scale "hardening" is observed with strain rate increase, probably because the oxide is allowed less creep deformation. Once any creep has been eliminated, values obtained seem to tend toward hot hardness given by [Vagn]. Our main assumption is that this limit ratio can be used in the following for tensile test or hot rolling.

Comparison between experimental and numerical load-deflection curves is represented Figure IV-80 and Figure IV-81 for two steel grades, respectively Ex-LC and ReN. In both cases, identification gives rather good results.

Remark:

The oxidized specimens deformed at high temperature (900°C) and very low velocity (1 mm/mn) show more flat load-deflection curve in the plastic deformation zone. Another kind of law could be used under such conditions; the result of a pure plastic identification (Constitutive equation: $\sigma = K$) has therefore also been plotted on Figure IV-80 (900°C). This phenomenon can have several origins such as creep, with a "steady state" deformation (strain hardening quasi-equal to zero), or interfacial sliding or a slight decohesion.

Even if this law seems to be, in this case, better suited, the previous one (elastic-viscoplastic) will be used in all cases for comparison purposes.
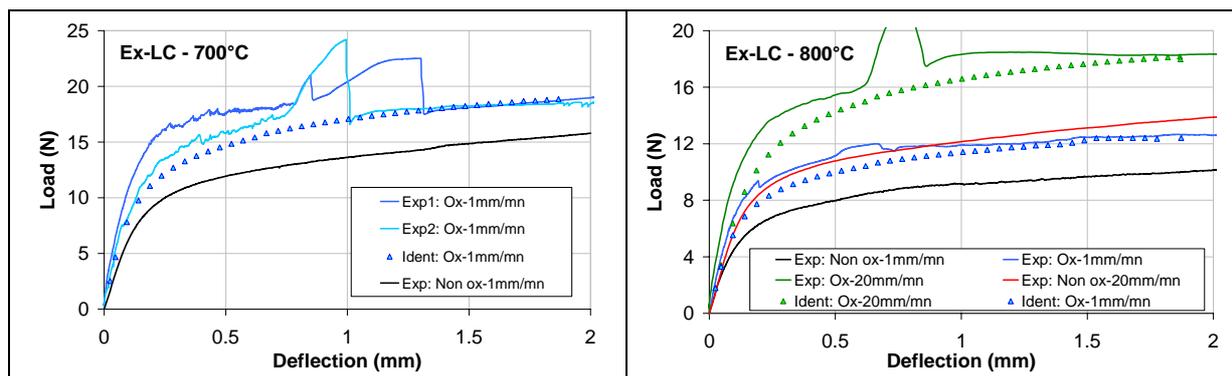
Figure IV-80: Superposition of experimental and numerical load-deflection curves obtained using 4-PHBT of Ex-LC specimens covered by an oxide scale. No transverse cracks are observed during these tests.

Superposition des courbes force-flèche expérimentales et numériques obtenues en f4p d'éprouvettes ExDx couvertes de calamine. Pas de fissures transverses observées pendant ces tests.
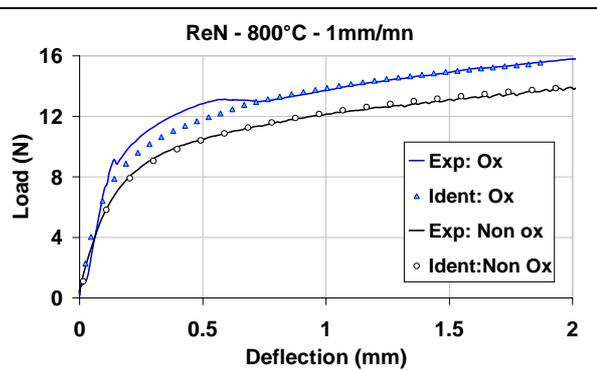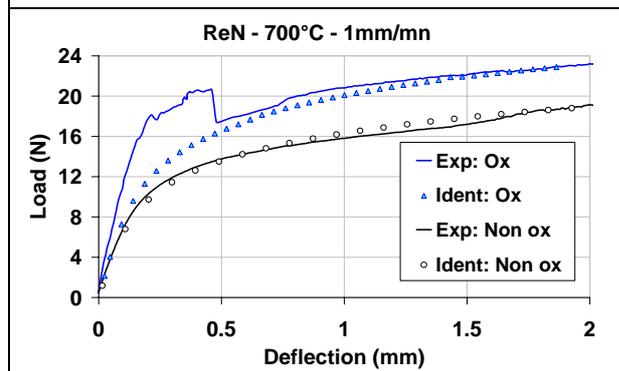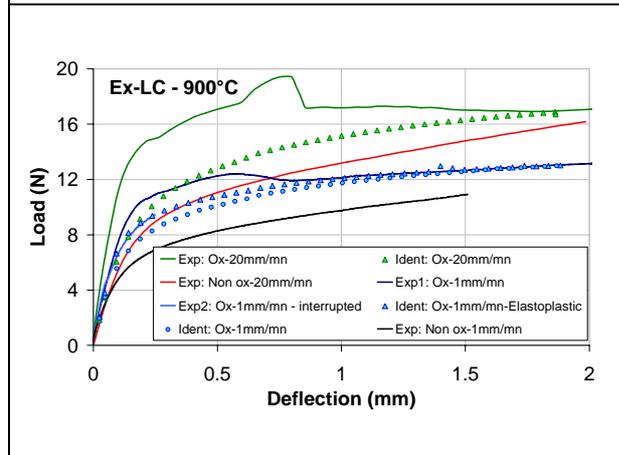
Figure IV-81: Superposition of experimental and numerical load-deflection curves obtained using 4-PHBT of ReN specimens.

Superposition des courbes force-flèche expérimentales et numériques obtenues en f4p d'éprouvettes ReN.

VI.3.3. Extrapolation to 600°C / 700°C

Once the oxide scale constitutive equations for undamaged layers have been identified, it is necessary to investigate damaged specimens.

Extrapolation of hardness ratios after [Vagn] will provide constitutive equations for damaged specimens (Figure IV-82) : at high strain rate, the ratio is 3.4 at 800°C, 3.6 at 700°C and 3.2 at 600°C; using the constitutive parameters of steel, those of the oxide are immediately deduced. At lower strain rates, the same *evolution* with temperature, from 800°C to 700°C and 600°C, is assumed, starting from the measured hardness ratios at 800°C (2.2 at 20 mm.s^{-1}, 1.6 at 1 mm.s^{-1}). Again, the strain-rate dependent hardness ratios at 700°C and 600°C give access to oxide constitutive parameters at these temperatures.
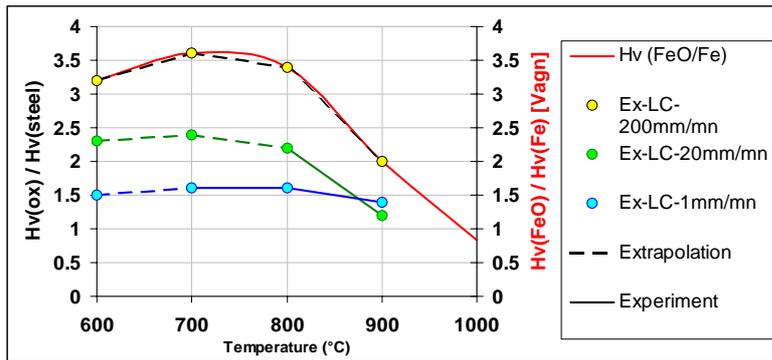
Figure IV-82: Extrapolation of hardness ratios obtained Figure IV-79, for damaged specimens.

Extrapolation des rapports de consistances obtenus Figure IV-79, pour des éprouvettes endommagées, c'est-à-dire aux plus basses températures (600°C et 700 °C).

We have used these results in our simulations. As we will see in the next sections, extrapolations give very good results.

VII. SIMULATION AND DETERMINATION OF CRITICAL STRESSES

VII.1. Determination of critical stresses
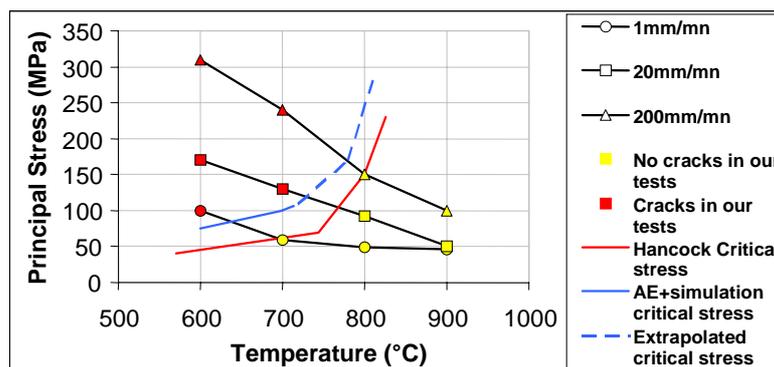
Figure IV-83: Representation of simulated maximal principal stresses reached in a 100 µm-thick scale covering Ex-LC steel samples, at a deflection of 2 mm. Representation of critical principal stress obtained by AE and extrapolation. Comparison with Hancock results [Han].

Représentation des contraintes principales maximales simulées atteintes dans une couche d'oxyde de 100µm couvrant des éprouvettes d'acier ExDx, pour une flèche de 2mm. Représentation des contraintes principales critiques obtenues par EA et extrapolation. Comparaison avec les résultats de Hancock [Han].

A combination of AE analysis and numerical simulations enables to determine the critical stress values of the oxide scale. Indeed, AE detects the instant of crack initiation. Numerical simulation then gives us the corresponding maximal tensile stress in the oxide scale.

Maximal principal tensile stress values obtained in oxide scale during 4-PHBT simulations (with numerical cracking disabled) are represented Figure IV-83 for each strain rate and temperature. Points in yellow report on crack-less experimental 4-PHBT. In red are represented those in which cracks have been experimentally observed.

Critical data determined by Hancock for Armco Iron are plotted on the same graph (see chapter II, section III.4.2.2). These results are very close to our critical values. Hancock's data allow us to extrapolate our results to higher temperature. This extrapolation highlights that stresses reached in our tests at 800°C are too low to involve crack initiation.

VII.2. <u>Influence of deformation</u>

In Figure IV-85, we compare experimental and simulated 4-PHBT load-deflection curves at 600°C and 1mm/mn. In the experiments, the presence of the stiff oxide layer causes an increase of the load. Among the three "oxidized" curves measured under identical conditions, one leads to a higher load followed by discontinuities. Initially, the latter were attributed to transverse cracks in the oxide. However, the combination of surface crack density measurements (very similar on samples 2a and 3a, Figure IV-84), numerical simulation and AE recordings convinced us that they were due to major spalling at the tool / oxide interface (of no interest for our purpose). When only transverse cracks are present, the curve is smooth. It has to be noted that the curves finally merge, once spalling of the oxide under the tools has destroyed the source of high friction.
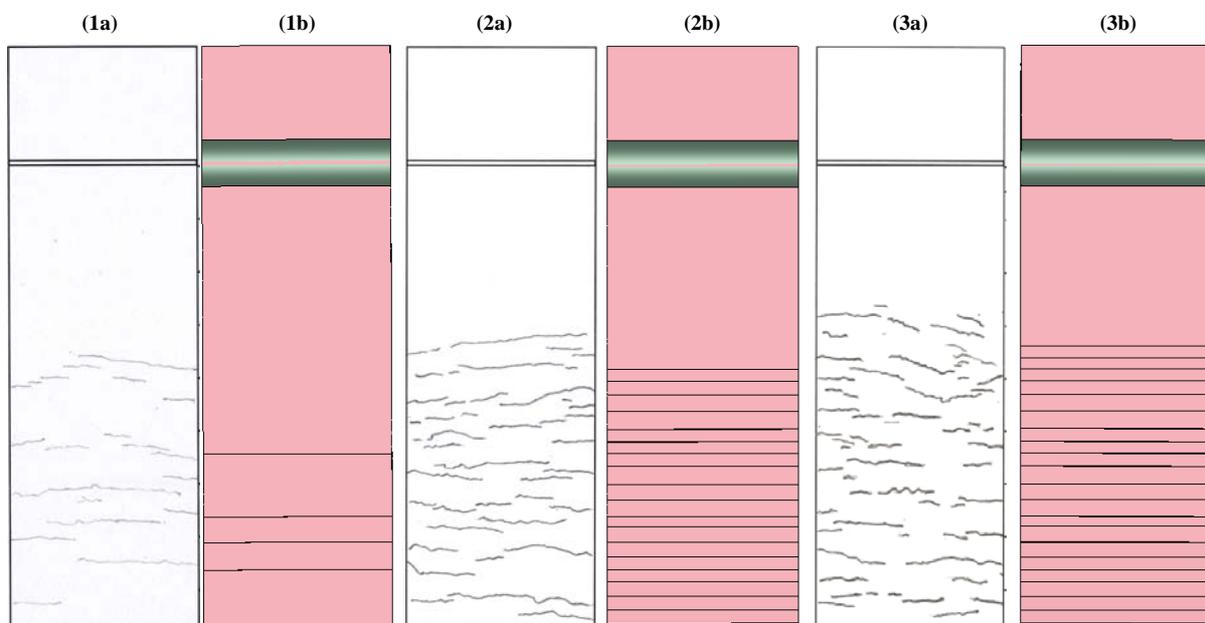
Figure IV-84: Ex-LC deformed using 4-PHBT: 600°C – 1 mm/min - oxide: 100 µm. (a) crack mapping of experimental oxidized samples (b) 2D simulation, represented in a 3D configuration for clarity. (1) Deflection = 0.25 mm (2) deflection = 1.2 mm (3) deflection = 2 mm.

ExDx déformé en f4p : 600°C-1mm/mn-oxyde:100µm. (a) Cartes de fissuration des éprouvettes expérimentales oxydées (b) simulations 2D, représentées en configuration 3D pour plus de clarté. (1) Flèche = 0.25mm (2) flèche = 1.2mm (3) flèche = 2mm.

Figure IV-84 represents the experimental and numerical evolution of crack mapping with the strain increase. Numerical simulations are performed using the previously identified materials constitutive equations and damage criteria (critical tensile stress). Another example of interrupted test on specimens with a 70µm-thick oxide layer is available in [Pic2].
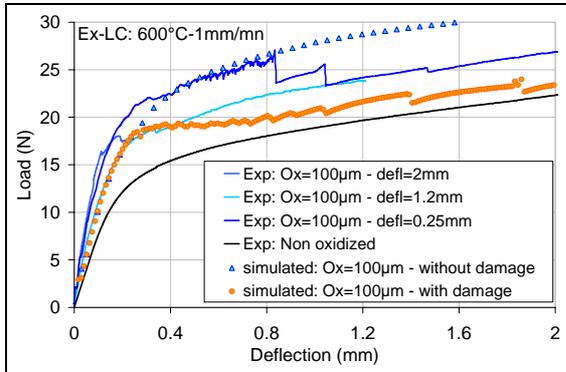
Figure IV-85: Ex-LC deformed using 4-PHBT: 600°C – 1 mm/min - oxide: 100 µm. Experimental and numerical load-deflection curves.

ExDx déformé en f4p : 600°C-1mm/min-oxyde: 100µm. Courbes force-flèche expérimentales et numériques.
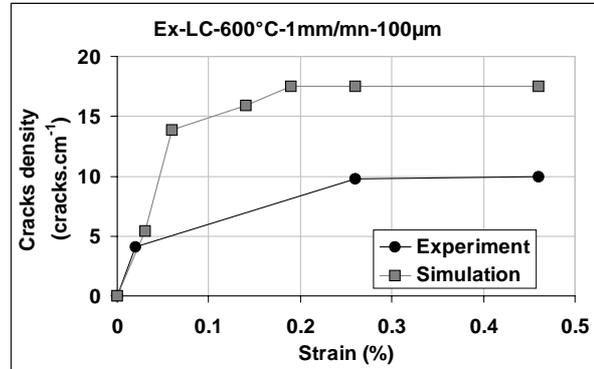
Figure IV-86: Crack density obtained experimentally and numerically using the developed damage model.

Densités de fissures obtenues expérimentalement et numériquement en utilisant le modèle d'endommagement développé.

Even if numerical results seem to be in good agreement with experiment (as seen Figure IV-84), Figure IV-86 shows that the experimental crack spacing is higher than the numerical one (crack density lower). This is certainly due to the creep behavior and the **crack healing** mechanism allowed by extremely low strain rates. Another explanation could be a stress relaxation by grain boundary sliding at the metal-oxide interface. It would be interesting to observe the behavior at higher strain rate.
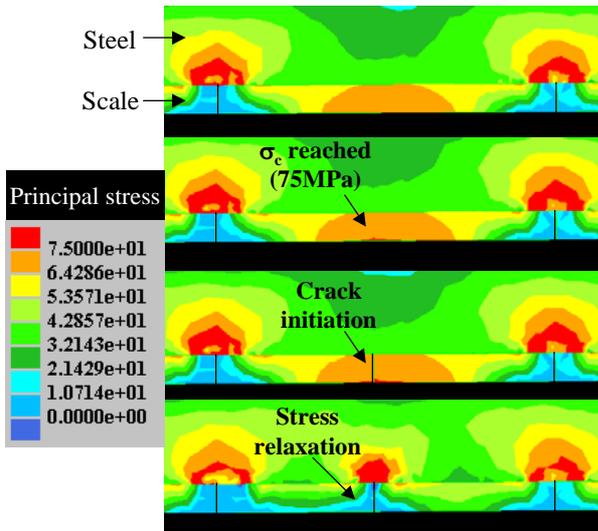
Figure IV-87: Crack initiation halfway between two existing cracks: principal tensile stress is maximal. Simulation at 600°C and 200mm/mn.

Initiation d'une fissure au milieu de deux existantes : la contrainte principale de traction est maximale. Simulation à 600°C et 200mm/mn.
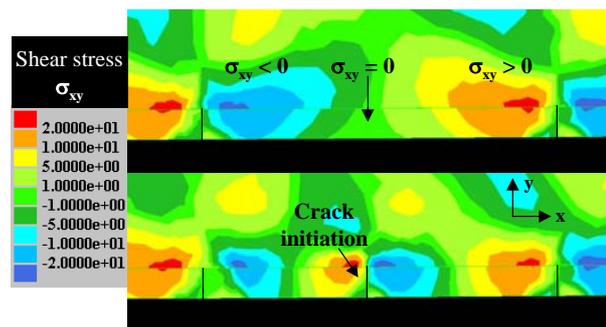
Figure IV-88: Crack initiation halfway between two cracks: shear stress is equal to zero. Simulation at 600°C and 200mm/mn.

Initiation d'une fissure au milieu des deux existantes : la contrainte de cisaillement est nulle. Simulation à 600°C et 200mm/mn.

It can also be noted that 2D numerical simulations necessarily create full-width transverse cracks, whereas real cracks are shorter: this is why, numerical simulations lead to a larger drop in mechanical properties, see Figure IV-85**.**

The mechanism of the numerical crack density increase is represented Figure IV-87 and Figure IV-88. A new crack initiates between two cracks, approximately halfway (due to the local deformation homogeneity), at the position where principal stress is maximal and shear stress is equal to zero. The stress field is in good agreement with the theoretical stress distribution obtained between two cracks and represented in chapter II (section III.4.2.2: distance between cracks [agr] : axial stress: sin^2 behavior between cracks, eq. II-39 ; shear stress: sin behavior, eq. II-38).

VII.3. Temperature / strain rate influences

At 700°C, tests at 1 mm/min did not show any transverse crack, whereas at 20 mm/min, cracks were found again: the behavior is strongly strain-rate and temperature dependent. These dependencies have been reproduced numerically thanks to the viscoplastic term introduced in the constitutive equations for the oxide.

At 800°C or 900°C, ductile deformation without transverse cracks was experienced whatever the velocity.
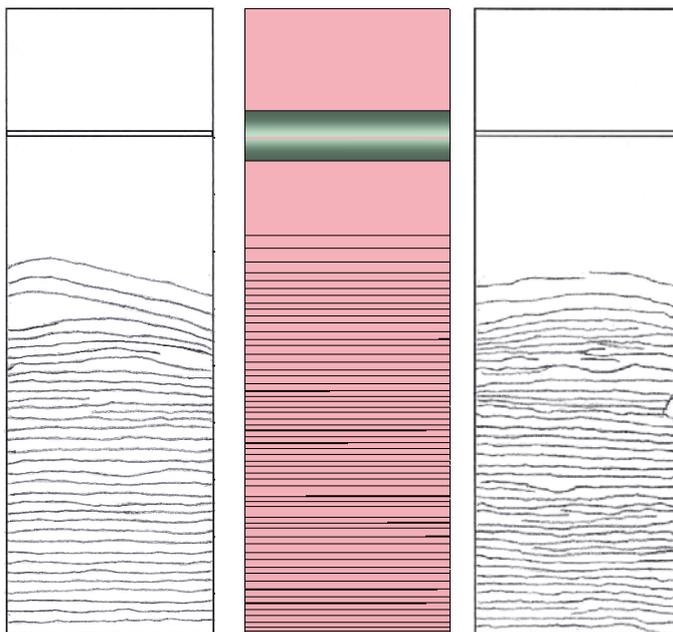
The simulation of a test performed at low temperature and high strain rate is represented Figure IV-89. Simulations are close to experiments. Here, relaxation by creep had no time to occur. Propagation across the specimen width seems to be instantaneous. That is probably why numerical results are here closer to experimental ones than at lower strain rate.

Crack densities obtained at each strain rate and temperature are reported in Figure IV-90.

Figure IV-89: Sample deformed at 600°C and 200 mm/min. Middle: Ex-LC simulation. On either side: crack mapping for DDS (left) and ReN (right), already represented Figure IV-54

Eprouvettes déformées à 600°C et 200mm/mn. Milieu: simulation ExDx. De chaque côté: DDS (gauche) et ReN (droite). Cartographies des fissures déjà représentées Figure IV-54

At high strain rate and low temperature, where the scale has a brittle behavior, oxide spallation can be observed on several steel grades such as on ReP steel. Such a behavior has been simulated using specimens deformed at 200 mm/mn. To model this phenomenon, a

decohesion criteria has been introduced in the data file using an interfacial critical normal stress. Its value has been chosen equal to the one used for transverse crack initiation (80 Mpa), due to the lack of data on specimens with decohesion.
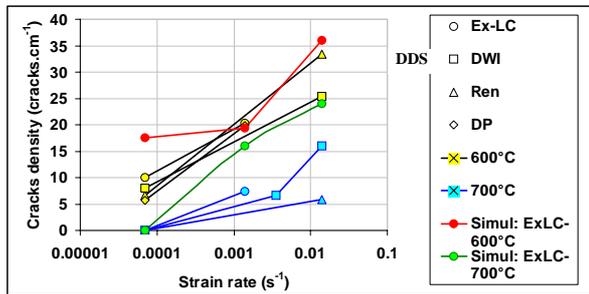
Figure IV-90: Crack density obtained experimentally and numerically.

Densités de fissures obtenues expérimentalement et numériquement.

One more time, we observe that numerical results are farther from experimental ones whenever creep occurs (i.e. at lower strain rates and higher temperatures).

Nevertheless, **numerical results are judged satisfactory,** having regard to the complexity of the oxide scale behavior.
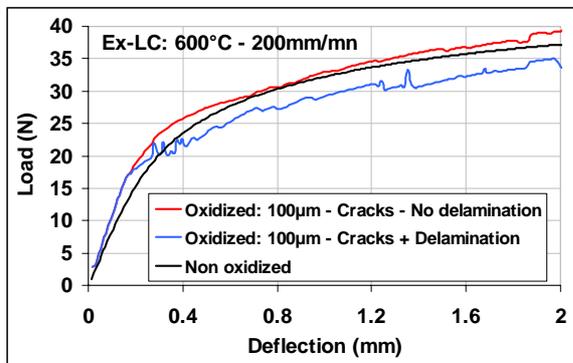
Figure IV-91: Specimen deformed at 200 mm/min and 600°C. Numerical load-deflection curves with and without decohesion.

Echantillon déformé à 200 mm/mn et 600°C. Courbes numériques force-flèche avec et sans délamination.
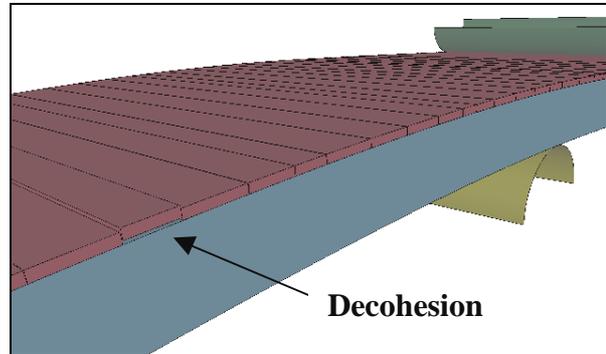
Figure IV-92: Simulation of specimen deformed at 200 mm/mn and 600°C, with decohesion.

Simulation d'un échantillon déformé à 200 mm/mn et 600°C, avec un critère de décohésion.

The results of these simulations are represented Figure IV-92. Decohesion of a scale raft can be observed. In reality, there is more spallation in the simulation than what can be observed on this figure, but due to the plastic character of the oxide scale, scale parts are not "numerically" expelled at the onset of spallation : the pieces are put in contact again at the next increment. Nevertheless, the calculation is quite good in terms of spallation-induced relaxation efficiency. The influence of decohesion is proved by plotting load-deflection curves calculated with cracking only and with cracking + decohesion. The curve (Figure IV-91) using the decohesion criterion is extremely similar to the experimental curves for ReP steel, obtained under the same conditions (see Figure IV-49). In both cases, the "oxidized" curve lies below the "non oxidized".

When decohesion is allowed, the crack density is also lower due to stress relaxation at the interface. This numerical observation can perhaps be another explanation of the high crack density obtained in our simulations. Perhaps we should introduce decohesion in all our simulations. The problem is that it is difficult to quantify and to model this phenomenon which has not been clearly observed yet.

VIII. CONCLUSION

This 4-PHBT study has been carried out to reproduce the mechanical behavior of oxide scales at the entry of the roll gap. In both cases, the surface is bent, which induces tensile stresses within the oxide scale. An experimental procedure has been established to be as close as possible to the finishing-mill conditions. Thermal and chemical cycles have been chosen identical for all tests after the observation of their influence on materials behavior. Tests have been performed on several steel grades, at different temperatures, strain and strain rate, and with oxide scales between 70 and 100 µm thick.

Steel behavior during 4-PHBT has been studied using inverse analysis. 4-PHBT results on its Young's modulus are interesting because only few data are available for steel in this temperature (600°C-1000°C) and strain (below 0.01) range. The 4-PHBT, as performed at IRSID, is therefore a very good tool for the mechanical characterization of steel at high temperature and very small deformation.

Oxide scale behavior has also been determined. It can be divided in two categories:

- At low temperature, the oxide scale is brittle. The interface is strong. During deformation, through-thickness cracks appear, perpendicular to the stress direction. Intergranular cracks propagate across the specimen width.
- At higher temperature, the oxide scale is more plastic and can be deformed without any crack. Nevertheless, the interface seems to be weaker and interfacial decohesion can be observed.

The influence of several parameters has been disclosed using microscopic observations and crack mapping on a combination of deformed specimens.

- Strain: The number of cracks increases with strain until a dense network of equidistant cracks is obtained. Distance between cracks decreases when the strain increases. Increasing strain also facilitates the crack propagation through the specimen width.
- Strain rate: A high strain rate sensitivity has been evidenced. The crack number significantly increases with strain rate. Cracks can be promoted at higher temperature by using higher strain rate.
- Scale thickness: When the thickness decreases, a slight increase of the crack number and a stronger adherence of oxide scales on steel substrates are observed.
- Steel grade: Steel grade has a significant influence on the oxide scale behavior during 4-PHBT, principally in terms of adherence at the interface.

Evolution of crack density as a function of strain, strain rate, temperature and steel grade have been studied. It increases when the temperature decreases and when the strain and strain rate increase. Roughly, crack density increases when oxide becomes harder and more brittle.

In order to simulate oxide scale behavior, several stages have been necessary:

- The 4-PHBT rig has been instrumented with AE technique. The latter has shown that accidents observed on load-deflection curves of oxidized specimens were not due to damage initiation. Indeed, a joint use of AE analysis, guiding microscopic observations of cracked surfaces, and interpretation of the force-deflection curves backed up by numerical

simulation results, has permitted to correct our past erroneous procedure. The accidents were due to very high friction and adhesion between the oxide scale and tools, which should be counteracted in future experiments.

- From this, constitutive equations of steel and scale have been identified by an inverse analysis method, for high temperature (non-damaged) specimens (depending on T, $\dot{\varepsilon}$, ε).
- Constitutive equations at lower temperature (damaged specimens) have been identified by extrapolation of the previous results.
- AE has also made it possible to identify the kind of damage and the instant of its initiation during the test. Coupling these results with numerical simulations, critical tensile stress values for through-thickness cracks initiation have been determined ; they depend on temperature and strain rate. Results obtained are in good agreement with the few data existing in the literature.

A final part on 4-PHBT numerical simulation has proved the efficiency of the approach presented in this chapter. Indeed, simulations reproduce experiments quite well. The few differences observed are mainly met when creep is present. This behavior as well as crack healing is extremely difficult to take into account.
Experimental tests have brought to light the crack propagation in the width direction during deformation. This behavior also makes our 2-D FEM approximate : loads are more relaxed and the crack number is probably higher than in experiments.

Nevertheless, the main conclusion concerns 4-PHBT itself. The interpretation of the 4-PHBT results has to be done with **much care**. The 4-PHBT mimics perfectly the bending solicitation at the entry of a roll gap in a finishing mill. But this bending in hot rolling (due to its thickness reduction) represents only a part of the steel-scale system deformation.
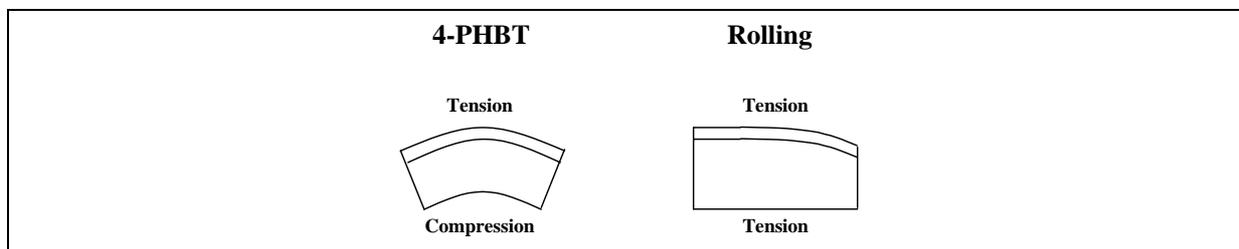
The major part of tensile stresses involved in the critical zone is due to the work-roll rotation, which puts the strip skin under high tension.
In the same way, 4-PHBT has shown the high strain rate influence on the oxide scale behavior. Comparing the strain rate in this mechanical test (between 7.10^{-5} s^{-1} and $1.4.10^{-2}$ s^{-1}) with hot rolling ($\sim$10 s^{-1}), doubts are justified on the use of all our 4-PHBT results in rolling simulations. The best argument is the occurrence of defects in the finishing mill at the entry of the roll gap, where oxide scale temperatures are between 850 and 1000°C. According to our 4-PHBT, no crack should be seen at such a temperature.

The 4-PHBT is an ideal test to understand the mechanisms of deformation and damage in the oxide scale. Thanks to low velocities, it is possible to separate and analyze the influence of the different parameters on the oxide scales behavior such as temperature, strain, strain rate, steel grade, and scale thickness. Nevertheless, the other data concerning principally the damage critical stresses have to be completed. **The main parameter that necessitates an additional study is the strain rate**. Tensile tests have therefore been performed and are presented in next chapter V.

IX. REFERENCES

[Agr]   D.C.Agrawal, R.Raj, Measurement of the ultimate shear strength of a metal-ceramic interface, Acta Met. vol.37 n°4, (1989), pp.1265-1270.

[Bruh]   O.T.Bruhns, N.K.Gupta, A.T.M.Meyers, H.Xiao, Bending of an elastoplastic strip with isotropic and kinetic hardening, Arch. Appl. Mech. 72, (2003), pp.759-778.

[Brun]   C.Bruns, M.Schütze, Investigation of the mechanical properties of oxide scales on Nickel and TiAl, Oxid. Met., vol.55, Nos.1/2, (2001), pp.35-67.

[Dal]   D.Dalmas, S.Benmedakhene, C.Richard, A.Laksimi, G.Beranger, T. Gregoire, Caractérisation par émission acoustique de l'adhérence et de l'endommagement d'un revêtement: cas d'un revêtement WC-CO sur acier, Chimie des surfaces et catalyse, (2001), pp345-350. *In french*

[Dune]   H.L.Dunegan, A.T. Green, Factors Effecting Acoustic Emission Response of Materials, Materials Research and Standards, MTRSA, 11(3), (March 1971), pp.21-24.

[Echs]   H.Echsler, S.Ito, M.Schütze, Mechanical properties of oxide scales on mild steel at 800 and 1000°C, Oxid. Met., vol.60, Nos.3/4, (2002), pp241-269.

[Fav]   Y.Favennec, V.Labbe, F.Bay, Identification of physical parameters involved in induction heating processes, In: *Proc. ESAFORM'00*, Stuttgart, (2000), pp.19-22.

[Fle]   J.D.Fletcher, Y.H.Li, J.H.Beynon, C.M.Sellars, The influence of surface conditions in hot forming determined by ring upsetting: a numerical and experimental investigation, Proc. Instn. Mech.Engrs. Vol. 212 part J, (1998), pp.453-465.

[Han]   P.Hancock, J.R.Nicholls, Application of fracture mechanics to failure of surface oxide scales, Mater. Sci. Technol. 4, (May 1988), pp.398-406.

[Koz]   P.F.Kozlowski, B.G.Thomas, J.A.Azzi, H.Wang, simple constitutive equations for steel at high temperature, Met. Trans. A, volume 23A, (March 1992), pp.903-918.

[Mor]   R. Morrel: Handbook of properties of technical and engineering ceramics, HSMO, London, (1987).

[Mou1]   M.H.Essid, Etude du comportement de la calamine sur un acier extra doux en flexion 4 points, mémoire de DEA, (2003). Encadrant: G. Moulin. *In french.*

[Mou2]   A.Makni, influence des paramètres sur le comportement mécanique en flexion 4 points en température des calamines formées sur acier, mémoire de DEA, (2003). Encadrant: G. Moulin. *In french.*

[Pic1]   B.Picqué, Y.Favennec, A.Paccini, V.Lanteri, P.O.Bouchard, P.Montmitonnet, Identification of the mechanical behaviour of oxide scales by inverse analysis of a

hot four point bending test, in M. Pietrzyk, Z. Mitura & J. Kaczmar (eds.): Proc. ESAFORM 5, Akapit, Krakow, 2002, pp.187-190.

[Pic2]   B.Picqué, S.Mouret, M.Picard, P.O.Bouchard, P.Montmitonnet, behaviour of iron oxide scale : experimental and numerical study, 2nd International Conference on Tribology in Manufacturing Processes (ICTMP), Nyborg, Denmark, (June 2004), pp.15-18.

[Pie]   M.Pietrzyk, J.G.Lenard, A study of thermal-mechanical modelling of flat rolling, J. Mater. Shaping Technol. Vol.7 n°2, (1989), pp.117-126.

[Schü]   M.Schütze, S.Ito, W.Przybilla, H.Echsler, C.Bruns, Test methods and data on the mechanical properties of protective oxide scales, Mater. High Temp. 18 (1), (2001), pp.39-50.

[Vagn]   G.Vagnard, J.Manenc, Etude de la plasticité du protoxyde de fer et de l'oxyde cuivreux, Mém. Sci. Rev. Mét., LXI, n°11, (1964), pp.768-776. *In french.*

[Zhou]   Y.C.Zhou, T.Tonomori, A.Yoshiba, L.Liu, G.Bignall, T.Hashida, Fracture characteristics of thermal barrier coatings after tensile and bending tests, Surf. Coat. Technol. 157, (2002), pp.118-127.

Extension to other strain and stress states:

Tension and Compression

Résumé

Ce chapitre est consacré à l'essai de traction à chaud (pour reproduire le comportement de la calamine mise en traction par la rotation des cylindres) et à l'essai de bipoinçonnement (comportement sous emprise). Dans chaque cas, une étude numérique a été réalisée pour compléter et enrichir les résultats expérimentaux.

L'essai de traction

Les essais de traction mettent en évidence des comportements de la calamine non examinés en F4P. Une des informations supplémentaires majeures est l'apparition de fissures en traction à de très hautes températures (900°C), comme en laminage. La déformation et la vitesse de déformation ont la même influence qu'en F4P, mais avec des effets plus prononcés (apparition de fissures transverses, propagation le long de l'interface métal – calamine, délamination).
Le modèle numérique développé est capable de reproduire correctement l'endommagement observé sur les éprouvettes déformées en traction à chaud.
Ces essais s'avèrent être un très bon complément de la F4P dans le but de comprendre le comportement complexe de la calamine.

L'essai de bipoinçonnement

Plusieurs points intéressants sont notés dans cette étude du comportement de la calamine en compression.
  - *Le premier est que malgré les contraintes de traction extrêmement élevées en bipoinçonnement, les critères de fissuration déterminés en traction ne peuvent être utilisés en compression. Ce comportement est principalement lié au fait que les contraintes compressives apportent de la ductilité pendant la déformation ;*
  - *L'ouverture de la fissure avant d'entrer sous les cylindres a un rôle prépondérant sur la formation du défaut d'incrustation ;*
  - *Les hautes températures favorisent le co-laminage ;*
  - *Un frottement faible favorise le co-laminage et diminue le phénomène d'extrusion.*

Finalement, ce chapitre permet de mieux appréhender les différentes sollicitations subies par la calamine en entrée et dans l'emprise d'une cage de finisseur. Différents mécanismes influençant l'apparition de défauts d'incrustation ont été mis en évidence. Un choix rationnel peut être fait pour éliminer ce défaut. Cependant les nombreux couplages et interactions entre les paramètres rendent cela très difficile.

Malgré le manque d'information concernant le comportement de la calamine sous emprise (en compression), nous disposons à la fin de ce chapitre de suffisamment de données pour simuler le comportement de la calamine en laminage à chaud dans de bonnes conditions.

The investigated 4-PHBT is most representative of the **bending solicitation at the roll gap entry**, due to the slab thickness reduction in the bite. This bending involves such tensile stresses within the oxide scale that through-thickness cracks can initiate. Nevertheless this origin of rolled-in scaled defect is only one among several.

Secondary scale defects are initiated when oxide cannot be rolled in the same way than the strip in the finishing mill. We have seen that all these defects are called rolled-in scale, but this common name may cover different mechanisms (Figure V-1).
Basically four main issues linked to the appearance of rolled-in scale have been identified:
- **Descaling** creating non-homogenous scale.
- **Roll**: damaged roll surface has a printing effect. Most of the time the chemical analysis of the oxide shows little amounts of Cr, Mo and other elements typical of work-rolls.
- **Strip**: scale too thick or too brittle to undergo deformation.
- **Roll bite**: too high stress in the bite.

These topics are generally strongly connected and it is very difficult to solve rolled-in scale by acting only on one of the previous items. So the rolling scale problem is complex and requires some fundamental work to better clarify its origin.
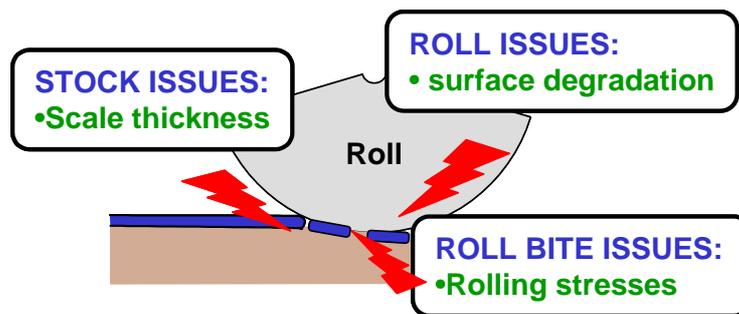
Figure V-1: Schematic representation of the complex interaction involved in rolled-in scale.

Représentation schématique des interactions complexes impliquées dans le défaut d'incrustation.

Our interest in this section concerns **strip** and **roll bite issues**. Considering these points, rolled-in scale damage comes from a combination of **three phenomena**:
- Breaking of the oxide layer occurs before the roll bite, because of the tensile stress associated with the bending of the surface there. This bending is due to the strip thickness reduction in the bite.
- Cracks initiation by **surface scale pulling**, due to the work-rolls rotation. This phenomenon involves higher tensile stresses in the oxide scale than the previous mechanism. It is able to initiate and open through-thickness cracks.
- **Scale embedding** and **soft steel extrusion** inside gaps formed by opened cracks. These phenomena happen in the bite, due to the high compressive stresses under the rolls. At this location, initiation and opening of cracks are also possible. Indeed, the thickness reduction involves an elongation of the slab; the oxide scale, here cooled by the cold rolls, may be less deformable than steel.

This chapter is then devoted to the last two points, using respectively hot tensile tests (HTT) and plane strain compression tests (PSCT). In each case, a numerical study has been performed to complete and enrich experimental results.

I.   HOT TENSILE TEST (HTT)

The advantage of tensile tests compared to the 4-PHBT is to allow much larger strain (several percent) and strain rate (up to 0.2 s^{-1}), much closer to those encountered at the inlet side of a Hot Strip Mill finishing stand. This is probably why, although the stress state in the oxide layer is the same (pure tension as in the 4-PHBT), cracking has been observed at all temperatures (up to 900°C).

I.1. A focused bibliographic study

Tensile behaviour has been presented in details in chapter II. In this section, we report on the very interesting work carried out by Beynon and Krzyzanowski [Krz1,Krz2,Krz3,Krz4], at the University of Sheffield. This group is the most active one on oxide scale behavior under HSM conditions. Their approach is always based on the combination of experimental measurements (here, HTT) and finite element modeling.

For them, the aim of HTT is two-fold:

- To determine the temperature ranges for different types of oxide scale damage;
- To evaluate the separation loads for oxide scale failure in tension.

Many different experimental tests have been performed. Our interest is mainly in the two following HTT, particularly close to our objectives and experiments. Even if the authors are more interested in the roughing mill than in the finishing mill, useful parameters ranges are approximately the same. In the first test, mild steel axisymmetric specimens are cut in two equal parts, connected together before the oxidation just preceding tensile tests (Figure V-2).
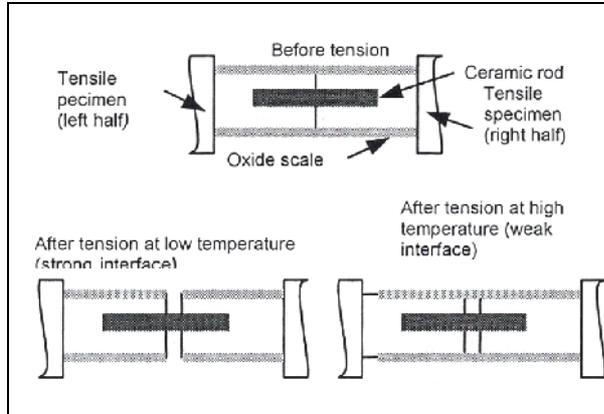
Figure V-2: Schematic measurement of separation loads during oxide failure in tension [Krz1].

Schémas de mesures des forces de séparation au cours de la fissuration de la calamine en traction [Krz1].
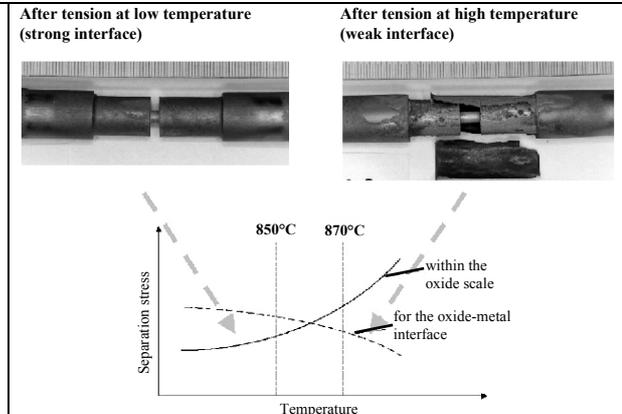
Figure V-3: Two different modes of oxide failure in tension during measurement of separation loads [Krz1,Krz2,Krz4].

Deux modes différents de fissuration d'oxyde en traction au cours de mesures des forces de séparation [Krz1,Krz2,Krz4].

During these tests, mild steel oxide exhibits two kinds of damage depending on temperature. The transition between both phenomena is around 860°C for the steel investigated (Figure V-2, Figure V-3). For temperatures below the transition, the oxide-metal interface is strong. A through thickness crack is initiated when the two half-specimens separate. The other mechanism, for higher temperature, comes from the fact that the interface becomes weaker than the oxide scale. After interfacial decohesion, the oxide scale slides along the interface without cracking.

	Amount (wt%)		
Element	Steel 1	Steel 2	Accuracy
C	0.19	0.18	±0.01
Si	0.18	0.36	±0.02
Mn	0.79	1.33	±0.02
Cr	0.05	0.03	±0.02
Ni	0.07	0.02	±0.02
Cu	0.14	0.08	±0.02
Mo	<0.02	<0.02	—
Nb	<0.01	0.041	±0.003
Al	<0.005	0.034	±0.003
V	<0.01	<0.01	—
P	<0.005	0.025	±0.002
S	0.030	0.010	±0.002

Table V-1: Chemical content of steel grades used for hot tensile testing [Krz3].

Composition chimique des aciers utilisés en traction à chaud [Krz3].

The second test corresponds to classical HTT on axisymmetric specimens. The influence of steel grade is investigated with two mild steels (Table V-1).

One more time, oxide scales exhibit two kinds of damage leading here to oxide spallation (Figure V-4). The first delamination mechanism occurs below a transition temperature, where the oxide-metal interface is strong. It begins with the initiation of through-thickness cracks, followed by a crack along the oxide-metal interface. For higher temperature, the behavior is identical to the previous test, with a weak oxide-metal interface.
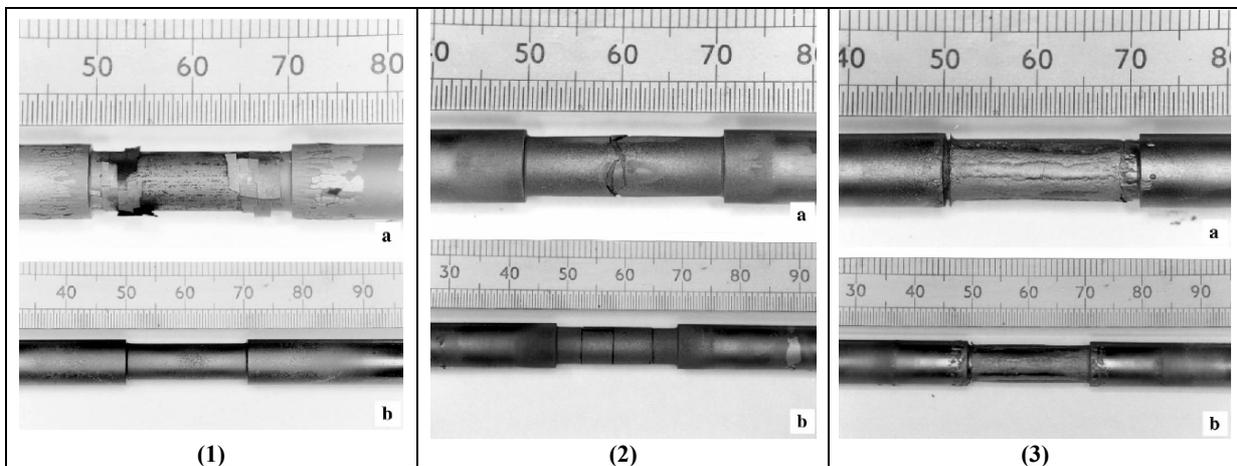
Figure V-4: Oxide scale on the tensile specimen after testing. (a) steel 1; (b) steel 2. (1) T=830°C, ε=2%, $\dot{\varepsilon}$ =0.2s^{-1}. T$_{ox}$=830°C, t$_{ox}$=800s (60 μm). (2) T=975°C, ε=5%, $\dot{\varepsilon}$ =2s^{-1}. T$_{ox}$=975°C, t$_{ox}$=800s (178μm). (3) T=1150°C, ε=5%, $\dot{\varepsilon}$ =4s^{-1}. T$_{ox}$=1150°C, t$_{ox}$=100s (172μm) [Krz1, Krz3].

Calamine sur des éprouvettes de traction après différents tests. (a) acier 1; (b) acier 2. (1) T=830°C, ε=2%, $\dot{\varepsilon}$ =0.2s^{-1}. T$_{ox}$=830°C, t$_{ox}$=800s (60μm). (2) T=975°C, ε=5%, $\dot{\varepsilon}$ =2s^{-1}. T$_{ox}$=975°C, t$_{ox}$=800s (178μm). (3) T=1150°C, ε=5%, $\dot{\varepsilon}$ =4s^{-1}. T$_{ox}$=1150°C, t$_{ox}$=100s (172μm) [Krz1,Krz3].
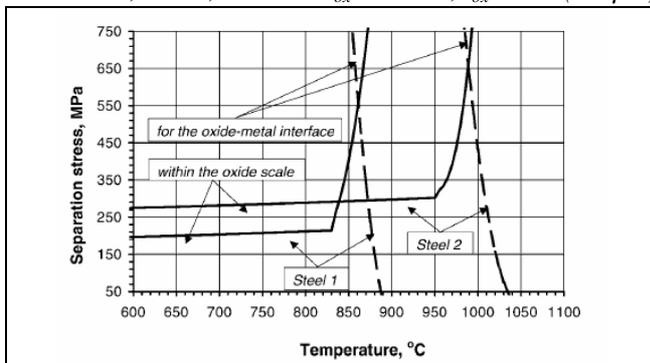
Figure V-5: Effect of temperature on the separation stresses of scale/metal system for two mild steel grades. Model assumption [Krz1,Krz3].

Effet de la température sur les contraintes de séparation du système calamine/métal pour deux nuances d'acier doux. Hypothèse du modèle [Krz1,Krz3].

Steel grade influence can be observed on Figure V-4. Both mechanisms described above appear in both cases. However a temperature shift can be observed between the two grades. Figure V-5 highlights this phenomenon and gives an estimate of the separation stresses. Yet these two mild steels are very close in composition. The oxide behavior is therefore very sensitive to small changes in chemical composition of the steel substrates. For the authors, the higher adherence of steel 2 is mainly due to its higher Si and Mn content.

185

The commercial FE code MARC K7.2 is used to simulate metal/scale flow, heat transfer, viscous sliding and failure of the oxide scale. All the components of the model are thermo-mechanically coupled. Critical failure parameters are obtained from HTT. Oxide scales are simulated with scale fragments joined together to form a continuous layer. The length of each scale fragment is set to be several times less than the smallest spacing of through-thickness cracks observed in experiments.
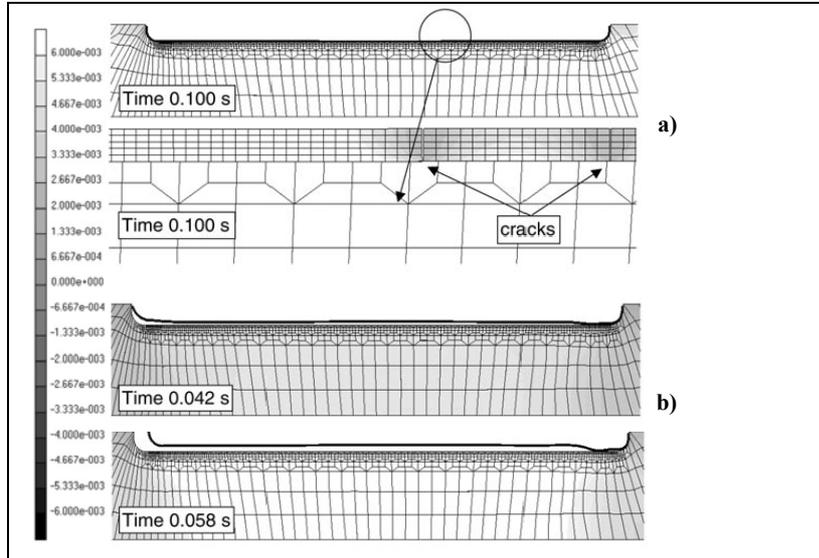
Figure V-6: Distribution of ε_x strain component predicted for steel at the different time moments during tension under T=975°C, ε=5%, $\dot{\varepsilon}$ =0.2s^{-1} and δ_{ox}=170μm. a) Steel 2 b) steel 1 [Krz1,Krz3].

Distribution de la composante ε_x des déformations prédites pour de l'acier à différents moments pendant la traction : T=975°C, ε=5%, $\dot{\varepsilon}$ =0.2s^{-1} et δ_{ox}=170μm.   a) acier 2 b) acier 1 [Krz1,Krz3].

Linear elastic fracture mechanics is also used in the model under the assumption that cracking is an essentially brittle process. The law used to simulate viscous sliding has been described in details in chapter II.

Both kinds of damage processes have been simulated (Figure V-6), using critical values presented on Figure V-5. Results agree correctly with experiments.

Microscopic observations of scales grown under different conditions of mechanical testing reflect precisely the morphological characteristics of oxides in their FE model (different oxide layers, voids, roughness of the interface).

However, this really great mesh is only represented in its initial state and during a rolling simulation. The 2-D mesh of this kind of porous scale does not necessarily give the most realistic results. Indeed, the 3-D extension of what was a void gives a cavity all along the specimen width, which weakens considerably the specimen. It would be interesting to compare simulation with and without these void being accounted for.
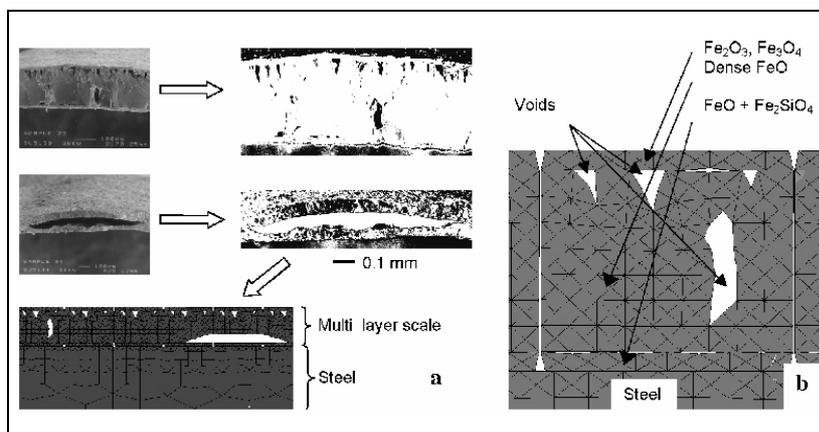
Figure V-7: Schematic representation of of characteristic morphological features of the oxide scale into the FE model (a) and detailed FE mesh representing the three-layers oxide scale (b) [Krz2].

Représentation schématique des particularités morphologiques de la calamine dans le modèle éléments finis (a) et maillage détaillé représentant le tri-couche d'oxydes (b) [Krz2].

Even though very interesting results on oxide scale behavior in hot rolling are provided, several remarks can be made :

- The first one concerns the thermal cycle used by the authors: specimen oxidation is performed at the temperature of deformation to avoid any influence of thermal stresses before deformation. Although relevant, it leads to different oxide scale morphologies depending on deformation temperature, different scale thickness which make the comparison between tests difficult.

- The second remark concerns their representation of the critical stress Figure V-3 and Figure V-5. We consider that the interfacial separation stress and oxide failure stress cannot be plotted in the same way. In other words, the transition between delamination modes (failure or decohesion) cannot be compared using the same stress component. The failure stress within the oxide scale has to be compared to the tension stress, whereas the decohesion stress has to be scaled against the normal interfacial stress (Figure V-8). The transition point is for all one knows the intersection of both separation stress curves. One mechanism follows the other, it is true, but not inevitably at the same stress value. Example: Let us take an oxide scale in tension. At a given stage of the test, the tension stress is 200 MPa and the normal interfacial stress is 60 MPa. If the critical failure stress within the scale is 220 MPa and the critical separation stress at the interface is 50MPa, interfacial failure will occur in spite of the lower stress. In addition, it seems to be really difficult to reach an oxide-metal interfacial stress of 650 MPa at 980°C (steel 2), since oxide is softer than or quasi-identical to steel at such a temperature.

Mechanism I: low temperature		Mechanism II: high temperature
Crack opening $\sigma_t > \sigma_{tc}$	**Crack propagation along the interface**	**Decohesion without cracking** $\sigma_n > \sigma_{adh}$
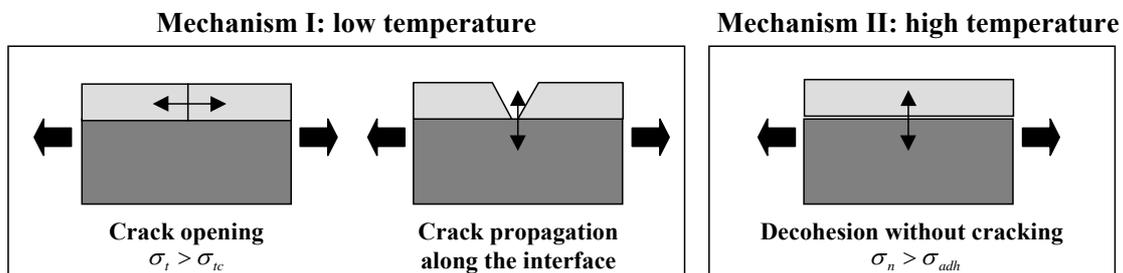
Figure V-8: Stress criteria of damage mechanisms at low and high temperature cannot be compared to a same separation stress. σ_t is the tensile stress within the oxide and σ_{tc} its critical value. σ_n is the normal stress at the interface and σ_{adh} its critical adherence.

Les critères en contrainte des mécanismes d'endommagement à faible et haute température ne peuvent pas être comparés aux mêmes contraintes de séparation. σ_t est la contrainte de traction dans l'oxyde et σ_{tc} sa valeur de fissuration critique. σ_n est la contrainte normale à l'interface et σ_{adh} sa valeur critique d'adhérence.

- Finally, concerning the numerical simulation, we have never seen the simulation of interfacial cracks, following through-thickness cracks at low temperature. Perhaps this is due to impossibility to remesh during calculation. We also think that the use of pre-existing cracks can distort the results by concentrating stresses at the junction of each oxide rafts, especially with the "V" shape at each top and bottom pre-crack (Figure V-6b).

I.2. **Our experimental device**

HTT have been performed on mild steel E24 (A37). Its chemical composition is:
0.1%C - 0.59%Mn - 0.26% - 0.019%P - 0.018%S - 0.009%N.

The tensile test system used in this study has been placed on a hydraulic tension-compression **Instron 1341H** testing machine (Figure V-9). It allows, in theory, displacement rates between $1.67 \ 10^{-4}$ mm.s^{-1} (0.01 mm/min) and 167 mm.s^{-1} (10000 mm/min) with a maximum load of 200 kN. Mechanical data are measured by a load cell placed at the top of the upper bar (+/- 5 kN). The resistance furnace is able to heat up to 1000°C. Two K-thermocouples are placed within the specimen on either side to control the temperature gradient. For this, samples are bored until the beginning of the gauge length (Figure V-10). A Pentium III PC (500 MHz) controls the test parameters and records the data.
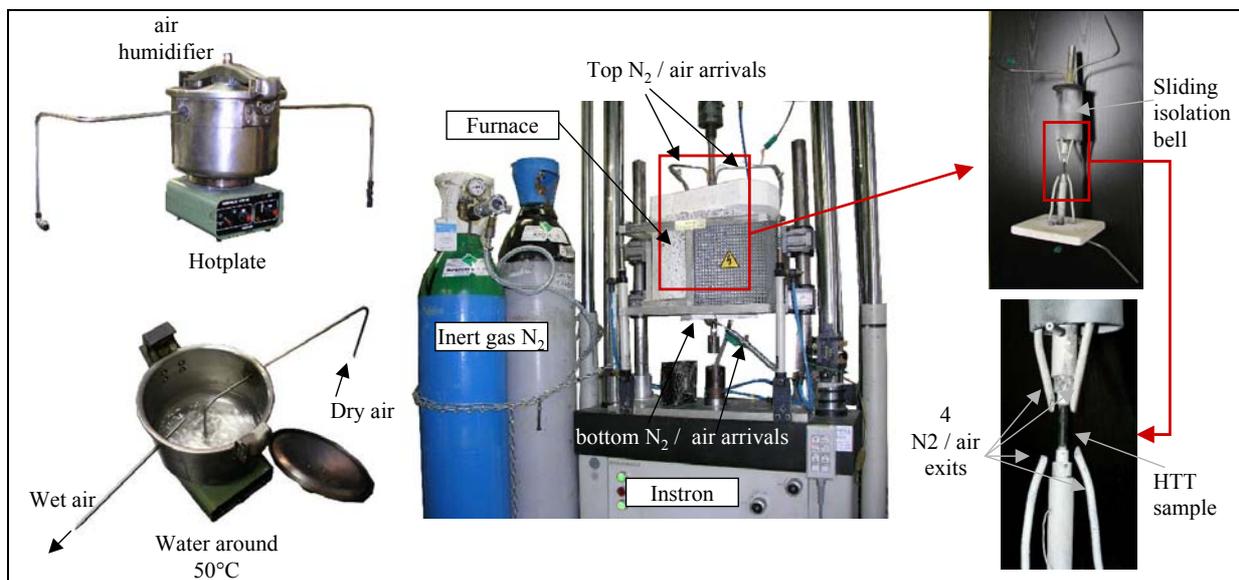
Figure V-9: HTT experimental device.

Dispositif expérimental du test de traction à chaud (TTC).

Thermal and chemical cycles used in this hot tensile test are identical to the 4-PHBT one. But HTT is significantly less accurate than 4-PHBT concerning thermal and atmosphere control:

- The specimen is not placed in a silica tube. Inerting atmosphere is therefore impossible. Air-tightness stages during the tests are ensured by projecting N_2 jets directly on the specimen. The oxidating atmosphere is injected on the specimen in the same way. A bell is placed around the specimen to localize the gaseous atmosphere and limit the hot gas "chimney effect".
- The heated wet air generator used for specimen oxidation is a quite rough system. Indeed, a pressure cooker is bored in two locations. The first hole is used to let in the dry air, which is plunged in distilled water heated at ~50°C. Dry air pressure is set such as to create only a few little bubbles at the water surface. From the inside pressure, wet air is obtained at the exit of the second hole (Figure V-9, left part). No condensation-preventing pipe heating system has been provided between the wet air generator and the furnace; nevertheless protection against oxidation for non-oxidized tests has proved efficient enough. Pure N_2 or Pure Ar (grade: Ar2) is necessary to hinder oxidation.

The cylindrical specimens used are schematically represented Figure V-10. In the case of "non-oxidized" tests, the entire specimen is protected by an anti-corrosion spray. When "oxidized" tests are performed, the gauge length (33 mm) is left unprotected.
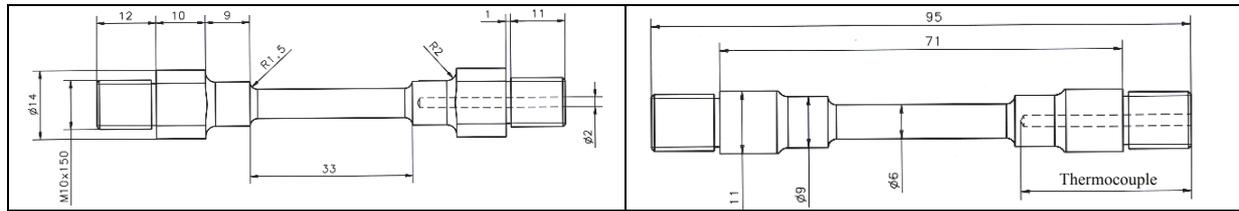
Figure V-10: Schematic representation of tension samples.

Représentation schématique des éprouvettes de traction.

I.3. Useful data

The hydraulic system of the tensile machine brings several difficulties in terms of velocity / displacement adjustment. Due to the initial velocity ramp, it has been impossible to obtain the same velocity for the different elongations. Thus, elongations of 0.5 mm, 1 mm and 2 mm used in the following, correspond respectively to velocities of 6, 8 and 16mm/s. Speed / strain rate and elongation / deformation correspondence used in next sections are also given Table V-2.

Elongation (mm)	ε (%)	Speed (mm/s)	$\dot{\varepsilon}$ (s^{-1})
0.6	2	0.045	0.0015
1	3.3	8	0.27
1.7	5.7	10	0.33
2	6.7	20	0.67

Table V-2: Calculated speed / strain rate and elongation / strain correspondence. Gauge length: 30mm

Vitesse et vitesse de déformation calculées, et correspondance élongation / déformation. Longueur utile : 30mm

I.4. Experimental results and parameters influence

The influence of several parameters such as temperature, strain, strain rate and scale thickness, have been studied.

I.4.1. Influence of temperature

Figure V-12 represents HTT oxidized samples elongated by 2mm between 700°C and 900°C. The oxide scale behavior seems to be the result of an interface / oxide brittleness competition, depending on temperature at constant strain.

At 700°C: the oxide scale is extremely brittle. Through-thickness cracks are initiated and propagate along the steel / oxide interface. The oxide scale is completely delaminated. In terms of stress, this case corresponds to $\sigma_t \gg \sigma_{tc}$, $\sigma_{n\_tip} > \sigma_{ip}$ and $\sigma_n \ll \sigma_{adh}$ (referring to notations of Figure V-8). σ_t is the tensile stress within the oxide and σ_{n_tip} the normal stress at the interface, at the through-scale crack tip. σ_n is the normal stress at the interface without

though-scale crack influence. Subscripts *c, ip* and *adh* indicate respectively the critical values for Cracking, Interfacial Propagation and Adherence.

At 800°C: The scale, although brittle, exhibits more ductility due to the temperature increase. In this case through-scale cracks are initiated but are not energetic enough to propagate all along the interface, as at 700°C. Only areas near the cracks are delaminated. Scale is adherent, which means in terms of stresses, $\sigma_t > \sigma_{tc}$, $\sigma_{n\_tip} \approx \sigma_{ip}$ and $\sigma_n < \sigma_{adh}$.

At 900°C: this temperature represents, in the literature, the limit between fracture and decohesion process. Several cracks are initiated, sometimes slightly delaminated near through-scale crack tips. $\sigma_t \geq \sigma_{tc}$ and $\sigma_{n\_tip} \approx \sigma_{ip}$; $\sigma_n \approx \sigma_{adh}$.

At T>900°C: From Beynon's tensile test results of Figure V-4(3), the extrapolation of our stress-based rationale gives $\sigma_t < \sigma_{tc}$, $\sigma_{n\_tip} << \sigma_{ip}$ and $\sigma_n > \sigma_{adh}$, which implies interfacial decohesion without through-thickness cracking. The oxide scale slips along the interface.
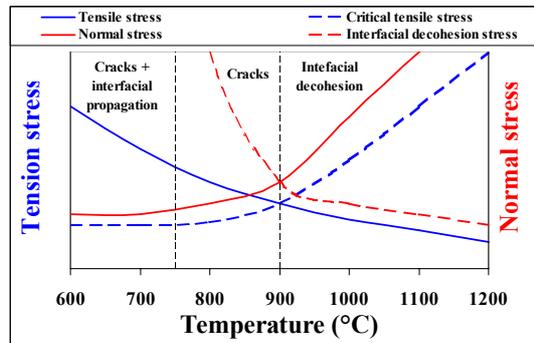
Figure V-11: Schematic representation of competition between damage processes depending on temperature. Interfacial propagation of cracks is not represented.

Représentation schématique de la compétition entre les procédés d'endommagement en fonction de la température. La propagation interfaciale de fissures n'est pas représentée.

I.4.2. Influence of strain

In the range of temperature tested, the interface is stronger than the oxide scale itself. Figure V-12 represents the HTT performed at temperatures between 700°C and 900°C for two elongations: 1 mm and 2 mm. Damage evolution is clear. First, through-thickness cracks are initiated. At low temperature (700°C), when deformation increases, a stress concentration at the crack tip propagates through-scale cracks along the interface. Figure V-13 shows more clearly the opening of cracks and the interfacial propagation as the deformation of the specimen increases.
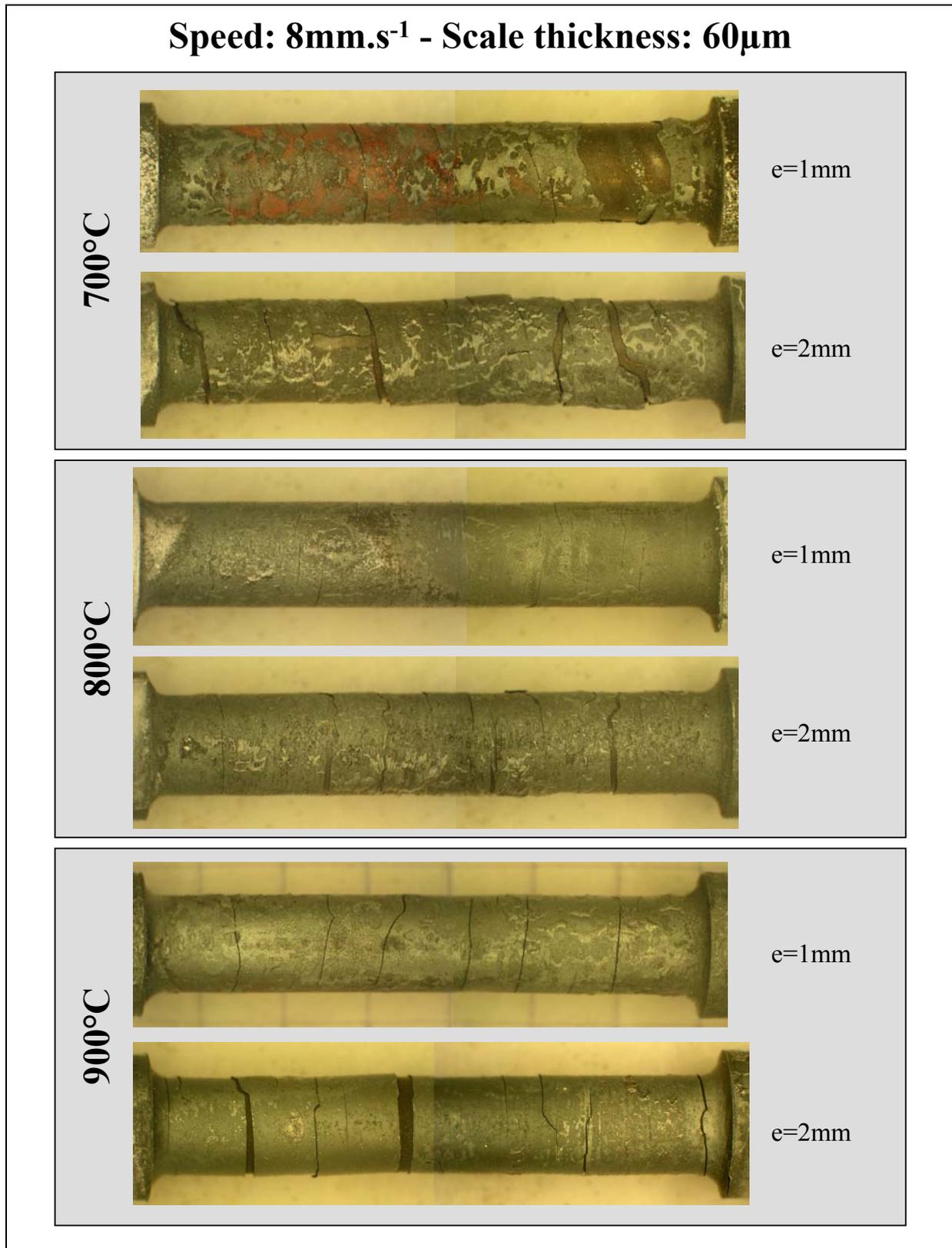
Figure V-12: Specimens covered by an oxide scale 60 µm thick using HTT. Test speed: 8 mm.s⁻¹.

Eprouvettes couvertes de calamine d'épaisseur 60µm en TTC. Vitesse du test: 8 mm.s⁻¹.
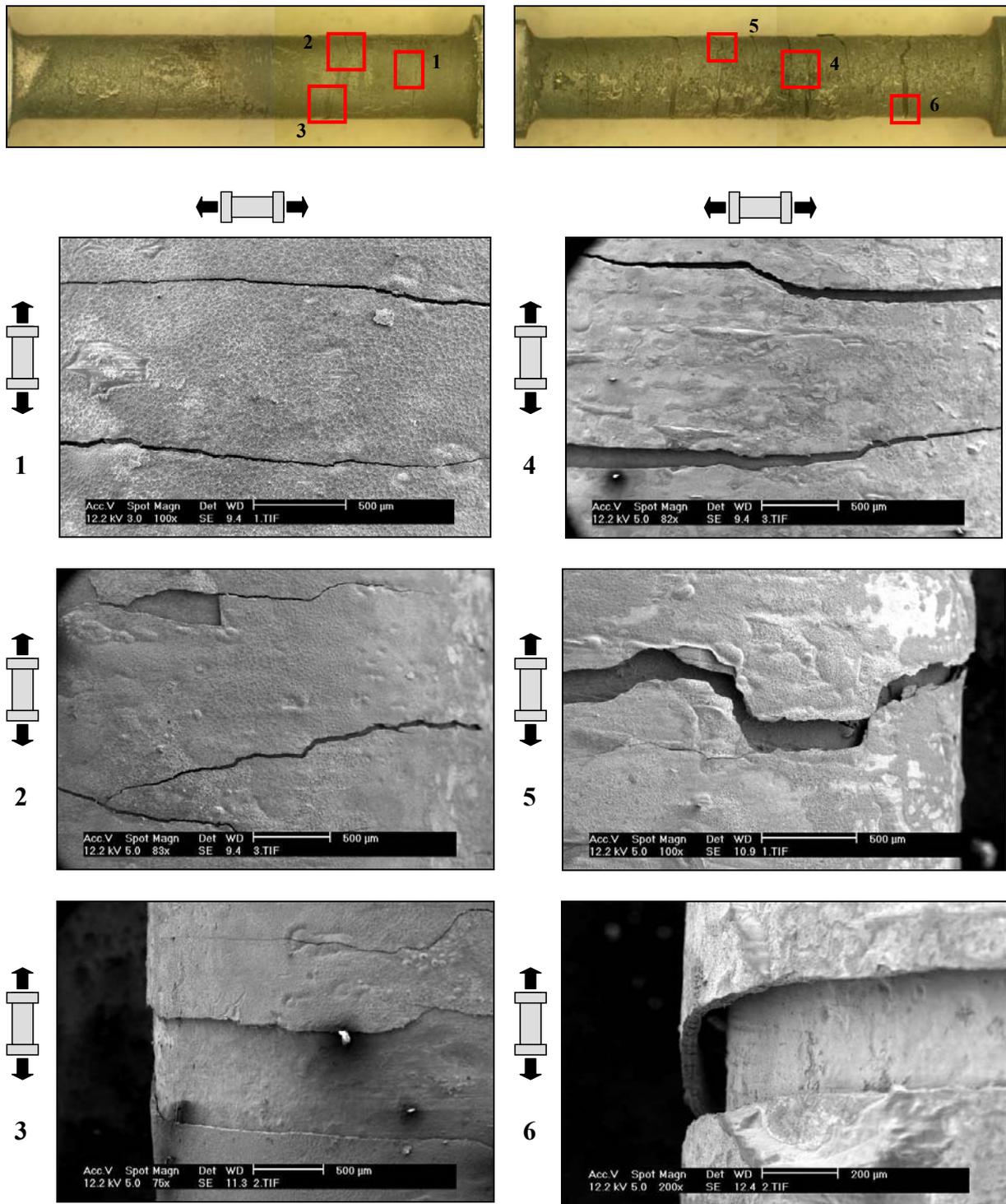
Figure V-13: HTT performed at 800°C and 8 mm.s⁻¹ – Left: elongation=1 mm. Right: elongation=2 mm.

TTC réalisés à 800°C et 8 mm.s⁻¹ – Gauche: élongation=1 mm. Droite: élongation=2 mm.

I.4.3. Influence of strain rate
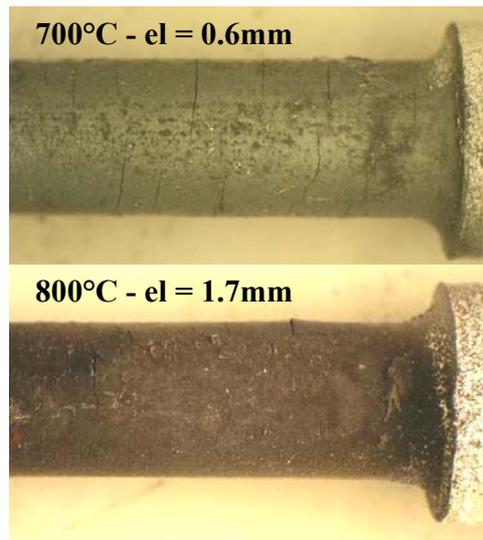
Figure V-14: HTT: samples deformed at 0.045 mm.min⁻¹.

TTC: éprouvettes déformées à 0.045 mm.min⁻¹

It was important to evaluate precisely the strain rate sensitivity of oxide scale during HTT. Thus, several tests have been performed at extremely low strain rate (v=0.045 mm/min $\Leftrightarrow$ $\dot{\varepsilon} = 1.5.10^{-3} s^{-1}$) to be as close as possible to 4-PHBT conditions. Specimens observations brought to light a tendency close to 4-PHBT conclusions (Figure V-14) : cracks started to be replaced by plastic deformation around 800°C. The transition temperature increase compared to 4-PHBT is due to a significantly higher specimen deformation (1.67% , i.e. an elongation of 0.5mm).

These tests performed at 0.045mm/mn are compared to those at 10 mm/min of Figure V-12. At 700°C, tests performed at low strain rate show a more plastic behavior and more adherent oxide scale than at higher strain rate. At 800°C, a significant increase of the crack number is observed at higher strain rate.

I.4.4. Influence of scale thickness

HTT have been performed with samples covered by oxide scale 60µm and 25µm thick. Their comparison has shown that, for the thinner oxide (Figure V-15) :

- Oxide spallation is not observed anymore. Cracks do not propagate along the interface.
- Cracks are less open due to a higher crack density, among other things.

Both observations are similar to 4-PHBT experiments.

V=8mm/s - elongation=1mm

700°C

Oxidation time: 8min - Scale: 60µm

Oxidation time: 2min - Scale: 25µm

900°C

Oxidation time: 8min - Scale: 60µm

Oxidation time: 2min - Scale: 25µm
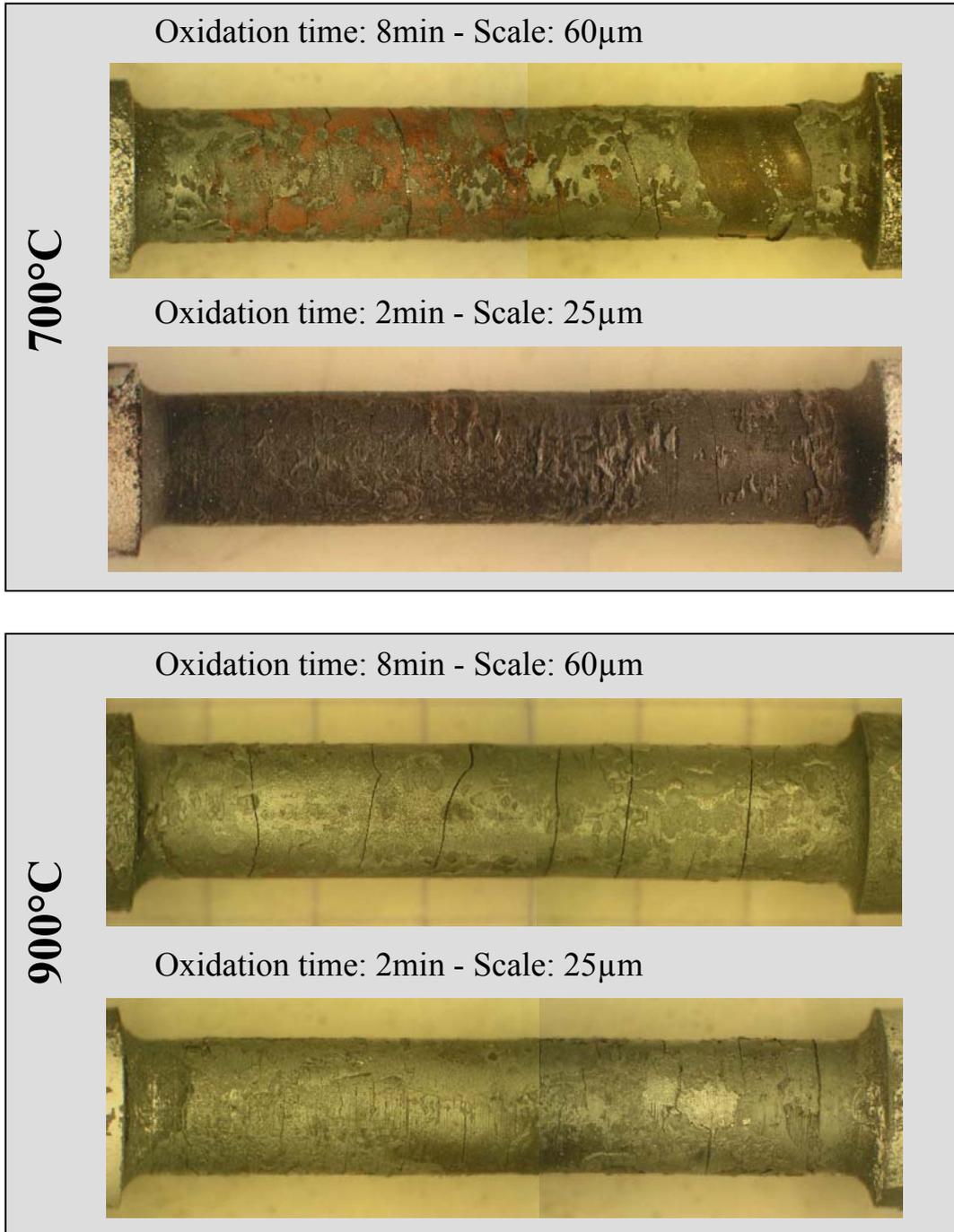
Figure V-15: Influence of scale thickness in HTT.

Influence de l'épaisseur de la couche d'oxyde en TTC.

I.4.5.   LC steel and Ex-LC steel

Steel grade influence has not been really investigated. It has been limited to a comparison between mild steel grade, used in HTT, and Ex-LC steel samples used previously in 4-PHBT. Our purpose was to estimate similarities between them in order to judge if HTT results obtained using LC steel could be compared with 4-PHBT.
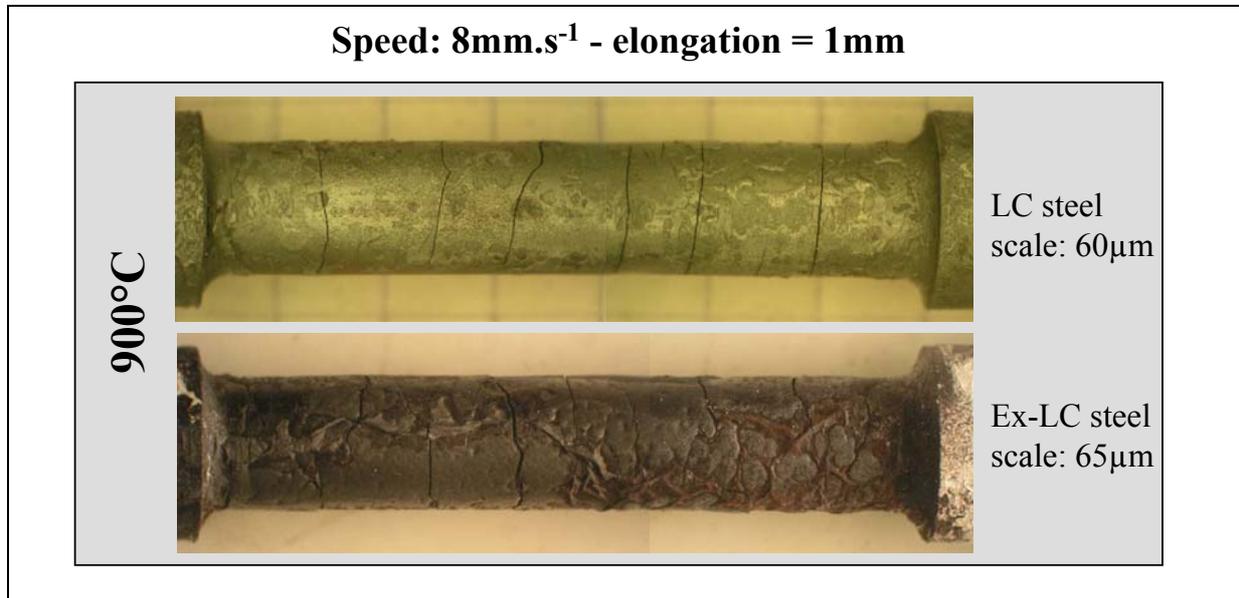
Figure V-16: Comparison between LC and Ex-LC steel grades deformed using HTT.

Figure V-17: Comparaison entre des nuances d'aciers doux et extra-doux déformées en TTC.

Really close behaviors between both steel grades have been found, in terms of damage. The number of cracks as well as their propagation all around samples and their opening are very similar: the steel grades used in 4-PHBT and HTT have sufficiently close mechanical behaviors to be compared.

I.5. <u>Load-elongation curves</u>

During the test, load and crosshead displacement (elongation) are recorded vs time. The curves obtained must be taken with much care due to their lack of reproducibility and a quite insufficient number of points. Nevertheless, several points can be noted.

The general shape of load-elongation curves is represented Figure V-18. It is constituted of an initial linear part, corresponding to a combination of specimen and machine elastic behaviours, and to the velocity increase to the target value. Then, the load reaches a quasi-constant value, which corresponds to the flow strength. Finally, load decreases as the velocity does (damping system).

A spring-back (200 µm max) can happen randomly at the end of tests, as seen in Figure V-18. Specimens are screwed in tubular tools, themselves fixed to crosshead via a pin. A clearance is purposely introduced at the pin position to compensate for this spring-back (Figure V-18).
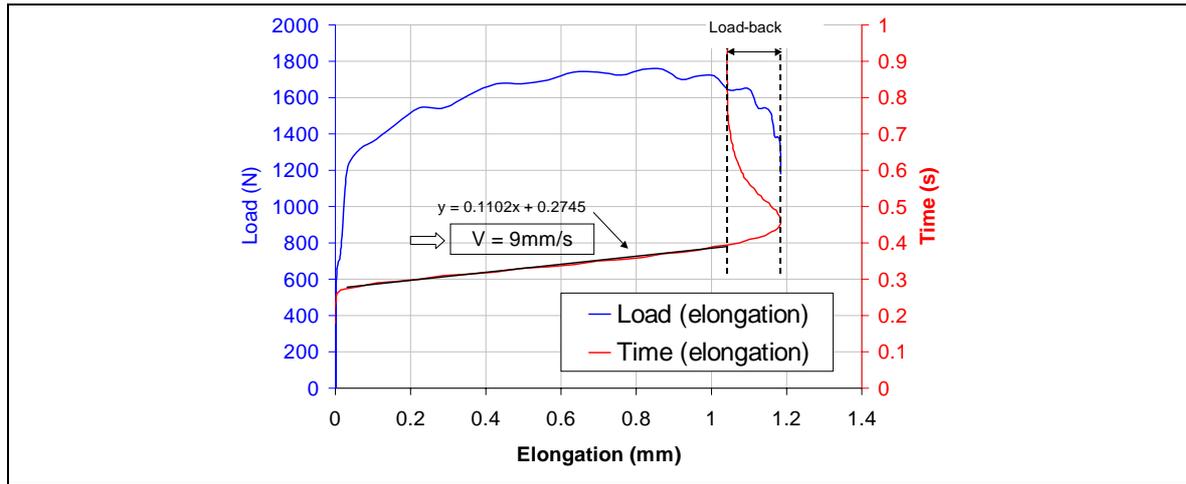
Figure V-18: Representation of HTT load-elongation curve shape. HTT performed at 800°C.

Représentation de la forme des courbes force-élongation en TTC. Tests réalisés à 800°C.

I.6. <u>Numerical simulation of tensile test</u>

A 8 mm/s crosshead velocity has been selected for the simulations presented in this section. This velocity makes little difference in the results anyway.

For the mild steel, the following constitutive behavior has been taken from literature [Piet]:

$$\overline{\sigma} = 98.1\left[17.8\exp\left(-0.0029\,T\right)\right]\left(1.79\,\overline{\varepsilon}^{\,0.252}\right)\left(0.72\,\dot{\overline{\varepsilon}}^{\,0.143}\right) \qquad \textbf{eq. V-1}$$

E = 145 GPa, ν = 0.33

Constitutive equations of oxide scale are selected in accordance with the results presented in chapter IV. Thus, we started from the steel behavior law associated with hardness ratio *r* determined in the previous chapter. To reproduce at best the elasticity at high strain rate, a threshold $K_{ox,1}$ has been added. It corresponds to the oxide scale yield stress determined from FeO Vickers hardness *Hv* seen in [Vag].

$$\overline{\sigma}\,(MPa) = K_{ox,1} + K_{ox,2}.\overline{\varepsilon}^{\,n_{ox}}.\dot{\overline{\varepsilon}}^{\,m_{ox}} = K_{ox,1} + r(T)\times\left\{98.1\left[17.8\exp\left(-0.0029T\right)\right]\left(1.79\overline{\varepsilon}^{\,0.252}\right)\left(0.72\dot{\overline{\varepsilon}}^{\,0.143}\right)\right\}$$

$$K_{ox,1} = \frac{1}{3}Hv_{ox} \qquad \textbf{eq. V-2}$$

This procedure gave the following parameters:
$E_{ox}(700°C) = 150$ GPa, $E_{ox}(900°C) = 150$ GPa, $\nu_{ox} = 0.33$
$K_{ox,1}(700°C) = 200$ Mpa, $K_{ox,1}(900°C) = 100$ MPa

Fitting of experimental results and simulations gave critical stresses:
σ_{tc} (700°C ≤ T ≤ 900°C)= 180 Mpa
σ_{ip} (700°C)= 180 MPa, σ_{ip} (900°C)= 130 MPa.

No interfacial sliding has been evidenced in the experiments; therefore, this mechanism has not been activated in the simulations.

| Experiment | Simulation |

1mm 2mm   1mm 2mm

Symmetry axis

Figure V-19: Samples deformed at 900°C and 10 mm.s^{-1} using HTT. Experiment / simulation comparison.

Eprouvettes déformées à 900°C et 10 mm.s^{-1} en TTC. Comparaison expérience / simulation.
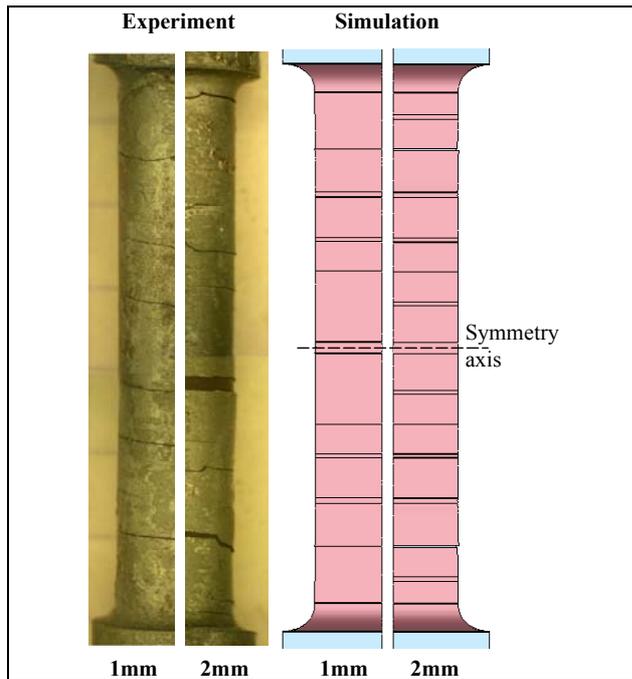
Evolution of oxide scale damage during deformation is well reproduced by simulations. Figure V-19 proves the numerical model efficiency. In both experiments and simulations, the crack number changes little between 1 and 2 mm elongation.

The first step of the deformation is the initiation of through-thickness cracks. In a second step, the crack number does not increase anymore, leaving place to interface decohesion. This phenomenon is demonstrated on Figure V-20, which compares the evolution of delamination in experiments (a,b) and simulations (c,d). Numerical simulations reproduce well, at least qualitatively, cracking and spalling events observed in experiments.

(a)

(b)

(c)

(d)

Figure V-20: HTT performed at 8 mm.s^{-1}. Oxide thickness: 60 μm, elongation 2 mm (a) experimental 700°C (b) experimental 900°C (c) numerical 700°C, σ_{tc} = 180 MPa, σ_{ip} = 180 MPa (d) numerical 900°C, σ_{tc} = 180 MPa, σ_{ip} = 130 MPa.

TTC réalisés à 8 mm.s^{-1}. Oxyde: 60 μm, élongation 2 mm (a) expérimental 700°C (b) expérimental 900°C (c) numérique 700°C, σ_{tc} = 180 MPa, σ_{ip} = 180 MPa (d) numérique 900°C, σ_{tc} = 180 MPa, σ_{ip} = 130 MPa.
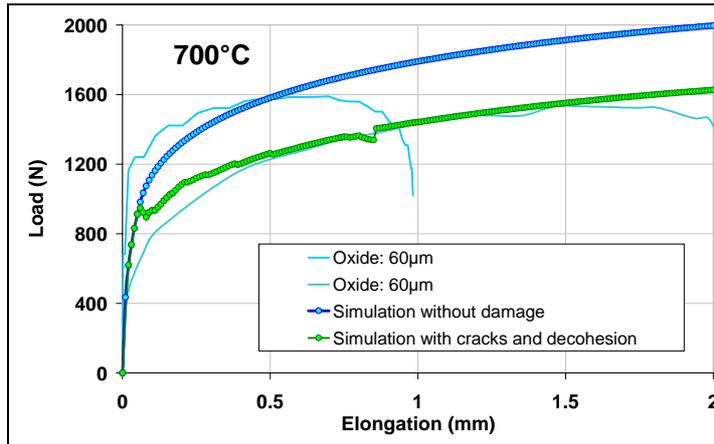
Figure V-21: Superposition of experimental and numerical load-elongation curves of HTT performed using oxidized specimens (oxide: 60 μm) at 700°C.

Superposition des courbes force-élongation expérimentales et numériques d' éprouvettes oxydées (oxyde: 60 μm) déformées en TTC à 700°C.

Experimental and numerical load-elongation curves obtained at 700°C are superimposed on Figure V-21.

Experiments have shown that for an elongation of 1 mm, the greatest part of the scale remained adherent. At 2mm, the oxide scale was totally delaminated (Figure V-13). The result of simulations with damage (Figure V-20c) and without shows that the impact of decohesion on load-elongation curves (Figure V-21) is also correctly estimated.

This shows that playing with the values of σ_{tc} and σ_{ip} with respect to the oxide plasticity parameters, the competition between the deformation mechanisms can be analyzed. In particular in the present case, the analysis suggests that the toughness of the oxide increases with temperature, both for transverse and interfacial cracks, which has to be referred to the ratios $\sigma_{ip}/\overline{\sigma}$ and $\sigma_{tc}/\overline{\sigma}$. It has to be noted however that our quasi-static approach, based on simple nodal stress criteria, has no ambition to follow precisely interfacial crack propagation or to predict precisely its velocity.

Extrapolation of numerical results has been performed, for higher temperature (Figure V-22).
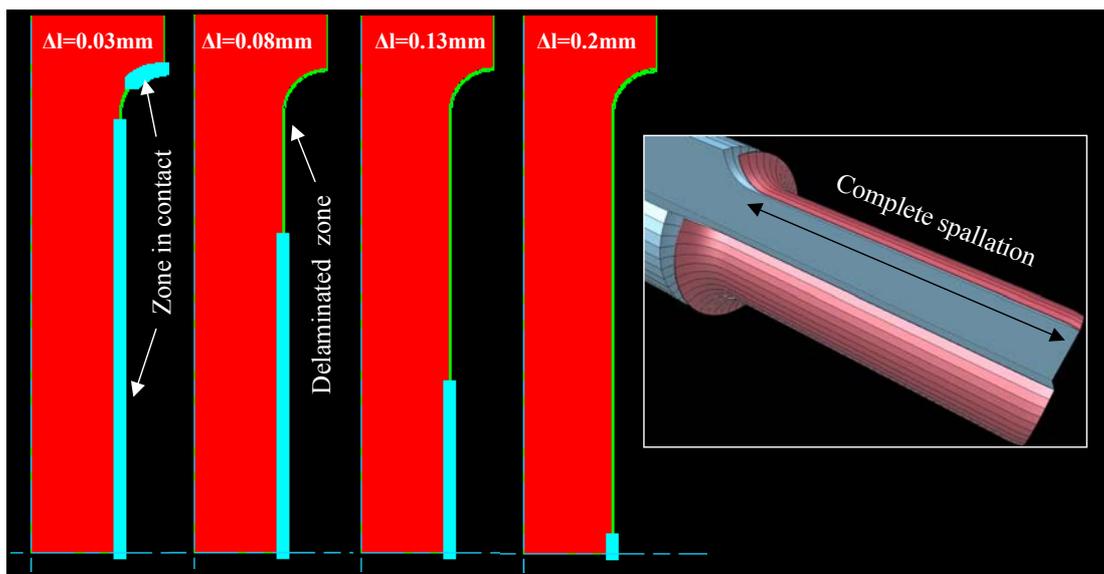
Figure V-22: Simulation of hot tensile test deformed at high temperature (T=1000°C). Evolution of delamination process.

Simulation d'un test de traction à chaud réalisé à haute température (T=1000°C). Evolution du processus de délamination.

1000°C - 20mm.s⁻¹ - scale: 60μm
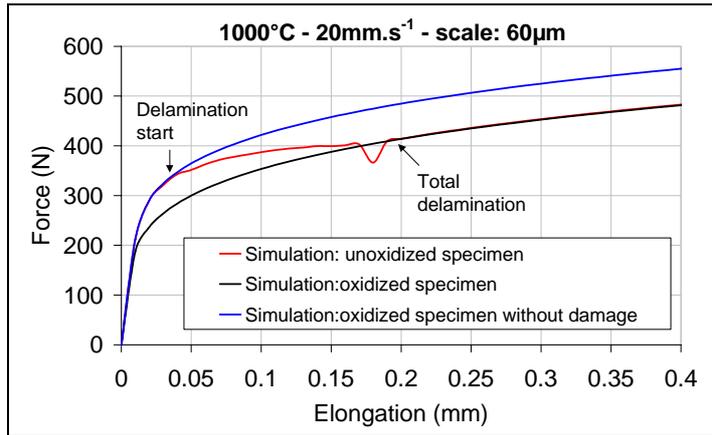
Figure V-23: Load-elongation curves obtained from hot tensile test simulation at 1000°C. Red curve represents simulation seen Figure V-22.

Courbes force -élongation obtenues par simulation d'un TTC à 1000°C. La courbe rouge représente la simulation vue Figure V-22.

Results are in good agreement with Beynon and Krzyzanowski's experimental and numerical results. The delamination process can be observed, Figure V-23, on the load-elongation curves corresponding to the simulation presented Figure V-22. From the beginning of delamination, the curve slows down to reach at the instant of the total delamination the "non-oxidized" curve.

I.7. <u>Conclusion on the hot tensile test</u>

The non-exhaustive HTT performed have evidenced several oxide scale behaviors that had not been observed using 4-PHBT. The main new information is the **oxide scale damage at high temperature such as 900°C**. The strain and strain rate influence seen in 4- PHBT has been found again in HTT, **amplified by larger strain and strain rate)**. Indeed, through-scale cracks initiate at 900°C. **Propagation of these cracks along the interface has also been observed**, more or less depending on the temperature. HTT have not been performed at high enough temperature to observe the oxide scale **delamination** and the **interfacial sliding** without previous occurrence of brittle through-thickness cracks, as in [Krz1].

The **numerical model** is able to **reproduce correctly damage** observed on samples deformed using HTT.

These HTT are therefore a very good complement to 4-PHBT, they help better understand the complex behaviour of oxide scales.

II. PLANE STRAIN COMPRESSION TEST (PSCT)

The second part of this chapter is devoted to what happens in a roll bite, **under work-rolls**. This subject is really **rarely studied** by the research groups interested in rolled-in scale defect, despite its **important role**. Thus, a preliminary PSCT study has been carried out several years ago at IRSID. The little number of tests does not provide quantitative results ; however, it gives several indications on the importance of this kind of work. Our numerical model has been used to interpret and complete experimental results.

II.1. A hot rolling model

Various laboratories use the PSCT to simulate metal flows (of aluminum, or steel) in a HSM (Figure V-24). PSCT has a greater flexibility compared to a pilot rolling mill. In particular, it allows an easier control of operational parameters such as the temperature or the oxidation atmosphere.

The objective of this exploratory research was to develop at IRSID a test able to simulate the typical flow in a roll bite (Figure V-25). Such a test appears interesting for various research projects:

- The study of thermo-mechanical cycles of surface layers during rolling;
- The study of the mechanical and microstructural evolutions in hot rolling;
- The calculation of rolling loads;
- The study of texture formations;
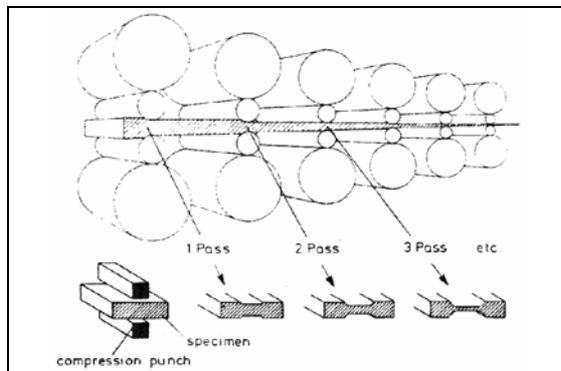
Figure V-24: Principe of HSM simulation using PSCT [Paw].

Principe de la simulation d'un train à bande par bipoinçonnement [Paw].
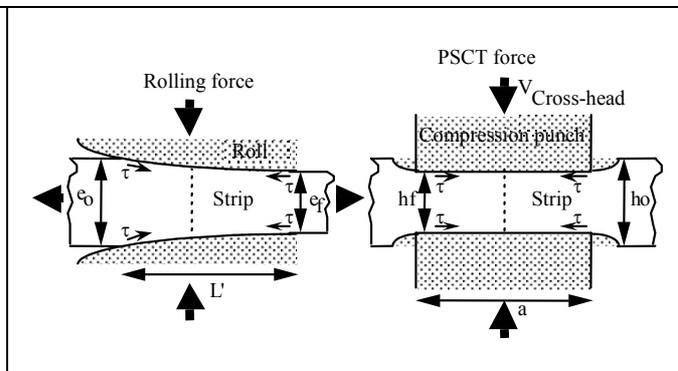
Figure V-25: Flow similarity in hot rolling and PSCT.

Similitude des écoulements entre laminage à chaud et test de bipoinçonnement.

	Contact length	Initial thickness	Slenderness	Reduction	Deformation	Strain rate
Rolling	L'	e_0	$\dfrac{e_0}{L'}$	$\dfrac{e_0 - e_f}{e_0}$	$\bar{\varepsilon} = \dfrac{2}{\sqrt{3}}.\ln(e_0/e_f)$	$\dot{\bar{\varepsilon}} = \dfrac{\bar{\varepsilon}}{t}$
PSCT	a	h_0	$\dfrac{h_0}{a}$	$\dfrac{h_0 - h_f}{h_0}$	$\bar{\varepsilon} = \dfrac{2}{\sqrt{3}}.\ln(h_0/h_f)$	$\dot{\bar{\varepsilon}} = \dfrac{2}{\sqrt{3}}.\dfrac{V_{crosshead}}{h_0 - h_f}$

Table V-3: Hot rolling /PSCT equivalence.

Equivalences laminage à chaud / test de bipoinçonnement..

And finally, our main interest is:

- The oxide scales behavior under compression.

For all these various studies, it is necessary to ensure that PSCT is really able to mimic the hot rolling flow. Thus, before beginning the PSCT campaign, a numerical study has been carried out at IRSID on rolling / PSCT equivalence. From several ARCELOR HSM process databases, typical rolling schemes have been selected (in priority those in which rolled-in scale problems occurred). From these schemes, **equivalent** variables have been calculated (in other words, variables that ensure the similarity between rolling and PSCT flows). These variables are the strain, the strain rate and the slenderness ratio (thickness / contact length ratio). The latter governs the geometrical similarity of the flow.

Dimensions of compression punches have been selected from experimental constraints. Indeed, for a given stand, the punch used is the one giving the slenderness ratio closest to rolling (Table V-4).

Strip rolling mill data	F1	F2	F3	F4	F5	F6	F7
Initial strip thickness : e_O (mm)	40,14	21,76	12,07	7,76	5,37	3,84	3,13
Exit strip thickness: e_f (mm)	21,76	12,07	7,76	5,37	3,84	3,13	2,86
Rolls speed: ϖ (rd/mn)	26,38	44,38	66,62	95,3	145,03	171,66	184,27
Initial roll radius: R (mm)	338,1	361,2	374,25	380,15	351,65	373,2	385,75
Rolling force: F (tons)	2420,1	2281,2	2268,7	2076	1938,2	1659,7	928,2
Calculation of "equivalent" variables							
Reduction: $\rho = 1-e_O/e_f$ (%)	45.8	44.6	35.7	30.7	28.6	18.3	8.7
Deformation	0,707	0,681	0,510	0,424	0,389	0,234	0,105
Deformed rolls radius (Hitchcock's formula): R' (mm)	349,3	382,5	423,6	463,2	462,7	594,1	715,7
Contact arc length: $L'=\sqrt{(R'.\Delta h)}$ (mm)	80,1	60,9	42,7	33,2	26,7	20,4	14,0
Strip velocity under rolls: Vstrip $= 2\pi\varpi R/1000$ (m/mn)	56,0	100,7	156,6	227,6	320,4	402,5	446,6
Contact time: t=L'*60/(Vbande*1000) (s)	0,0858	0,0363	0,0164	0,0088	0,0050	0,0030	0,0019
Strain rate (s^{-1})	8,2	18,8	31,2	48,4	77,9	76,7	55,9
Slenderness ratio (= Thickness / roll gap length)	0,5010	0,3573	0,2824	0,2335	0,2014	0,1877	0,2245
PSCT							
Initial sample thickness: h_o (mm)	6,4	6,4	6,4	6,4	6,4	6,4	6,4
Final sample thickness : $h_f=h_o.(1-\rho)$ (mm)	3,5	3,5	4,1	4,4	4,6	5,2	5,8
Test time (s)	0,0858	0,0363	0,0164	0,0088	0,0050	0,0030	0,0019
Punch speed: V (mm/s)	34,2	78,6	139,7	224,5	366,7	385,0	296,4
Contact length (mm)	13	18	25	25	35	35	25
Hot rolling / PSCT equivalence							
Slenderness ratio in PSCT ./ Slenderness ratio in rolling	1,7 %	0,5%	9,4%	9,6%	9,2%	2,6%	14,0%

Table V-4: Example of Sollac/Fos finishing mill scheme. PSCT equivalent variables.

Exemple d'un schéma de finisseur Sollac/Fos. Variables équivalentes de bipoinçonnement.

3-D numerical calculations of rolling and PSCT have been performed using the LAM3 FE software. A comparison of thermo-mechanical solicitations between rolling and PSCT has been investigated. A complete rolling scheme has been simulated as well as the equivalent PSCT. Thus, it has been possible for the IRSID researchers to obtain the mechanical equivalence, in volume and surface, between rolling process and PSCT.

In volume, equivalent stress distribution is well reproduced using PSCT (Figure V-26). Specimens as wide as possible have to be chosen in order to respect the plane strain condition.

Concerning the equivalent strain, it is quasi-equal at the end of the rolling process to those calculated in PSCT. This is in perfect agreement with Pawelski's work, which experimentally showed that PSCT reproduces quite well mechanical properties and microstructures of metals deformed by hot rolling [Paw].
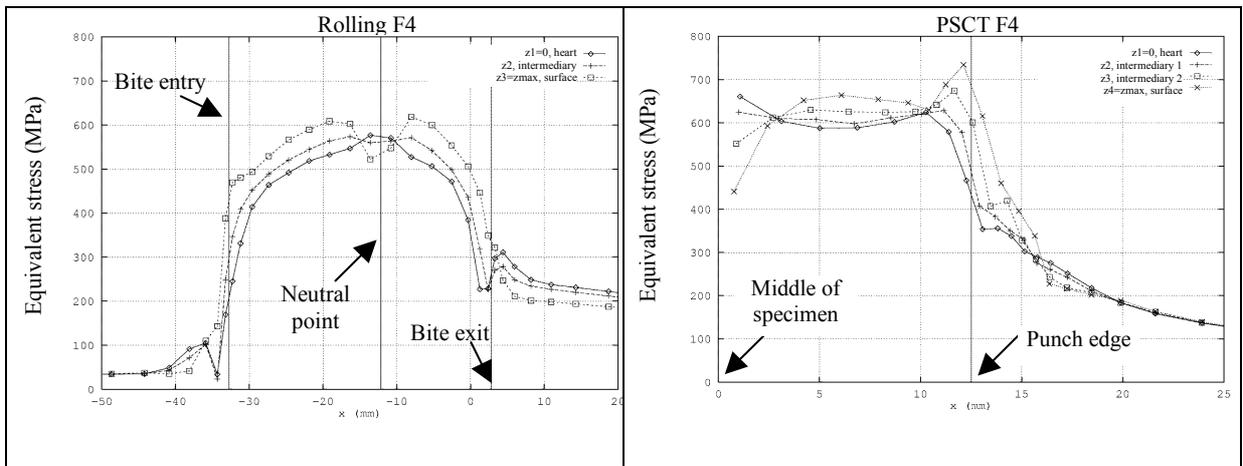
Figure V-26: In bite equivalent stress distribution σ_{eq}, at the strip center.

Distribution de contrainte équivalente σ_{eq} sous emprise, au centre de la bande.

On the surface, the shear strength is well reproduced using PSCT (Figure V-27), but normal and longitudinal stresses are higher than in rolling.
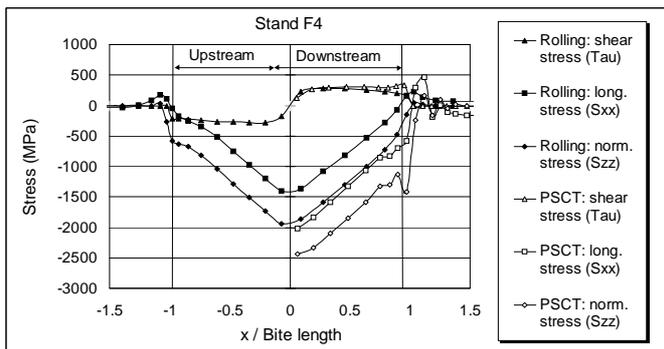
Figure V-27: Summary of stresses on surface, in rolling and PSCT. History of a material point.

Résumé des contraintes de surface, en laminage et en bipoinçonnement. Histoire d'un point matériel.
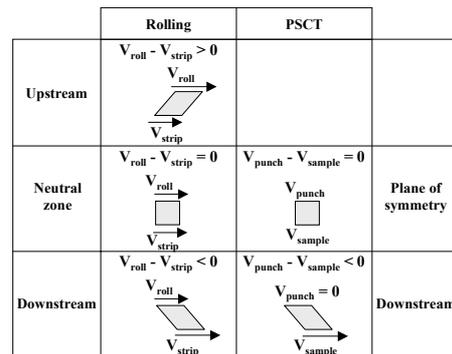
Figure V-28: Simulation of a roll bite using PSCT schematic strain pattern

Simulation d'une emprise de laminage par bipoinçonnement : schéma de déofrmation.

Finally, it is important to note that, for a material point, the shearing is **alternative** in rolling, depending on the location compared to the neutral point (shearing < 0 in the upstream part

and > 0 in the downstream part), whereas it is **monotonic** in PSCT (Figure V-28 : shearing > 0 as in the downstream part). **It is difficult to estimate the impact of this difference**.

In spite of several limitations, PSCT is one of the rare laboratory tests able to deform an oxide surface layer under conditions (stress, strain, temperature…) close to those encountered in a finishing mill roll bite.

II.2. The experimental device

The PSCT fixture has been installed on a 630 T Loire press (Figure V-29). As for the 4-PHBT, it is possible to perform tests under a controlled atmosphere. The oxide scale growth is done with atmosphere control varying the O_2 and H_2O content. The fixture is placed inside a tight silica tube. Punches are in ceramic (SiC).
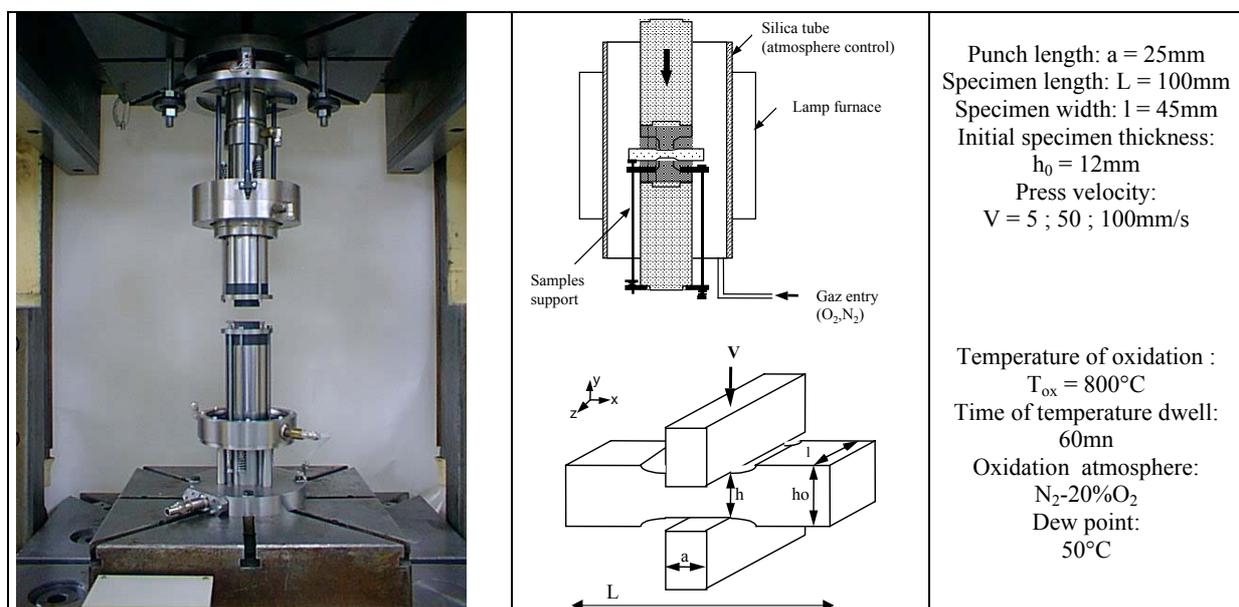
Figure V-29: The PSCT fixture and its schematic representation. Description of PSCT thermal and chemical cycles.

Machine de bipoinçonnement et représentation schématique. Description des cycles thermique et chimique des tests de bipoinçonnement.

II.3. Mechanical behavior of the oxide scale during PSCT

The performed PSCT have displayed several parameters influence on scale and interface deformation under compressive stress simulating a hot rolling pass. These parameters are the reduction, the temperature of deformation, the oxide homogeneity, the steel grade and the strain rate. The effects of these parameters have been evaluated separately.

From cross-sectional microscopic observations of deformed specimens, it is possible to measure the scale thickness before and after each test, by the observation of zones located respectively out of and in the bite (

Figure V- 30). The steel-scale interface quality is controlled in the same way.

(a)   **(b)**
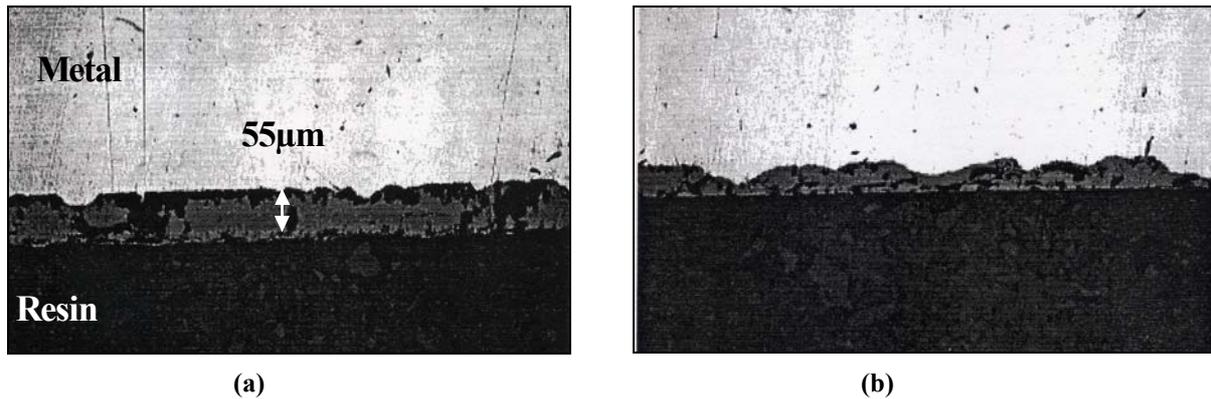
Figure V- 30: Micrographs of a DDS specimen cross section after a PSCT. Temp: 800°C, reduction: 50%, velocity: 5 mm/s, initial scale thickness: 55 μm, (a) outer free zone (b) inner compressed zone.

Micrographies de coupes d'éprouvettes DDS après bipoinçonnement. Temp: 800°C, réduction: 50%, vitesse: 5 mm/s, épaisseur initiale: 55 μm, (a) zone extérieure libre (b) zone intérieure en compression.

Reduction:

Tests have been performed for two reduction ratios (30% and 50%) at low temperature (800°C) and low velocity (5 mm/s) with identical scale thickness (60 μm). The **reduction increase** leads to **increased interface transformations and metal extrusion** (Figure V-31).
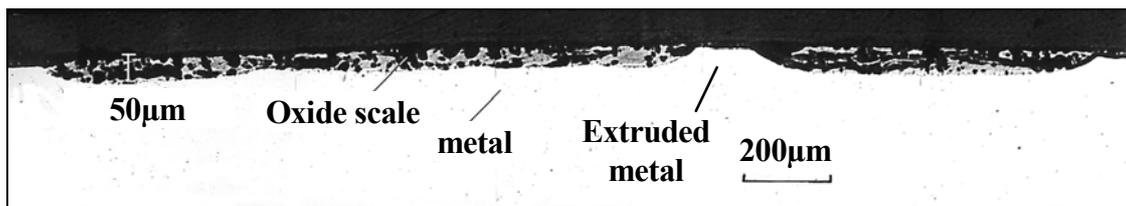
Figure V-31: Micrographic cross section of a deformed specimen after a PSCT. Steel grade: DDS, Temperature of deformation: 800°C, specimen reduction: 50%, velocity: 5 mm/s, initial scale thickness: 60 μm. Oxide scale reduction ~8%.

Micrographies de coupes d'éprouvettes DDS après bipoinçonnement. Température de déformation : 800°C, réduction: 50%, vitesse: 5 mm/s, épaisseur initiale: 60 μm. Réduction de la calamine ~8%.

Temperature:

Tests have been performed at low velocity (5 mm/s) and with reductions usual for the first stand of a finishing mill (45%). When the temperature increases (800°C, 900°C, 950°C), the interface is less deformed. This is in good agreement with the decrease of the hardness ratio between the oxide scale and the steel when the temperature increases, leading to quasi-homogeneous bimaterial co-deformation.

Steel grade:

Two steel grades have been tested: DDS and ReN. In the case of ReN steel, oxide scale parts remain stuck to the tools after the test, often leading to the full delamination of the oxide scale. As under tension conditions, the oxide scale adherence remains a key parameter in compression. An oxide scale that sticks to the rolls in a finishing mill stand is catastrophic for two reasons:

- After re-oxidation, the interface will be irregular and will cause scale embedding in the next stand, as represented on Figure V-32;
- The oxide scale stuck on the roll will cause scale embedding in each roll-rotation, due to the extra thickness.

Strain rate:
Tests have been performed at three velocities (5 mm/s, 50 mm/s and 100 mm/s), at high reduction ratio (70%) and high temperature (960°C). The strain rate does not seem to have major effects on the interface aspect. Nevertheless the reduction might be too high to observe them.

N.B: The initial interface is not always well controlled; sometimes defects due to an irregular oxidation are present. Thus, oxidation waves appear even in the non-deformed zone (Figure V-32). The embedding of such waves causes large defects.

(a)   (b)
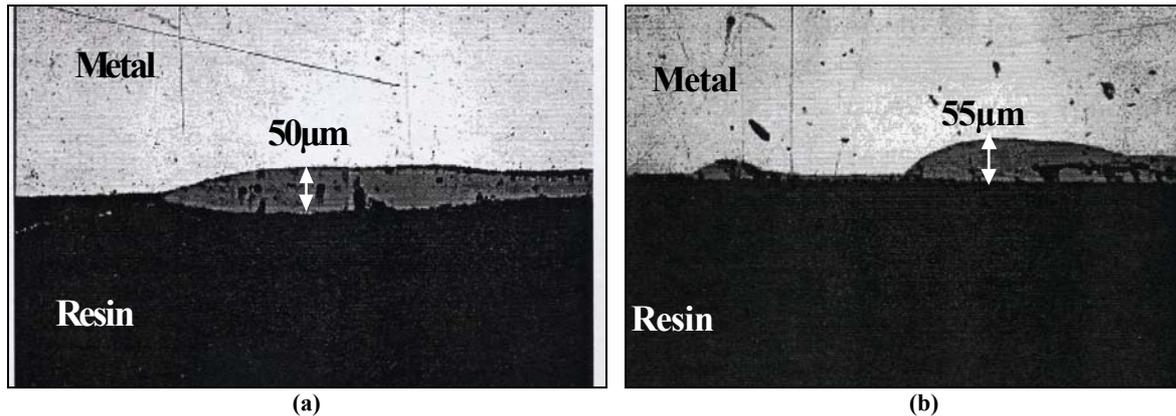
Figure V-32: Micrographs of a deformed specimen cross section after a PSCT. Steel grade: DDS, Temperature of deformation: 800°C, reduction: 30%, velocity: 5 mm/s, initial scale thickness: 50 μm. (a) Free zone (b) Compressed zone.

Micrographies de coupes d'éprouvettes DDS après bipoinçonnement. Température de déformation : 800°C, réduction: 30%, vitesse: 5 mm/s, épaisseur initiale: 50 μm. (a) zone libre (b) zone comprimée .

II.4. Simplified numerical simulation of PSCT

II.4.1. A simplified model

Based on the mechanical properties described in chapter 4 and 5, numerical simulations of these old PSC Tests have been performed, using oxide-covered steel specimens.
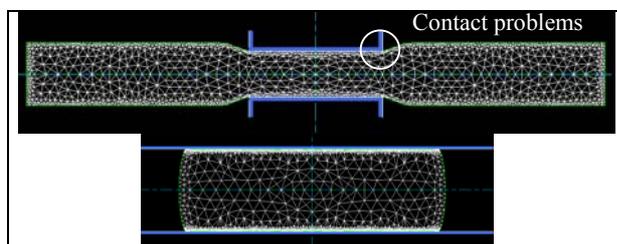
Figure V-33: numerical simulations of PSCT. Simplification of the test.

Simulation numérique du bipoinçonnement. Simplification du test.

Figure V-33 represents two generations of PSCT simulations investigated. The simplified shape below has been selected in order to save calculation time and avoid contact problems at punch corners. In spite of the change of shape, results are identical as far as the oxide scale behaviour under the tools is concerned.

The **main observation** done thanks to PSCT simulations is the **significant difference,** in terms of damage, **with tests soliciting the oxide scale in tension (HTT or 4-PHBT)**. Indeed, PSCT promotes high elongation (in the horizontal direction) under compressive stress (higher

than in 4-PHBT and HTT) due to sample thickness reduction. The present simulations have proved cracking criteria determined previously to be inadapted to compressive conditions : they gave heavily cracked oxide scales, extremely different from the experimental observations (compare Figure V-34 and Figure V-31).
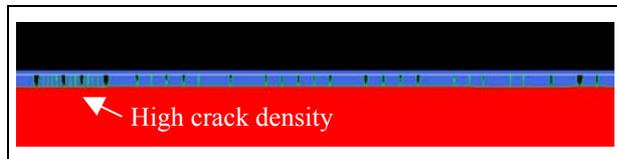
Figure V-34: Compression test simulation: Temp: 800°C – red: 30% - V_comp = 5 mm/s.

Simulation du test de compression: Temp: 800°C – réduction: 30% - V_comp=5 mm/s.

Thus criteria developed using tensile tests are not applicable under compressive conditions, due probably to the hydrostatic pressure, which tends to maintain the integrity of the oxide scale. Therefore, a more **qualitative** study of compression has been undertaken to determine the main parameters of rolled-in scale defects, and their influence.

II.4.2. Influence of diverse parameters on extrusion

In this section, simulations start using pre-cracked oxide scales. The scale as well as the steel substrate are deformable. Their evolution is studied as a function of the key parameters evidenced by the experiments. The constitutive equations of materials used are the same as in HTT simulations. A sticking contact is selected at the oxide scale-steel interface and a frictionless one (μ=0) at the punch-oxide scale interface.
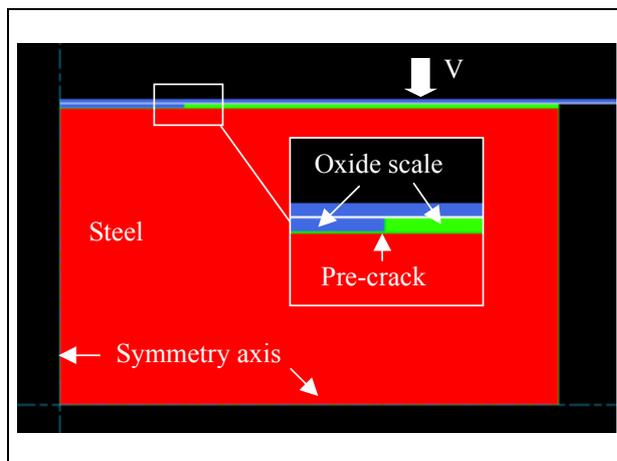
Figure V-35: Numerical simulation of compression test: 800°C - V_comp=50 mm/s. Pre-crack closed. Initial scale thickness: 100 μm.

Simulation du test de compression: 800°C - V_comp=50mm/s. Pré-fissure fermée. Epaisseur initiale d'oxyde: 100 μm.
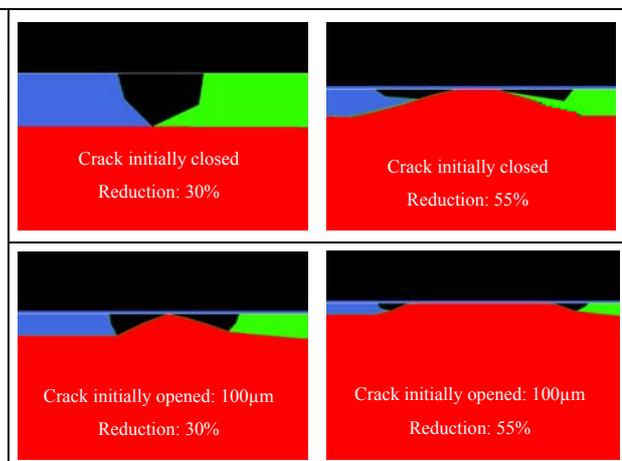
Figure V-36: Extrusion evolution depending on strain and crack initial state.

Evolution de l'extrusion en fonction de la déformation et de l'état initial de la fissure.

Influence of crack opening before compression

It is important to bear in mind that PSCT only mimics approximately what occurs in the roll bite. At this location, three oxide scale configurations are possible:

- the scale is undamaged: in this case, we have seen just previously that it was impossible for us to determine compression damage criteria due to a lack of experimental data;
- the scale is cracked and cracks are closed;
- the scale is cracked and cracks are open.

Simulation results of the last two points are represented on Figure V-36. Only one crack has been initially created (Figure V-35). Figure V-36 and Figure V-37 show that extrusion is easier and cracks opening is quicker when the crack is initially open.
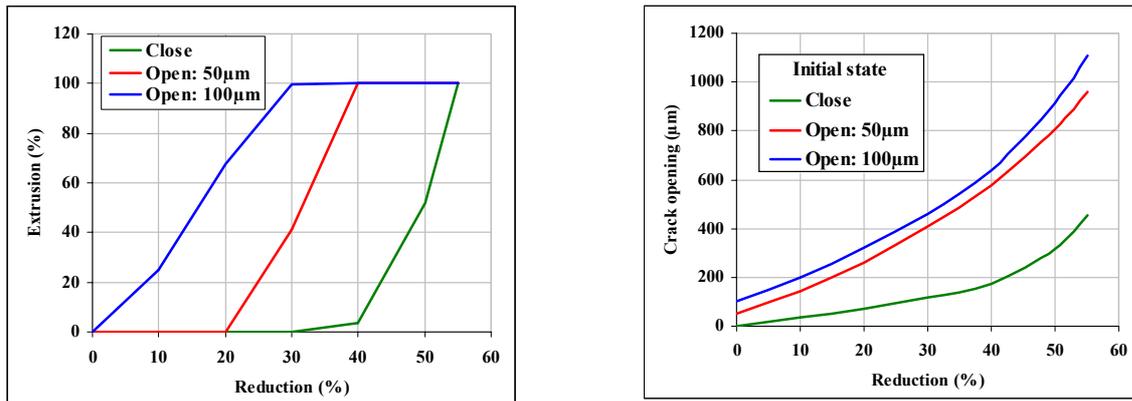
Figure V-37: Compression test: 800°C - V$_{comp}$=50 mm/s. Extrusion and crack opening vs total reduction. (No extrusion: 0% - Total extrusion: 100%).

Test de compression: 800°C - V$_{comp}$=50 mm/s. Extrusion et ouverture de fissure en fonction de la réduction totale. (Pas d'extrusion: 0% - Extrusion totale: 100%).

Of course, simulation of extrusion depends on the mesh size. But even if results are quantitatively questionable, tests can be correctly compared to one another, the mesh being the same in all cases. Moreover, numerical simulations disclose an important phenomenon. The extrusion can be dissociated in two parts:

- the extrusion of steel in gaps formed by the cracks;
- the embedding of oxide bits inside the steel when cracks are open.

Indeed, in the case of an initially closed crack, Figure V-36 as well as Figure V-37 show the progressive opening of the crack under compressive stress. Then, the steel pushes and crushes the oxide scale at this location. This mechanism represents the steel extrusion.

In the case of initially open crack, the extrusion is significantly easier, due to the immediate possibility for steel to be extruded in the free space, but also because of the embedding of scale fragments in the softer steel.

Temperature influence

The temperature influence is directly linked to the constitutive equations of both materials. In our case, it depends on the bimaterial flow strength i.e. on the hardness ratio. Thus, at 1000°C, the hardness ratio between steel and scale is ~1, so that simulation shows co-rolling of both materials (same reduction): the crack opens very slightly. At 600°C, the ratio is ~3: crack opening and extrusion are strong (stronger than at 900°C: hardness ratio=2). The higher scale hardness prevents its extending as much as its softer steel substrate.
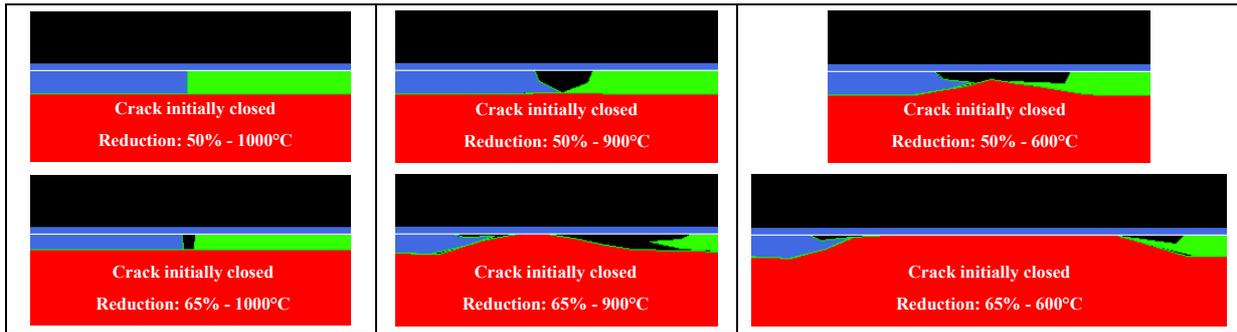
Figure V-38: Influence of bimaterial temperature and reduction on steel extrusion. Initial scale thickness 100 μm – V=50 mm/s.

Influences de la température et de la réduction du bimatériau sur l'extrusion de l'acier. Epaisseur initiale de calamine 100μm – V=50 mm/s.

This temperature influence has been also noted previously from experimental observations. We also assume that this phenomenon is probably amplified in hot rolling, when oxide scale is cooled due to its contact with cold rolls while the steel strip is maintained at an approximately constant temperature.

Tool-scale contact and scale reduction
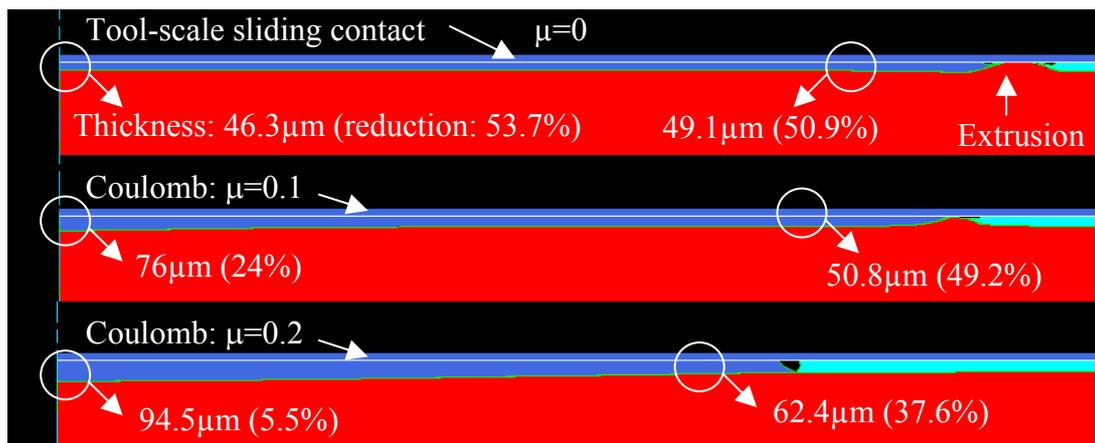
Figure V-39: Influence of tool-scale friction on scale reduction and steel extrusion. Strip reduction: 55% - Initial scale thickness 100 μm – Temperature: 800°C – V_{comp}=50 mm/s.

Influence du frottement outil-calamine sur la réduction de calamine et l'extrusion de l'acier. Réduction de la bande: 55% - Epaisseur de calamine initiale 100 μm – Température: 800°C – V_{comp}=50 mm/s.

The contact between the oxide scale and the tool is very important for scale thickness, crack opening and consequently for extrusion (

Figure V-39). The co-rolling tendency (identical reduction of the oxide scale and the steel) vanishes when friction increases. The limit cases are:

- the frictionless, sliding contact : the oxide and steel are co-deformed with identical reductions, even at 800°C where the hardness ratio is 3;
- the sticking contact: only the steel substrate is deformed, the sticking contact prevents the extension of the oxide scale during the deformation.

Figure V-40 shows that the scale reduction also depends on the oxide scale damage. Indeed, once a crack is opened and the extrusion is possible, the matter is able to undergo deformation without extension. The reduction is instantaneously stopped.

The defect is enhanced near the gap formed by the crack opening. Indeed, once the extrusion starts, the metal pushes the oxide scale sideways to be extruded in between. This phenomenon causes the oxide scale to swell locally.
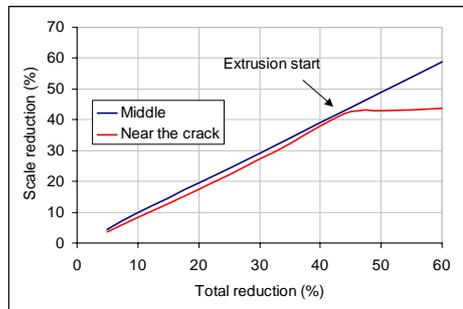
Figure V-40: Extrusion influence on scale reduction (near a crack).

Influence de l'extrusion sur la réduction de la calamine (près d'une fissure).
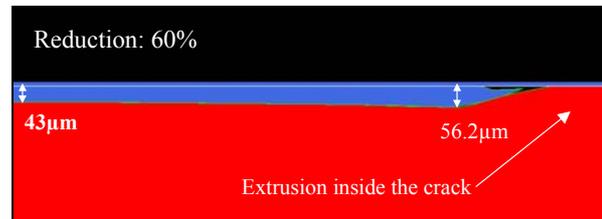
Figure V-41: Scale swelling near the extrusion. Initial scale: 100µm – Temp: 800°C – V_{comp}=50 mm/s.

Gonflement de la couche près de l'extrusion. Epaisseur initiale : 100µm – Temp: 800°C – V_{comp}=50 mm/s.

Experimental observations have shown different tendencies for oxide scale reduction (sometimes a quite perfect co-rolling of oxide scale and steel, in other cases no reduction of the scale). Based on our present results, two explanations may be given :

- The lack of tool-scale friction control;
- The initiation, or not, of cracks.

Influence of scale thickness and strain rate

No significant differences have been observed in simulations using several oxide thickness.

II.5. Extrusion study using PSCT

The extrusion phenomenon depends on many parameters, the major one being the oxide scale evolution (toughness, opening…). We have found it interesting to perform a short numerical study centered on the extrusion phenomenon.

The crack in itself is not a problem. It is however the origin of hot steel extrusion, which degrades rolls by two mechanisms : it promotes a locally strong heat transfer to cold work-rolls, and sticking of steel particles to the rolls.

As for the strip, apart from defects induced by degraded rolls, its surface roughness is directly impacted by micro-extrusion. **It is therefore primordial to control and limit the extrusion phenomenon.**

Thus, numerical PSCT have been performed, this time under conditions as close as possible (velocity, materials size…) to the roll bite of the second stand of a finishing mill, and using a rigid oxide scale, which in this case is the "tool" in the Forge2® sense. The extrusion behavior is evaluated from different crack configurations.
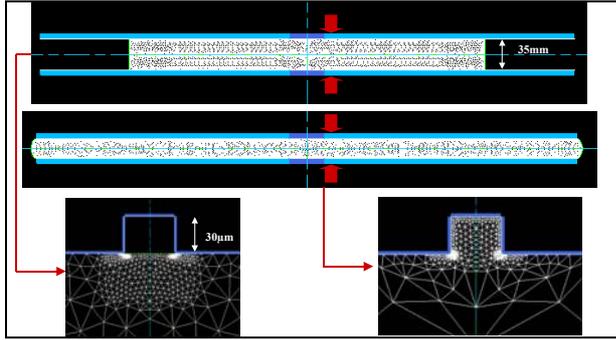
Figure V-42: Simulation of PSCT to study extrusion in cracks. Dimensions used reproduced as close as possible industrial F2 finishing mill stand.

Simulation de bipoinçonnement pour étudier l'extrusion dans des fissures. Les dimensions utilisées reproduisent de manière aussi proche que possible une cage F2 de finisseur industriel.

Specimen width as well as compression punch velocity have been chosen as close as possible to the rolling process. The width has been selected so that the specimen edge effects do not influence the steel extrusion. The compression punch velocity has been calculated to reproduce the vertical velocity of the strip surface V_{comp} in the roll bite (Figure V-43).

Here, the oxide scale with cracks is represented by a rigid tool in order to focus on the extrusion phenomenon without any perturbation coming from the scale behavior. Contact with steel is assumed sticking (Figure V-42).
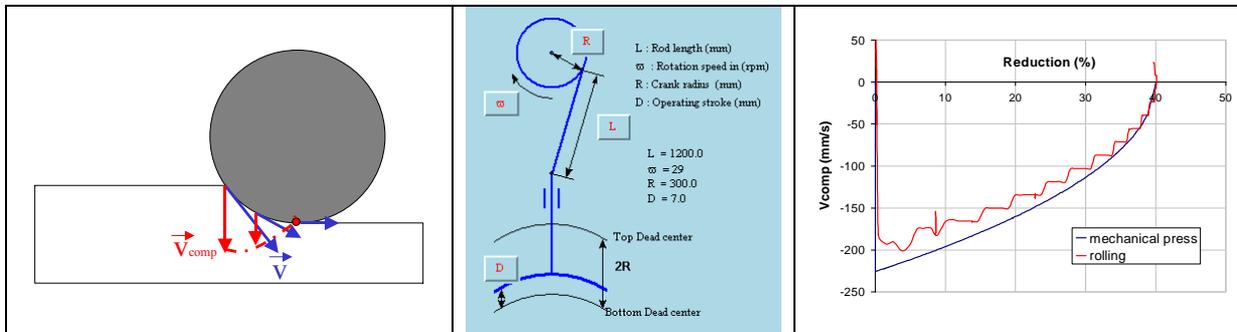
Figure V-43: Identical vertical velocity in rolling and PSCT. Use of the "mechanical press" option of Forge2®.

Vitesse verticale identique en laminage et bipoinçonnement. Utilisation d'une option "presse mécanique" Forge2®.

Evolution of steel extrusion is studied through three parameters of the rigid "scale-tool":

- the crack width,
- the crack number,
- the inter-crack distance.

Results are respectively represented Figure V-44, Figure V-45 and Figure V-46. An example of simulation can also be seen in Figure V-48.

Results are more or less conform to intuition:

- Extrusion is quicker when crack width increases (Figure V-44). This is the most influencial parameter.
- Extrusion is quicker when the crack number is higher (Figure V-46).
- Extrusion is quicker when the distance between cracks is shorter (Figure V-45). Indeed, if only one crack is open (which represents the extreme case of very distant cracks), the zone to extrude is extremely large. The material below the crack sinks down, entrained by the

neighbouring zones (Figure V-50). If several cracks are close to one another, the extrusion zones are significantly shorter, which allows the extrusion of the steel into the free gaps. An embedding of oxide rafts between cracks also contributes to the extrusion.
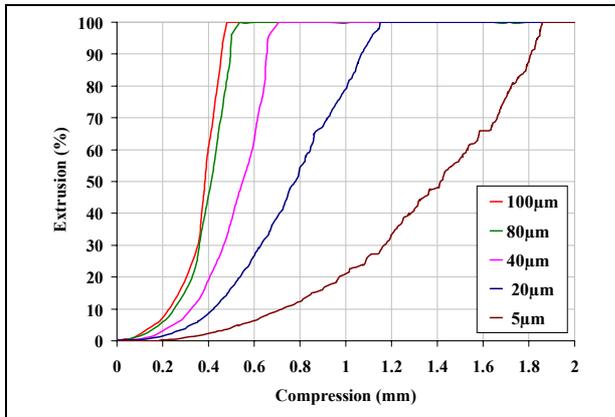
Figure V-44: Evolution of steel extrusion in PSCT as a function of cracks width.

Evolution de l'extrusion de l'acier en bipoinçonnement en fonction de la largeur des fissures.
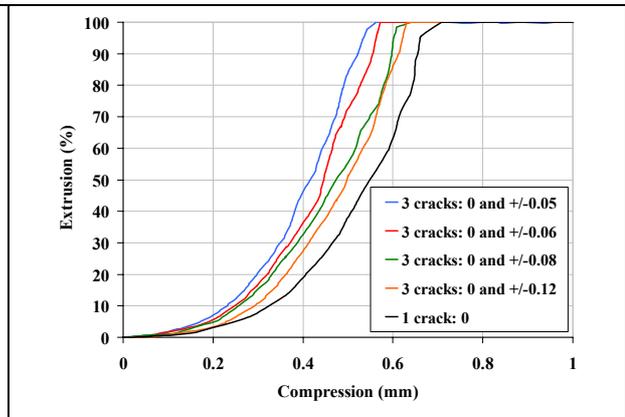
Figure V-45: Evolution of steel extrusion in PSCT as a function of distance between cracks. Crack width: 40 µm.

Evolution de l'extrusion de l'acier en bipoinçonnement en fonction de la distance entre les fissures. Largeur des fissures : 40 µm.
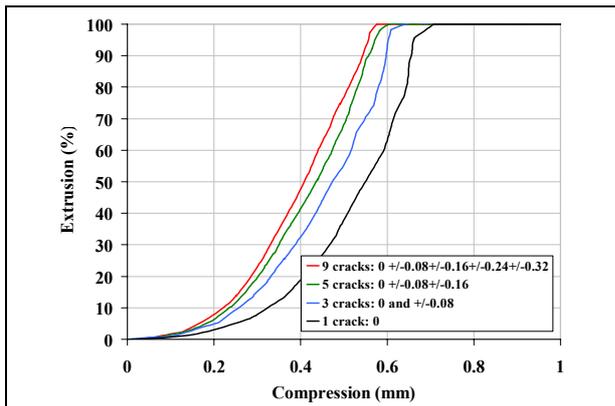
Figure V-46: Evolution of steel extrusion in PSCT as a function of crack number. Cracks of 40 µm width and distant of 80 µm.

Figure V-47: Evolution de l'extrusion de l'acier en bipoinçonnement en fonction du nombre de fissures. Fissures larges de 40 µm et distantes de 80 µm.
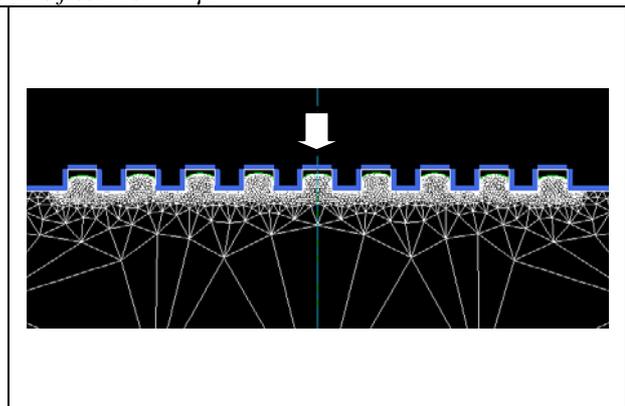
Figure V-48: Simulation of compression tests: extrusion in 9 cracks corresponding to the red curve plotted Figure V-46. Stroke = 0.52 mm.

Figure V-49: Simulation du test de compression: extrusion dans 9 fissures correspondant à la courbe rouge tracée Figure V-46: Course = 0.52mm.
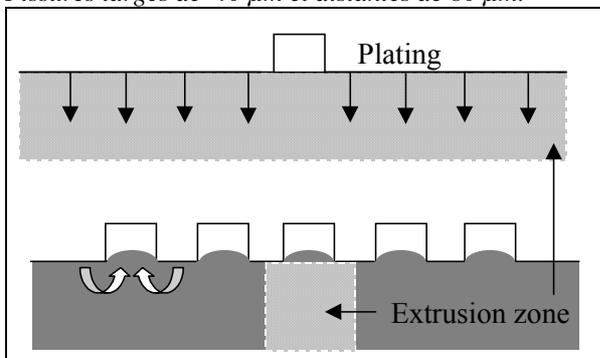
Figure V-50: nearby cracks enhance extrusion.

Les fissures proches facilitent l'extrusion.

II.6. Conclusion on PSCT

Several interesting points have been noted in this study of the oxide scale behavior under compressive stresses.

- Even though tensile stresses are extremely high in PSCT, **fracture criteria previously determined under tensile conditions (using 4-PHBT and HTT) cannot be applied under highly compressive conditions**, which give oxide some ductility during the deformation.

- The second point, and probably the most important, concerns the **crack opening before its entry in the roll gap**. We have seen that closed cracks will to avoid steel extrusion. Remembering HTT results, showing how the scale thickness influences crack opening (thin scale = closed cracks), we can understand a part of the critical thickness concept in hot rolling. In other words, when the oxide scale is thin, cracks caused by tensile stresses remain closed (see HTT results). This makes extrusion more difficult and significantly delayed it (PSCT results). We may thus conclude that **below a critical thickness, the extrusion is delayed enough not to be initiated or at least not to be completed**.

- Third, high temperatures promote co-rolling, with two positive consequences : first, if materials are deformed in the same way, cracks cannot open and extrusion does not occur. Second, even if cracks open before the roll bite, they will not open further in the bite. Moreover, due to the significant scale thinning, the extrusion thickness would be limited. An important remark has to be done here. Despite these results, we have to bear in mind that **all parameters interact**. For example, if we increase the temperature to promote co-rolling in the bite, it will also have a strong impact before the entry in the roll gap : a temperature increase makes oxide growth kinetics faster, thus increasing the oxide scale thickness – which is detrimental. **The problem is then really extremely complicated**.

- The last important information concerns the low friction contact, which supports the co-rolling and decreases the extrusion phenomenon. Decreasing friction also decreases tensile stresses before the entry in the roll bite. This explains why high friction due to damaged rolls enhances the risk of rolled-in scale. However, friction must be sufficient to meet the entrainment condition.

III.   CONCLUSION

The objective of this chapter was to better apprehend the different solicitations undergone by the oxide scale before and inside the roll bite in a finishing mill. Several mechanisms influencing rolled-in scale damage have been analyzed. A rational choice of rolling conditions can be made to avoid rolled-in scale. However, multiple couplings and feed-back between parameters make this a very difficult task, as any single parameter may have negative as well as positive effects.

A more complete database is also available in terms of oxide scale constitutive equations and tensile damage criteria. Nevertheless, additional work has to be carried out to determine the oxide scale behaviour and damage criteria under compressive stresses.

In spite of this lack of information concerning the oxide scale behaviour under the rolls, we have now sufficient data to simulate the oxide scale behavior during hot rolling. This is the purpose of the next, final chapter. The efficiency of our numerical model in the different configurations in which it has been tested makes us confident for these future rolling simulation results.

IV.   REFERENCES

[Krz1]   M.Krzyzanowski, J.H.Beynon, Oxide behavior in hot rolling, in Metal Forming Science and Practice, a state of the art volume in honour of Pr J.A.Schey's 80th birthday, edited by J.G.Lenard, (2002), pp.85-114.

[Krz2]   M.Krzyzanowski, C.M.Sellars, J.H.Beynon, Characterisation of oxide scale in thermomechanical processing of steel, Proc. Int. Conf. on Thermomechanical Processing: Mechanics, Microstructure and Control, Sheffield (2003). Plamiere, Mahlouf & Pinna, Eds, , pp.91-102.

[Krz3]   M.Krzyzanowski, J.H.Beynon, Modelling the boundary conditions for thermo-mechanical processing – oxide scale behaviour and composition effects, Mod. Simul. Mater. Sci. Eng. 8, (2000), pp.927-945.

[Krz4]   M.Krzyzanowski, J.H.Beynon, Finite element model of steel oxide failure during tensile testing under hot rolling conditions, Mat. Sci. Technol. vol.15 (October 1999) pp.1191-1198.

[Paw]   O.Pawelski, V.Gopinathan, " Comparison of material flow and deformation resistance of HSLA steel deformed by hot rolling and by flat compression under simulated conditions ", J. Mech. Working Technol. **5** (1981) pp.267-280.

[Piet]   M. Pietrzyk, J.G. Lenard: Thermal-Mechanical Modelling of the Flat Rolling Process, Springer-Verlag, Berlin, 1991.

[Vagn]   G.Vagnard, J.Manenc, Etude de la plasticité du protoxyde de fer et de l'oxyde cuivreux, Mém. Sci. Rev. Mét. LXI, n°11, (1964), pp.768-776. *In french.*

Hot Rolling Simulations

Résumé

Un nombre significatif d'outils et de données est maintenant disponible pour simuler numériquement le laminage à chaud d'une bande d'acier recouverte d'une fine couche de calamine.

En effet, les données mécaniques concernant l'acier et l'oxyde (lois de comportement) ont été obtenues dans la littérature ou identifiées grâce à des tests expérimentaux.
Les données thermiques (oxyde ; acier ; interfaces) proviennent de la littérature et de l'IRSID. Elles interviennent au premier rang dans la formation de défauts de type calamine incrustée.
Le comportement de la calamine a également été identifié, ainsi que sa dépendance à certains paramètres tels que la température, son épaisseur, la déformation et la vitesse de déformation. Des critères d'endommagement ont été déterminés grâce aux différents tests mécaniques, et peuvent maintenant être utilisés en laminage. Par contre, le problème du comportement de la calamine soumise à des contraintes compressives demeure. En effet, aucun endommagement n'est simulé en laminage sous l'emprise. Cependant, tout endommagement engendré en entrée d'emprise continue d'évoluer sous les cylindres (ouverture de fissure, extrusion).

Dans ce chapitre, les simulations de laminage ont été réalisées en prenant comme référence les conditions d'une cage F2 d'un finisseur.

Les résultats des simulations de laminage obtenus mettent en évidence l'efficacité et le bien fondé à la fois des données utilisées et des développements numériques réalisés. L'influence des paramètres principaux (température, réduction, épaisseur de calamine) est démontrée.

Néanmoins, à la fin de ce chapitre, une étude plus quantitative reste à faire. Cette nouvelle approche nécessitera en premier lieu de mieux connaître le comportement de la calamine en compression ainsi que d'affiner l'analyse thermique notamment des cylindres.

I. INTRODUCTION

A significant number of tools and data are now available to perform hot rolling numerical simulations of steel slabs covered by a thin oxide scale.

- All **mechanical data** concerning steel and oxide (constitutive equations) have been obtained in the literature or identified using our experimental tests. Data reported from the literature or coming from IRSID have been summarized in [APPENDIX 1]. For oxide scale, the method of hardness ratio elaborated in chapters 4 and 5 is applied.

- **Thermal data** come from literature or IRSID. They can be found in [APPENDIX 2]. These data are of prime importance because all parameters depend on temperature, and heat transfer is intimately connected to rolled-in scale. These data concern both materials (steel and oxide), but also two interfaces (roll / oxide scale - oxide scale / steel).

- We have identified the **oxide scale behavior**, which depends on several parameters such as temperature, scale thickness, strain and strain rate. **Damage criteria** have also been determined using 4-PHBT and HTT, and can now be used in rolling.

- The problem of the oxide scale mechanical behavior under compressive stresses (i.e. under the rolls) remains open**. No damage will be initiated under the rolls during simulations**. Nevertheless, all the cracks created ahead of the contact continue to evolve inside the roll bite (crack opening, steel extrusion).

In most cases, simulations have been performed taking with **the F2 stand of the FM as a reference**, because it is considered as one of the most critical. A central configuration has been chosen, and several parameters have been modified to evaluate their influence on rolled-in scale damage.

II. A FOCUSED BIBLIOGRAPHIC STUDY

Many researchers have investigated the numerical modeling of hot rolling [Zhou,Krz1,Piet]. Nevertheless, only the Sheffield University team (to the best of our knowledge) is able to simulate the oxide scale behavior in a roll bite. Their major results are summarized below.
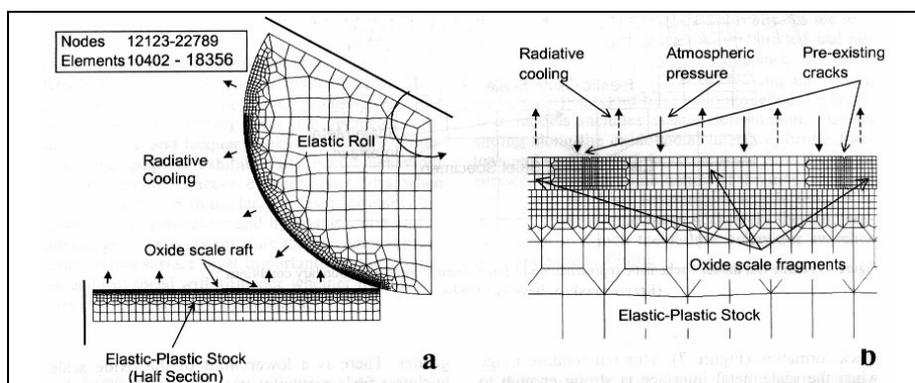
Figure VI-1: Macro and micro views of hot flat rolling model. Schematic view of FE mesh [Krz1].

Vues Macro et micro d'un modèle de laminage à chaud. Vue schématique du maillage éléments finis [Krz1].

They used the commercial FE code MARC, already presented in chapter V. Their mathematical model is constituted of a macro level that computes strains, strain rates and stresses in the strip during rolling, and a micro level that examines the oxide scale behavior (Figure VI-1). For them, the initial slab **temperature** is the **major factor** for **oxide scale failure**. When the range of temperature corresponds to a brittle oxide scale, **through thickness cracks** can appear. These cracks are due to a longitudinal tensile strain at the stock surface, found inevitably before the entry in the roll gap (Figure VI-2).
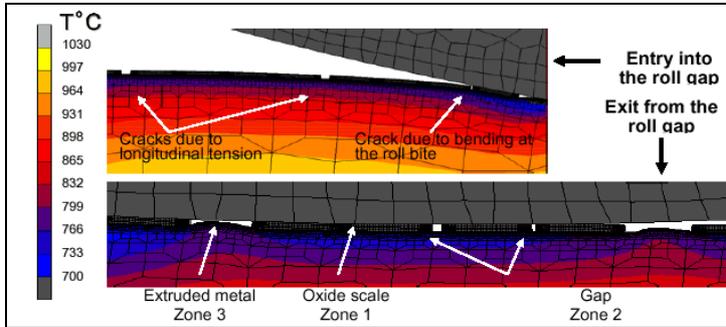
Figure VI-2: Temperature and crack distribution at the oxidized stock-roll interface during hot rolling [Krz3].

Température et distribution de fissures à l'interface bande-cylindre pendant le laminage [Krz3].

This behavior is very sensitive to small changes of steel chemical composition. At higher temperature, the oxide scale deformation is ductile, without any crack (Figure VI-3) [Krz2].

When the fractured scale undergoes extreme pressure under the rolls, the hot metal can be extruded into the gaps formed by cracks (Figure VI-2).

Such extrusion phenomena, detailed in [Krz4], are not always followed by full contact between the fresh hot metal and the cold roll. Nevertheless, it always disturbs the heat transfer at the roll / stock interface.
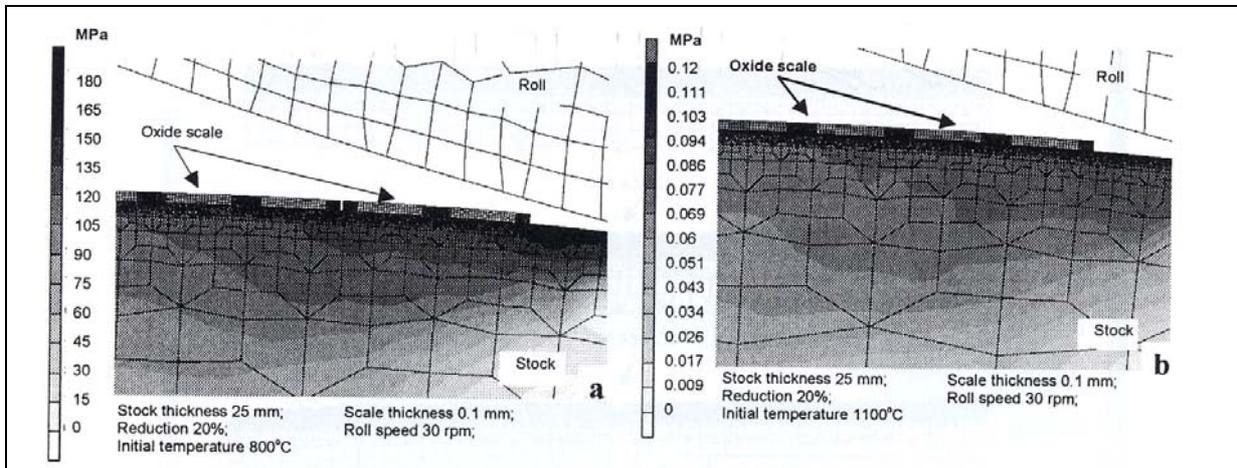
Figure VI-3: σ_x stress predicted at the moment of the entry into the roll gap. Initial temperature: a) 800°C b) 1100°C (no cracking) [Krz1,Krz4].

Contrainte σ_x prédite en entrée d'emprise. Température initiale : a) 800°C b) 1100°C (pas de fissures) [Krz1,Krz4].

Authors also explain that there is a **minimum thickness** (depending on steel grade and rolling parameters) below which **through-thickness cracks are not initiated**. If the scale thickness is higher than this limit, the crack pattern is sensitive to the scale thickness (Figure VI-4) [Krz1,Krz4]. In [Krz3] the influence of the strain rate on the scale damage is observed (Figure VI-5).
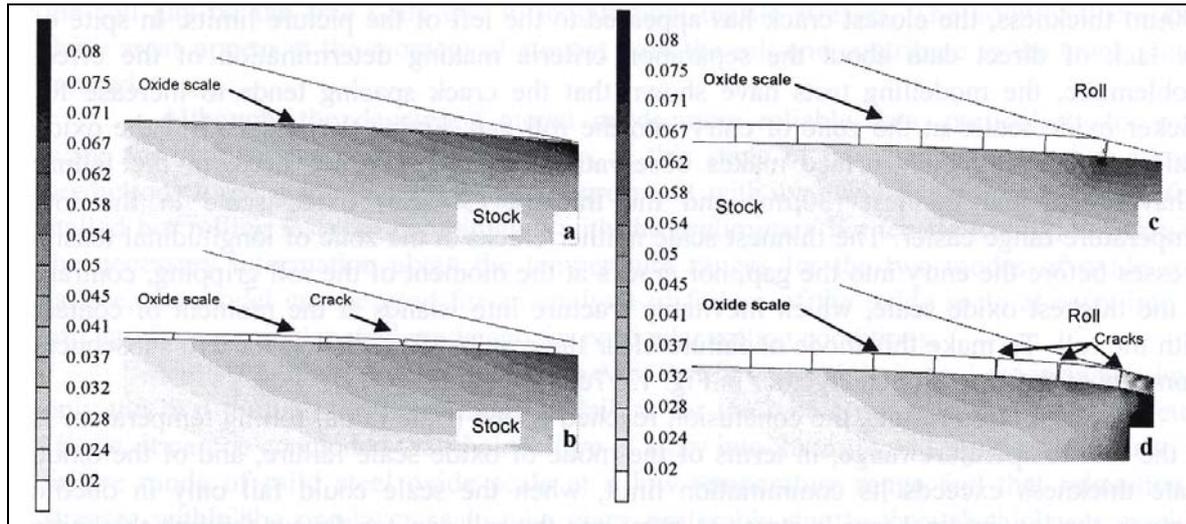
Figure VI-4: ε_x strain predicted at the moment of the entry into the roll gap for stock thickness 5.5 mm, reduction 30%, roll speed 10 rpm, initial temperature 700°C and different oxide scale thickness: a) 0.03 mm b) 0.1 mm c) 0.3 mm, time 0.272s d) 0.3 mm, time 0.2788s [Krz1,Krz4].

Déformation ε_x prédite en entrée d'emprise. Epaisseur de bande 5.5 mm, réduction 30%, vitesse cylindre 10 tours/minute, température initiale 700°C et différentes épaisseurs d'oxyde: a) 0.03 mm b) 0.1 mm c) 0.3 mm, temps 0.272s d) 0.3mm, temps 0.2788s [Krz1,Krz4].
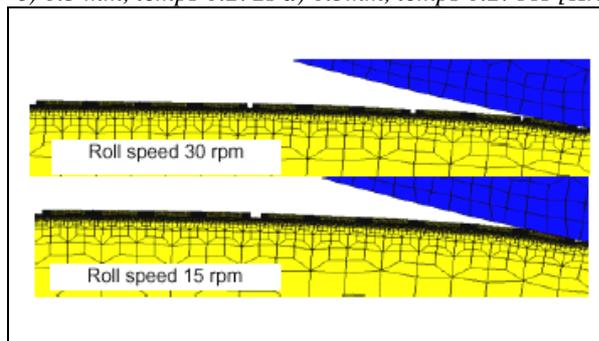
Figure VI-5: Different scale crack patterns formed at entry into the roll gap for the different roll speeds ; roll diameter 136.6 mm, reduction 20%, initial stock thickness 25 mm, temperature 800°C and oxide scale thickness 0.1 mm [Krz3].

Influence de la vitesse sur la fissuration de calamine en entrée d'emprise. Diamètre de cylindre 136.6 mm, réduction 20%, épaisseur de bande initiale 25 mm, température 800°C, épaisseur de calamine 0.1 mm [Krz3].

Other interesting influences have also been investigated, such as multi-layer steel oxides (Si-Mn steel for example). In this case, in addition to through-thickness cracks, delamination between the sub-layers can occur at the entry of the roll gap (Figure VI-6). They have also shown the influence of the **oxide scale which covers the rolls** (Figure VI-7), which can contribute to break the strip oxide scale at the moment of roll gripping at the entry into the roll gap. The roll scale reduces heat transfer into the roll, maintaining the strip oxide scale longer at high temperature ; it can thus be deformed in a ductile manner.

Finally, an adjustment of the model for technological operations has been performed [Krz2], to study the state of secondary oxide scale after hot rolling, in order to evaluate the quality of the surface finish (which is exactly our focus). In order to maintain short computation times despite of the high complexity of the problem, they have distinguished two zones: the entry into the roll gap including the contact with the roll, and the roll gap including exit. The model for the second zone has been reduced to a small segment of the stock/roll interface. Then, they applied to the small segment the boundary conditions, they kept from corresponding nodes of the macro-model. Then, they change the origin of the coordinate system and they refine the interface. In the end, the model is ready for numerical analysis (Figure VI-8). Such a "zoom method" enables to simulate precisely the interface in a reasonable CPU time (several hours rather than weeks for the corresponding full model).
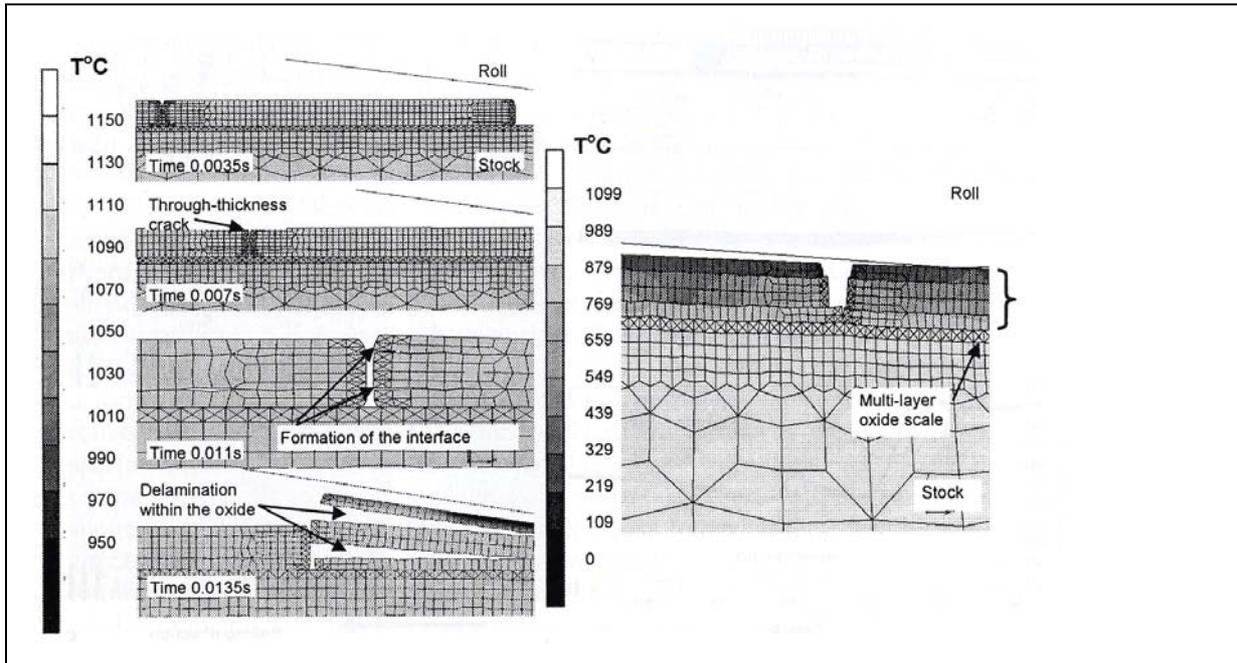
Figure VI-6: Left: Development of through-thickness cracks and delamination within the multi-layer Si-Mn steel oxide scale. Right: Adherence of the inner scale layer with uninterrupted shape [Krz4, Tan].

Gauche: Fissure transverse et délamination à travers la multicouche de calamine de l'acier Si-Mn.
Droite: Adhérence de la couche interne ininterrompue [Krz4, Tan].
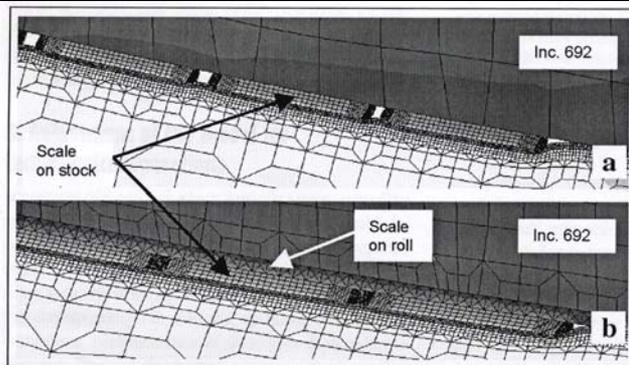
Figure VI-7: Difference in crack opening of the stock scale within the roll gap predicted for non-oxidized (a) and oxidized (b) roll. Differences are related to temperature changes at the interface.

Différence d'ouverture de fissure prédite dans la calamine sous emprise avec cylindre non oxydé (a) et oxydé (b). Différence liée au changement de température interfaciale.
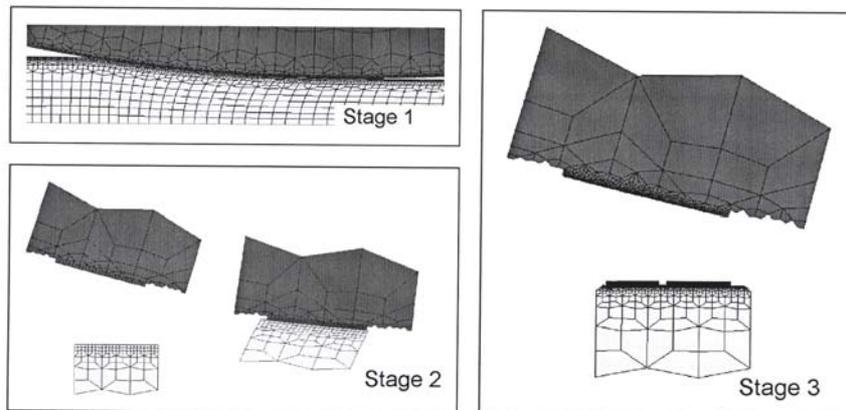
Figure VI-8: Schematic representation of model adjustment stages for evaluating the final state of the surface layer after flat hot rolling.
Stage 1: macro model run; no scale.
Stage 2: reduction to characteristic sizes. Change of origin of coordinate system. No scale.
Stage 3: FE mesh refinement at the interface. Introduction of the oxide scale.

Représentation schématique du modèle à différentes étapes pour évaluer l'état final de la calamine après laminage à plat. Etape 1 : lancement du modèle macro, sans calamine.
Etape 2 : Réduction à la taille caractéristique. Changement d'origine des coordonnées. Sans calamine.
Etape 3 : Raffinement du maillage à l'interface. Introduction de la couche d'oxyde.

III. REFINEMENT BOXES

Difficulties appeared at the beginning of the hot rolling numerical modeling using Forge2®, as soon as pre-cracks and extrusion have been taken into account.
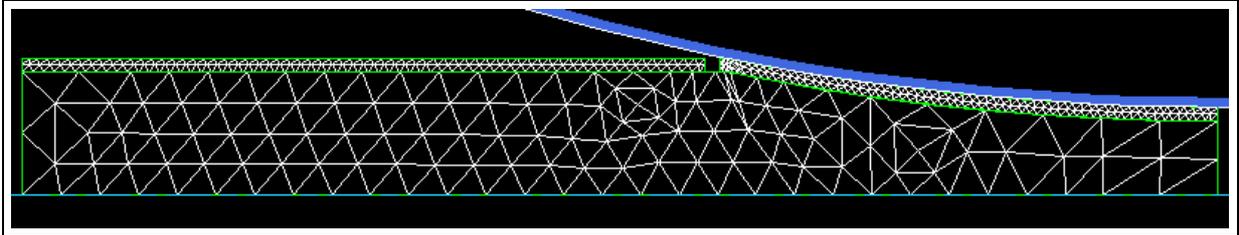
Figure VI-9: Numerical simulation of a finishing mill F2 stand. Oxide scale extremely thick (2 mm).

Simulation numérique d'une cage F2 de finisseur. Calamine extrêmement épaisse (2 mm).

Figure VI-9 represents one of our first simulations of a pre-formed crack evolution during a hot rolling pass. The simulated oxide scale was extremely thick compared to reality (2 mm instead of 20-30 µm). As soon as the crack is under the roll, the extrusion process should begin. However, as shown in Figure VI-10, extrusion proved impossible. The difference between the crack width (of the same order of magnitude as the scale thickness) and the steel mesh size prevented the steel extrusion between the two oxide parts.

Note for example that a scale 20µm thick requires extremely fine elements at the corners of the oxide scale fragments. This adds to the difficulty of such two-scale simulations where the whole strip is 20 mm thick and the oxide layer is 1000 times thinner (meshes are non-coincident at the interface).
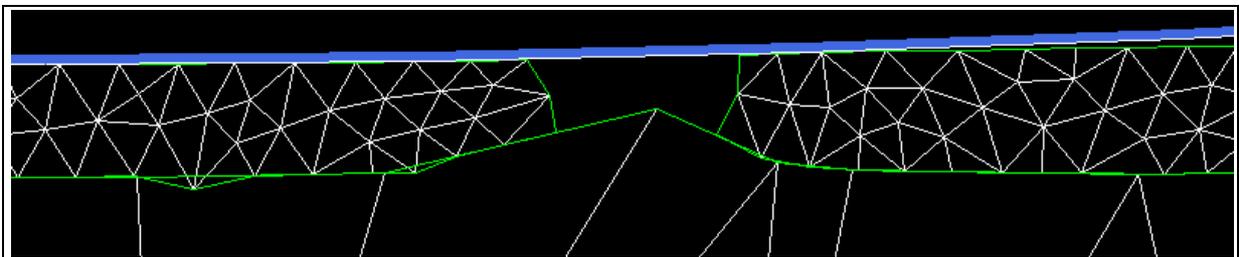
Figure VI-10: extrusion of steel in the roll bite is Impossible due to too large a mesh size for steel.

Extrusion impossible dans l'emprise due à un maillage trop grossier de l'acier.

The meshing of steel had to be refined. Refining the entire steel body was impossible, it would have lead to too many nodes. The solution implemented consisted in developing specific refinement boxes, able to follow a material point during the computation: a zone centered at the pre-crack tip location is refined, and is preserved after each remeshing stage.
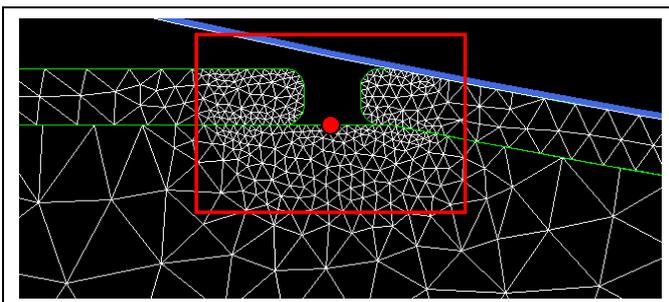
Figure VI-11: Positioning of the initial refinement box by the user, around the pre-crack.

Positionnement de la boite de raffinement initiale par l'utilisateur, autour de la pré-fissure.

Figure VI-11 represents the second computation increment, just after a remeshing and the creation of the mesh refinement box around the crack. The position of the center, the dimension and the mesh size of the box can be chosen by the user. The successive steps are:

- At the first increment, the mesh border node closest to the box center chosen by the user is selected. This central node number is recorded.
- Before each remeshing, **coordinates** of the central node are recorded.
- Once the remeshing has been made, the border node closest to the coordinates of the previous centre is recorded: this is the new centre. The mesh is then refined inside the box, which has kept characteristics identical to the initial ones.

The last two steps are repeated before and after each remeshing until the end of the simulation. This method of refinement allows extrusion of the metal inside cracks (Figure VI-12, Figure VI-13). Figure VI-14 demonstrates the efficiency of these developments : a complete extrusion is observed, until contact between the cold work-roll and the soft hot steel.
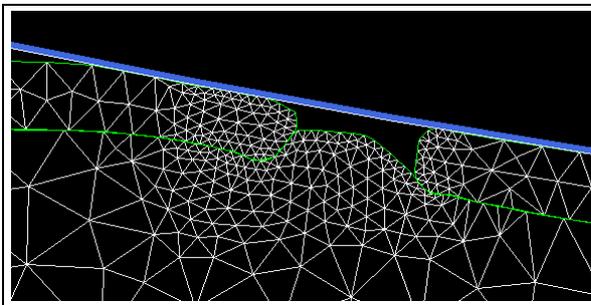
Figure VI-12: Oxide scale embedding – Steel extrusion.

Incrustation de calamine – Extrusion de l'acier.
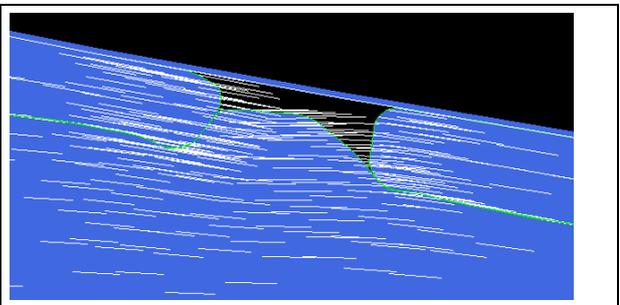
Figure VI-13: Velocity field close to the extrusion zone.

Champ de vitesse près de la zone d'extrusion..
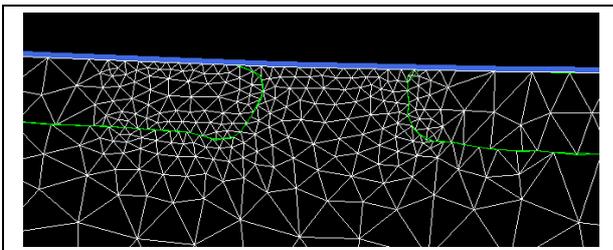
Figure VI-14: Complete extrusion.

Extrusion complète.
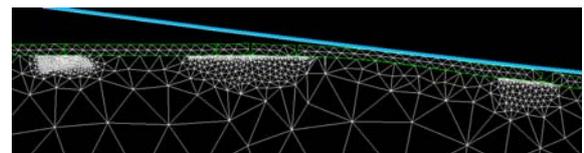
Figure VI-15: Steel mesh refinement at each crack initiation.

Raffinement du maillage de l'acier à chaque initiation de fissure.

In a second stage , this method has been **adapted to the crack initiation model** (without pre-formation). **A refinement box is systematically and instantaneously placed at crack tips, each time they initiate during the numerical computation**. Figure VI-15 shows the position of boxes at each crack tip created during the computation, when the tensile stress of a surface node has reached a critical stress chosen by the user. Only the steel part needs to be refined (Figure VI-15, Figure VI-16), even if the refinement is also possible for the oxide scale (Figure VI-11).
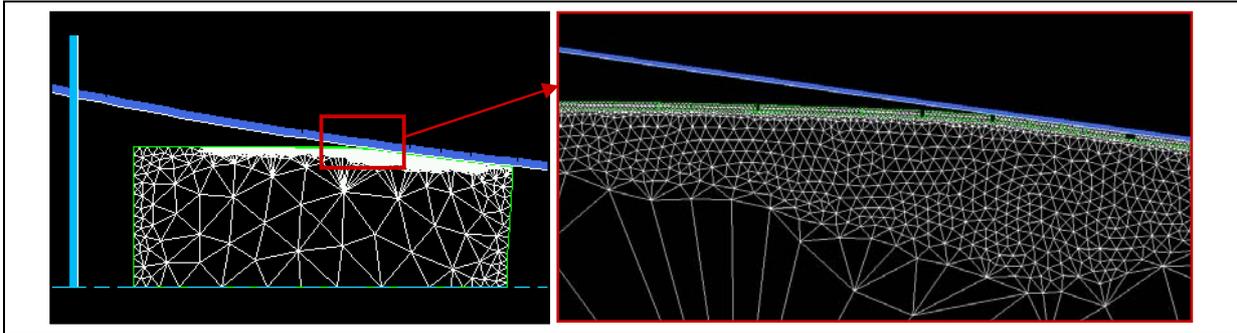
Figure VI-16: Steel mesh refinement at the location and at the moment of the crack initiation.

Raffinement du maillage de l'acier à l'endroit et au moment de l'initiation de la fissure.

Thus, a rolling simulation in the FM, under conditions such that scale is damaged (cracking of oxide and steel extrusion occur) starts with **~2000 nodes** and ends with **~8000 nodes** in the most refined cases (for the thinnest scale: 20µm). In terms of **computation time**, such a complete simulation takes **~100 hours** instead of between **35 and 45 hours** (depending on the reduction) for a 200 µm thick scale.

IV. SIMULATION OF HOT STRIP ROLLING IN A F2 STAND

IV.1. The F2 stand as a reference

The simulation conditions correspond to the 2nd stand of a Hot Strip Finishing Mill, which is supposed to be the most critical one for the rolled-in-scale defects.

Roll:
Diameter: 700mm; speed: 2.19m.s^{-1}
The roll temperature is an important limitation in Forge2®. Indeed, it is simulated by a rigid tool, i.e. it is not meshed and its strain and temperature field are not computed: its temperature is inevitably constant during the computation, which impacts thermal exchanges. In other words, if a roll at 50°C at the beginning of a simulation is put in contact with a hot steel strip at 900°C, the latter will be cooled as if the roll was maintained at 50°C, whereas in reality, the extreme surface of the roll is heated by friction and heat transfer from the hot strip to an unknown temperature, sometimes in excess of 400°C. In our simulations, we have decided to take in most cases a roll average temperature of 200°C.

Strip:
 Inlet thickness: 20mm; Exit thickness: 11mm (45% reduction); Temperature at entry: 900°C.

Oxide:
Thickness: 25µm; Temperature at entry: 900°C.

In a first simulation, we have chosen an extremely hard oxide scale, with a yield strength of 600 MPa. An identical value has been selected for the critical stress at 900°C (σ_{crit}=600 Mpa). Delamination has not been activated here (thin oxide is assumed very adherent).
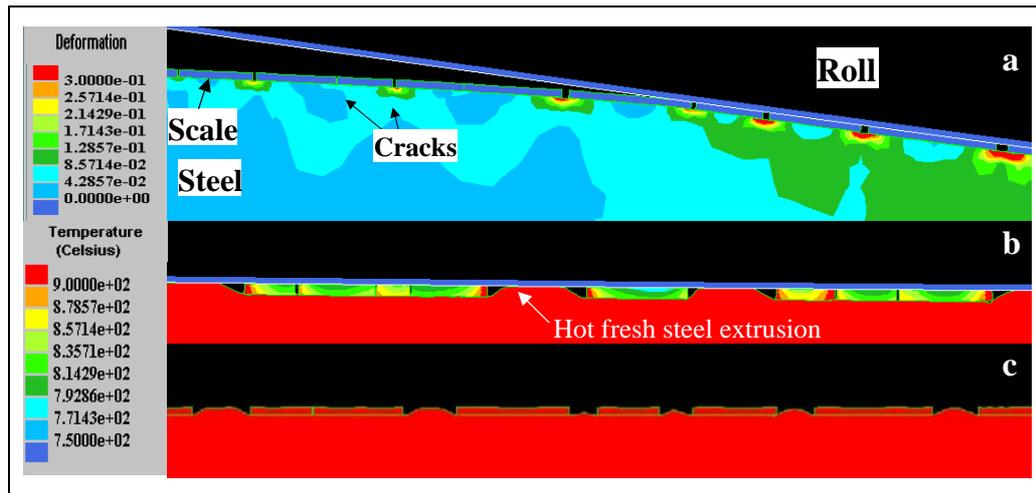
Figure VI-17: Fracture of the oxide layer before the roll bite and subsequent micro-extrusion.

Initial scale thickness: 25 µm; reduction 35%; µ= 0.3; roll velocity: 2.19 m/s; Initial strip temperature : 900°C.

Fissuration de la couche d'oxyde avant emprise suivie de la micro-extrusion de l'acier : épaisseur de calamine initiale : 25 µm; réduction 35%; µ= 0.3; vitesse cylindre : 2.19 m/s; Température initiale de la bande : 900°C.

As expected, the oxide layer breaks before the roll bite, due to tensile stresses at this location (Figure VI-17a). Transverse cracks initiate in a quasi-periodic manner: after each crack occurrence, the surrounding stresses are relaxed, until further advance has created enough stress for the criterion to be met.

In the bite, cracks opened before the entry tend to open more widely and fresh metal gets **micro-extruded** in the gaps between the fragments (Figure VI-17b,c), in accordance with the results obtained before by Beynon and Kzyzanowski.

In the present study, fragmentation of the oxide scale within the roll bite has been forbidden. It is highly probable that such cracks open not only by longitudinal tension, but rather by multi-fragmentation under local indentation by roll roughness peaks. It is indeed well known in practice that rolled-in scale defects occur preferably with used rolls, where transfer of oxide particles has created sharp asperities.

Cracks initiation at the entry of a F2 roll bite is described in several successive increments, the phenomenon being the same until the end of the simulation (Figure VI-18). **In this case, and in all following cases, oxide scale behavior laws will be based on hardness ratio determined in the previous chapter.**

Figure VI-18 clearly shows the initiation of through-thickness cracks at the entry of the roll gap, before the contact with the roll. The initiation of a crack relaxes a zone around it. The width of this zone depends on several parameters (scale thickness, oxide temperature, reduction…). Sometimes a crack forms between two others.

IV.2. <u>Location on the strip</u>

An important remark has to be done on the stock length. Indeed, a long enough stock is necessary to take into account correctly all the phenomena involved in a rolling pass. The defect is more or less important depending on its location on the stock (end effects). An example of longitudinal cross section taken (in the steady state stage) is represented Figure VI-19.
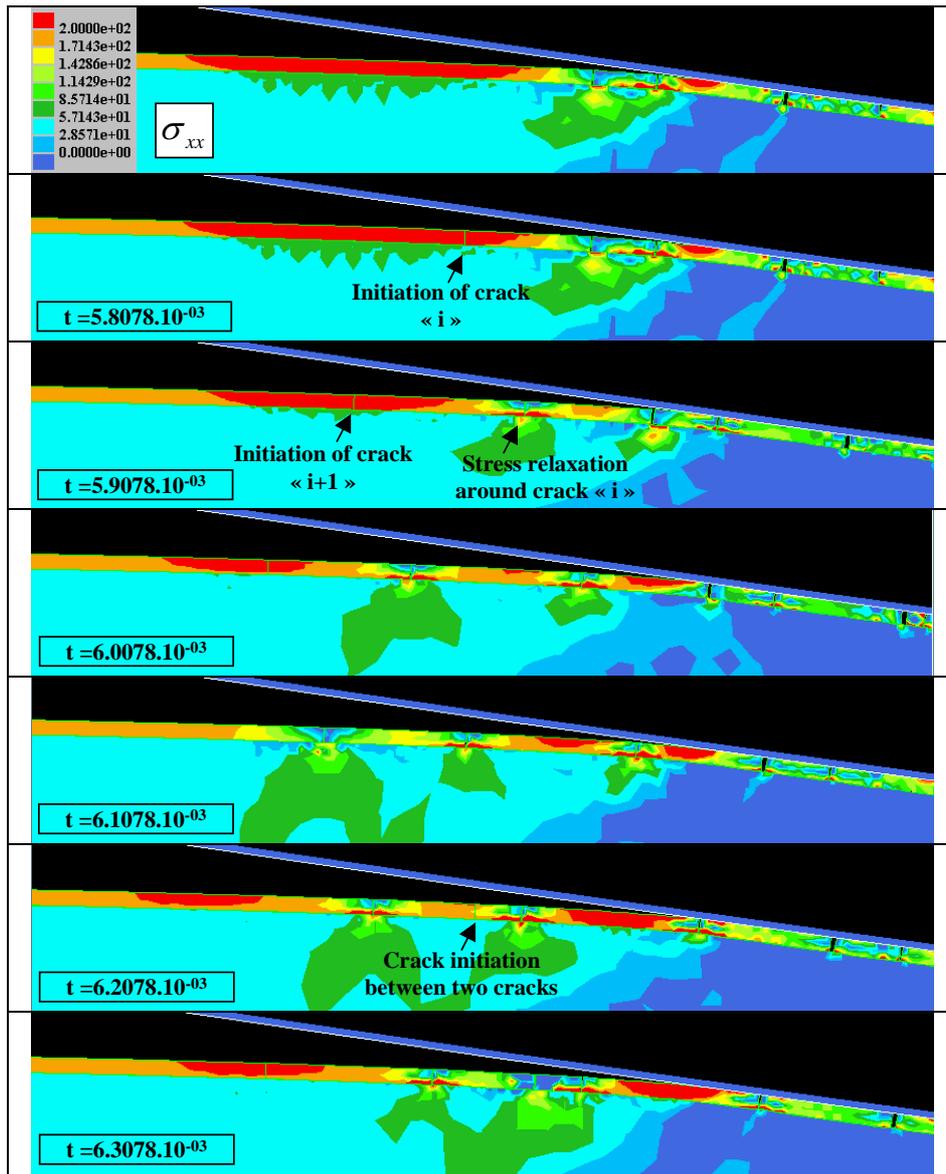
Figure VI-18: F2 conditions. Scale thickness: 50μm.

Conditions cage F2. Epaisseur de calamine : 50μm.
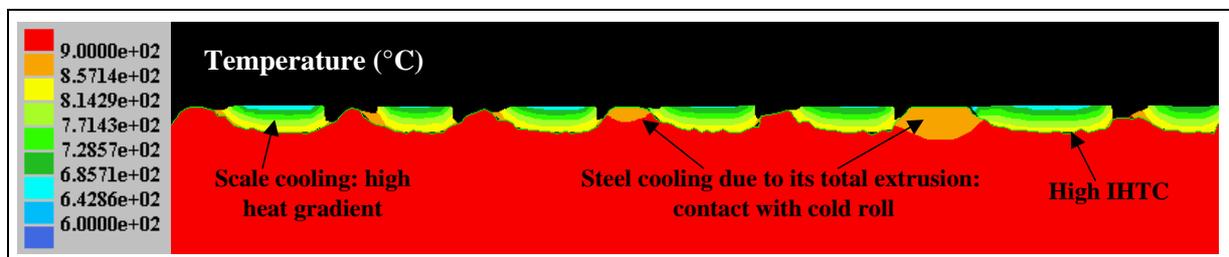
Figure VI-19: Interface cross section at the exit of the roll bite, in the middle of the stock length. Initial scale thickness: 200 μm; reduction 45%; μ= 0.6; roll velocity: 2.19 m/s; Strip initial temperature: 900°C.

Coupe de l'interface en sortie d'emprise, au milieu de la bande. Epaisseur initiale de calamine : 200 μm; réduction 45%; μ= 0.6; vitesse cylindre : 2.19 m/s; température initiale de la bande : 900°C.

On Figure VI-20, only the metal surface without the oxide fragments has been represented, more or less analogue to the surface after descaling. Its roughness after the exit of the roll bite is significantly larger in the middle of the rolled stock than at its head. This is mainly due to two phenomena:

- We have chosen a stock long enough for the extremities to be outside the roll bite, when the middle of the stock is rolled (tail is not yet rolled and head is already rolled). Head and tail are then in tension, which tends to open cracks.
- The second point is due to end effects under the rolls. In the middle of the stock, the soft steel flow is blocked on either side, which helps the extrusion process.
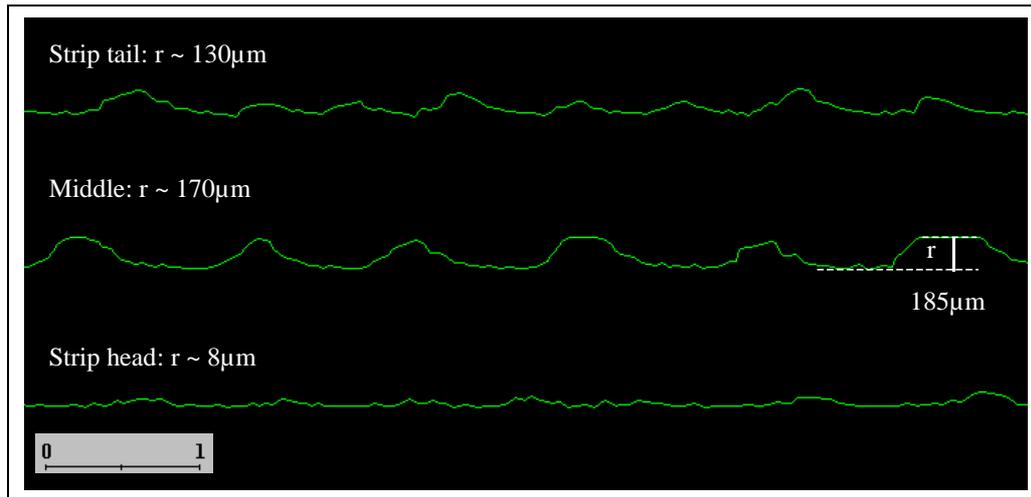
Figure VI-20: Interface roughness due to scale parts embedding. Surface aspect after descaling. Initial scale : 200 μm thick; reduction 45%; roll / scale friction: μ= 0.6; Strip initial temperature: 900°C.

Rugosité d'interface liée à l'incrustation de morceaux d'oxyde. Aspect de surface après décalaminage. Epaisseur d'oxyde initiale: 200 μm; réduction 45%; frottement cylindre-calamine: μ= 0.6; température initiale de la bande: 900°C.

IV.3. <u>Influence of temperature</u>

IV.3.1. Oxide temperature
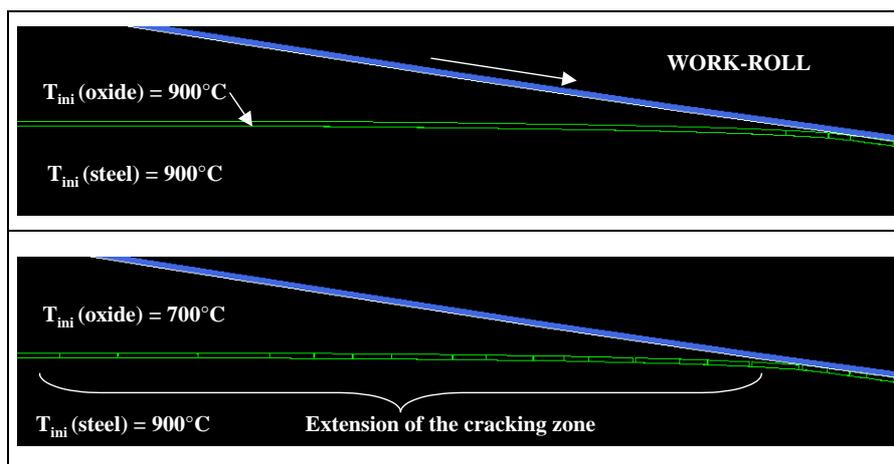
Figure VI-21: Strip cross section at the entry of the roll bite. Oxide thickness: 50 μm; reduction 35%; roll / scale contact: μ= 0.3; initial temperature of the oxide scale : 700°C and 900°C.
Coupe en entrée d'emprise. Epaisseur d'oxyde: 50 μm; réduction 35%; μ= 0.3; températures initiales de calamine : 700 °C et 900°C.

As has been explained in the bibliographic part of this chapter, the **oxide scale temperature is probably the most important parameter for the rolled-in scale defect**. Decreasing the initial oxide scale temperature, through water-cooling for example, gives a more **brittle** oxide scale. Tensile stresses ahead of the roll bite are significantly higher and the stress field

extends farther. **Cracks therefore initiate earlier** (Figure VI-21). As a consequence, their **number is higher and they are more widely open:** extrusion is easier (Figure VI-22).
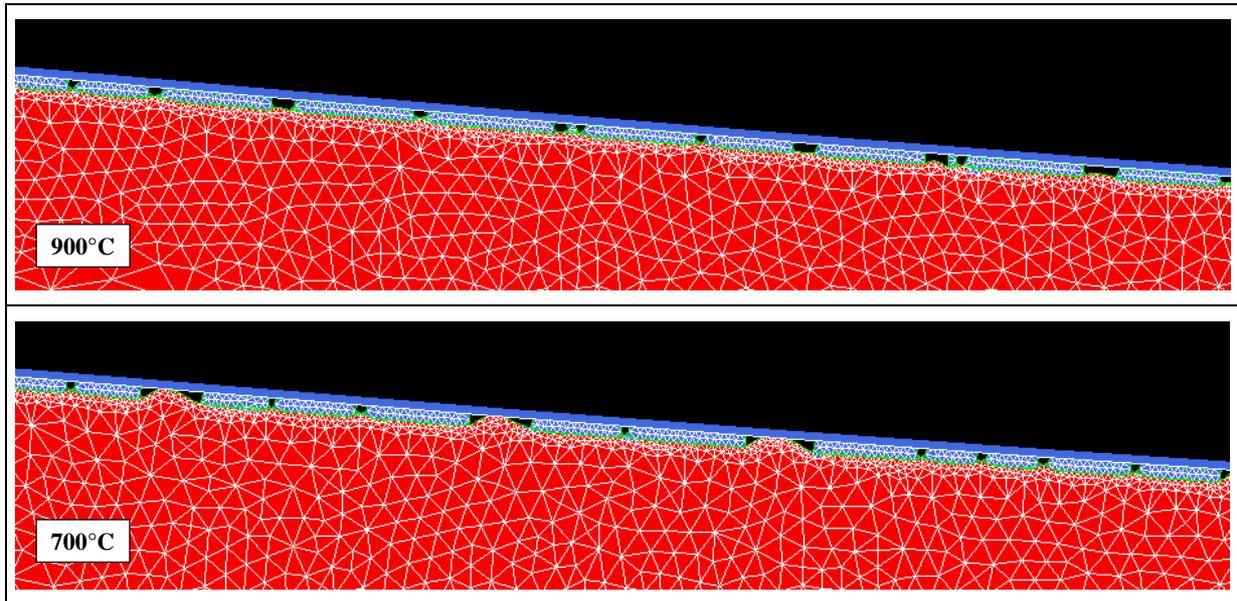
Figure VI-22: Strip cross sections inside the roll bite, under the rolls, at the same location. Same simulations as on Figure VI-21.

Coupe de deux bandes sous emprise, au même emplacement. Mêmes simulations que sur la Figure VI-21.

A simulation of steel strip covered by an oxide scale at 1100°C has been performed (steel and oxide). In this case, no crack initiates. The oxide scale is **co-rolled** with the same reduction as steel. It is important to point out that the contact between oxide and steel has been selected as adherent before the simulation. Indeed, despite the literature results showing sliding contact at such a temperature, we have no data concerning critical sliding or decohesion at 1100°C.

IV.3.2. Work-roll temperature
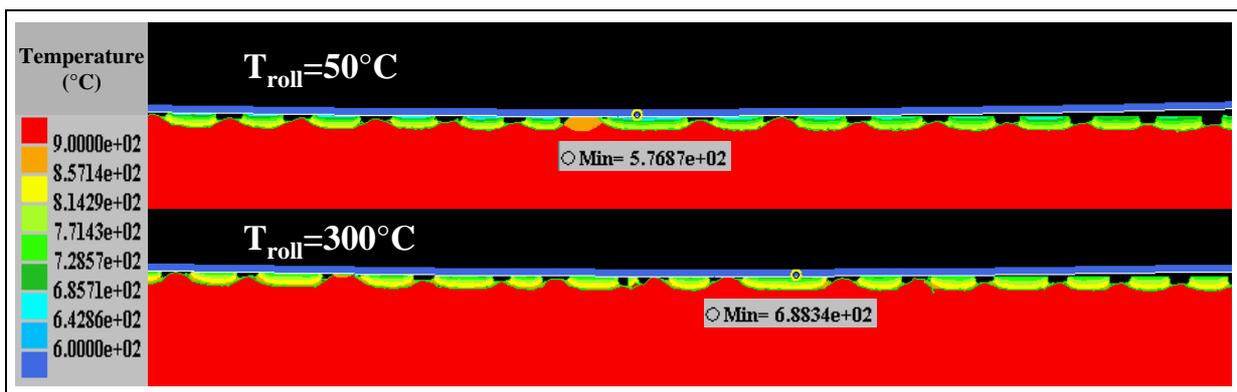
Figure VI-23: Influence of the work-roll average temperature. Strip cross section inside and at the exit of the roll bite. Initial scale thickness: 200 μm; reduction 45%; roll / scale contact: μ= 0.3; initial strip and scale temperature: 900°C.

Influence de la température moyenne du cylindre. Coupe sous et après emprise. Calamine initiale: 200 μm; réduction 45%; contact cylindre-calamine: μ= 0.3; température initiale bande + oxyde: 900°C.

It has been mentioned previously that the roll temperature cannot vary during the computation. Therefore, several values of the *average* temperature have been tested (Figure VI-23): 50°C corresponds to a roll keeping its initial temperature despite its contact with the hot strip; 300°C corresponds to a roll reaching a peak temperature of ~600°C, this can be regarded as an upper bound. No significant differences are observed in terms of rolled-in scale damage. Nevertheless, the oxide scale is cooler when rolls are at 50°C (~580°C, instead of 690°C when rolls are at 300°C). We can however note that strong cooling tends to give a harder scale, slightly less reduced ($T_{roll} = 50°C$: scale 185µm thick; $T_{roll} = 300°C$: 175µm). Co-rolling is slightly more difficult, cracks open wider ; finally extrusion is more advanced.

But the **major effect** of the roll temperature and of the stronger cooling of the oxide scale is not accounted for here : the **scale damage under the rolls**. Such a cold scale is **extremely brittle**. **Fragmentation** of the scale in this case is more than probable. Unfortunately, for want of a damage criterion valid under compressive stresses, we are unable to describe this phenomenon. This is probably a stringent limitation to the determination of the influence of roll temperature.

IV.4. Influence of reduction

Together with the temperature, the thickness reduction is the most influential parameter for rolled-in scale damage.
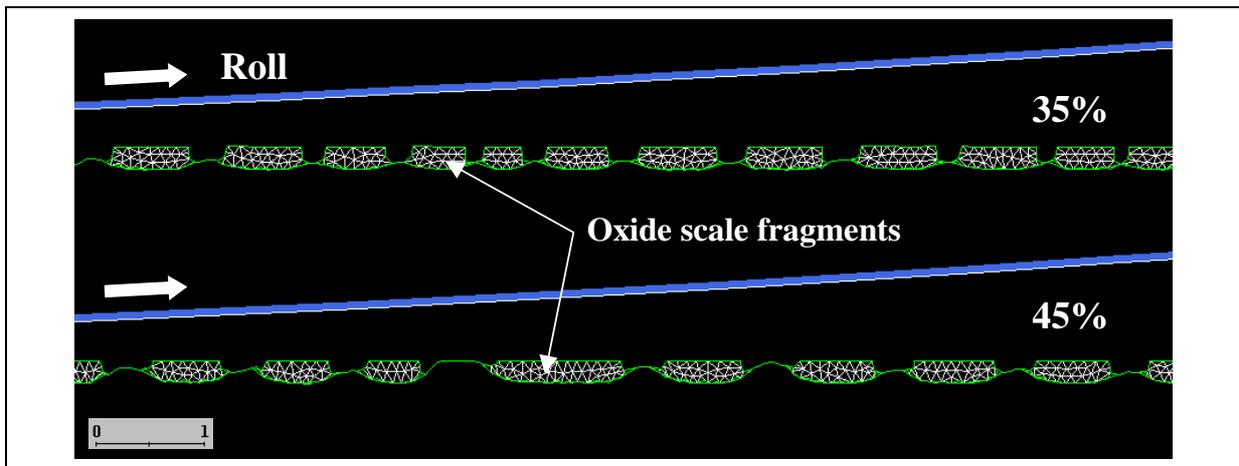
Figure VI-24: influence of reduction. Strip cross sections at the roll bite exit, in the middle of the stock length. Initial scale thickness: 200 µm; roll / scale contact: µ= 0.3.

Influence de la réduction. Coupe du milieu de la bande en sortie d'emprise.
Epaisseur de calamine initiale: 200 µm; contact cylindre-calamine: µ= 0.3.
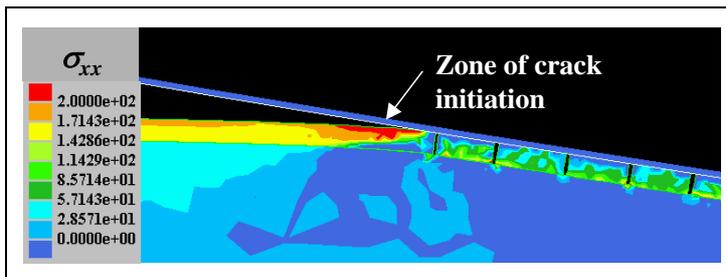
Figure VI-25: Same simulation as Figure VI-24: reduction 45%. The crack initiation zone does not extend. Results are identical to those obtained with a reduction of 35%.
Même simulation que Figure VI-24: réduction 45%. Zone de fissuration pas plus étendue. Résultats identiques obtenus avec une réduction de 35%.

Higher reductions open cracks wider, and compressive stresses in the bite are significantly higher ($\sigma_{yy} \sim$ -140 Mpa at 35% reduction, $\sigma_{yy} \sim$ -180 Mpa at 45%): steel extrusion is easier, as reflected Figure VI-24. It is to be noted here that cracks open in the bite, not before entry. Indeed, for both reductions, cracks appear just at the entry and do not have time to open (Figure VI-25). In both cases, the reduction of the oxide scale is extremely low. Indeed, it cracks instead of extending with steel (For 45%: scale 185-190µm thick. For 35%: 190µm).

IV.5. <u>Influence of scale thickness</u>

The scale thickness is extremely important for several reasons. The main one is that thin oxide scales are more adherent; thicker scale decohesion into rafts opens large free spaces in which the metal can easily be extruded. The other point is that, with thin scales, the shear stress gradient through the scale is milder. Crack opening is therefore limited and the extrusion is hindered : the extrusion "height" is smaller, and the final roughness after descaling is lower than with thicker scales, for which only the contact with rolls eventually stops extrusion (Figure VI-26).
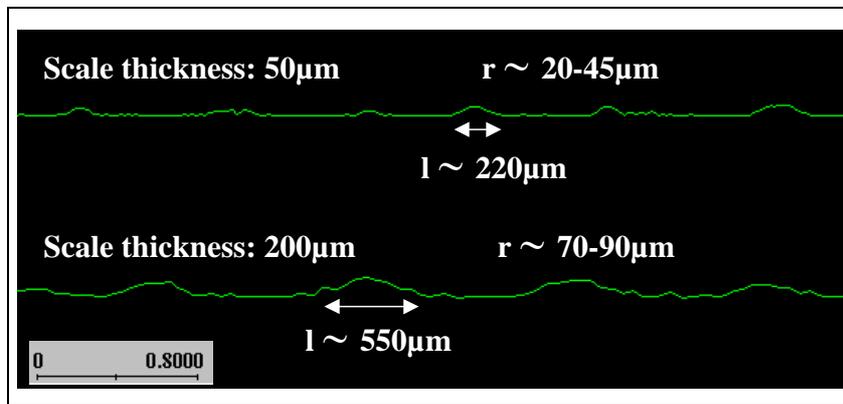
Figure VI-26: Scale thickness influence. Strip cross sections at the roll bite exit, in the middle of the stock length. Roll / scale contact: µ= 0.3; reduction 35%. *Influence de l'épaisseur de calamine. Coupe en sortie d'emprise, au milieu de la partie laminée. Contact cylindre-calamine: µ= 0.3; réduction 35%.*

Remark: With intensive cracking and extrusion, the scale at the exit of the roll bite can be thicker than at entry, as the oxide is in longitudinal compression due to the extrusion on both sides of rafts. Thus, in the case of the 50µm thick scale of Figure VI-26, scale thickness can reach 60µm locally. This phenomenon increases the amplitude of the surface roughness in the case of a complete extrusion.

IV.6. <u>Influence of rolling speed</u>
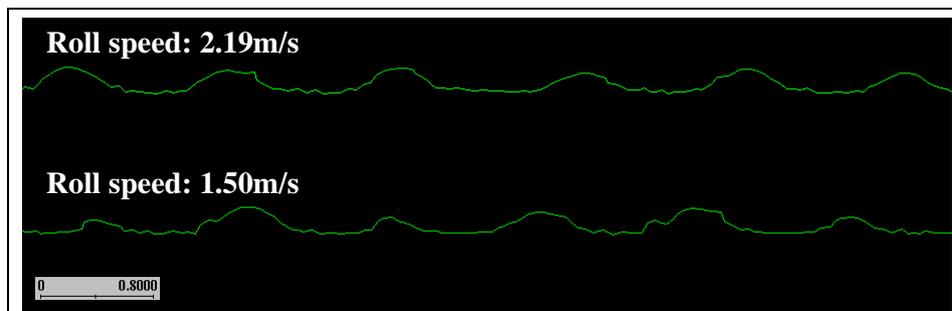
Figure VI-27: Speed influence. Surface roughness at the roll bite exit. Roll / scale friction: µ= 0.3; reduction 45%; scale: 200 µm.

Influence de la vitesse sur la rugosité de surface en sortie d'emprise. Contact cylindre-calamine : µ=0.3 ; réduction 45% ; calamine: 200 µm.

The rolling speed does not seem to be a major factor for strip surface roughness at the exit of the roll bite, even if extrusion very slightly increases with speed (Figure VI-27). Let us note again that the main effect of the speed may show under the rolls. Indeed, when roll speed increases, so do the relative strip / roll velocity on either side of the neutral point, the shear strain and friction at the oxide / roll surface.

IV.7. <u>Influence of friction</u>

The friction coefficient does have an influence on extrusion. Indeed, as observed previously in simulations of compression tests (chapter V), a high friction coefficient tends to slow down crack opening and hinder extrusion (Figure VI-28).
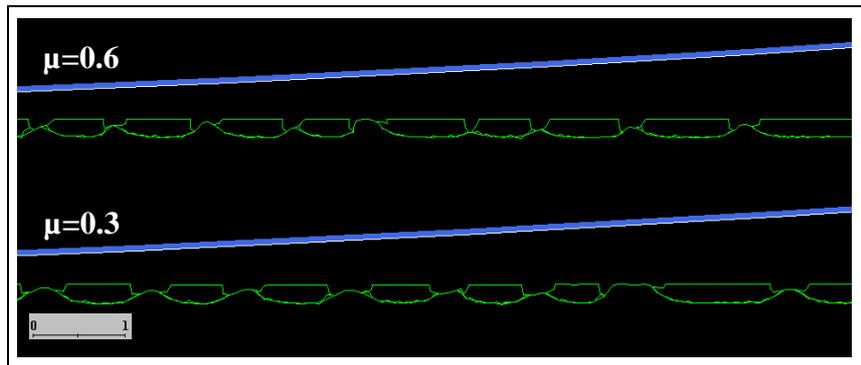
Figure VI-28: Roll / scale friction influence on the steel extrusion.

Influence du frottement cylindre-calamine sur l'extrusion de l'acier.

V. Behaviour of defects of the initial oxide layer

Several kinds of defects are known to promote rolled-in scale defects: oxidation heterogeneities, cold residues of oxide (coming from rolls or from descaling), or blisters at the metal oxide interface. **These features are simulated hereafter ; neither through-scale cracking nor delamination has been enabled.**

V.1. <u>Over-oxidation</u>
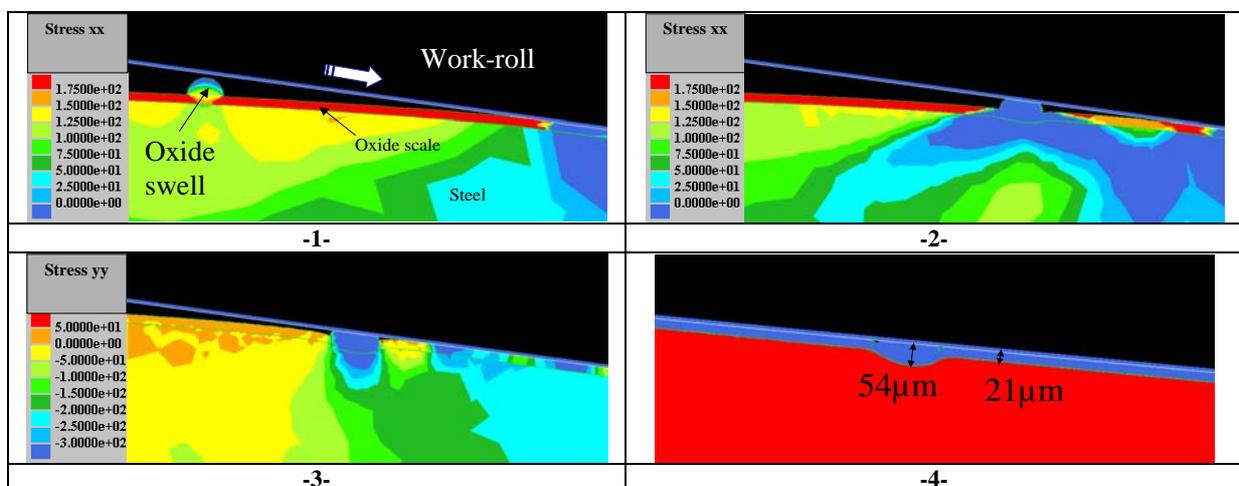
Figure VI-29: Oxide swell evolution in a F2 stand. *Surépaisseur d'oxyde dans une cage F2.*

The first case is a local over-oxidation of the oxide scale, for example due to local, non-descaled piece of oxide, giving an extra-thickness after re-oxidation. Figure VI-29 displays its evolution in the bite of a typical F2 stand : this kind of defect leads to the embedding of the oxide "ball" within the soft steel. Significant rolled-in scale defects may result.

V.2. <u>Cold oxide residue</u>

The presence of cold oxide residues on the strip, coming from descaling or from the rolls, seems inevitable to anyone who has seen a strip in a finishing mill, with all the oxide projections. Figure VI-30 presents the evolution of this kind of projection, which is rolled with the strip it lies on.

Figure VI-30: Embedding of cold oxide scale residue. Sticking contact between the residue and the oxide scale.

Incrustation d'un résidu d'oxyde froid. Contact collant entre le résidu et la calamine.
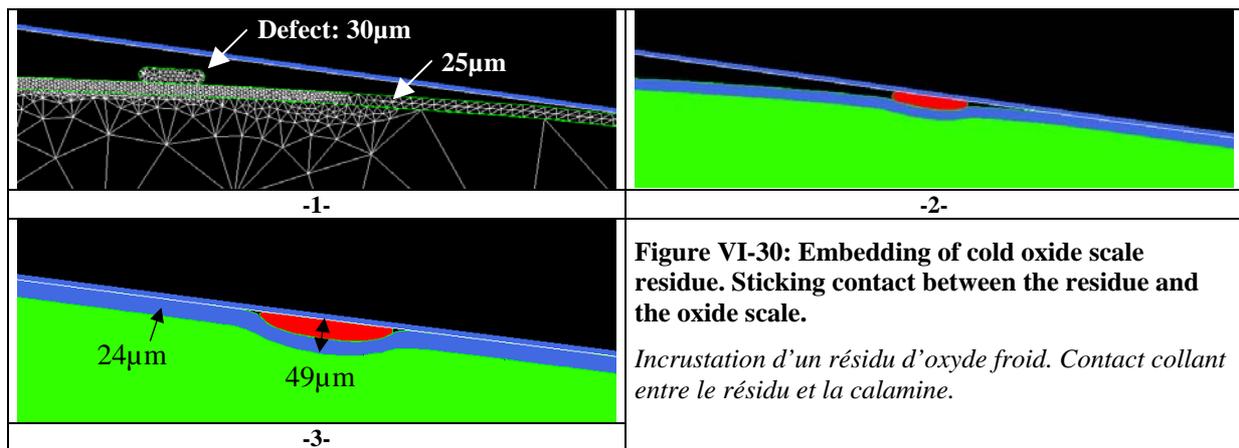
Once more, the consequences are not negligible. The effect of such defects in enhanced by their succession, through the creation of high tension zones between them, possibly initiating cracks (which makes embedding easier) (Figure VI-31,Figure VI-32).

Figure VI-31: Three successive oxide residues, with tensile zones between them.

Trois résidus d'oxyde successifs. Apparition d'une zone de traction.

Figure VI-32: Possible apparition of cracks in tensile zones, facilitating the oxide embedding.

Possible apparition de fissures dans les zones de traction, facilitant l'incrustation de calamine.
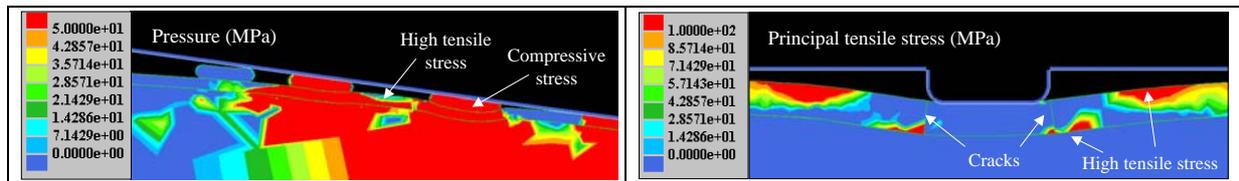
V.3. <u>Blister defect</u>

The last defect presented is the blister, often observed with oxide scales. Several shapes have been simulated. Figure VI-33 represents the most critical case, an hemisphere (large dome height, short width). Figure VI-34 shows the evolution of the blister at the entry of the roll bite. It is flattened due to the extension of the steel substrate and crushed by the roll compression. Figure VI-35 shows that this defect finally has no consequences in terms of rolled-in scale defect. This academic example contradicts several bibliographic illustrations representing bulbs obtained under identical conditions. In reality, it is extremely probable that the blister would crack at its base, the fragments may then behave as in paragraph V.2.
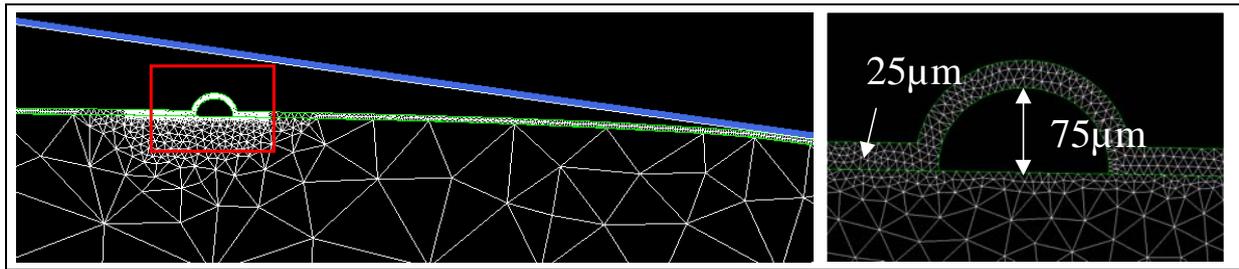
Figure VI-33: Numerical representation of an initial blister defect.

Représentation numérique d'un défaut initial de type boursouflure.
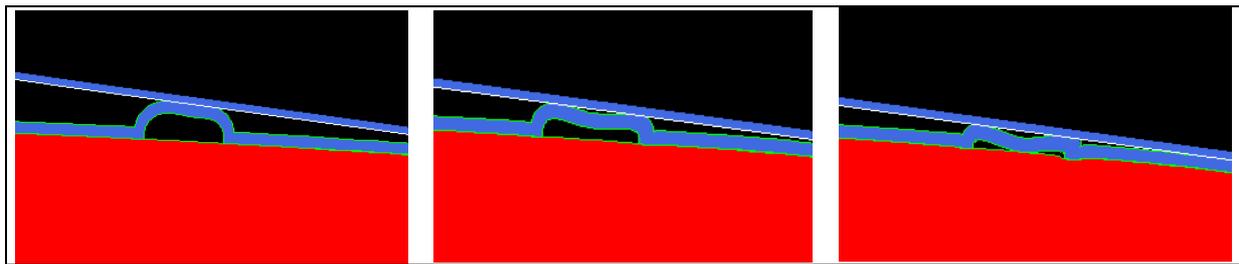
Figure VI-34: Evolution of the blister shape at the entry in the roll bite.

Evolution d'une boursouflure en entrée d'emprise.
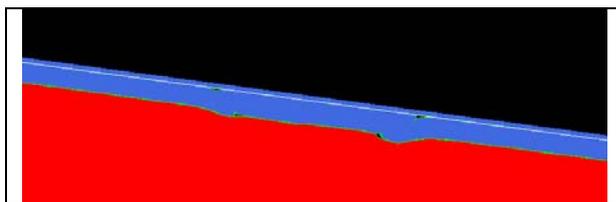
Figure VI-35: A negligible defect.

Un défaut négligeable.

VI. CONCLUSIONS

This last chapter highlights the efficiency of (1) numerical developments and (2) the measured mechanical data, to reproduce the oxide scale damage in a FM stand. Major influences have been shown such as the temperature, the reduction and the scale thickness before the roll bite entry. It must however be emphasized that the simulation presented here and their conclusions / comparisons with industrial tendencies are essentially qualitative. A quantitative approach would require:

- Oxide constitutive modeling under high hydrostatic pressure (as in the roll bite);
- A refined thermal analysis of the bite especially of the rolls ("deformable tools" in Forge2®).

Finally, the consequences of the observed phenomena (cracks, extrusion…) on heat transfer parameters and friction remain to be analyzed.

VII. REFERENCES

[Krz1]   M.Krzyzanowski, J.H.Beynon, C.M.Sellars, Analysis of secondary oxide-scale Failure at entry into the roll gap, Met. Mat. Trans. B, vol. 31B, (December 2000), pp.1483-1490.

[Krz2]   M.Krzyzanowski, C.M.Sellars, J.H.Beynon, Characterisation of oxide scale in thermomechanical processing of steel, Proceedings of Int. Conf. On Thermomechanical Processing : Mechanics, Microstructure and Control, Sheffield, (2003). Plamiere, Mahlouf & Pinna, Eds. pp.91-102.

[Krz3]   M.Krzyzanowski, J.H.Beynon, Evaluation of interfacial heat transfer during hot steel rolling assuming scale failure effects, Proc 10th Int. Symp. "Plasticity'03": Dislocations, Plasticity and Metal Forming, Quebec City, Canada, (July 2003). A.S. Khan ed. pp.184-186.

[Krz4]   M.Krzyzanowski, J.H.Beynon, Oxide behavior in hot rolling, in "Metal Forming Science and Practice, a state of the art volume in honour of Pr J.A.Schey's 80th birthday", edited by J.G.Lenard (2002), pp.85-114.

[Piet]   M.Pietrzyk, J.G.Lenard, Thermal-Mechanical Modelling of the Flat Rolling Process, Springer-Verlag, Berlin, (1991).

[Tan]   K.S.Tan, M.Krzyzanowski, J.H.Beynon, Effect of steel composition on failure of oxide scales in tension under hot rolling conditions, Steel Res. (2001), pp.250-258.

[Zhou]   Y.C.Zhou, T.Tonomori, A.Yoshiba, L.Liu, G.Bignall, T.Hashida, Fracture characteristics of thermal barrier coatings after tensile and bending tests, Surf. Coating Technol. 157 (2002), pp.118-127.

General Conclusion and Perspectives

GENERAL CONCLUSION AND PERSPECTIVES

The objective of this study was to release constraints in operating conditions due to a lack of knowledge on the **rolled-in scale defect**. The final goal is to increase **ARCELOR's equipment productivity**.

Rolled-in scale defects have several origins, which depend on many parameters such as temperature, scale thickness, reduction… Most of them are interconnected and impede other aspects of the rolling process, so that they cannot be freely adjusted. The main origin is **cracking of the ferrous oxide layer** under **tensile stresses** just before the entry of finishing mill roll bites. These cracks open and widen, the softer steel can **extrude** within the gaps under compressive stresses undergone within the roll bite. **Interfacial propagation of through-thickness cracks**, **decohesion** and viscous **sliding** can also be observed.

The developed numerical simulation is a well-adapted tool to reproduce these mechanisms and give us an insight into non-measurable data. During this study, we have used the **Forge2® finite element software package**.

* * * * *

The formation of rolled-in scale defects involves through-thickness cracks, interfacial cracks, decohesion, interfacial sliding of two materials of very different thickness. So a numerical simulation able to reproduce the oxide layer damage at the origin of the rolled-in scale defect must handle all the mentioned phenomenon.

Several numerical developments have been performed in Forge2® to deal with our industrial process. Layer decohesion, interfacial cracking and sliding can now be managed in an automatic manner. Developments have been based on **contact management** models at the interface between two bodies. These models have been extended and adapted to our application.

Concerning **transverse cracking**, a numerical method allowing crack initiation in an initially **non-cracked mesh** was developed. This technique of transverse and interfacial cracking of coatings is **innovative** and allows **modeling damage mechanisms** of oxide scales and more generally in brittle **coatings**.

* * * * *

Once these numerical developments have been completed, it has been necessary to introduce mechanical data of the actual materials used in our process. This has required different stages.

First, an extensive **bibliographic study** was performed to evaluate existing data in the literature on iron oxide mechanical and physical behaviors, and on the hot rolling process. Unfortunately, data found in the literature appeared to be **unsuited** to the extremely complex conditions applied by the hot rolling process. Therefore, missing data had to be identified.

We have determined **behavior laws** of steel and scale as a function of temperature, strain, strain rate, steel grade… For this, we used a mechanical test applying solicitations **as close as**

possible to those undergone by the matter just ahead of the roll bite: the **4-Point Hot Bending Test.** An important work was done to add measuring devices to the test (thermal cycle, chemical cycle, load deflection measurement…) and to analyze their results. The **inverse analysis method** gave constitutive parameters for the different materials used in our study.

Another interesting point concerns the oxide scale damage, with the **determination of critical stresses**. For this, an original and efficient method has been used: **the Acoustic Emission**. This method, **rarely used at high temperature**, proved to be a **major tool** in the determination of **critical fracture stresses**, but also in the understanding of experimental **artifacts** connected with the mechanical test.

Strains and especially strain rates undergone by materials during hot rolling **are much higher** than the ones reached by 4-PHBT. This is why we have complemented our study **with Hot Tensile Tests**. These allowed us to observe specific damage mechanisms (which did not exist or were not visible using 4-PHBT) such as **decohesion** or **interfacial propagation**. These tests have also **extended the damage existence domain** (for example, cracking is initiated at higher temperature when the strain rate increases).

Using previously **identified constitutive laws**, **determined damage critical stresses** and **the numerical developments**, an **excellent agreement** has been observed between **experimental results** and **numerical simulations**, both **qualitatively** and **quantitatively**.

To clarify the damage conditions prevailing in the bite, we have also simulated **compression tests.** It was possible to compare simulations with a few experimental Plane Strain Compression Tests performed several years ago at IRSID. We have thus shown that fracture criteria determined using 4-PHBT and HTT were not adapted to compression, probably due to hydrostatic pressure enhancing oxide ductility. More sophisticated constitutive models, e.g. including damage variables sensitive to the hydrostatic pressure, would be necessary to cover all strain states found in strip rolling.

This study nevertheless gave the **sensitivity of the extrusion phenomenon to several parameters** (crack width, reduction, temperature, strain rate…). This is extremely important because this **extrusion phenomenon represents in fact the critical stage for the rolled-in scale defect**. Indeed, cracks too narrow for extrusion **are not harmful** for the final product.

* * * * *

Finally, the **numerical simulation of the hot rolling process** has been performed, taking a **F2 stand** as the reference. This **feasibility study** has shown Forge2® to be able to **simulate the extreme conditions** met in the process (high speed, thin oxide scale…). The developments to simulate damage have proved **efficient** and **instructive**. Several configurations have been tested: we have evaluated the **influence of several parameters** (reduction, scale thickness, strip location…), as well as the **evolution of defects** formed before the roll bite (residue, blister…).

* * * * *

From an industrial point of view, this study has allowed, as expected, to identify and understand phenomena at the origin of rolled-in scale defects. Forge2® is presently able to simulate the hot rolling of a bi-material with damage initiation depending on mechanical conditions. This first feasibility study will help Arcelor Research S.A **reduce safety factors** at

each stand of the finishing mill, through a **parametric study** we unfortunately did not have enough time to perform.

* * * * *

The knowledge obtained during this work will now be used within Arcelor to define a more robust rolled-in-scale alarm criterion. Present alarms are based on rolling conditions including roll bite stresses. They do not include any description of the behavior of iron oxide layer. Using more physically based description of scale behavior, more robust indicators may now be defined.

Scale breaking in front of the bite is not the only one mechanism suspected to create rolled-in scale. An important class of defects is connected with roll degradation. Ongoing studies on work roll grade will certainly help to lessen these defects. But a single roll degradation does not always lead to surface defect, as the surface heterogeneity created in one stand may be erased in the next one. There is certainly some benefit for the HSM to have a clear view of **phenomena appearing under work-rolls** (printing effect), or the link between the oxide layer shape after the bite and the appearance of defects in the pickling tank.

The scientific knowledge obtained needs to be extended. It is now possible to depict the ferrous oxide layer behavior ahead of the rolling bite, but not under the bite. For this, it is necessary to **deepen the understanding of damage** initiated under compression, including the impact of **roll wear**. The effect of the hydrostatic pressure on the scale fracture criterion is to be added as well. The final point is **thermal transfer** in the bite, a very important item which should be modeled more precisely.

CONCLUSION GENERALE ET PERSPECTIVES

L'objectif de cette étude était de lever les contraintes sur les conditions opératoires dues au manque de connaissance sur **les défauts de calamine incrustée.** L'objectif final est l'augmentation de la **productivité d'ARCELOR.**

Les défauts d'incrustations ont plusieurs origines qui dépendent de plusieurs paramètres tels que la température, l'épaisseur de calamine, la réduction… La majorité d'entre eux sont liés et mettent en jeu d'autres aspects du procédé de laminage, ce qui les rend difficiles à ajuster. La principale origine est la **fissuration de la calamine sous les contraintes de traction** juste avant l'entrée des emprises des cages du finisseur. Les fissures s'ouvrent et s'élargissent, l'acier, mou, peut alors s'**extruder** à l'intérieur des vides sous les contraintes compressives engendrées dans l'emprise. La propagation **des fissures transverses le long de l'interface**, la **décohésion** et le **glissement visqueux** peuvent aussi être observés.

La simulation numérique que nous avons développée est un outil bien adapté pour reproduire ces mécanismes et nous permettre d'obtenir des données non mesurables. Nous avons utilisé au cours de cette étude le **logiciel éléments finis Forge2®.**

* * * * *

La formation du défaut d'incrustation implique fissures transverses, fissures interfaciales, glissement interfacial de deux matériaux ayant des épaisseurs très différentes. Donc, une simulation numérique capable de reproduire l'endommagement de la calamine à l'origine du défaut de type calamine incrustée doit pouvoir reproduire tous ces phénomènes.

Plusieurs développements numériques ont été réalisés dans le logiciel pour imiter notre procédé industriel. Décohésion de couche, fissuration interfaciale et glissement peuvent maintenant être contrôlés de manière automatique dans Forge2®. Les développements ont été basés sur des modèles de **gestion du contact** à l'interface entre deux corps. Ces modèles ont été étendus et adaptés à nos applications.

Concernant la **fissuration transverse**, une méthode numérique permettant d'initier des fissures dans un maillage initialement non fissuré a été développée. Cette technique de fissuration transverse et interfaciale de couches est **innovante et permet de modéliser les mécanismes d'endommagement des calamines et plus généralement des revêtements.**

* * * * *

Une fois ces développements numériques achevés, il a été nécessaire d'introduire les données mécaniques des matériaux réels utilisés dans notre procédé. Ceci a requis différentes étapes.

Tout d'abord, une **étude bibliographique** a été réalisée pour évaluer les données existantes dans la littérature sur les comportements physiques et mécaniques des oxydes de fer, et sur le procédé de laminage à chaud. Malheureusement, les données trouvées dans la littérature apparaissent peu adaptées aux conditions extrêmement complexes engendrées par le procédé de laminage. Les données manquantes ont donc dû être identifiées.

Nous avons alors déterminé les **lois de comportement** de l'acier et de la calamine en fonction de la température, la déformation, la vitesse de déformation, la nuance d'acier… Pour cela, nous avons utilisé un test mécanique impliquant des sollicitations **aussi proches que possible** de celles rencontrées par la matière juste avant l'entrée d'emprise : **le test de Flexion 4 Points à chaud.** Un important travail a été effectué pour ajouter des appareils de mesure au test (cycle thermique, mesure de force – flèche…) et analyser leurs résultats. L'analyse inverse nous a permis d'obtenir les lois de comportement pour les différents matériaux utilisés dans notre étude.

Un autre point intéressant concerne la fissuration de la calamine, avec la **détermination de contraintes critiques**. Pour cela, une méthode originale et performante a été utilisée : l'**Emission Acoustique**. Cette méthode, **rarement utilisée à haute température**, s'est révélée être un **outil majeur** dans la détermination des valeurs critiques de fissuration, mais aussi dans la compréhension d'**artefacts expérimentaux** liés au test mécanique.

Les déformations et principalement les vitesses de déformation subies par les matériaux pendant le laminage à chaud sont **beaucoup plus élevées** que celles rencontrées en flexion 4 points. Nous avons donc complété notre étude par des **tests de traction à chaud**.

Ces **tests de traction à chaud** ont permis d'observer des mécanismes d'endommagement spécifiques (qui n'existaient pas ou n'étaient pas visibles en flexion 4 points) tels que la **décohésion** ou la **propagation interfaciale**. Les tests ont alors permis d'**étendre le domaine d'existence de l'endommagement** (par exemple, le domaine fragile s'étend vers les plus hautes températures quand la vitesse de déformation augmente).

A partir des **lois d'écoulement précédemment identifiées**, des **contraintes critiques de rupture déterminées** et des **développements numériques réalisés**, un excellent accord a été observé entre les **résultats expérimentaux** et les **simulations numériques**, à la fois **qualitativement** et **quantitativement**.

Pour déterminer la condition d'endommagement prédominante dans l'emprise, nous avons simulé des tests de compression. Il a été possible de comparer la simulation avec quelques tests expérimentaux de bipoinçonnement réalisés quelques années auparavant à l'IRSID. Nous avons alors montré que les critères de rupture déterminés en flexion 4 points et en traction à chaud n'étaient pas adaptés à la compression (influence de la pression hydrostatique, qui rend la calamine plus ductile). Des modèles constitutifs plus sophistiqués, c'est-à-dire incluant des variables d'endommagement sensibles à la pression hydrostatique, seraient nécessaires pour couvrir tous les états de déformation trouvés dans une bande en cours de laminage.

Cette étude a permis d'évaluer l'influence **de certains paramètres** (largeur de fissure, réduction, température, vitesse de déformation…) sur le phénomène d'extrusion. Ceci est extrêmement important pour nous parce que cette **extrusion représente en fait le facteur critique du défaut de calamine incrustée**. En effet, des fissures sans aucune extrusion ne sont pas nuisibles pour le produit final.

* * * * *

Finalement, la **simulation numérique du procédé de laminage à chaud** a été réalisée, en prenant comme référence une **cage F2**. Cette **étude de faisabilité** a montré que Forge2® était

capable de **simuler les conditions extrêmes** rencontrées dans le process (grande vitesse, fine couche d'oxyde…). Les développements pour simuler l'endommagement se sont montrés **réellement efficaces** et **instructifs**. Plusieurs configurations ont été testées : nous avons évalué l'**influence de plusieurs paramètres** (réduction, épaisseur de calamine, emplacement sur la bande…), ainsi que l'**évolution de défauts** formés avant l'emprise (résidu, boursouflure…).

* * * * *

D'un point de vue industriel, cette étude a permis, comme espéré, d'identifier et de comprendre les phénomènes à l'origine des défauts de calamine incrustée. Forge2® est actuellement capable de simuler le laminage à chaud d'un bi-matériau avec l'initiation d'endommagement dépendant de conditions mécaniques. Cette première étude de sensibilité permettra à Arcelor Research S.A d'envisager de **réduire les marges de sécurité** à chaque cage du finisseur, au travers d'une étude paramétrique que nous n'avons malheureusement pas eu le temps de réaliser.

* * * * *

La connaissance acquise lors de cette étude pourra maintenant être utilisée par Arcelor pour définir un système d'alarme plus robuste pour les défauts de type calamine incrustée. Les alarmes actuelles sont basées sur les conditions de laminage incluant les contraintes de l'emprise. Elles ne prennent en compte aucune description du comportement des couches d'oxyde de fer. L'introduction d'une description plus physique du comportement de la calamine permettra de définir un indicateur plus robuste.

La fissuration de la calamine en entrée d'emprise n'est pas le seul mécanisme suspecté de créer des défauts d'incrustation. Une importante classe de défauts est liée à la dégradation des cylindres. Les études en cours sur les nuances de cylindre vont certainement aider à diminuer ces défauts. Mais une simple dégradation de cylindre ne mène pas toujours à un défaut de surface car une hétérogénéité de surface créée dans une cage peut être effacée dans la suivante. Il y a certainement pour les lamineurs plusieurs bénéfices à avoir une vision claire des **phénomènes apparaissant sous les cylindres** : effet d'impression, lien entre la forme de la couche d'oxyde après emprise et l'apparition de défauts au décapage.

La connaissance scientifique obtenue a besoin d'être étendue. Il est maintenant possible de dépeindre le comportement des couches d'oxyde de fer avant l'emprise, mais pas dessous. Pour cela il serait nécessaire d'approfondir la compréhension de l'endommagement initié en compression, ce qui nécessiterait de prendre en compte l'usure des cylindres. L'effet de la pression hydrostatique sur le critère de fissuration de la calamine doit être ajouté. Enfin, les transferts thermiques sous emprise sont fondamentaux, et leur prise en compte doit absolument être affinée.

APPENDIX 1: Behavior laws of materials

<u>Steel behavior</u>

<u>Elastic parameters</u>

Young's modulus:

Young's modulus of steel is rarely used in high deformation material processes (usually due to high deformation). Only few expressions exist in the literature [Pie2].

$$E = \left[2.07 + 0.87438\left(\frac{T}{1000}\right) - 10.0906\left(\frac{T}{1000}\right)^2 + 14.48466\left(\frac{T}{1000}\right)^3 - 6.20767\left(\frac{T}{1000}\right)^4 \right].10^5$$

where T is explained in °C.

Values obtained with this formula are smaller than those generally found in publications. Values of E are graphically represented as a function of temperature for this equation and other references [Pie2, Fle,Tak,OTU] in Figure A1-1. In the last two references, many steel grades are studied.
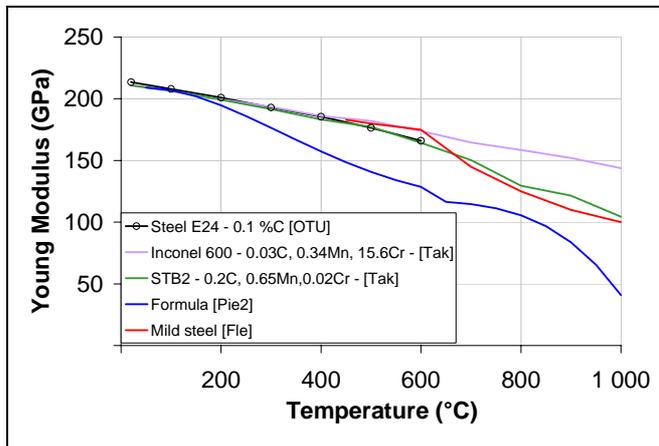
Figure A1-1: Young' modulus of steel vs. Temperature.

Module d'Young d'aciers en fonction de la température.

Poisson coefficient ν:

Some values of ν are available in [Fle] for mild steel or in [OTU] for many steel grades. In the former, the Poisson coefficient is equal to 0.327 at 600°C, 0.335 at 700°C, 0.344 at 800°C, 0.352 at 900°C and 0.36 at 1000°C, vs 0.31 at 600°C in the second reference for a low carbon steel (0.1 %C).

<u>Viscoplastic parameters</u>

A first way of representing the plastic deformation of steel is to use **Hajduk's** equations [Pie1,Tru]:

$$\overline{\sigma} = \sigma_0 K_T K_\varepsilon K_u$$

where $\sigma_0, K_T, K_\varepsilon, K_u$ are respectively functions of the material, temperature, strain and strain rate. They established this equation for several low and medium carbon steels. Below is an example for a carbon steel containing 0.13%C and 01.4%Mn:

$$\overline{\sigma} = 98.1\left[17.8\exp\left(-0.0029T\right)\right].\left(1.79\overline{\varepsilon}^{0.252}\right).\left(0.72\dot{\overline{\varepsilon}}^{0.143}\right)$$

$\overline{\sigma}$ is expressed in MPa, $\dot{\varepsilon}$ in s^{-1} and T in °C.

Pietrzyk's equation based on the relation determined by Sellars and Tegart [Sel] can be employed for the yield stress of low carbon steel as:

$$\overline{\sigma}(MPa) = 100\varepsilon^{0.2}\sinh^{-1}\left(2.10^{-13}Z\right)^{0.2}$$

where Z is the Zener-Hollomon parameter, $Z = \dot{\varepsilon}\exp\left(\dfrac{Q}{RT}\right)$, in which the activation energy is

Q=350kJ/mol

One of the most comprehensive sets of empirical equations for high temperature behavior of carbon steels was developed by **Shida** [Shi,Lee]. The flow stress $\overline{\sigma}$ was given in terms of strain ε, strain rate $\dot{\varepsilon}$, temperature T (in °C) and carbon content C (in weight percent) .

$$\overline{\sigma} = \sigma_f f\left(\frac{\dot{\varepsilon}}{10}\right)^m$$

with $\begin{cases} f = 1.3(5\varepsilon)^n - 1.5\varepsilon \\ n = 0.41 - 0.07C \end{cases}$

Let $\overline{T}$ be defined as: $\overline{T} = (T + 273)/1000$

- For $\overline{T} \geq 0.95\dfrac{C+0.41}{C+0.32}$

$\begin{cases} \sigma_f = 2.75.\exp\left(\dfrac{5}{\overline{T}} - \dfrac{0.01}{C+0.05}\right) \\ m = \left(-0.019C + 0.126\right)\overline{T} + \left(0.075C - 0.05\right) \end{cases}$

with σ_f is expressed in MPa.

- For $\overline{T} < 0.95\dfrac{C+0.41}{C+0.32}$

$\begin{cases} \sigma_f = 2.75.q(C,\overline{T})\exp\left[\dfrac{C+0.32}{0.19(C+0.41)} - \dfrac{0.01}{C+0.05}\right] \\ q(C,\overline{T}) = 30(C+0.9)\left(\overline{T} - 0.95\dfrac{C+0.49}{C+0.42}\right)^2 + \dfrac{C+0.06}{C+0.09} \\ m = (0.081C + 0.154)\overline{T} - 0.019C + 0.207 + \dfrac{0.027}{C+0.32} \end{cases}$

For low carbon steel, C=0.16, the transition $\overline{T} = 0.95\dfrac{C+0.41}{C+0.32}$ occurs at T = 855°C.

The authors point out that the form of the equation has no physical meaning. The validity range of Shida's equations is given as:

Carbon content $< 1.2\%$; Temperature: 700-1200°C; Strain rate: $0.1\text{-}100\text{s}^{-1}$; Strain: $< 70\%$.
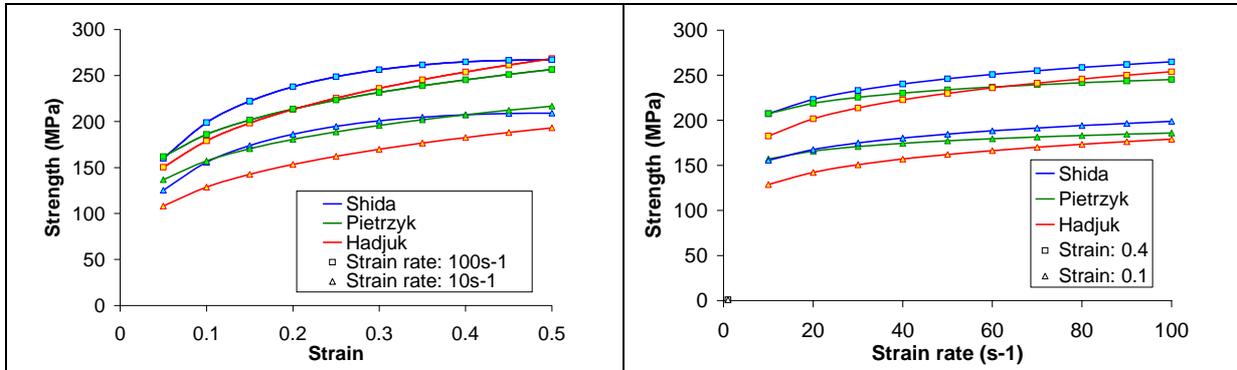
Figure A1-2: a) Strength vs strain.　　　　**b) Strength vs strain rate**

a) Contrainte d'écoulement en fonction de la déformation.　　　*b) Contrainte d'écoulement en fonction de la vitesse de déformation.*

Work-rolls

The work-rolls are elastically deformed during a pass. Young's modulus at room temperature is available Figure A1-3.

	Work-roll Skin			Work-roll heart	
	URFAC: Hi-Cr	**URVAC: Hi-V**	**URMAC: Hi-V**	**Cast iron 1**	**Cast iron 2**
Young modulus E (GPa) at 20°C	225	235	229	120	175

Figure A1-3: Young's modulus of rolls.

Module d'Young des cylindres.

APPENDICES

APPENDIX 2: Thermal properties

The objective of this appendix is to compile thermal properties of the different materials found in the finishing mill (steel slab, oxide scale covering it, work-roll), in order to understand and finally simulate the hot rolling process.

<u>Steel</u>

	Steel	600	700	800	900	1000	ref.
density (kg/m3)	steel XC6	7668	7628	7598	7602	7550	IRSID
	mild steel	7659	7703	7651	7600	7548	[Fle]
	Low carbon steel	7779	7761	7743	7721	7699	[Pie1]
	Carbon steel	7577	7540	7502	7739	7689	[Zho]
	mild steel E24 (0.1%C)	7649	7610	7612	7563	7518	[OTU]
Specific heat capacity (J/(Kg.K)	steel XC6	753	866	1104	874	845	IRSID
	mild steel	787	1431	736	648	648	[Fle]
	carbon steel	737	911	888	747	621	[Zho]
	Average steel OTUA	720	810	510	540	570	[OTU]
conductivity (W/(mK))	steel XC6	36.4	33.9	28.5		27.6	IRSID
	mild steel	33.78	30.19	24.49	26.64	25.08	[Fle]
	Low carbon steel	32.03	30.4	29.08	27.99	27.11	[Pie1]
	Carbon steel	29.59	28.13	27.37	28.52	29.45	[Zho]
	mild steel E24 (0.1%C)	35	30	24	25	26	[OTU]

Table A2-1: Thermal properties of steel from different references. [Zho] and [Pie1] data are obtained from formulas explained Figure A2-1 and Figure A2-2. Formulas in [Zho] are valid for carbon steels. To give an idea of parameter values, a 0.5%C steel has be chosen.
Propriétés thermiques d'aciers à partir de différentes références. Les données de [Zho] et [Pie1] sont obtenues à partir des formules Figure A2-1 et Figure A2-2. Les formules de [Zho] sont adaptées aux aciers doux. Pour donner une idée des valeurs des paramètres, un acier à 0.5%C a été choisi. .

Figure A2-1: Formulas of [Zho] for the thermal properties, given in Table A2-1.
Formules des propriétés thermiques de [Zho] utilisées Table A2-1.

Figure A2-2: Formulas of [Pie1] for the thermal properties, given in Table A2-1.
Formules des propriétés thermiques de [Pie1] utilisées Table A2-1.

Oxide scale

		600	700	800	900	1000	Ref.
density (kg/m3)	Oxide scale	5500					IRSID
	Oxide scale	5700					[Krz1]
	FeO / Fe3O4 / Fe2O3	7750 / 5000 / 4900					[Torr]
Specific heat capacity (J/(KgK))	Oxide scale	766		779		791	IRSID
	Oxide scale (1)	853	883	913	942	972	[Krz1]
	FeO / Fe3O4 / Fe2O3	725 / 870 / 980					[Torr]
conductivity (W/(mK))	Oxide scale	3					IRSID
	Oxide scale (2)	1.68	1.76	1.84	1.92	2	[Krz1]
	FeO / Fe3O4 / Fe2O3	3.2 / 1.5 / 1.2					[Torr]

(1) $Cp = 679.959 + 0.297T - 4.367.10^{-5}T$ for $T \in 600 - 1100°C$

(2) $\lambda = 1 + 7.833.10^{-4}T$ for $T \in 600 - 1200°C$

Table A2-2: Thermal properties of oxide scale from different references.
Propriétés thermiques de la calamine à partir de différentes références.

Table A2-2 highlights the very low conductivity values of the oxide scale, more than ten times smaller than steel. Its role of thermal barrier is evident.

Work-rolls

		Work-roll Skin				Work-roll heart	
		URFAC: Hi-Cr	Hi-Cr [Zho]	URVAC: Hi-V	URMAC: Hi-V	Cast iron 1	Cast iron 2
density (kg/m3)	20	7532	7760	8100	7630	7137	7028
	200	7483	7676			7085	6977
	600	7365	7495			6950	6826
Specific heat capacity (J/(KgK))	20	492	518	443	434	476	520
	200	538	535			558	562
	600	684	571			727	725
conductivity (W/(mK))	20	13.8	20	20.5	22.12	33.7	24.2
	200	14.5	20			33.9	24.7
	600	19.2	20			29.6	22.9

For [Zho]: $Cp = 493.6\exp(1.66.10^{-4}T)$ and $\rho = 7870[1 - 44.643.10^{-6}T\exp(2.31.10^{-4}T)]$

For URFAC, URVAC, URMAC, density is given at +/-1%, specific heat capacity at +/- 5% and conductivity at +/- 7% (IRSID data)

Table A2-3: Work-rolls thermal properties. Hi-Cr: High Chromium content; Hi-V: High Vanadium content.
Propriétés thermiques des cylindres. Hi-Cr : Haute teneur en chrome ; Hi-V : Haute teneur en Vanadium.

Interface exchanges

IHTC (Kg/(s3.K))	Scale / Steel	30000	[Krz1],IRSID
	Scale / Roll	20000	IRSID
	Scale / air	8	IRSID
	Steel / air	8	IRSID

Table A2-4: Thermal exchanges between hot rolling materials (Interfacial Heat Transfer Coefficient).
Echanges thermiques entre les matériaux du laminage.

APPENDIX 3: The Acoustic Emission Technique

An Acoustic Emission signal (AE) is a piece of information received by a low amplitude vibration sensor, afterwards amplified and recorded for later treatment. Each signal, or burst, is generated by an event taking place in the volume of the material tested. The most common sources of AE in metals are:

- plastic deformation (dislocation movement, grain boundary slip, twinning…, etc),
- phase transformations,
- friction,
- impacts,
- crack initiation and growth,
- delamination and interface cracks…

Generalities:

Let us consider a material containing a defect and subjected to applied stresses. If the defect moves under this stress, it becomes a source of AE at the origin of elastic transitory waves, which will propagate in the material. So AE allows **real-time** detection of events occurring inside a sample volume, and their evolution.

More precisely, a micro-elementary displacement called "**event**" involves a spherical elastic wave, which propagates in all directions, attenuating as $1/r^2$. When this wave reaches the surface, a surface wave attenuated as $1/r$ is created.

Each type of sensor has a different bandwidth and an optimum response frequency range. The vibration is converted into an electric signal and pre-amplified before being monitored and recorded by the AE computer. Different AE signals can be observed, depending on which kinds of phenomena takes place in the material during the test.

AE is a transient phenomenon and signals delivered by the transducer (piezo-electric ceramic) show up as **bursts**. When bursts can be separated from each others, AE is discontinuous. In the opposite case, it is called continuous. In the latter case, its existence is detected by the augmentation of the amplitude of the background noise.

Each event is characterized by its **shape**. The acquisition hardware can record complete shapes or just the parameters that characterize the wave. The former is much more costly in terms of storage and treatment time, so that in general, only parameters are recorded.

Acoustic Emission signals. 'Shape' characteristics

The stress wave is first translated into an electric tension by a linear amplifier; the amplitude may then be sent to a logarithmic amplifier for translation into decibels (dB).

For continuous emission:

Measures particularly adapted for this kind of emission are the root mean square (RMS) and the average signal logarithmic (ASL) of the tension delivered by the transducer.

RMS:
This value is the result of the average, calculated by intervals of 1s, of the rectified signal (the absolute value of the signal) after *linear* amplification. So, the RMS is not specifically representative of detected bursts but of the level of noise continually detected.

ASL:
This value is the result of the average, calculated by intervals of 1s, of the rectified signal after *logarithmic* amplification.

A	Maximal amplitude
N	Total number of counts
C	Counts to peak
D	Duration (above the threshold)
RT	Rise time
To	Instant of detection of the burst
E	Energy
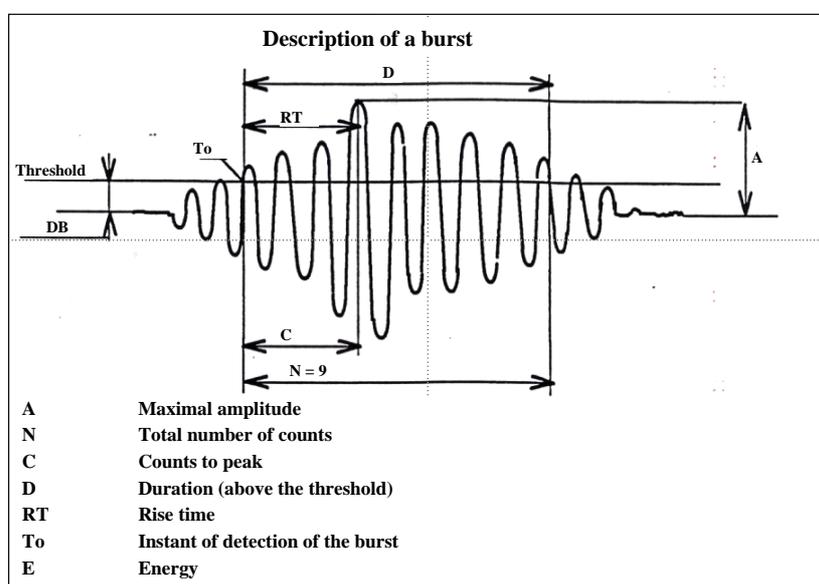
Figure A3-1: Characteristic parameters of a single transient AE wave.

Paramètres caractéristiques d'une onde d'émission acoustique transitoire

For discontinuous emission:

Bursts can be characterized using the following principal shape parameters (Figure A3-1):

Threshold:
A value that separates the background noise from the relevant signals (events). It has to be carefully selected by the user.

Duration D (µs):
D is the time measured on a given burst, between the first and the last crossing of the threshold.

Amplitude A:
The signal maximal amplitude during the duration of a burst. This parameter is very important because it controls the detectability of an event. To be detected, a burst must have an amplitude larger than the threshold chosen by the user.

Conventionally, its unit is the decibel. 0 dB corresponds to 1µV at the transducer exit. The conversion of volt into dB is done by the logarithmic amplifier.

Counts N:
N is equal to the number of alternations in a single burst, with tension higher than or equal to the threshold.

Rise time RT (µs):
RT is the time measured between the first alternation above the threshold and the one with the maximal amplitude in the burst.

Average frequency F (MHz):
F is the ratio between the number of counts N and its duration D.

Energy E:
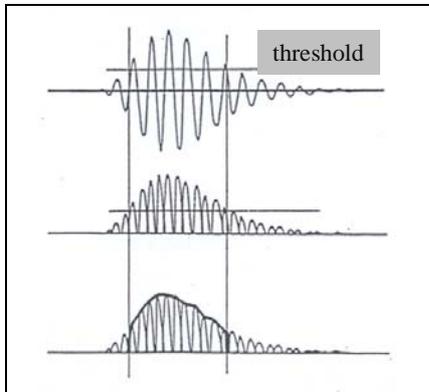
E is the value measured at the exit of the linear amplifier. It is proportional to the surface defined by the envelope of a rectified burst (the line which joins all the maxima of all alternations, Figure A3-2)
This tension is applied to an oscillator controlled in tension.

$$E = \sqrt{\frac{1}{D} \int_D [A(t)]^2 .dt} \qquad \text{in V.sec}$$

Figure A3-2: Energy of a burst

Energie d'une salve

APPENDICES

APPENDIX 4: Inverse analysis

The objective is to determine parameters of constitutive equations for steel and oxide, from the experimental load-deflection curves obtained in 4-PHBT, using an inverse analysis method based on FEM. To interpret the curves correctly, a good understanding of the layer damage during the test is necessary.

The parameter identification module has been written at CEMEF to identify magnetic and thermal parameters used in induction heating [Fav]. This program has been adapted for mechanical behavior inverse analysis. Identification is fully automatic.

<u>Definition</u>

Material and operational parameters constitute entry data (noted P). The direct model gives the system answer (M^c) as a function of P. This causal relation is summarized in the following equation:

$$M^c = D(P) \qquad\qquad \text{eq. A4-1}$$

Experimental quantities are described by the vector $M^{\exp} = \left\{ M_1^{\exp}, M_2^{\exp}, ..., M_s^{\exp} \right\}$ where s represents the experimental couples. If M^c is different from $M^{\exp}$ then, the input parameters P are not correct. The principle of inverse analysis is to determine P such that M^c approaches experimental values $M^{\exp}$ as well as possible. Consequently, inverting eq.A4-1:

$$P = D^{-1}\left(M^c \right) \qquad\qquad \text{eq. A4-2}$$

The difference between measurable calculated values (M^c) and experimental ones ($M^{\exp}$) is quantified using a cost function Q, which has to fulfil two conditions:

- To be definite positive $Q \geq 0$
- $Q=0$ only if $M^c = M^{\exp}$

If the direct model is perfect (this includes the form of the constitutive equations *and* the solution method), the cost function then admits a global minimum defined by the exact superposition between calculated load-deflection curves and experimental ones.

The inverse method thus consists in finding the set of parameters $\bar{P}$ such that:

$$Q(M^c(\bar{P}), M^{\exp}) = \min_{P \in \mathrm{P}} Q(M^c(P), M^{\exp})$$

where **P** defines the set of admissible physical values.

The key point of this methodology lies in the choice of the **minimization algorithm** and of the **cost function**.

Minimization of the Cost function

For the minimization, we use a deterministic iterative method (gradient-type). Each step applies a correction ΔP to the current estimate value P. The descent direction is calculated so that Q (P+ΔP) is minimum and so:

$$\frac{dQ}{dP}(P + \Delta P) = 0$$

eq. A4-3

The equations being non-linear, it is done in an iterative way:

$$P_{i+1} = P_i + \Delta P_i$$

The cost function is approached using a Taylor development:

$$\frac{dQ}{dP}(P + \Delta P) = \frac{dQ}{dP}(P) + \frac{d^2Q}{dP^2}(P)\Delta P + O(\Delta P^2)$$

eq. A4-4

Thus, eq. A4-3 takes the form:

$$A\Delta P + B = 0 \text{ with A=} \frac{d^2Q}{dP^2}(P) \text{ and } \text{B=} \frac{dQ}{dP}(P)$$

eq. A4-5

Choice of the cost function

Q is defined in the least squares sense:

$$Q = \sum_{i=1}^{s} \beta_i (M_i^{\exp} - M_i^{c})^2$$

eq. A4-6

with β_i an adimensionalisation weight coefficient equal to $\dfrac{1}{\left(M_i^{\exp}\right)^2}$.

This cost function is interesting because it respects both conditions imposed before. It is continuously differentiable, which is essential for the minimization method that we use. This kind of cost function allows us to use a Gauss-Newton algorithm, neglecting the 2nd order terms. Matrix A become:

$$A_{jk} = 2\sum_{i=1}^{s} \beta_i \frac{dM_i^c}{dP_j} \frac{dM_i^c}{dP_k}$$

eq. A4-7

The right-hand side vector B:

$$B_k = 2\sum_{i=1}^{s} \beta_i (M_i^c - M_i^{\exp}) \frac{dM_i^c}{dP_k}$$

eq. A4-8

$\dfrac{dM_i^c}{dP_k}$ (noted S_{ik}) is called **sensitivity matrix**.

Derivative computation

There are several methods to calculate the derivatives:

- **Analytical (direct** or **adjoint state)**. They present the advantage to be very precise, but require a complex coding in the core of the code. This could not be done in the time assigned.
- **Numerical** : these are easy to develop, however their disadvantages are the computing time (an iteration at the time of identification requires the calculation of N+1 direct models where N is the total number of parameters to be identified) as well as the precision (due to the perturbation parameter, and the round-off numerical).

Nevertheless, we have used the latter method as the best compromise. Derivatives can be written (decentered right finite difference method):

$$S_{ij} = \frac{M_i^c(P + \delta P_j) - M_i^c(P)}{\delta P_j}$$

eq. A4-9

where [S] is the sensitivity matrix. The smaller δP, the more accurate the derivative calculation is. Nevertheless, this value is limited by the rounding errors made on the calculation of M_i^c. The value of δP has been fixed at 10^{-2}.

Parameter identification algorithm by inverse analysis

Iterative minimization procedure of cost function:

1. Choice of initial set of parameters P^0 and initialization of i: i = 0
2. Cost function calculation $Q(P^i)$. If $Q(P^i) < \varepsilon$ (ε is an imposed value) $\Rightarrow$ parameters are supposed to be identified $\Rightarrow$ exit.
3. Calculation of sensitivity matrix: $S_{ik} = \dfrac{dM_i^c}{dP_k}$
4. Construction of the linear system with $B_k^i = \dfrac{dQ(P^i)}{dP_k}$ and $A_{jk}^i = \dfrac{d^2Q(P^i)}{dP_j dP_k}$
5. Calculation of ΔP^i by solution of $A^i \Delta P^i = -B^i$ (Gauss-Newton method)
6. Stagnation test: if $\left\| \Delta P^i / P^0 \right\|_2 \le \delta_S \Rightarrow$ cost function reached a minimum $\Rightarrow$ exit.
7. Else: re-initialisation $P^{i+1} = P^i + \Delta P^i$, i=i+1, and back to stage 2.

```
        ┌──────────┐
        │   I=0    │
        │  P=P^I   │
        └────┬─────┘
             │
  ┌──────────┼─────────▶
  │          ▼
┌───────┐  ╭────────────────────╮       ╭──────────────────╮
│ I=I+1 │  │ Direct simulation with│     │ Exp. Data M^ex   │
└───┬───┘  │   P^I → M^c(P^I)     │     ╰──────────────────╯
    ▲      ╰──────────┬─────────╯
┌──────────────┐      ▼
│P^{I+1}=P^I+δP^I│  ┌──────────────────────────┐
└──────┬───────┘  │ Q(P^I)=Q(P^I,M^c(P^I),M^ex) │◀─
       ▲          └──────────┬───────────────┘
       │                     ▼
       │            ┌──────────────┐
  No   │            │ Q(P^I) < ε ? │
◀──────┘            └──────┬───────┘
                      Yes  ▼
                   ┌────────────────┐
                   │ P^I is identified│
                   └────────────────┘
```
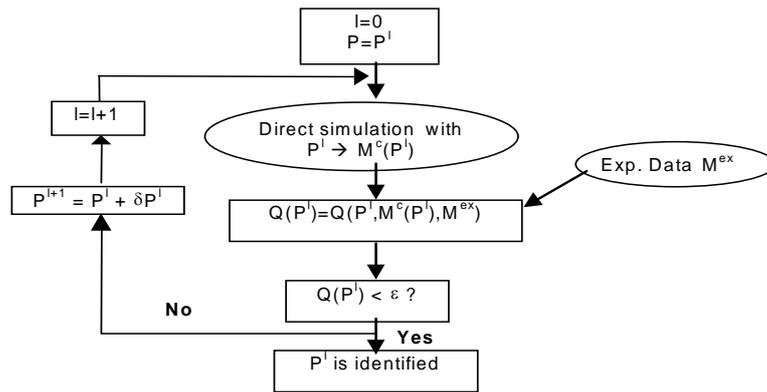
Figure A4-1: General flowchart for automatic identification

Diagramme général de l'identification automatique.

APPENDIX REFERENCES

[Fav]   Y.Favennec, V.Labbe, F.Bay, Identification of physical parameters involved in induction heating processes, In: *Proc. ESAFORM'00*, Stuttgart, (2000), pp.19-22.

[Fle]   J.D.Fletcher, Y.H.Li, J.H.Beynon, C.M.Sellars, The influence of surface conditions in hot forming determined by ring upsetting: a numerical and experimental investigation, Proc. Instn. Mech.Engrs. Vol. 212 part J, (1998), pp.453-465.

[Krz1]   M.Krzyzanowski, J.H.Beynon, C.M.Sellars, Analysis of secondary oxide-scale failure at entry into the roll gap, Met. Mat. Trans. B, vol.31B, (December 2000), pp.1483-1490.

[Lee]   Y.Lee, B.M.Kim, K.J.Park, S.W.Seo, O.Min, A study for the constitutive equation of carbon steel subjected to large strains, high temperatures and high strain rates, J. Mater. Process. Technol. 130-131, (2002), pp.181-188.

[OTU]   (anonymous) : Brochure rassemblant un certain nombre de données tirées de la bibliographie sur les propriétés de quelques aciers à usage fréquent. OTUA (Office technique de l'utilisation de l'acier) - in French

[Pie1]   M.Pietrzyk, J.G.Lenard, Thermal-Mechanical Modelling of the Flat Rolling Process, Springer-Verlag, Berlin, (1991).

[Pie2]   M.Pietrzyk, J.G.Lenard, A study of thermal-mechanical modelling of flat rolling, J. Mater. Shaping Technol. Vol.7 n°2, (1989), pp.117-126.

[Schü]   M. Schütze: Mechanical properties of oxide scales, Oxid. Met. 44 n°1-2, (1995) pp.29-60.

[Sel]   C. M.Sellars, W.J.Mc.G.Tegart: La relation entre la résistance et la structure dans la déformation à chaud, Mém. Sci. Rev. Mét. 63 (1966), pp.731-746.

[Shi]   S. **Shida**, Empirical formulae of flow stress of **carbon steels**, J. Japan Soc. Technol. Plasticity 10, 103 (1969), pp.610-615.

[Tak]   Y. Takeuti, S. Komori : Thermal stress problems in industry. 3 : temperature dependency of elastic moduli for several metals from –196°C to 1000°C, J. Thermal Stresses 2, (1979), pp.223-250.

[Torr]   M.Torres, R.Colas, A model for heat conduction through the oxide layer of steel during hot rolling, J. Mater. Process. Technol. 105, (2000), pp.258-263

[Tru]   M.Trull, J.H.Beynon, High temperature tension tests and oxide scale failure, Mater. Sci. Technol. vol.19, (June 2003), pp.749-755.

[Zho]   S.X.Zhou, An integrated model for hot rolling of steel strips, J. Mater. Process. Technol. 134, (2003), pp.338-351.

APPENDICES

Résumé

Le laminage à chaud des aciers représente une des étapes les plus critiques dans l'obtention de produits finis ayant une bonne qualité de surface. L'augmentation de la productivité ajoutée à l'accroissement des besoins du client induit des règles de plus en plus sévères pour les trains à bandes. L'aspect de surface d'une bande est un enjeu très important en termes de coûts d'opération du laminoir et de limitation de productivité.

Parmi tous les défauts de surface, le plus défavorable provient de la couche d'oxyde (calamine) formée à la surface de l'acier pendant le laminage à chaud, à l'entrée du finisseur (dernière partie du laminoir) : la calamine secondaire dont le comportement mécanique est toujours mal connu.

La calamine secondaire peut être fissurée sous les contraintes imposées par les passes successives de laminage, et peut être incrustée dans son substrat en acier ; ce défaut est appelé « défaut de calamine incrustée ». De plus, l'extrusion du métal sous-jacent dans les fissures de calamine engendre d'importantes modifications locales des conditions de frottement et de transfert thermique. En conséquence, une description précise des mécanismes de déformation de la calamine est nécessaire pour définir au mieux les conditions aux limites sous emprise, et mieux comprendre les mécanismes de défauts d'incrustation.

Notre objectif scientifique est donc de réaliser un modèle physique et numérique réaliste, capable de simuler l'écoulement de la calamine dans une emprise de laminage, et en particulier son endommagement.

Après la présentation du procédé industriel et du contexte de l'étude, les propriétés physiques et mécaniques des calamines dans le finisseur sont mises en évidences. Le logiciel éléments finis Forge2® sélectionné pour cette étude pour simuler le comportement de la calamine dans une cage de finisseur est présenté. Les développements numériques réalisés pour simuler les différents types d'endommagement de la calamine (fissure, décohésion, glissement, extrusion) sont décrits. Trois tests mécaniques ont été sélectionnés pour reproduire les sollicitations subies par la couche d'oxyde en entrée d'emprise et pouvant conduire à sa fissuration : le test de flexion 4 points, le test de traction et le bipoinçonnement. Une étude numérique est réalisée en parallèle.

Avec ces trois essais mécaniques, réalisés à chaud, la description mécanique d'une cage de laminage est suffisamment complète pour simuler le procédé industriel dans de bonnes conditions.

Mots clefs : calamine, laminage à chaud, finisseur, simulation numérique, fissures, méthode éléments finis, émission acoustique, test de flexion 4 points

---

Abstract

Hot rolling of steels represents one of the most critical steps to achieve finished products with high surface quality. The increasing productivity added to the rising customer requirements result in more and more severe scheduling rules for the HSM. Strip surface aspect is very important in terms of HSM operation costs and productivity limitation.

Among all surface defects, the most crippling comes from the oxide scale formed at the surface of the steel during the hot rolling, at the entry of the finishing mill (last part of the hot strip mill): the secondary scale, mechanical behaviour of which is still poorly known.

The secondary scale may fracture under the stresses imposed by the successive rolling passes, and can be embedded in the steel strip surface : this defect is called "rolled-in scale defect".

In addition, the extrusion of the subjacent metal inside the oxide cracks induces large local modifications of friction and heat transfer conditions. Consequently, a precise description of oxide scale deformation mechanisms is necessary to better define the boundary conditions in a roll bite and to better understand the initiation mechanisms of rolled-in scale defects.

Our scientific objective is then to provide a realistic physical and numerical model to simulate the oxide scale flow in the roll bite and in particular, its damage.

After the presentation of the industrial process and the context of this study, the physical and mechanical properties of the oxide scale in the finishing mill are investigated. We introduce the Forge2® finite element software, selected for this study to simulate the oxide scale behaviour in a finishing mill stand. The numerical developments performed to simulate the different kinds of oxide damage are described. Three mechanical tests have been selected to approach the solicitations undergone by the oxide scale at the entry of the roll gap, suspected to be critical for damage: the 4-point hot bending test, the hot tension test and the hot plane strain compression test. A numerical study is performed in parallel.

Based on constitutive data obtained from these three mechanical tests, the mechanical description of a rolling stand is sufficient for satisfactory simulation of the industrial process.

Keywords : oxide scale, steel, hot rolling, finishing mill, numerical simulation, cracks, finite element method, acoustic emission, 4-point bending test